R. C. Patel Educational Trust's
R. C. Patel Arts, Commerce and Science College
Shirpur-425405, Karvand Naka, Dist.- Dhule (Maharashtra)
E-mail - principal@rcpasc.ac.in

Affiliated to: K. B. C. North Maharashtra University, Jalgaon-425001

Self Study Report (SSR): 2024 (4th Cycle)

Criteria - 3
Research, Innovations and Extension

Key Indicator – 3.3
Research Publication and Awards

Metric No. – 3.3.1 (QnM)

Number of research papers published per teacher in the Journals as notified on UGC CARE list during the last five years

Submitted to

National Assessment and Accreditation Council, Bangalore

R. C. Patel Educational Trust's
R. C. Patel Arts, Commerce and Science College
Karvand Naka, Shirpur 425405, Dist - Dhule, Maharashtra
☎: (02563) 299328
E-mail: principal@rcpasc.ac.in

President
Hon. Bhupeshbhai Patel

Principal
Dr. D. R. Patil

Date: 15/06/2024

Declaration

This is to declare that, the information, reports, true copies of the supporting documents, numerical data etc. submitted in these files is verified by Internal Quality Assurance Cell (IQAC) and it is correct as per the office record.

This declaration is for the purpose of NAAC accreditation of the HEI for the 4th cycle assessment period 2018-19 to 2022-23.

Place: Shirpur

Date: 15/06/2024

Dr. Sandip P. Patil
IQAC Co-ordinator
IQAC Coordinator
R. C. Patel Educational Trust's
R. C. Patel Arts, Commerce and Science College
Shirpur, Dist.-Dhule (M.S.) 425405

R. C. Patel Arts Commerce and Science College Shirpur ★ R. C. Patel Educational Trust's

Dr. D. R. Patil
IQAC Chairman & Principal
PRINCIPAL
R. C. Patel Educational Trust's
R. C. Patel Arts, Commerce and Science College
Shirpur, Dist.-Dhule (M.S.) 425405

Journal Pre-proof

Growth mechanism and transport properties of chemically deposited $Pb_xCd_{1-x}S$ thin film's photoelectrochemical (PEC) solar cell

K.E. Suryavanshi, R.B. Dhake, A.M. Patil, M.R. Sonawane

PII: S0030-4026(20)30844-5

DOI: https://doi.org/10.1016/j.ijleo.2020.165008

Reference: IJLEO 165008

To appear in: *Optik*

Received Date: 22 February 2020

Revised Date: 20 May 2020

Accepted Date: 27 May 2020

Please cite this article as: Suryavanshi KE, Dhake RB, Patil AM, Sonawane MR, Growth mechanism and transport properties of chemically deposited $Pb_xCd_{1-x}S$ thin film's photoelectrochemical (PEC) solar cell, *Optik* (2020), doi: https://doi.org/10.1016/j.ijleo.2020.165008

"Growth mechanism and transport properties of chemically deposited $Pb_xCd_{1-x}S$ thin film's photoelectrochemical (PEC) solar cell"

K. E. Suryavanshi[a,*], R. B. Dhake[b], A. M. Patil[c], M. R. Sonawane[c],

[a] *Department of Applied Science, R. C. Patel Institute of Technology, Shirpur-425405, India.*
[b] *Department of Chemistry, Dadasaheb D. N. Bhole College, Bhusawal-425201, India.*
[c]*Department of Physics, R. C. Patel Arts, Commerce and Science College, Shirpur-425405,* India.

ABSTRACT

The dc conductivity and thermoelectric power of $Pb_xCd_{1-x}S$ ($0 \leq x \leq 1$) thin films were fabricated and investigated for the solar cell efficiency. The deposition parameters such as time, concentration, temperature, and pH of the solution were optimized to get superior quality thin films. The optical properties revealed that the band gap of the films decreased as the composition parameter '*x*' increased. XRD results show the films are polycrystalline with an individual hexagonal (CdS) and cubic (PbS) structure. FESEM revealed that the films have uniform surface morphology over the entire substrate. The crystallite size measured by XRD and FESEM studies was found to be varied with composition '*x*'. EDXS shows a compositional analysis of prepared films.

The four probe technique is used to estimates the electrical conductivity (σ) and thermal activation energy at room temperature. The TEP data are analyzed to calculate electron carrier density (n) and mobility (μ) of $Pb_xCd_{1-x}S$ thin films at a temperature of 45 °C to 110 °C. In the photoconduction study, it is observed that dark current rises linearly with applied voltage and photocurrent varies with applied voltage. $Pb_xCd_{1-x}S$ thin film's PEC solar cell was characterized by determining the open-circuit voltage (V_{oc}), short circuit current (I_{sc}), maximum power (P_{max}), fill factor (ff) and efficiency (η %). The area 0.2 cm^2 is selected for the sample cell and was illuminated by a 90 mW/cm^2 solar radiation. From the I-V higher magnitudes fill factor 37.02 % and conversion efficiency 0.10940 % is obtained for composition $Pb_{0.2}Cd_{0.8}S$.

Keywords:$Pb_xCd_{1-x}S$ thin films, CBD, Electrical, TEP, Photoconduction properties, PEC solar cell.

1. Introduction

In the past few decades, II-VI and IV-VI group compound materials having unambiguous physical properties like high-efficiency, high optical absorbance, and direct band gap, are considered to be potential materials in respect for a wide spectrum of optoelectronic applications such as photodetectors, photovoltaic devices, lasers, IR detector, solar control coatings, solar cells etc. [1-4]. These materials can be deposited in thin film form by various techniques, such as vacuum deposition, chemical bath deposition, chemical vapor deposition, electro-deposition, spray pyrolysis and sol-gel methods [5-13]. The $Pb_xCd_{1-x}S$ thin films are well known key hi-tech material due to its major applications in various optical and electronic devices [14].

Lead sulphide (PbS) is IV- VI semiconductor material with band gap 0.41 eV and its band gap can be improved by decreasing size of crystallites. This change in band gap in PbS can be obtained for comparatively larger crystallite size as Bohr excitonic radius is comparatively larger than other chalcogenides [15]. Among the II-VI semiconductors, Cadmium sulphide (CdS) thin films are a representative n-type material with many applications such as large-area electronic devices and solar cells, it has a wide direct band gap (2.42 eV) so has been used as a window material together with several semiconductors such as CdS,Cu_2S etc. [16].

The band gap of CdS has been improved by mixing it with Pb ions. As we know that CdS and PbS are highly sensitive to light and in view of their practical application, a study of their mixed thin film structure is important as an electrochemical converter [17-18]. M. A. Barote, et.al reported that the broad and fine-tunable band gap properties of $Pb_xCd_{1-x}S$ thin films are suitable for many scientific studies and technological applications such as transparent electrodes, solar cells, gas sensors, piezoelectric and optoelectronic devices [18]. In this present paper, we report the deposition of $Pb_xCd_{1-x}S$ thin films on both corning glass and fluorine-doped tin oxide (FTO) substrates by using a chemical bath deposition method. The electrical properties, thermoelectric power, and photo conduction property are studied over room temperature and a wide range of temperatures respectively.

2. Experimental

2.1. Synthesis of $Pb_xCd_{1-x}S$ thin film

The chemical bath deposition technique was used to prepare $Pb_xCd_{1-x}S$ thin films. In this technique, bath solution was prepared by mixing the appropriate volumes of 0.1M Lead Acetate [$Pb(CH_3COO)_2.2H_2O$], 0.1M Cadmium Acetate [$Cd(CH_3COO)_2.2H_2O$], 1M Thiourea [$(NH_2)_2.CS$]. The bath solution was made alkaline by adding 6M Ammonia [NH_3], under a constant stirring process. The ultrasonically cleaned substrate is used for the deposition of $Pb_xCd_{1-x}S$ thin film and then substrate washed by using distilled water and Acetone, after that dry it completely [8].

Take bath solution in a glass beaker and place this beaker in a chemical bath and set temperature 75 °C. When the temperature reaches 50 °C place substrate vertically in solution and adds 20ml of 1M Thiourea drop by drop in a beaker until the temperature rises from 50 °C to 75 °C. After deposition cools it to room temperature and cleaned with distilled water and dried in air. All $Pb_xCd_{1-x}S$ films exhibited yellowish to deep black color [19].

2.2. Characterization of $Pb_xCd_{1-x}S$ thin film

UV-Visible 2400 spectrophotometer used to optical measurements of thin films at room temperature at wavelengths ranging from 400 to 800 nm. Bruker D8 Advance diffractometer with CuKα1 radiation X-ray diffraction (XRD) techniqueis used to investigate the structural property of the thin films. The scanning ranges 20° to 90° used for thin films for 20 min.

The scanning electron micrographs (SEM) of different films were also investigated by using Hitachi S-4800-Type-II (Hitachi High Technology Corporation). For compositional analysis Energy-dispersive X-ray Spectroscope (EDXS) technique is used and is done by using X-Flash detector 5030, Bruker (Berlin-Germany) attached to the SEM [8, 19, 20].

The electrical property of the $Pb_xCd_{1-x}S$ thin films was measured by the conventional four-probe technique using direct current at room temperature and thermoelectric power was investigated by using thermoelectric power measurement at temperature 45 °C to 110 °C.

Photoconductivity measurements were carried out at room temperature by connecting it in series with a Pico ammeter and a dc power supply [21].

2.3. Growth mechanism of thin film

$Pb_xCd_{1-x}S$ thin films are prepared by the decomposition of thiourea in an alkaline solution containing lead and cadmium salts.The growth mechanism and rate of formation of $Pb_xCd_{1-x}S$ thin film are most relevant on the rate of release of Pb^{2+}, Cd^{2+}, and S^{2-} ions from the complex state which condense on an ion by ion basis on the glass substrate.

Generally, the $Pb_xCd_{1-x}S$ thin film occurs on a substrate and formed when the ionic product (IP) of Pb^{2+}, Cd^{2+},and S^{2-}exceeds solubility product (SP) of PbS and CdS. The ratio (IP/SP) = S gives the supersaturation of the ions over the $Pb_xCd_{1-x}S$ layer.

A slow release of lead or cadmium (Pb^{2+} or Cd^{2+}) ions is reached by the dissociation of a complex species of lead or cadmium such as tetra amine lead II $[Pb(NH_3)_4]^{2+}$ or tetra amine cadmium II $[Cd(NH_3)_4]^{2+}$ complexion. S^{2-} ions are supplied by the decomposition of organic sulphur compounds, such as thiourea. The $Pb_xCd_{1-x}S$ precipitate was formed by the controlled chemical bath deposition technique. The S^{2-} ion, released from thiourea, in alkaline medium reacts with Pb^{2+} and Cd^{2+} ions and forms the $Pb_xCd_{1-x}S$ compound as per the following reaction [7].

The formation of $Pb_xCd_{1-x}S$ ($0 \leq x \leq 1$) thin film may involve the following steps [7, 9, 22-24].

i) Formation of ammonia ion: - The hydrolysis of ammonia in water gives ammonia ion and hydroxide ions [25].

$$NH_3 + H_2O \longrightarrow NH^+_4 + OH^- \quad \ldots (1)$$

ii) Formation of lead complex

$$Pb(CH_3COO)_2 \longrightarrow Pb^{2+} + 2CH_3COO^{2-} \quad \ldots (2)$$

$$Pb^{2+} + 4NH_3 \longrightarrow Pb(NH_3)^{2+}_4 \quad \ldots (3)$$

iii) Formation of cadmium complex

$$Cd(CH_3COO)_2 \longrightarrow Cd^{2+} + 2CH_3COO^{2-} \quad \ldots (4)$$

$$Cd^{2+} + 4NH_3 \longrightarrow Cd(NH_3)^{2+}_4 \quad \ldots (5)$$

iv) Formation of the S^{2-}ion

In the alkaline medium dissociation of $CS(NH_2)_2$ takes place

$$CS(NH_2)_2 + OH^- \longrightarrow CH_2N_2 + H_2O + SH^- \quad \ldots (6)$$

$$SH^- + OH^- \longrightarrow S^{2-} + H_2O \quad \ldots (7)$$

Then the overall chemical reaction is as follows

$$_x[Pb(NH_3)_4]^{2+} + {}_{1-x}[Cd(NH_3)_4]^{2+} + S^{2-} \longrightarrow Pb_xCd_{1-x}S + \text{Waste product.} \quad \ldots (8)$$

2.4. Construction of Photoelectrochemical (PEC) solar cell

For the construction Photoelectrochemical cell, it consists of a semiconductor photoelectrode and the counter electrode which dipped in an electrolyte solution consisting of redox species. The most important fact to construction PEC cell is the long-term stability of cells that show reasonable conversion efficiencies. The desired device structure is, FTO/$Pb_xCd_{1-x}S$/liquid electrolyte/platinum-coated FTO as a back contact as shown in fig. 1.

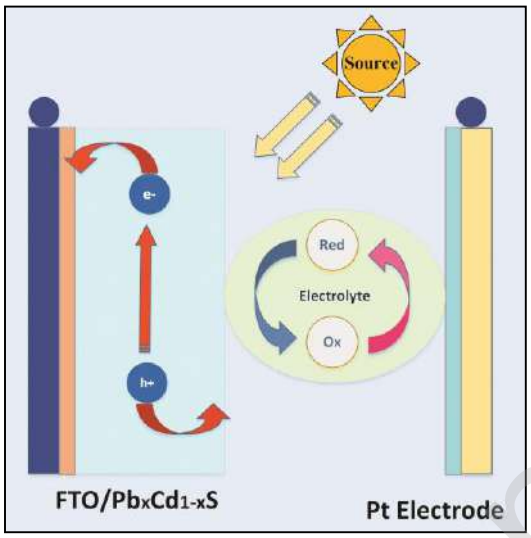

Fig. 1. Device structure

2.5. Photoelectrochemical (PEC) solar cell characterization

The $Pb_xCd_{1-x}S$ materials deposited on the FTO substrates were used for the construction of PEC solar cell. A polysulphide was used as a liquid electrolyte. After assembling the whole setup it is used to characterize the cell in dark and under illumination, a variable voltage was applied across the junction and the current flowing through it was measured.

The measurement of current-voltage (I-V) was performed in forward bias with a computer-controlled instrument Keithley 2611 under the standard condition of cell temperature 25 °C, under the illumination of simulated solar radiation of 90 mW/cm^2. The area of the sample is selected at 0.2 cm^2.

3. Results and discussion

3.1. Significance of the growth mechanism

In a growth mechanism, it is revealed that the film growth and color of the deposited $Pb_xCd_{1-x}S$ thin films changed from yellowish to deep black color. It was found that the growth and thickness of the prepared thin film are increased with the composition parameter. Because at high temperature the rate of release of Cd^{2+} and S^{2-} ions are higher that increases the rate of film growth and the film thickness is increases than earlier reports [25]. The surface profilometer technique was used to calculate the thickness of the $Pb_xCd_{1-x}S$ thin film.The calculated thickness of the film with varying compositions '*x*' listed in table 1.

Table 1. Calculated thickness (nm) of $Pb_xCd_{1-x}S$ thin films

Composition (*x*)	Thickness (nm)
0.0	407
0.2	492
0.4	575
0.6	603
0.8	642
1.0	687

3.2. Optical properties

The optical absorption spectra (fig.2.) of prepared $Pb_xCd_{1-x}S$ thin films were also investigated to evaluate the forbidden energy band gap (Eg). Optical absorbance spectra for the films were recorded by a UV- 2450 spectrophotometer.The spectrum is a plot of absorbance against wavelength obtained at temperature 75 °C. The spectrum shows that the deposited $Pb_xCd_{1-x}S$ thin film starts absorbing at a wavelength of 400 nm which then increases until it reaches a maximum at 800 nm before it starts to decrease. The absorption edge lies between UV-Visible regions.

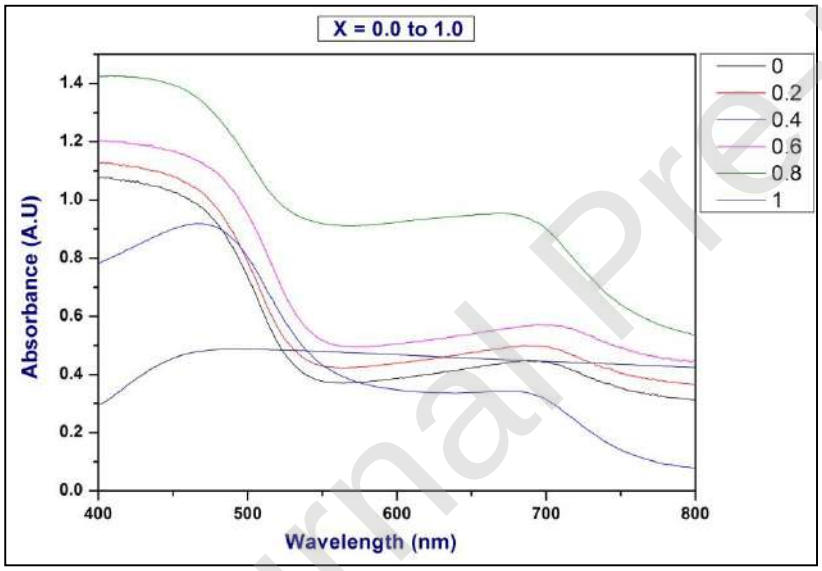

Fig. 2. Absorbance spectra for the $Pb_xCd_{1-x}S$ thin films

The forbidden energy gap (Eg) of synthesized films was determined by using the Tauc formula [26], as shown in equation (9).

$$\alpha h\nu = A\,(h\nu - Eg)^m \quad \ldots (9)$$

Where,
α = Absorption coefficient
h*ν*= Photon energy
Eg = Optical band gap

A = Constant which related to effective masses associated with valance band and conduction band.
m = Assume the value of 1/2, 2, 3/2 and 3 for allowed direct, allowed indirect, forbidden direct and forbidden indirect transition, respectively.

Graphs (Tauc plot) between $(\alpha h\nu)^2$ versus hν is plotted for $Pb_xCd_{1-x}S$ ($0 \leq x \leq 1$) thin films are shown in fig. 3. and the intercept of extra plotted straight line at $(\alpha h\nu)^2 = 0$ axis gives the value of band gap of the material.

The band gap of deposited films was found to be in the range of 2.34 -1.40 eV which very high as compared to the bulk PbS (0.41eV) shown in table 2. Also, it is observed that the band gap of the films reduces with increasing Pb doping content in CdS. This decrease in band gap is consistent with dependence on crystallite size and the alloying of PbS with CdS. As the CdS and PbS are highly sensitive to light and in view of their practical application, a study of their mixed thin film structure as electrochemical converters is of technical importance [7].

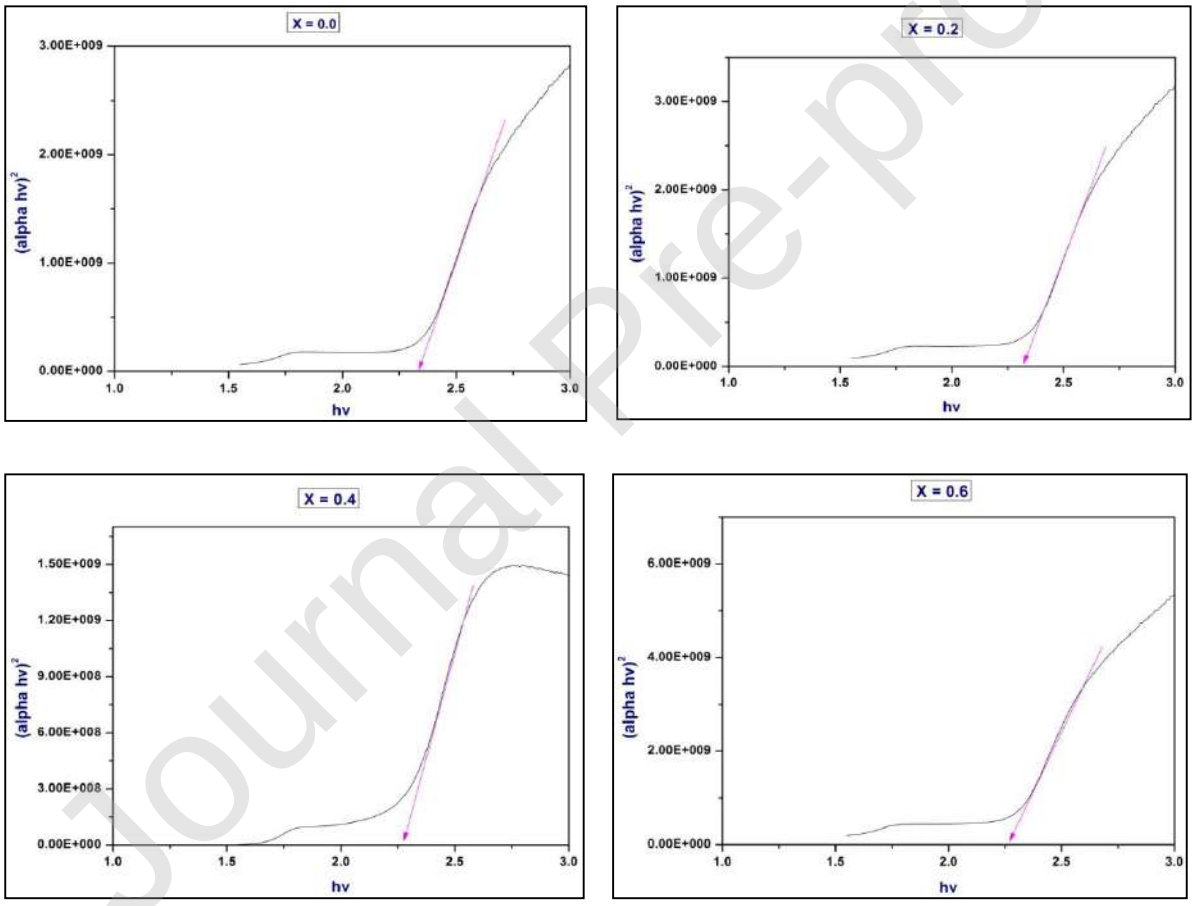

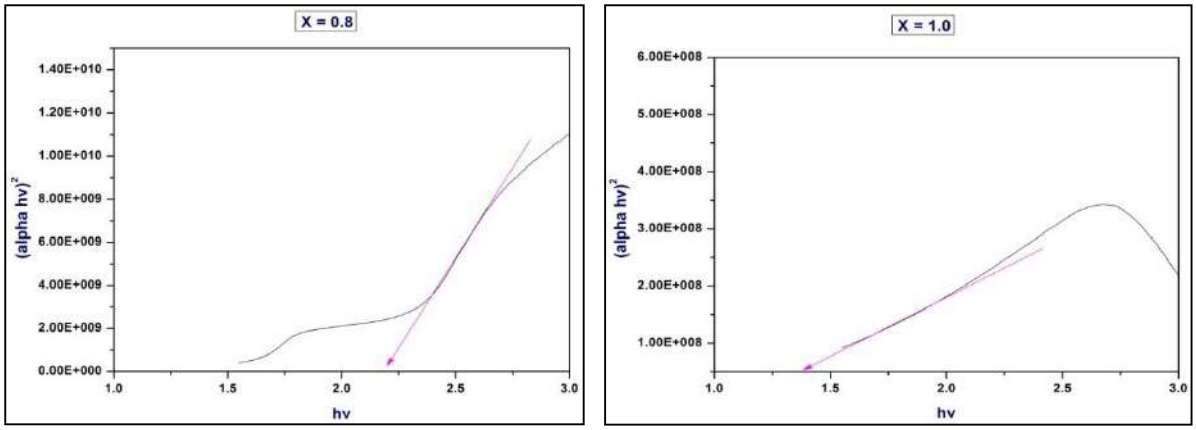

Fig. 3. Shows plots of $(\alpha h\nu)^2$ versus hν for $Pb_xCd_{1-x}S$ thin films

Table 2. Shows composition (*x*) with band gap (eV) of $Pb_xCd_{1-x}S$ thin films

Composition (*x*)	Band gap (eV)
0.0	2.34
0.2	2.31
0.4	2.27
0.6	2.23
0.8	2.18
1.0	1.40

3.3 Structural properties

In order to study the crystalline nature of prepared $Pb_xCd_{1-x}S$ thin films, the XRD pattern was recorded in the 2θ range 20° to 90° shown in fig. 4. The XRD results for films with different compositions show that the films are polycrystalline in nature.

It is observed that CdS exhibits a zinc blend (Hexagonal) crystal structure match with JCPDS (89-2944) [27-29]. Also, PbS is present in cubic crystal form match with JCPDS (78-1058) which reports in some earlier papers [30, 31]. For the $Pb_xCd_{1-x}S$ thin films growth occurs due to strong orientation of (100) plane which analogous to substrate. This orientation change from composition 0.0 to 1.0. This arises due to decrese the intensity of (002) plane reflection and increase intensity of (111) plane reflection. Which indicate that concentration of film changes from Cd to Pb not only the orientation of crystallites but also the cubic content [19, 35]. All the match values for prepared thin films are given in table 3.

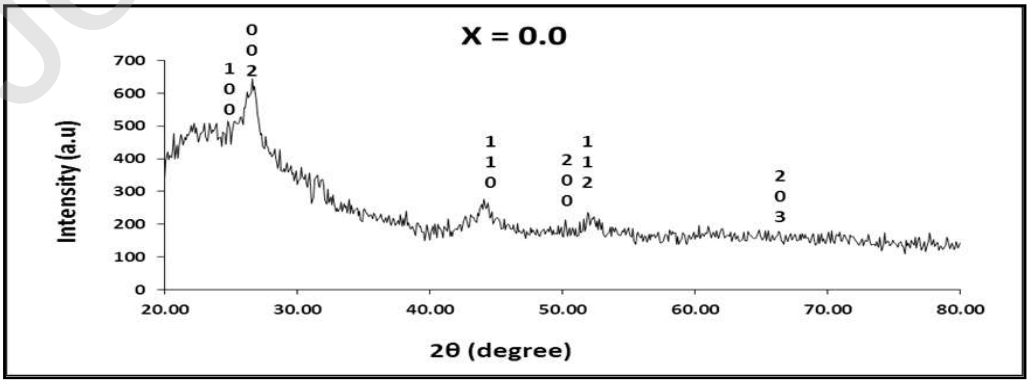

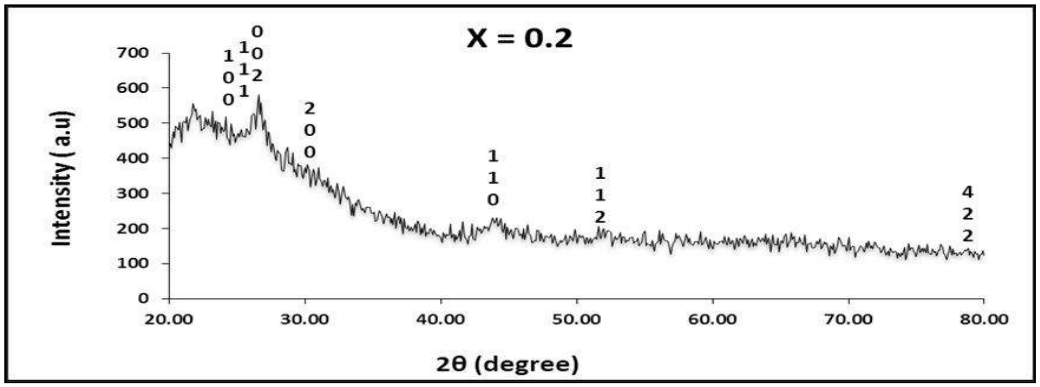

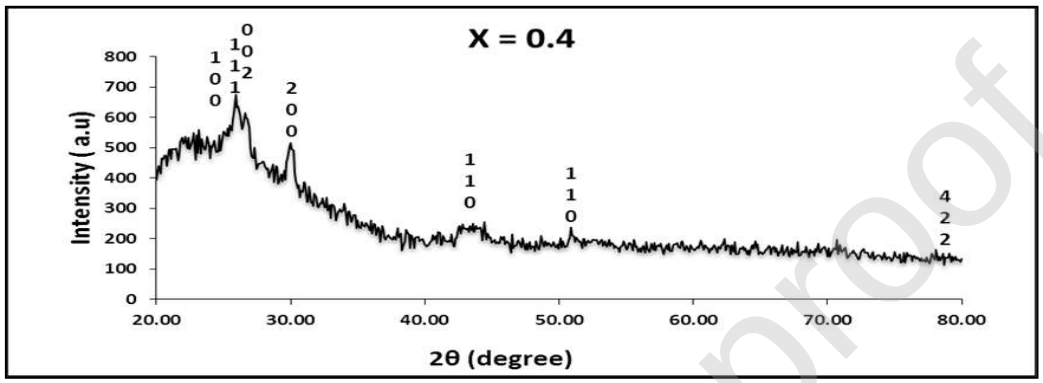

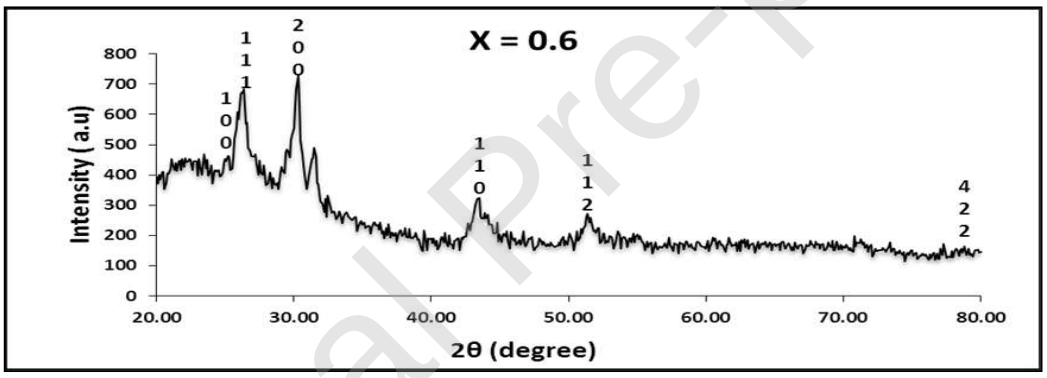

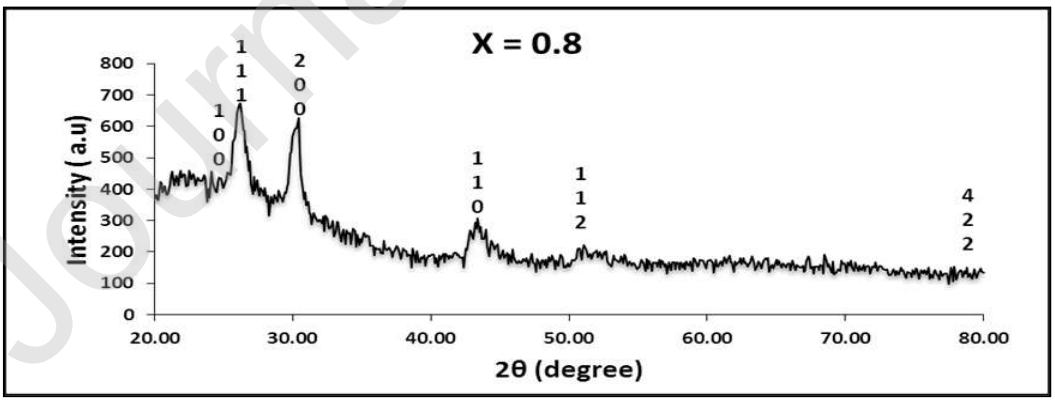

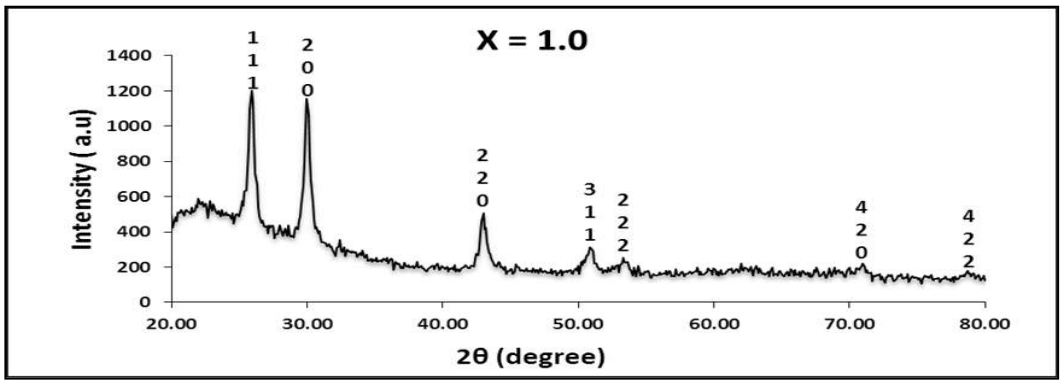

Fig. 4. XRD of $Pb_xCd_{1-x}S$ thin films

All major diffraction peaks for all samples were chosen to estimate the average size of the crystallites byusing DebyeScherer's equation (10).

$$D = 0.94 \lambda / \beta \cos\theta \quad \text{... (10)}$$

Where,
λ is the wavelength of X-ray used,
β is the full width at half maximum in radian, and
θ is the Bragg's diffraction angle.

The crystallite size calculated for the $Pb_xCd_{1-x}S$ thin films having different compositions shown in table 3. The average crystallites size is calculated was ranging between 16.31 nm and 32.61 nm.

Table 3. XRD analysis of the of $Pb_xCd_{1-x}S$ thin films

Composition (*x*)	**2θ theta**	**2d (Std.)**	**2d (Obs.)**	**hkl values**			**Crystal Size (nm)**
***x* = 0.0**	24.80	3.5853	3.5872	1	0	0	23.32
	26.60	3.3575	3.3484	0	0	2	
	44.40	2.0700	2.0387	1	1	0	
	50.20	1.7926	1.8159	2	0	0	
	51.90	1.7620	1.7603	2	0	1	
	66.80	1.3992	1.3993	2	0	3	
***x* = 0.2**	24.80	3.5853	3.5872	1	0	0	27.21
	26.00	3.4245	3.4243	1	1	1	
	26.50	3.3575	3.3608	0	0	2	
	30.10	2.9657	2.9666	2	0	0	
	43.60	2.0700	2.0780	1	1	0	
	51.90	1.7620	1.7603	1	1	2	
	79.00	1.2107	1.2110	4	2	2	
***x* = 0.4**	24.80	3.5853	3.5872	1	0	0	
	26.00	3.4245	3.4243	1	1	1	
	26.50	3.3575	3.3608	0	0	2	

	30.10	2.9657	2.9666	2	0	0	18.12
	43.60	2.0700	2.0742	1	1	0	
	51.80	1.7620	1.7635	1	1	2	
	79.00	1.2107	1.2110	4	2	2	
***x* = 0.6**	24.80	3.5853	3.5872	1	0	0	20.40
	26.00	3.4245	3.4243	1	1	1	
	30.10	2.9657	2.9666	2	0	0	
	43.60	2.0700	2.0742	1	1	0	
	51.60	1.7620	1.7614	1	1	2	
	79.00	1.2107	1.2110	4	2	2	
***x* = 0.8**	24.80	3.5853	3.5872	1	0	0	16.31
	26.00	3.4245	3.4243	1	1	1	
	30.10	2.9657	2.9666	2	0	0	
	43.60	2.0700	2.0742	1	1	0	
	51.20	1.7620	1.7827	1	1	2	
	79.00	1.2107	1.2110	4	2	2	
***x* = 1.0**	26.00	3.4245	3.4243	1	1	1	32.61
	30.10	2.9657	2.9666	2	0	0	
	43.10	2.0971	2.0971	2	2	0	
	51.10	1.7884	1.7860	3	1	1	
	53.50	1.7122	1.7114	2	2	2	
	71.00	1.3263	1.3265	4	2	0	
	79.00	1.2107	1.2110	4	2	2	

(Some XRD data and images already published [32] and are reprinted by permission of journal by mail dated Sat, Aug 31, 7:39 AM)

3.4. Scanning electron microscopy (SEM) studies

Scanning electron microscopy technique used to study the surface morphology of prepared thin films. The SEM micrographs of all the films show uniform surface morphology over the entire substrate shown in fig. 5. It is revealed that SEM images consist of a dense layer with small crystallites and adhere well to substarte without any crash. It can also be seen that in all compositions all small crystals converted to larger crystals and covered entire substarte well during deposition temperature.

It was observed that the surface morphology of composition (x = 0.0, 0.2) shows a sand rose-like structure [25], for composition (x = 0.6) it shows a rice-like structure [9], for composition (x = 0.4, 0.8) it shows a ball-like structure [33] and for composition (x = 1.0) it shows cubic structure [34]. The cubic crystal are more in the case of lead sulphide (x =1.0) composition.

The crystal size was calculated using a standard scale bar method. The scale bar length is 2 μm. It observed that crystal size is different for every change in composition. The crystal sizes of $Pb_xCd_{1-x}S$ thin films obtained by SEM are given in table 4. The average crystal size is calculated was ranging between 20.3 nm and 84.1 nm.

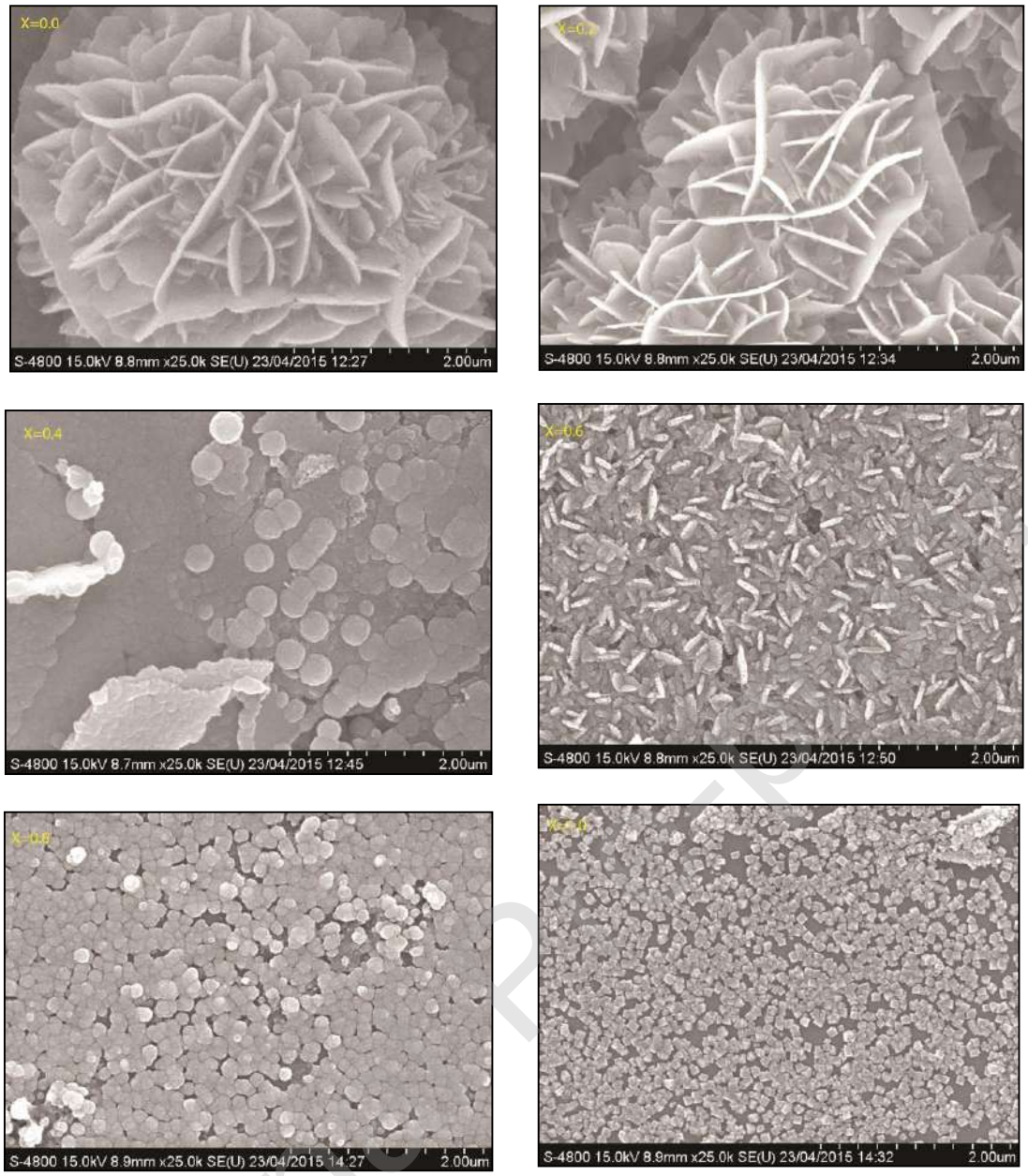

Fig. 5. SEM images of $Pb_xCd_{1-x}S$ thin films

(Some SEM data and images already published [32] and are reprinted by permission of journal by mail dated Sat, Aug 31, 7:39 AM)

Table 4. Crystal sizes of $Pb_xCd_{1-x}S$ thin films

Composition (*x*)	**Crystal Size (nm)**
0	73
0.2	48.4
0.4	70
0.6	20.3
0.8	25.5
1	84.1

3. 5. Energy-dispersive x-ray spectroscope (EDXS) studies

The EDXS analysis of deposit $Pb_xCd_{1-x}S$ thin films is shown in fig. 6. (x = 0.0, 0.6, 1.0). The spectrum shows the presence of Pb, Cd and S elements on substrates. The compositional analysis of the deposited $Pb_xCd_{1-x}S$ thin films is done by using EDXS, shown in table 5. The presence of Pb, Cd, and S in the EDXS analysis is dueto the precursors, lead acetate, cadmium acetate and thiourea respectively. The atomic percentage of the elements in thin films is in close agreement with the volumetric ratio of the elemental precursor chemical solutions taken in the bath during deposition.

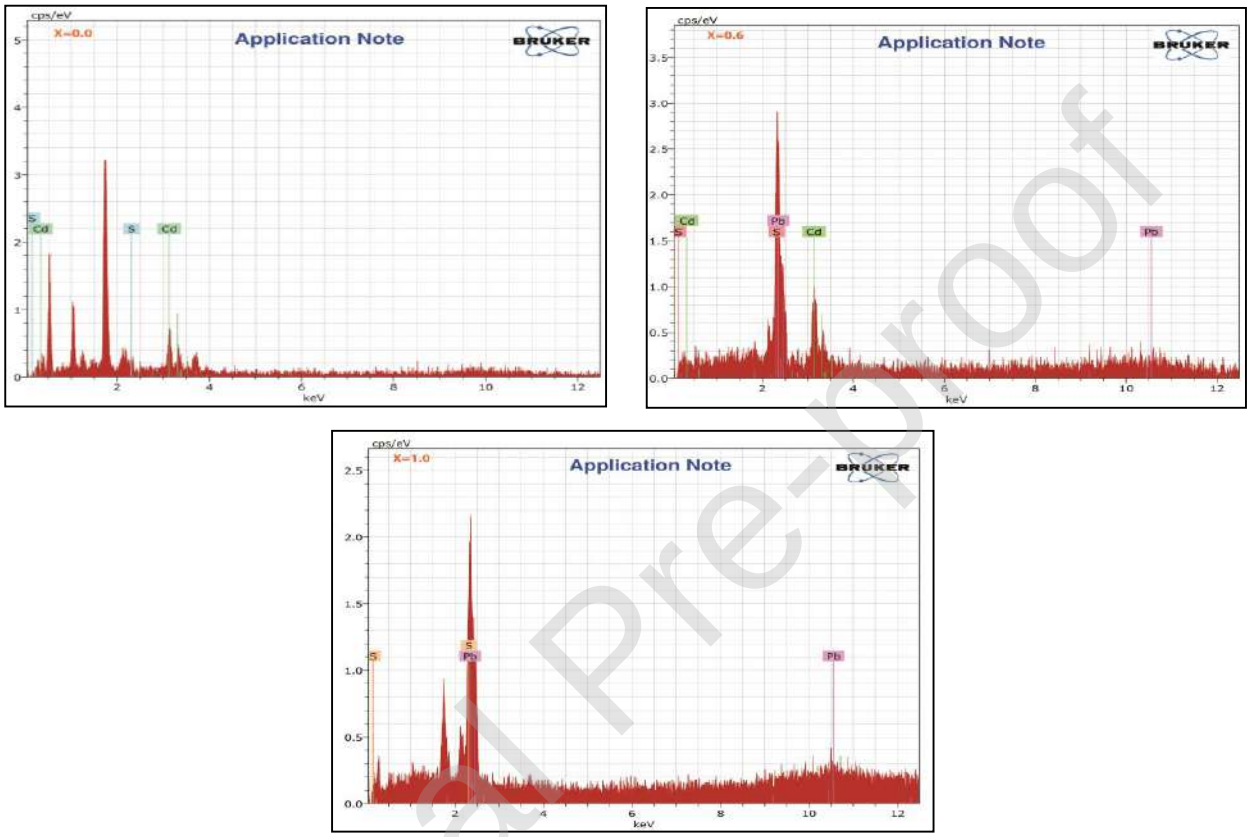

Fig. 6. EDXS Spectrum of x = 0.0 (CdS), x = 0.6 (PbCdS) and x = 1.0 (PbS)

(Some EDXS data and images already published [32] and are reprinted by permission of journal by mail dated Sat, Aug 31, 7:39 AM)

Table 5. Compositional analysis of deposited $Pb_xCd_{1-x}S$ thin films

Composition (x)	**Bath solution of film (%)**			**EDAX analysis (%)**		
	Pb	**Cd**	**S**	**Pb**	**Cd**	**S**
CdS	0	50	50	0	52.13	47.14
$Pb_{0.2}Cd_{0.8}S$	10	40	50	6.15	49.12	43.36
$Pb_{0.4}Cd_{0.6}S$	20	30	50	15.24	36.38	48.16
$Pb_{0.6}Cd_{0.4}S$	30	20	50	28.17	19.63	48.63
$Pb_{0.8}Cd_{0.2}S$	40	10	50	38.54	8.74	47.85
PbS	50	0	50	48.25	0	48.65

3.6. Electrical properties

The electrical properties are of great importance in deciding the quality of the semiconductor device. It involves the measurement of electrical conductivity, thermal activation energy and the nature of conduction mechanism.

The thermal activation energy of $Pb_xCd_{1-x}S$ thin films for different composition was obtained from electrical conductivity studies that are carried out at room temperature. Fig.7. Shows the plot variation of log σ vs 1000/T for $Pb_xCd_{1-x}S$ thin films. The electrical conductivity (σ) is related to temperature (T) according to the Arrhenius relation (11).

$$\sigma = \sigma_0 \exp^{(-Ea/KT)} \quad \ldots (11)$$

Where, σ is the conductivity at temperature T, σ_0 is conductivity at temperature absolute zero, E_a is the activation energy, K is the Boltzmann constant and T is the absolute temperature.

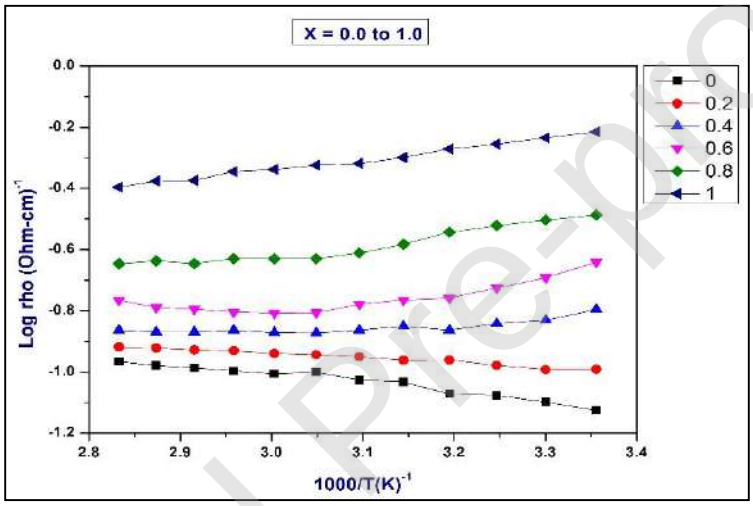

Fig. 7. Variation of log σ versus 1000/T for $Pb_xCd_{1-x}S$ thin films

From fig.7. It has been found that the conductivity decreases thoroughly with an increase in the composition parameter '*x*' in $Pb_xCd_{1-x}S$ thin films and these observations are in good agreement with the earlier reports [25, 35]. An increase in the amount of Pb in the $Pb_xCd_{1-x}S$ thin films leads to an increase in the compensation of sulphur vacancies in the structures and thus it causes resistivity increases and conductivity decreases [35].

Table 6. Shows thermal activation energy values were calculated from the linear portion of these plots [fig. 8]. It is observed that activation energy decreases with increasing '*x*' composition in $Pb_xCd_{1-x}S$ thin films. Because PbS and CdS are deposited simultaneously, an increase in the Pb content in $Pb_xCd_{1-x}S$ thin films indications to an increased amount of PbS formation i.e. it becomes lead rich for higher values of '*x*' leading to an increased concentration of sulphur vacancies and thus in free carrier density [35].

Table 6. Thermal activation energy values of $Pb_xCd_{1-x}S$ thin films

Composition (*x*)	**Thermal activation energy (eV)**
0.0	1.180
0.2	0.949
0.4	0.659
0.6	0.435
0.8	0.222
1.0	0.162

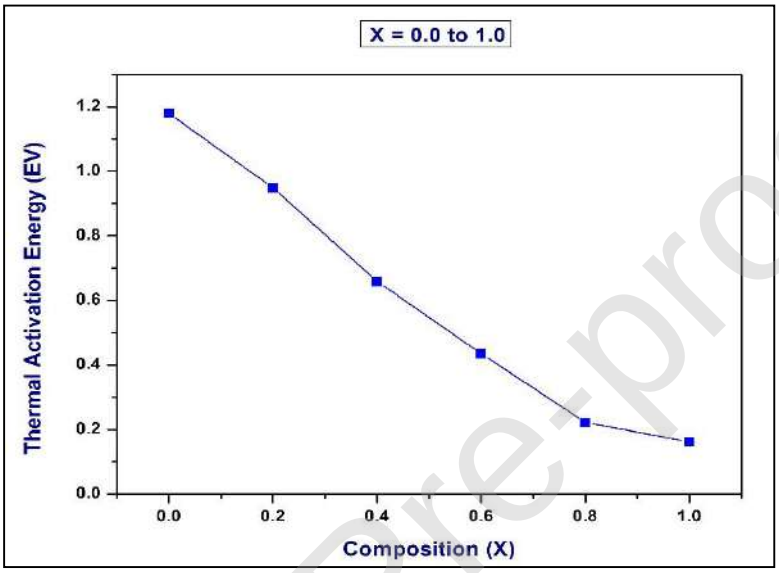

Fig. 8. Variation of thermal activation energy with the composition '*x*' in $Pb_xCd_{1-x}S$ thin films

The activation energy of electrical conduction has been determined from the slope of log σ vs 1000/T plot and its variation with the composition parameter '*x*' in $Pb_xCd_{1-x}S$ thin films is shown in fig. 8. It is observed that activation energy is slowly decreasing from composition x = 0.0 to 1.0 in prepared $Pb_xCd_{1-x}S$ thin films.

3.7. Thermo electric power (TEP)

A temperature difference between the two ends of a semiconductor gives rise to an emf, known as thermo-emf. The thermo-emf is also called as the Seebeck coefficient or thermoelectric power. It is obtained from the ratio of the voltage generated and the applied temperature difference. It is found that the generated thermo-emf is proportional to the temperature difference and is given by the following relation,

$$S = \Delta V/\Delta T \quad \ldots (12)$$

The most key importance of thermo-emf is that it permits one to calculate the values of carrier mobility (μ) and carrier density (n) of a semiconductor given by the following equation (13)

$$TEP = -k/eA + \ln[2[2p\, m_c^{*}\, kT]^{3/2}/nh^3 \quad \ldots (13)$$

Where, A is a thermoelectric factor, n is electron density, h is Plank's constant and mc* is the effective mass of the electron.

After substitution of various constants in the above equation, it simplifies to the following equation,

$$\text{Log } n = 3/2 \log T - 0.005TEP + 15.719 \quad \ldots (14)$$

Also, the electron density was calculated using the equation (15),

$$\mu = \sigma / ne \quad \ldots (15)$$

Where, σ is conductivity, n is electron density and e is a charge.

The type of electrical conductivity revealed by $Pb_xCd_{1-x}S$ thin film is determined by thermo-emf measurement. The measurement of thermo-emf is simple and its sign gives vital information about the type of conduction in semiconductors whether it is p-type or n-type. Thermo-emf is that it enables one to calculate the values of carrier density (n) and carrier mobility (μ) of a semiconductor.

3. 7. 1. Dependence of thermoelectric power (TEP) on temperature

Fig. 9. Shows the plot of thermoelectric power (TEP) versus the temperature of $Pb_xCd_{1-x}S$ thin films for different compositions. It was seen that thermoelectric power increases with an increase in temperature in all compositions. From the figure, it is clear that the thermoelectric power of all samples was found to be negative at all temperaturesfrom 45 °C to 110 °C. The negative value of thermoelectric power indicates that the films are of n-type, majority charge carriers are electrons. For each temperature considered, the increasing amount of Pb concentration increases the magnitude of thermoelectric power.

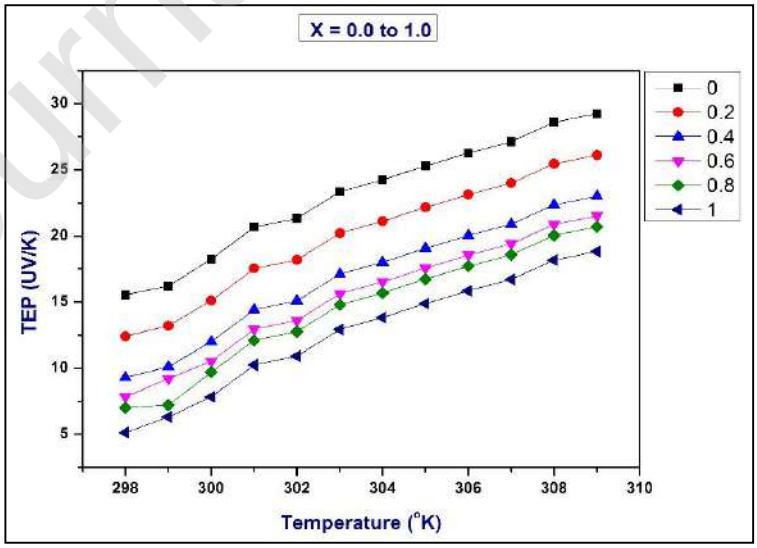

Fig. 9. Variation of TEP vs temperature of $Pb_xCd_{1-x}S$ thin films.

3. 7. 2. Variation of carrier density with reciprocal of absolute temperature

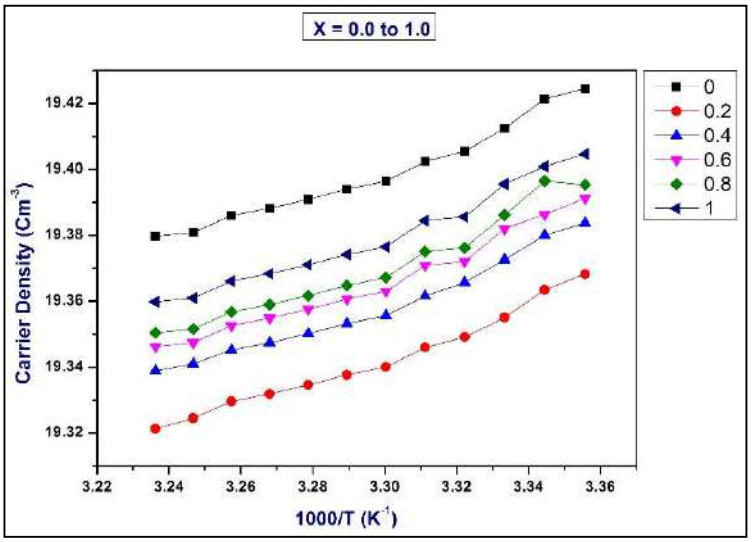

Fig. 10. Variation of carrier density vs 1000/T of $Pb_xCd_{1-x}S$ thin films.

Fig. 10. Shows the variation of carrier density with the reciprocal of the absolute temperature of $Pb_xCd_{1-x}S$ thin films for a different composition. From the figure, it is observed that carrier density is temperature-dependent and an increase in the amount of Pb concentration decreases the magnitude of carrier density.

3. 7. 3. Variation of mobility with reciprocal of absolute temperature

Fig. 11. Shows the variation of mobility with the reciprocal of the absolute temperature of $Pb_xCd_{1-x}S$ thin films for a different composition.

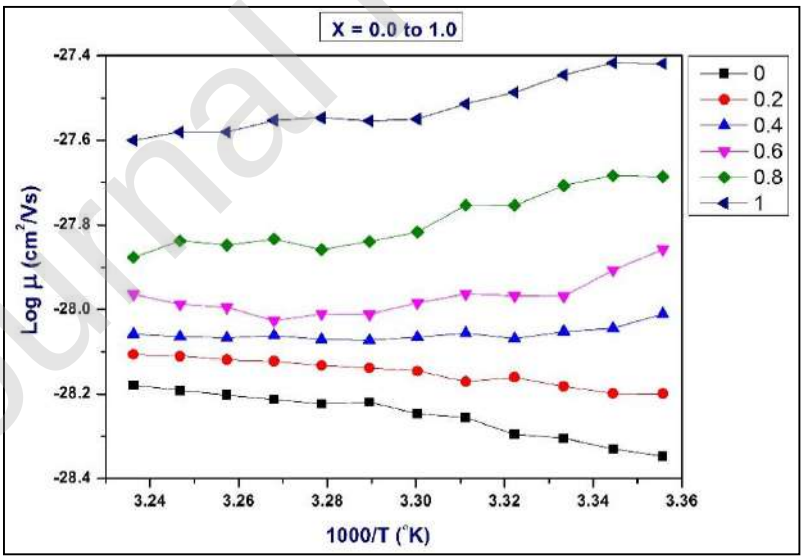

Fig. 11. Shows variation of mobility vs 1000/T of $Pb_xCd_{1-x}S$ thin films.

From the figure, it is observed that mobility increases with temperature, whereas the decrease for increasing Pb concentration in $Pb_xCd_{1-x}S$ thin films. Mobility activation energy

values were calculated from the linear portion of these plots [fig. 11] and presented in table 7. It is observed that mobility activation energy decreases as the Pb concentration increases in $Pb_xCd_{1-x}S$ thin films. It may attribute to a more resistive nature of films having a higher concentration of Pb in $Pb_xCd_{1-x}S$ composition.

Table 7. Mobility activation energy values of $Pb_xCd_{1-x}S$ thin films.

Composition (*x*)	**Mobility activation energy (eV)**
0	1.322
0.2	1.017
0.4	0.904
0.6	0.512
0.8	0.325
1	0.175

A mobility activation energy has been determined from the slope of log μ versus 1000/T. It shows mobility activation energy slowly decreases with composition parameter '*x*' in $Pb_xCd_{1-x}S$ thin films shown in fig. 12.

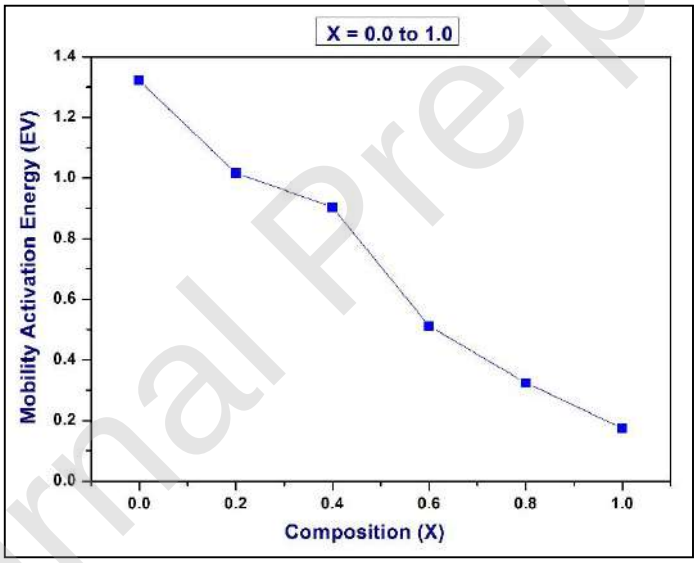

Fig. 12. Variation of mobility activation energy with the composition '*x*' in $Pb_xCd_{1-x}S$ thin films

3. 8. Photoconductivity measurement

The word photoconductivity indicates the improvement of the electrical conductivity of material with the absorption of a suitable photon. On the basis of this definition, every insulator and semiconductor is a photoconductor. Photoconductivity studies of $Pb_xCd_{1-x}S$ i.e. CdS and PbS thin films find wide technological applications in xerography, light detectors, photovoltaic solar energy conversion, and thin film transistors, etc.

In the present study, photoconductivity measurements were done on chemically deposited $Pb_xCd_{1-x}S$ thin films of different compositions at room temperature. The dependence of

photoconductivity on the effect of accelerating voltage into the film was also studied. Experimental set up for photoconductivity measurement as shown in fig. 13.

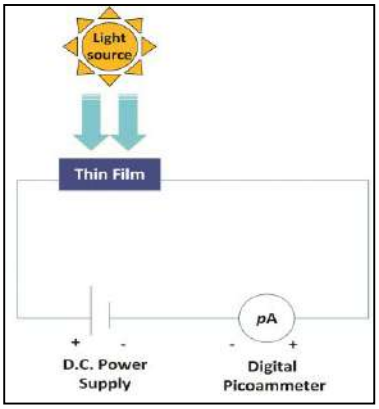

Fig. 13. Circuit diagram for photoconductivity measurement.

3. 8. 1. Effect of accelerating voltage

i) Dark current - accelerating voltage characteristics

To verify the ohmic nature of thin films, the evaporated indium contacts made on to these thin films and the relationship of dark current with applied d. c. voltage was determined. It is clear from the fig. 14. that the dark current rises approximately linearly with applied voltage and decreases with increasing composition in $Pb_xCd_{1-x}S$ thin film. This behavior confirms the ohmic nature of films under investigation.

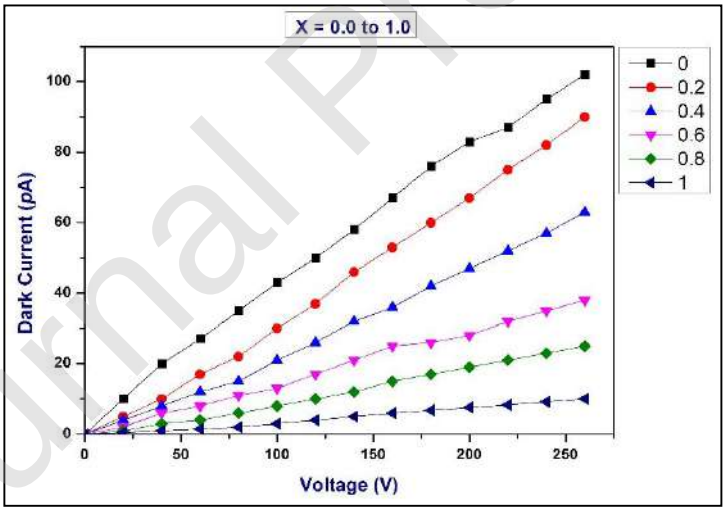

Fig. 14. Effect of accelerating voltage on dark current for $Pb_xCd_{1-x}S$ thin films.

ii) Photocurrent - accelerating voltage characteristics

The variation of photocurrent of each of the $Pb_xCd_{1-x}S$ thin films with applied d. c. voltage at a fixed photoexcitation was observed. In fig. 15. It is observed that photocurrent increases with applied voltage. The increase of photocurrent is much rapid which may be attributed to the fact that; i) The creation of free charge carriers by photoexcitation from valence band and also imperfections states. ii) The contribution to photoconductivity from inter-particle barrier

height modulation by light excitation. The effect of absorption of light in the vicinity of barrier. This efficiently decreases in barrier height and subsequently, a large current is permitted. iii) Increase in carrier lifetime applied fields. The effect of the high field is to reduce the probability of re-trapping considerably and hence, to increase the life time, which results in a rapid rise in a photocurrent with applied fields.

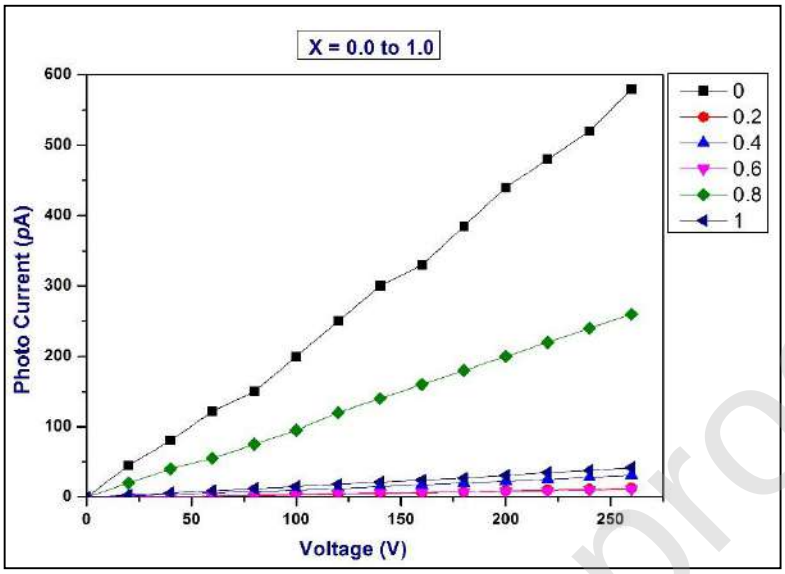

Fig. 15. Effect of accelerating voltage on photocurrent for $Pb_xCd_{1-x}S$ thin films.

The need for ohmic contacts sets an upper limit to the maximum electric field applied to the photoconductor. If the field is increased beyond a critical value, the injection of charge carriers from ohmic cathode will dominate the conductivity process in the material, rather than photoexcitation of carriers. In view of this difficulty, all the electrical and photo conducting measurements have been carried out by applying D.C. potential which falls in the ohmic range of variation.

3. 8. 2. PEC solar cell characteristics

Fig. 16. Shows the current-voltage (I-V) curves for the deposited $Pb_xCd_{1-x}S$ thin films in dark and under a light with visible light. All the films under visible illumination in terms of open-circuit voltage (V_{oc}), short circuit current density (I_{sc}), fill factor (ff) and electron conversion efficiency (η) are matched in table 8.

These (I-V) curves in the dark indicate good junction rectification property. From the I-V measurements it is observed that the higher magnitudes fill factor 37.02 % and conversion efficiency 0.10940 % is obtained for composition $Pb_{0.2}Cd_{0.8}S$. This is a significant improvement as compared to other compositions [19].

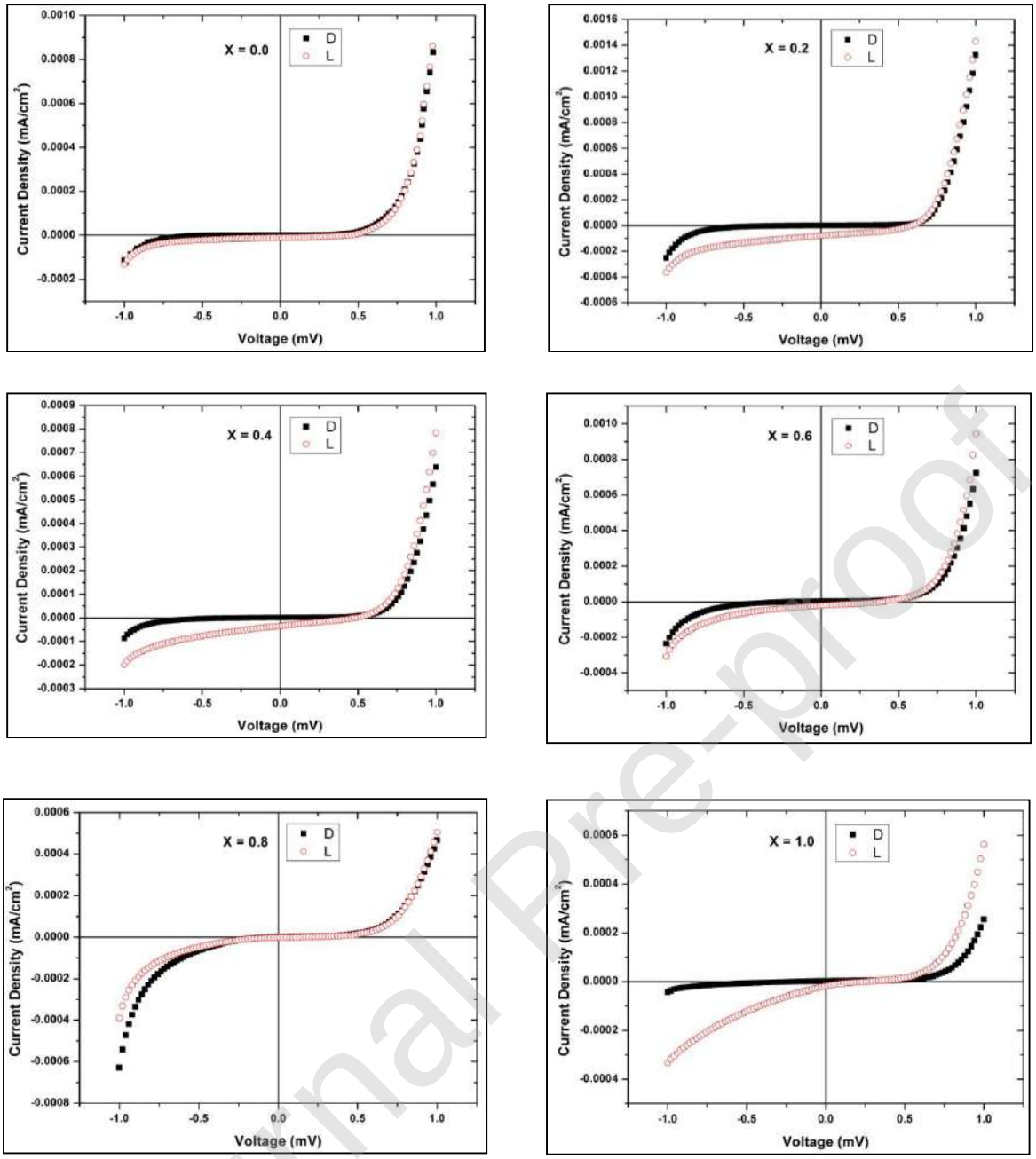

Fig. 16. Shows the current-voltage (I-V) curves for the deposited $Pb_xCd_{1-x}S$ thin films

The improvement in the efficiency of the solar cell is a result of good crystalline structures of the thin film during deposition, where no oxides are formed. This may result in an increase in the resistance due to the good quality of the films. This also implies that no holes or cracks were found in the films, which may cause transmission loss. The solar cell efficiency in the present study is higher and more promising than some other solar cell fabricated by the chemical bath deposition technique. The device stability is tested up to thirty days. Because after thirty days device is corroded due to the continuous use of electrolyte. So that it loses its stability and loss its efficiency.

Table 8. Photoelectrochemical parameters of the $Pb_xCd_{1-x}S$ thin films

Sample (*x*)	**I_{sc} (mA/cm^2)**	**V_{oc} (mV)**	**P_{max} (mA/cm^2)**	**Fill factor (ff %)**	**Conversion efficiency (η %)**
0	0.06041	455.55	10.09	36.96	0.01132
0.2	0.44787	595.86	98.47	37.02	0.10940
0.4	0.19106	494.80	24.17	25.57	0.02793
0.6	0.12236	413.95	13.97	27.59	0.00782
0.8	0.01244	171.55	0.79	36.98	0.00084
1.0	0.10996	272.57	4.55	15.20	0.00500

Table 8. Shows the dependence of the conversion efficiency and fill factor on the composition parameter. This appreciable change into fill factor and conversion efficiency is due to increment in surface area to volume ratio with crystal size.

From the above discussion, we observed that the close-packed morphology of thin films hasan impact on the performance of the solar cells. Because densely-packed compact layered films can provide a faster conduction pathway for charge and electron transport. It can be seen that the cell performance is greatly improved as compared to other films reported [19, 36].

4. Conclusions

a) $Pb_xCd_{1-x}S$ ternary thin films are grown by chemical bath deposition technique and film shows semiconducting nature.
b) Lead, cadmium and sulphur composition varied thoroughly in $Pb_xCd_{1-x}S$ ternary thin films.
c) The film's growth and color of the deposited $Pb_xCd_{1-x}S$ thin films changed from yellowish to deep black color. The optical band gap of deposited films was found to be in the range of 2.34 to 1.40 eV.
d) XRD studies show that the deposited thin films are polycrystalline in nature with cubic, hexagonal and cubic phases. SEM micrographs show uniform morphology with sand rose-like, ball-like, rice-like and cubic structure. Formation of Pb, Cd and S elements in compositions was also confirmed from EDXS spectra. The crystal size for deposited thin films is measured by X-ray diffraction (16.31 nm to 32.61 nm.) and scanning electron microscopy (20.3 nm to 84.1 nm).
e) The electrical conductivity in $Pb_xCd_{1-x}S$ thin films decreases systematically with an increase in the composition parameter '*x*'. Also, it is observed that activation energy decreases with increasing '*x*' composition in $Pb_xCd_{1-x}S$ thin films.
f) Thermoelectric power of all samples was found to be negative at all temperature and the negative value of TEP indicates that the films are of n-type, majority charge carriers are electrons. Also, the increase in the amount of Pb concentration decreases the magnitude of carrier density and mobility activation energy slowly decreases with the composition parameter '*x*' in $Pb_xCd_{1-x}S$ thin films.

g) In photoconductivity, study photocurrent increases with applied voltage and dark current rises approximately linearly with applied voltage and decreases with increasing composition '*x*' in $Pb_xCd_{1-x}S$ thin film. This behavior confirms the ohmic nature of films.
h) In the present study, a photoelectrochemical (PEC) solar cell of FTO/$Pb_xCd_{1-x}S$/liquid electrolyte/platinum-coated FTO as a back contact structure was prepared by using the CBD technique. Due to the good quality of the thin films fabricated PEC solar cell shows conversion efficiency 0.10940 %.

Acknowledgments

The authors are thankful to,

1. Dr. M. S. Wagh, Associate Professor, Department of physics, Pratap College Amalner, for providing transport properties analysis facilities.
2. Dr. Prashant Baviskar, Research Scholar, KBC NMU, Jalgaon, for providing PEC solar cell characterization facilities for this work.

Reference

[1] J. F. Mohammad, H. S. Al-jumaili, S. M. Abed, Int. J. of App. or Inno. In Engg and Mgmt., (2014) 3.
[2] R. Y. Mohammed, S. Abduol, A. M. Mousa, Int. Lett. of Chem., Phy. And Astr. 10 (2014) 91.
[3] A. S. Obaid, M. A. Mahdi, Z. Hassan, M. Bououdina,Int. Conf. on Edu., App. Sci. and Mgmt., Dubai (UAE), (2012).
[4] V. Popescu, G. L. Popescu, J. of optoele. And Adv. Mater. 13 (2011) 926.
[5] V. Popescu, H. I. Nascu, E. Darvasi, J.of Optoele. And Adv. Mater., 8 (2006)1187.
[6] M. Kamruzzaman, R. Dutta, J. Podder, Semi's., 46 (7) (2012) 979-983.
[7] M. A. Barote, A. A. Yadav, E. U. Masumdar, Chalco. Lett., 8 (2) (2011) 129-138.
[8] M. A. Mohammed, A. M. Mousa, J. P. Ponpon, J. of Semi.Tech.and Sci., 9 (2009) 117.
[9] H. S. AL-Jumaili, App. Phy. Res., 4 (2012) 75-82.
[10] K. E. Suryavanshi, R. B. Dhake, A. M. Patil, Int. J. of Adv. Sci. and Tech. Res., 4 (2) (2014) 858.
[11] E. Omotoso, G. A. Adegboyega, M. A. Eleruja, B. Olofinjana, O. O. Akinwunmia, O. O. Ilori, B. A. Taleatu, E. O. B. Ajayi, J. of Non-Oxide Glasses, 5 (1) (2013) 9.
[12] M. M. Abdulla, N. H. Hasan, H. I. Mohammed, G. H. Mohamed, K. A. Al-Hamdani, A. F. Abdulameer, J. of Elect. Devi, 12 (2012) 761.
[13] S. Lindroos, J. Puiso, S. Tamulevicius, M. Leskela, Solid State Pheno., 99 (2004) 243.
[14] J. C.Osuwa, C. I. Oriaku, E. C. Mgbaja, Chalco. Lett.,7 (2010) 679.
[15] J. L. Machol, F. W. Wise, R. C. Patel, D. B. Tanner, Physical Review B, 48 (1993) 2819 - 2822.
[16] Y. A. Salazar, R. Patino, J. L. Pena, W. Cauich, A. I. Oliva, Brazilian Journal of Physics, 36 (2006) 1058 - 1061.
[17] K. L. Chopra, S. Major, D. K. Panday, Thin Solid Films, 102 (1983) 1.
[18] M. A. Barote, A. A. Yadav, R.V.Suryawanshi, E. U. Masumdar. J. of Ovonic Research, 7 (2011) 45-50.

[19] L.P. Deshmukh, B. M. More, C. B. Rotti, G.S. Shahane, Materials Chemistry and Physics 45 (1996) 145-149.
[20] K. E. Suryavanshi, R. B. Dhake, 'Research journey' International Multidisciplinary E-Research Journal, 20, (2017) 15-24.
[21] M. Mukherjee, S. Bhushan, Optical Materials 22 (2003) 51–57.
[22] S. Thangavel, S. Ganesan, S. Chandramohan, P. Sudhagar, Y. S. Kang, Chang-Hee, Hong, Journal of Alloys And Compounds, 495 (2010) 234 - 237.
[23] A. U. Ubale, A. R. Junghare, N. A. Wadibhasme, A. S. Daryapukar, R. B.Mankar, V. S. Sangawar, Turkish Journal of Physics, 31 (2007) 279 - 286.
[24] R. Zahid, A. Zakaria, M. S. M. Ghazali, A. Jafari, U. D. Fasih, Din, R. Zamiri, International Journal of Molecular Science, 12 (2011) 1293 - 1305.
[25] M. A. Barote, A. A. Yadav, L. P. Deshmukhc, E. U. Masumdar, Journal of Non-Oxide Glasses, 2 (2010) 151 - 165.
[26] A. S. Obaid, M. A. Mahdi, Z. Hassan and M. Bououdina, Superlattice and Microstructure, 52 (2012) 816-823.
[27] A. Ayodeji Oladiran, A. Oluwaseun, S. Yekinni Kolawole, International Journal of Research and Reviews in Applied Sciences, 12 (2012) 420-426.
[28] M. A. Mahdi, S. J. Kasem, J. J. Hassen, A. A. Swadi, S. K. J.A l-Ani, International Journal of Nanoelectronics and Materials, 2 (2009) 163-172.
[29] I. O. Oladeji, L. Chowa, J. R. Liu, W. K. Chu, A. N. P. Bustamante, C. Fredricksen, A. F. Schulte, Thin Solid Films 359 (2000) 154-159.
[30] M. A. Barote, A. A. Yadav, T. V. Chavanetal, Digest Journal of Nanomaterials and Biostructures, 6 (2011) 979 – 990.
[31] A. S. Obaid, M. A. Mahdi, A. Ahmed Dih, Materials Science in Semiconductor Processing, 15 (2012) 564–571.
[32] K. E. Suryavanshi, A. M. Patil, R. B. Dhake, Journal of Applicable Chemistry 4 (4) (2015) 1227-1236.
[33] N. Murali, K. Vijaya Babu, K. Ephraim Babu, V. Veeraiah, J.Applicable.Chem, 3 (3) (2014) 1202.
[34] O. P. Moreno, M. C. Portillo, M. M. Flores , J. M. Juarez, G. A. Avila, R. L. Morales, O. Z. Ángel, J. of Mate. Sci. and Engg. A1, (2011) 759.
[35] L. P. Deshmukh, B. M. More, S. G. Holikatti, P. P. Hankare, Bulletin of Material Science, 17 (1994) 455 - 463.
[36] Jayesh Patel, Frej Mighri, Abdellah Ajji, Devendra Tiwari, Tapas K. Chaudhuri, Appl. Phys. A, (2014).

Microchemical Journal 169 (2021) 106567

Contents lists available at ScienceDirect

Microchemical Journal

journal homepage: www.elsevier.com/locate/microc

Review Article

Surface architectured metal organic frameworks-based biosensor for ultrasensitive detection of uric acid: Recent advancement and future perspectives

Sopan N. Nangare [a,1], Premnath M. Sangale [a,1], Ashwini G. Patil [b], Sai HS. Boddu [c], Prashant K. Deshmukh [d], Namdeo R. Jadhav [e], Rahul S. Tade [a], Dilip R. Patil [f], Abhijeet Pandey [g], Srinivas Mutalik [g], Jayvadan K. Patel [h], Arun M. Patil [f], Sanjaykumar B. Bari [a], Pravin O. Patil [a,*]

[a] Department of Pharmaceutical Chemistry, H. R. Patel Institute of Pharmaceutical Education and Research, Shirpur, Dist: Dhule, Maharashtra 425405, India
[b] Department of Microbiology, R. C. Patel Arts, Science, and Commerce College, Shirpur, Dist: Dhule, Maharashtra 425405, India
[c] Department of Pharmaceutical Sciences, College of Pharmacy and Health Sciences, Ajman University, Ajman, UAE and Center of Medical and Bio-allied Health Sciences Research, Ajman University, Ajman P.O. Box 346, United Arab Emirates
[d] Department of Pharmaceutics, Dr. Rajendra Gode College of Pharmacy, Malkapur, Dist- Buldhana, Maharashtra 425405, India
[e] Department of Pharmaceutics, Bharati Vidyapeeth College of Pharmacy, Kolhapur, Maharashtra 416013, India
[f] Department of Physics, R. C. Patel Arts, Science, and Commerce College, Shirpur, Dist: Dhule, Maharashtra 425405, India
[g] Department of Pharmaceutics, Manipal College of Pharmaceutical Sciences, Manipal Academy of Higher Education, Manipal, Karnataka, India
[h] Nootan Pharmacy College, Dean, Sankalchand Patel University, Visnagar, Gujarat 384315, India

ARTICLE INFO

Keywords:
Gout, uric acid
Metal–organic framework
Electrochemical biosensor
Fluorescent biosensor
Colorimetric biosensor

ABSTRACT

Gout is the world's most popular inflammatory arthritis and the prevalence of gout is rapidly rising worldwide. Typically, gout develops in a single joint as excessive swelling and intense pain wherein excessive deposition of uric acid (UA) crystals results in inflammation of the joint. Accordingly, UA is considered an effective biomarker to diagnose gout. Recently, the use of innovative sensors has attracted great attention, as it is effortless, responsive, quick, and powerful. While the traditional sensors for UA assessment are widely used, they pose many limitations and hurdles in terms of sensitivity, selectivity, and simplicity. In this vein, metal ions and organic ligand-based metal–organic framework (MOF) have gained much attention for the recognition of UA due to its larger surface area, porosity, high sensitivity, and defined selectivity. In this review, we provide details on the latest developments of MOF-centered biosensors for sensitive detection of UA. The status of gout, fundamentals of MOF, and MOF availed for detection of UA have been elaborated. Besides, we highlighted the nanoparticles and conjugates that rely on advanced strategies along with MOF that boost the sensitivity and selectivity towards the UA. Interestingly, different surface architectured MOFs biosensors showed a lower detection limit for UA from μM to nM. Finally, the threats and potential opportunities for MOF-based UA biosensors have been summarized. Therefore, based on ongoing research, the commercialization of this advanced platform for the biosensing of diverse biomarkers will open a new door for the *in vitro* diagnosis of assorted diseases.

1. Introduction

From its inception, arthritis is a severe health issue of a joint in almost all developed and developing nations. Arthritis is a term that derives from the Greek word "disease of the joint." Commonly, it can be stated as acute inflammation or chronic inflammation of the joint that is sometimes with the effect of pain and sometimes co-exists with structural damage [1]. As many as 100 classes of arthritis have been characterized according to the research. Generally, it can be classified into two type's namely non-inflammatory arthritis and inflammatory arthritis. In the first category, non-inflammatory arthritis is commonly known as osteoarthritis, while inflammatory arthritis is categorized

* Corresponding author.
E-mail address: rxpatilpravin@yahoo.co.in (P.O. Patil).
[1] These authors contributed equally as first authors.

https://doi.org/10.1016/j.microc.2021.106567
Received 11 April 2021; Received in revised form 18 June 2021; Accepted 22 June 2021
Available online 30 June 2021

based on the causes of inflammation. Especially, it involves the inflammation due to crystal deposition. For example gout, basic calcium phosphate disease and pseudogout. The second causative agent of inflammatory arthritis is autoimmune processes that results in psoriatic arthritis, rheumatoid arthritis, and ankylosing spondylitis. Additionally, infection due to crystal deposition also results in various inflammatory arthritis, such as Lyme's arthritis and septic arthritis [2]. From the beginning, different laboratory testing, and radiographic evaluation are commonly employed for the diagnosis of arthritis. Interestingly, it is based on the classification of arthritis and its severity. Additionally, inflammatory arthritis can be confirmed using the concentration levels of biomarkers in body fluids. In the context of biomarkers-based diagnosis, the anti-nuclear antibodies, UA, autoantibodies, rheumatoid factor, etc. are facilitating the precise diagnosis of arthritis at an early stage [2,3]. As we know, there are>100 types of arthritis and accurate diagnosis of arthritis is a prerequisite before starting the antiarthritic treatment. In recent times, advanced prognosis and diagnosis techniques are contributing to the main role. For example, the application of biosensors facilitated the accurate diagnosis and prognosis of arthritis. Accordingly, it helps to classify arthritis and provides an early diagnosis of arthritis [2]. Regardless of advanced technologies and management facilities for arthritis, the prevalence of gout has been significantly increased in the last two decades [4]. As a result, it is important to accurately diagnosis at an early stage so as to effectively treat gout. Therefore, the prevalence, distribution, treatments, and techniques of *in vitro* diagnostics are addressed in the next section.

1.1. Gout

Gout is a common form of crystal-induced arthritis [5], which is derived from the Latin word 'gutta' [6]. Abundant literature suggests that the precipitation of crystals of monosodium urate (MSU) in the joints and soft tissues trigger a flamboyant inflammation that results in gout [5,7,8]. As per published literature, the prevalence of gout is 0.58% to 2.89% of the total population. More specifically, the estimated prevalence of gout is less than 1% to 6.8% (per 1000 peoples)[9]. Moreover, statistical data indicated that gout affects 3% to 6% of men and 1% to 2% of women in western nations [10]. In the case of Asian countries, the prevalence of gout can rise to 10% in the future. On the other hand, the prevalence of gout varies with the age factor. As per literature, the overall severity in men is up to 10% and up to 6% in women over the age of 80 years. This data indicates a higher prevalence rate of gout in men (2–6 folds) as compared to women [7]. Besides, the prevalence of gout is also shown in the region-wise alteration. In the case of developing nations such as India, about 65% of gout patients are from rural areas [11]. Unfortunately, the prevalence of gout in India is unambiguous [6]. As per literature, various factors are serving to increase the prevalence of gout. Globally, the prevalence of gout is expected to multiply exponentially due to inadequate eating habits, including fast food, lack of physical activity, rising obesity, and metabolic syndrome [7,9]. Therefore, gout has gained much attention in the last couple of decades as understood from the gradual increase in the number of publications published until 2020. A total of 19,488 papers were published as per the PubMed database [12]. Fig. 1A depicts the number of

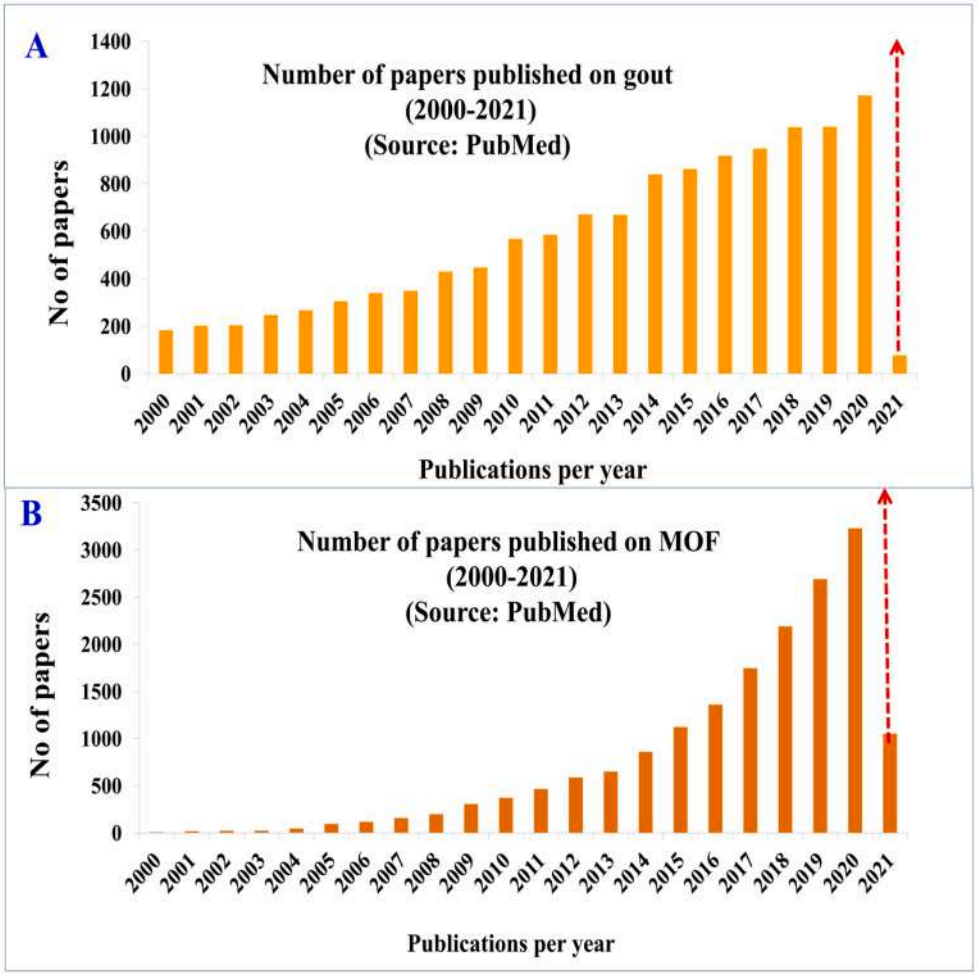

Fig. 1. Bar chart showing the number of papers published on gout (A) and MOF (B) every year as of given in PubMed.

papers published on gout every year as per the PubMed database. The literature survey divulged that the clinical scenario of gout is split into gouty arthritis, asymptomatic hyperuricemia, acute intercritical period, and chronic tophaceous gout [7]. Over the past 15–20 years, the hospitalization rates for gout have expanded by 50% to 100% in the developed nations including the United Kingdom (UK), United States (US), Sweden, etc. Taken as a whole, the appropriate prognosis and diagnosis of gout is an urgent need for society [8]. The diagnosis of gout has relied on laboratory investigation and radiological features [13]. The clinical diagnosis includes an assessment of various stages of gout such as asymptomatic hyperuricemia and acute gouty attack. The later stages include intercritical period and, finally chronic tophaceous gout. In the case of laboratory investigations, the serum UA (SUA) level is an important parameter to conclude the state and type of disease. More precisely, gout will grow every year by 0.09% in patients with SUA levels ranging from 7 mg/dL to 7.9 mg/dL. Only 0.4% may develop gout in patients with SUA levels between 8 mg/dl to 8.9 mg/dl, while 0.5% of the patients' group might have gout with hyperuricemia over 9 mg/dl SUA level [14]. As per the literature, an increase in the concentration of UA in the body fluids from its normal concentration level of about 1.5 mg/dL to 6.0 mg/dL for women, and about 2.5 mg/dL to 7.0 mg/dL for men is related to various medical conditions like gout, hyperuricemia, and kidney disease [15]. In general, the normal values of UA in the urine and blood should be 2×10^{-3} mol/L and 1.2–4.5 $\times 10^{-4}$ mol/L, respectively [16,17]. There is a dire need to resolve the issue of gout and related arthritis. The literature survey suggested that MSU pathogenic crystals can be dissolved into body fluids, which suppress the symptoms of gout and other related diseases [18]. Unfortunately, this method is suffers from some failures that may be due to a weak adherence to urate-declining medicines, which emphasizes the need for proper education to patients [7,18]. Recently published literature revealed the golden diagnostic standard for gout. It is based on the detection of MSU crystals by the polarized light microscopic technique in the synovial fluid [7]. The imaging strategies such as ultrasonography, conventional radiography, magnetic resonance imaging (MRI), positron emission tomography (PET), nuclear scintigraphy, conventional computed tomography, and dual-energy computed tomography are also reported for the diagnosis of gout [7,13]. However, all these methods are costly, time-consuming and requires expertise to handle and diagnose. Therefore, the trend of disease/disorder diagnosis has shifted to *in vitro* diagnosis using specific biomarkers [19]. In this perspective, various others methods have been reported for the assessment of UA in the body fluids. Therefore, in this subsequent section, we have summarized UA and its detection techniques.

1.2. UA as a gout biomarker

The study of an analyte and its biological significance is the primary step for the clinical diagnosis of diseases. It means the alteration in the level/concentration of biological analytes in the body fluids is a prime indication of different pathological manifestations [20]. As we know, gout is a disorder related to purine metabolism, wherein the end product of this metabolism is UA (2,6,8-trihydroxypurine), a predictor or biomarker of gout [21]. In general, UA is a natural antioxidant and is excreted by the kidneys through urine [15]. As per literature, UA (crystalline compound) was discovered in the kidney by Carl Wilhelm Scheele in 1776 [16]. Principally, the increased UA accumulation and/or decreased excretion in humans is associated with gout and hyperuricemia pathogenesis [13,21]. The susceptibility of the vascular and synovial membrane leads to the accumulation of UA crystals in the joints. Consequently, it affects the peripheral joints such as the big toe [7]. An abundant piece of literature divulged that the excessive production of UA is a consequence of a deficiency in the enzymes that contributed to purine metabolism. Furthermore, purine-rich foods such as animal and marine foods are playing a principal role in increasing the precursors of UA [22]. Based on the research findings, UA is widely preferred as a biomarker for the precise diagnosis of gout and other UA-associated health issues. Therefore, the assessment of the UA is the foremost step for the prognosis and diagnosis of gout and other UA-related health conditions. Owing to the need for routine measurements of UA, several research groups are working on biosensing and other strategies. Out of these methods, a few of them are highly sensitive and selective, which assess UA in the body fluids *in vitro* [15,23,24]. Specifically, the literature survey claimed that the enzyme-based assay format for UA assessment is the most accepted method in the biomedical field [25]. Although it is a commonly used procedure, it has a lot of drawbacks such as intruding with various biological analytes (bilirubin, ascorbate), strict pH requirement, high cost of enzymes, a longer incubation period (30 min), and less precision [26]. As per literature, the healthy person contains the 0.13–0.46 mM concentration of UA in serum and 1.49–4.50 mM concentration of UA in urine. As we recognize, the high (abnormal) level of UA in serum (termed hyperuricemia) is associated with arthritis and other diseases, whereas a low level of UA in serum is termed hypouricemia that is relates to multiple sclerosis. In conclusion, there is great importance of quantitative assessment of UA in serum and urine samples for clinical diagnosis in various associated diseases [27]. Significant growth in the biosensing sector was achieved over the last few years. Fascinatingly, several research articles on gout biosensing mentioned that the utilization of capillary electrophoresis, ultra violet (UV) spectroscopy, electrochemical sensor, chemiluminescence, and fluorescence could provide a precise assessment of UA in biological samples. Despite the notable merits of mentioned methods, all these techniques are suffering from several demerits including cost factor, speed, selectivity and sensitivity. For this reason, there is a limitation for successful applications in the diagnosis of gout. It could be overcome using suitable methods, which contains the aptitude of precise detection of UA [20]. Briefly, UA is an excellent biomarker for gout, and various types of techniques such as spectroscopic, electrical/electrochemical, and optical methods can measure the concentration of UA in clinical samples. Despite such remarkable development in the clinical analysis, there are still major challenging issues such as sensitivity, selectivity and detection speed for UA analysis. Hence, there is a need to design advanced biosensors for precise recognition of UA in complex samples.

2. Advanced biosensor for UA detection

A tool for the identification and quantification of metabolites/biomarkers is a fundamental route in diagnosing diseases or disorders in a rapid, simple, and accurate manner [15,28]. An elevated UA level in different body fluids is related to many medical problems and one of them is gout. Because of this, UA levels in body fluids must be regularly monitored. In this background, new analysis techniques have made significant developments for the detection of UA. A few techniques such as high-performance liquid chromatography (HPLC), chemical spectrophotometric analysis, enzyme electrode analysis, etc. are widely used in the UA assessment in the clinical sector and research fields [15]. The applications of different nanomaterials in the fabrication of biosensors are gaining much interest from scientific fraternities. Specifically, these nanomaterials include carbon materials, metal nanoparticles, and metal oxides. [28]. The application of various nanomaterials can offer several unique and utmost properties such as larger surface area, maximum binding sites for bioconjugation, and fast electron transfer, which are the prime requirements of the sensors [29]. Recently, a 2D form of MOF nanostructure has become a choice of nanomaterial for the development of a superior sensor for biological and chemical sensing that provides the boosted performance in terms of sensitivity, selectivity, detection speed and simplicity [30]. In this section, we have discussed advanced nanoarchitectured MOF synthesis, properties of MOF, and different types of MOF for biosensing of UA.

2.1. MOF as an advanced nanomaterial

A plethora of the literature suggested that 2D forms of nanomaterials have become a common research subject for scientists, particularly for designing different types of biosensors for biomedical applications [29]. Among 2D nanomaterials, the development of MOF has attracted the attention of research scholars for the last few years. Notably, it may because of their tunable and versatile properties, which include thermal properties, chemical properties, and physical properties [31]. Interestingly, MOF is a division of advanced materials produced using special types of metal ions and appropriate organic linkers or ligands [30]. Fig. 2 demonstrates the schematic representation of MOF synthesis. According to the literature, MOF has chemical and structural properties that make them a worthy alternative for the assessment of the concentration of biomarkers in body fluids. In the case of self-assembly of MOF, several organic ligands (building blocks) have been employed to design it. Along with an organic linker, different metals can also be incorporated into the MOF structure. MOF shows flexibility in properties through modifications of the original design. This provides good selectivity and high sensitivity towards the interest biomarker [32]. Generally, the organic ligand is composed of aromatic rings that can provide the ability to link with numerous functional groups [32,33]. The affinity receptors can improve the sensitivity and selectivity of biosensors for the recognition of the analyte [28]. Similarly, the incorporation of specific receptors can improve the performance of MOF-based biosensors in terms of sensitivity, and selectivity. [34]. The fabrication of MOF-based biosensor can be a new substitute for previously used nanomaterials for the fabrication of biosensors. Interestingly, the conjugated nanostructure, surface functional groups of MOF, larger surface area, porous nature can boost the overall performance of MOF-based sensors [33]. Due to its uniqueness, several studies have used MOF as an alternative substituent for carbon-based biosensing materials [35,36]. Since Yahgis *et al.* published the first study concerning these coordination polymers in 1994, MOF publications have risen exponentially. In 2002, the first sensors associated with MOFs were released. The first MOF-based biosensor example was identified in 2008 [37]. There has been a gradual enhancement in the number of publications published until 2020. A total of 15,829 papers were published as per the PubMed database [12]. Fig. 1B depicted the number of papers published on MOF every year as per the PubMed database. There is an urgent need to develop a device for rapid, easy-to-use diagnostics to identify, distinguish, and quantify UA in gout diagnosis and therapy. To date, only a few studies have constructed MOF-based sensors to identify UA concentrations directly. In the future, MOF-based biosensors would be an interesting area for researchers to design the exceptional biosensor for detection of interest biomarker [27]. In the following subsection, we have added a brief discussion on the properties, synthesis of MOF and types of MOF for designing of biosensors for detection of UA.

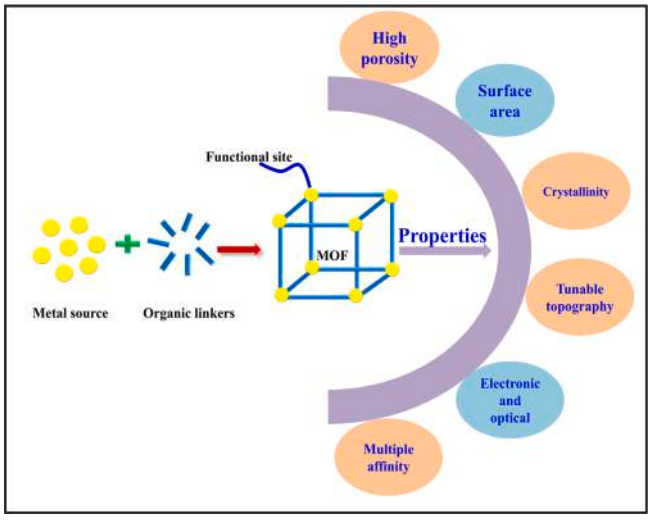

Fig. 2. Schematic representation of the MOF synthesis using metal ions and organic linkers.

2.1.1. Properties of MOF

The engineered MOFs are composted on organic ligands and contain aromatic ring structures that can be functionalized using diverse functionalities. The highly conjugated nanostructure and unique functionality of MOF provide magnificent biosensing applications (Fig. 2). It has been divulged that a highly conjugated nanostructure and the presence of different functionalities could help provide fluorescence properties to the MOF. The fluorescence characteristics of architectured MOFs are mainly sensitive to environmental changes, which opens a new avenue for biosensing. Architectured MOF-based nanomaterials have great promise as exceptional fluorescent biosensors for recognition of interest analyte [33]. Furthermore, the introduction of specific functional groups into MOF can help to boost the sensitivity and selectivity of biosensors [38,39]. Moreover, it provides the highest specificity to target clinical samples [38]. The published studies demonstrate that the synthesized MOF is a unique and highly porous nanostructure. Therefore, MOF is also called a 'porous coordination network'. Generally, MOF is considered a multifunctional hybrid material with tunable porosity and diversified functions. Primarily, it may due to the presence of organic linkers, and inorganic metal ions. Because of this, it has become a wide division of high-porous crystallized materials (up to 90% free volume). In addition, it exhibited a variety of features that includes thermal stability, ultra-low densities, a distinct ordered structure, a wide surface area (>6000 m^2/g), etc. [40]. Based on these properties, several types of MOF-based sensors have been fabricated for chemical and biological sensing. Nowadays, MOF-based electrochemical sensors have been majorly preferred for the detection of the target molecule in complex samples. Briefly, the suitable electrode could be designed by using numerous types of MOF followed by appropriate modifications. However, there are some foremost limitations for the development of electrochemical biosensors using MOF. Especially, the low conductivity of MOF affects the overall presentation of the sensor. The low conductivity demerits of MOF resulted in the development of various advanced MOFs. Along with that, suitable nanocomposites of metal nanoparticles (platinum nanoparticles), a carbon-based material, metal oxides, etc., have been used for the fabrication of highly sensitive and selective electrodes. MOF composites demonstrate enhanced efficiency of an electrochemical biosensor. MOF containing countless pores helps to introduce metal nanoparticles or carbon molecules into the inner nanospace. Interestingly, it assists to build MOFs as wonderful representatives for the fabrication of electrochemical sensors by integrating such advanced nanomaterials. Additionally, the shape and size of MOF also help in the incorporation of guest molecules into the MOF nanostructure [41]. As per literature, different organic ligands in MOF can be transformed into pristine carbon nanomaterial through controlling thermal decomposition conditions without using supplemental carbon precursors. Owing to the remarkable merits of MOF, the enzyme immobilization on the surface is requirements in the MOF-based sensor are simplified. Possibly, it may due to the larger network of nanosized holes plus cavities produced in MOF nanomaterial during the thermal decomposition method. The porous nature of nanocavities helps to increase the enzyme loading in the MOF-based biosensor [42]. Recently reported nanomaterial contains enzyme-like properties that are commonly known as nanozyme. It is an attention-grabbing field for the development of different types of the sensor without the need of enzymes for sensing of the target. Importantly, the electrochemical nanozyme (i.e.nanomaterial with enzyme-like properties) [43] centered biosensors require a very conductive and discriminatory architecture. Consequently, there is a massive obstacle in managing an efficient arrangement of binding sites and appropriate structures. MOFs

containing greater metal ion content, ordered cavity, customizable chemical characteristics, etc., act as organized catalysts for building porous metal–carbon hybrids. Therefore, MOF-based nanozymes have been utilized for the fabrication of biosensors [44]. Several studies confirmed that the MOFs are biocompatible and chemically stable. Besides, several reports suggested that most of the MOFs are biodegradable [30,45]. Therefore, MOF can be efficiently used in numerous biological functions [45]. In conclusion, MOF is a distinctive nanomaterial that is gaining much attention from researchers in several fields, including industrial development, the environment sector, and the biomedical area [46].

2.1.2. Synthesis of MOF

In the last few years, several types of MOFs have been examined for biomedical applications. Principally, MOFs are available in different shapes/frameworks and compositional elements. The size, shape, and composition of MOFs are important parameters that affect the entire performance of the sensor. Therefore, the size and shape of MOF must be monitored by selecting appropriate techniques, suitable combinations, and antecedents [47]. As per previously reported studies, several methods have been reported for MOF synthesis that offers feasible size, large surface area, good surface morphology, etc. Interestingly, the above-mentioned properties of MOF play a vital role in the sensing of the interest analyte. This results in high sensitivity and good selectivity in complex clinical samples. The main rationale of MOF designing is to construct tunable shape as well as surface morphology that relies on several factors. Fig. 3 shows various methods for the synthesis of MOF-based nanocomposites. Temperature (or heat) application is an important parameter in the conventional synthesis of MOF that depends on the synthesis environment. In general, heat-dependent MOF synthesis is classified into two types: solvothermal methods and non-solvothermal methods. In short, the solvothermal method-based production of MOF relys on solvents like water, whereas, the non-solvothermal method includes a solvent with a higher boiling point [30]. The second MOF synthesis method is microwave-assisted MOF synthesis that includes several imperative factors that aid in the synthesis of nano-sized MOF. The solvent preference for MOF synthesis is based on the microwave absorption ability of the solvent. Moreover, it requires efficient heating for the fabrication of nanoarchitectured MOF. On the whole, it is mandatory to utilize a suitable vessel of the desired capacity for MOF synthesis [48]. The third method for MOF synthesis is electrochemical synthesis of MOF wherein different metal ions are used that perform the role of the anode side. The selective ligand/linker molecule is further dissolved into the prepared reaction mixture in the presence of an electrolyte. In this method, metal ion accumulation from the anode onto the cathode can be suppressed through the application of selective protic solvent in the final reaction blend. This electrochemical method can be utilized for the non-stop manufacturing of MOF [49]. The fourth type of MOF synthesis is a sonochemical synthesis of MOF in which the high-energy ultrasound is used for the preparation of the MOF reaction mixture. Unfortunately, the application of sonochemical methods for the construction of MOF is quite limited. As per the literature, only a few MOFs have been engineered using this method [30]. Furthermore, the fifth MOF synthesis method is a mechanochemical synthesis of MOF wherein the mechanical energy is utilized in the reaction to produce the MOF. It relies on the mechanical brake of the intramolecular bond along with the chemical transformation. It can be performed at room temperature in the absence of solvent [30,50]. Therefore, based on suitability, the tunable MOF can be synthesized using a different method. In conclusion, by using above-mentioned methods, numerous MOFs have been synthesized for the biosensing application of UA. In the next section, we have discussed different MOFs utilized in the designing of MOF-based various sensors for UA sensing applications.

2.2. MOF based sensor for biomedical applications

Recently, plenteous research articles have been published on the account of MOFs-based sensors highlighting their applicability in several fields including biomedical, chemical, environmental, etc. [30,51]. As per the literature, 2D and porous MOF are also of high interest in future renewable energy applications. Taken as a whole, in recent times, more and more MOF applications are gaining popularity in

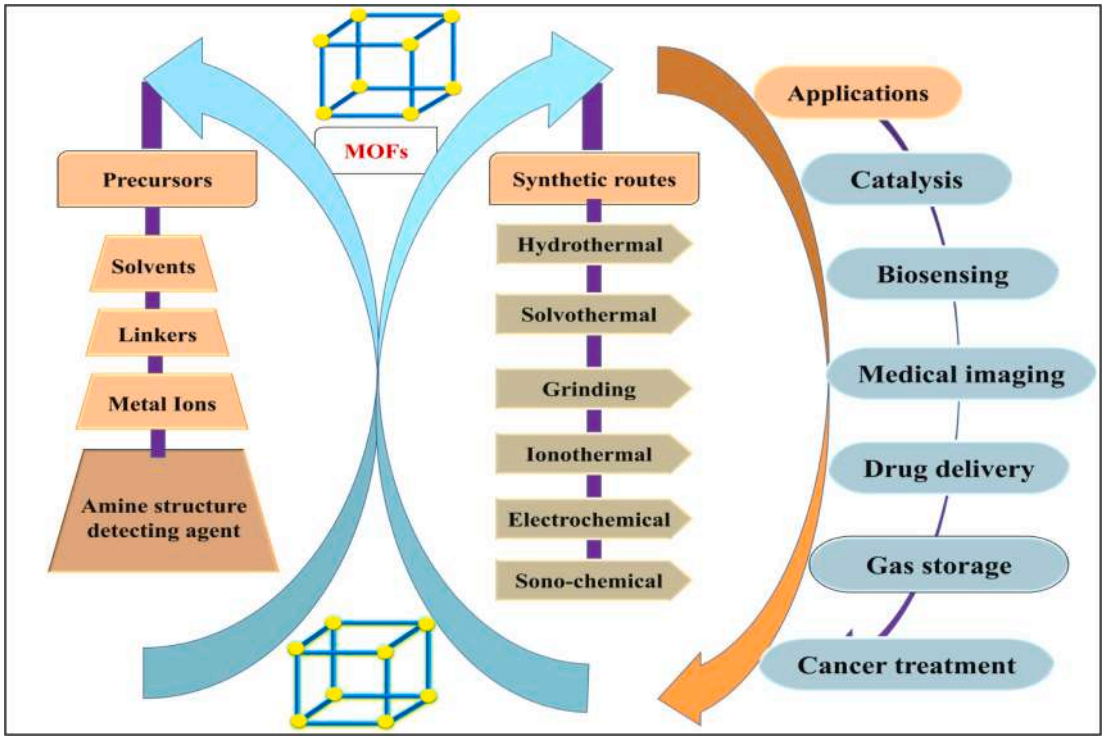

Fig. 3. Schematic representation of MOFs synthesis using different precursors and synthetic routes for biomedical applications.

thin-film tools, cancer biomarkers, drug delivery, therapeutics, and bioimaging (Fig. 3) [30,52–54]. Despite this, there is a further need for advancement in terms of sensitivity, selectivity, etc. In the future, the applicability of MOFs can expand into popular areas such as biomedicine, and biosensors. In this perspective, the incorporation of new or ideal functionality into the MOF framework is contributing to notable merits in recent times [55]. Plenty of literature suggested that the addition of specific functional groups (recognition sites) into MOF can boost the overall performance of the sensor in terms of sensitivity, specificity towards the interest target [39,56–58]. For example, amine-functionalized cerium based MOFs (Ce-MOFs) [59], nitrogen oxide (NO_2) functionalized zirconium-based MOFs [Zr-MOFs or UiO-66-NO_2 (Universitetet i Oslo = UiO-66)] [60], amine-functionalized Zr-MOFs (NH_2-Zr-MOFs or UiO-66-NH_2) [61], zinc metal ion and 2-amino-1,4-benzene dicarboxylate (NH_2BDC) linkers based amine-functionalized MOF (MOF-46) [62], etc., have been widely used for sensing of the UA that offers higher sensitivity and selectivity. Organic MOF ligand typically includes aromatic rings and can bind easily with different functionalities. Additionally, the literature mentioned that the highest combined frame and functional sides in MOF could provide remarkable fluorescence efficiency. The fluorescence properties of MOF-based dye conjugates or doping with fluorescent material are extremely susceptible to environmental changes. Consequently, MOF with such pristine material is capable of designing fluorescent sensors that can focus on different targets [27]. There are several examples of MOF utilized in the biomedical field for biosensing applications especially gout. Out of all MOFs, phosphonate MOF (MIL-91, MIL: Matérial Institut Lavoisier) [63], Lanthanide MOF (Ln-MOF) [64–66], Ce-MOF [67], and Thorium MOF (Th-MOF) [46] are preferred for UA detection. In addition, the Zeolitic Imidazolate Framework-67 (ZIF-67), Zeolitic Imidazolate frameworks-8 (ZIF-8) [68], Terbium (Tb)-158 MOFs (ZJU-158-Tb, ZJU = Zhejiang University) [69], Zr-MOF followed by post-synthetic modification (UiO-PSM), Europium (Eu) based MOF (Eu-MOF) [70] are reported for the highly sensitive and selective detection of UA. As per literature, standard nanocage-like MOF, namely MIL-101, has sufficient inter-connected three-dimensional (3D) cavities and it can be accessible by small pore windows. This structural characteristic allows the analyte transport using the interface of electrolyte/electrodes. Additionally, the excellent porous nature of MOF is also helping to prevent the aggregation of metal nanoparticles. Therefore, the incorporation of metal nanoparticles into porous MIL-101 provides high conductivity as compared to the bare MOF and thus results in a high sensitivity towards the target biomarker. In addition, the MIL-101 provides a larger surface area that offers a number of binding sites to interest analytes from clinical samples. Overall, the application of MIL-101 is more constructive in the development of electrochemical sensors with improved performance [71]. Ln-MOF has gathered great interest in research due to its features. It is synthesized by coupling of 'Ln' ions to conventional MOFs. Ln-MOF is used for a variety of applications including biosensor developments. Ln-MOF offers several merits in terms of porosity, luminescence, and magnetism. In addition, it demonstrates superb luminescence property that may because of the narrow emission and excellent color purity. The charge-transfer transitions (for example: metal–ligand charge transfer and ligand-to-metal charge transfer), inner shell containing 4f–4f transitions, 4f–5d charge transfer are the types of electronic transitions that plays an imperative role in luminescent properties of Ln-MOF. Literature survey divulged that the luminescent emission of different Ln-MOF such as Eu^{3+} (red light), Tm^{3+} (blue); Sm^{3+} (orange); Tb^{3+} (green), etc. In addition, Ln-MOF containing all framework components helps to heighten the luminescence property of MOF. Therefore, the development of a stable luminescent MOF, i.e. Ln-MOF has gained huge importance for sensing various biomarkers or metabolites [63]. Nowadays, the phosphonate-based Ln-MOFs MIL-91 (Al: Eu) (Al: Aluminium) and their derivative forms are broadly used in medicine and life sciences that may due to their good stability and excellent luminescent properties [64–66]. A phosphonate-based MOF is furnished with distinguished stability as compared to the carboxylate MOF. Therefore, it can be used with several chemicals containing media, for example $Cu^{2+@}$MIL-91(Al: Eu) (Cu: copper). According to the data, it offers the potential of an On-Off-On sensing mechanism in the presence of an interest analyte. The literature survey suggested that the designed form of $Cu^{2+@}$MIL-91(Al: Eu) MOF provides high selectivity, admirable sensitivity, good structural and fluorescence stability [63]. Yet another type of Ln such as Tb and Eu-based MOFs (Tb/Eu-MOF) nanomaterial is also an attraction-grabbing type of MOF. It offers outstanding fluorescent properties and multiple coordination sites. Therefore, lead to the fabrication of fluorescent probes with towering performances in terms of sensitivity and selectivity towards the target biomarker [70]. Ce-MOF is recently reported as a new type of MOF for sensing applications. Interestingly, the Ce-MOF showed excellent biocompatibility and ability of the oxygen vacancy formation. This oxygen vacancy helps to form Ce^{3+} ions that offer elevated electrocatalytic characteristics. Besides, the high isoelectric point at neutral pH provides a positive surface charge that can lead to the binding of the opposite charge analyte. Nowadays, the Ce-MOF with 2D carbon materials has been reported for sensing of target, which increases overall surface area, electric conductivity and decreases the cost of fabrication of electrochemical biosensors [67]. In recent times, the ZIF-67 based MOF is also majorly used for designing enzymes (termed as nanozyme) by the use of pyrolysis with different metal ions. Recently reported methods claimed that the tunable properties of ZIF-67 could provide several numbers of catalytic sites, porous carbon, or order cavity, a high number of metal ions. Consequently, it gives the highly active nanozyme electrochemical probe for biomarker sensing [44]. The bimetallic ZIFs (BMZIFs) is a combination of isoreticular MOF-8 (IRMOF-8) and ZIF-67 that is synthesized through a direct carbonization process. It is appealing that the combined form of this bimetallic MOF provides a larger surface area and high pore volume. Besides, it also provides good catalytic activity, and therefore, it enhances the overall conductivity and high sensitivity towards the target marker. Due to these outstanding properties, BMZIFs are majorly used in the designing of MOF-based electrochemical biosensors [68]. The advanced form of Zr-based MOF along with the primary amino group on its ligand is termed UiO-66-NH_2 [72], which furnishes marvelous chemical stability as well as water stability. Moreover, UiO-66-NH_2 offers the unsaturated coordination metal (Zr) active sites that permit the highly sensitive plus selective recognition of UA. In addition to the merits of MOF, there is a need for selective functionality on the surface of MOF. Recently existed PSM of MOF is playing a momentous role in the biosensing arena. In the case of PSM, different ligands or functional groups inserted into the skeleton of MOF offered specific detection sites and high fluorescent properties. Fascinatingly, the UiO-66-NH_2 containing primary amino functionalities helps to process MOF to PSM using different functional groups such as 2-picolinic acid (2-PA). The PSM of MOF offers high sensitivity and selectivity towards the analyte. Concisely, the fabrication of UiO-66-NH_2 based on different types of biosensors will open a new era for research fraternities [27]. In conclusion, with high sensitivity, good stability, and biocompatibility, precise selectivity can is achieved through designing advanced material-based MOF. Additionally, the MOF can be modified into different types of biosensors such as luminescent biosensors, electrochemical biosensors, colorimetric biosensors using different conjugating materials such as dyes, functional groups, and fluorescent materials. On the whole, MOF-based sensors have received more attention in biomarkers and chemical sensing [34], which may due to the assorted benefits such as an easy fabrication process, low cost, high sensitivity, and good selectivity [27]. In the future, the applications of MOF-based sensors in the biomedical field will open a new window. In the next section, we presented the advancements in MOF-based different biosensors for highly sensitive and selective UA detection in real-time clinical samples.

3. Applications of MOF biosensor for UA detection

Modern MOF manufacturing techniques have enabled the preparation of more precise, durable, and sensitive biosensors [37]. In this review article, we have discussed different MOF-based biosensors such as luminescent/fluorescent biosensor, electrochemical biosensors, colorimetric biosensors for UA sensing applications.

3.1. Fluorescent biosensor

The fluorescence-based assay is a very effective method for the analysis of interest targets, because it provides merits such as rapid detection, low cost, ease to use, high sensitivity, and selectivity [27]. Many research groups have reported the detection of UA in serum. Nevertheless, the maximum (up to 60% to 70%) concentration of UA excreted from the body is through urine. Therefore, there is a need to develop a new biosensor for the detection of UA in the urine sample [63,73]. Ln-MOFs offer much perspective for biosensing of different disease/disorder biomarkers due to their remarkable optical properties. These optical characteristics of Ln-MOFs depend on an immense network of coordinate bonding between organic ligands and 'Ln' ion centers. The luminescence property of Ln-MOF has drawn considerable interest among the many biosensing studies of novel functional MOFs for their conspicuous fluorescence properties. Notably, it may due to the trivalent 'Ln' ions (Ln^{3+}) containing plentiful 4f − 4f transitions. It also allows the prospects of exploiting 'Ln' cations containing luminescence performance, including extensive emission lifetimes with sharp and distinctive line emissions. Lian *et al.,* synthesized MIL-91(Al: Eu) MOF and their Cu^{2+}@MIL-91 (Al: Eu) (derivative composite) by the hydrothermal method using piperazine derivative ligand (N, N′-piperazinebismethyl phosphonic acid) as an alternative to the carboxylic ligand (Fig. 4). The MIL-91(Al: Eu) containing luminescence hereby ascribed to the conversion of energy from excited energy levels of an organic ligand to the ground state of the 'Ln' ions. Eu^{3+} demonstrated a sharp and strong emission, whereas the presence of UA could not affect the MIL-91(Al: Eu) fluorescence. On the contrary, the Cu^{2+}@MIL-91 (Al: Eu) derivative showed no fluorescence emission, whereas the addition of Cu^{2+} resulted in the quenching of 'Eu^{3+}' luminescence and later rebounded in the occurrence of UA. As a result, these engineered MOFs showed low limits of detection (LOD) of 1.6 μM/L, whereas the concentration range for this sensor was found to be 10–1200 μM/L (R^2 = 0.991). The Cu^{2+}@MIL-91 (Al: Eu) composites could be exploited to monitor UA that may due to the regeneration of luminescence in UA. Finally, the real urine samples containing UA detection confirmed the application of Cu^{2+}@MIL-91 (Al: Eu) in the diagnosis of hyperuricuria. In addition, the Cu^{2+}@MIL-91 (Al: Eu) based test paper confirmed the presence of UA in the urine, wherein the urine with a UA (1000 μmol/L) exhibited relucent red. Furthermore, the demonstration of different fluorescent colors of Cu^{2+}@MIL-91 based test paper confirmed the presence of UA in the urine through naked eyes. It showed high selectivity towards the UA in the presence of urea, creatinine, sodium chloride, and other urine chemicals. On the whole, Cu^{2+}@MIL-91 (Al: Eu) based powders and test papers can be used as a promising fluorescent biosensor to identify the UA in clinical urine samples [63].

Yet another similar line of work reported the use of Ln-MOF-based luminescent sensor for ultrasensitive and selective detection of UA, and other metabolites such as hippuric acid (HA), unrinyl thiodiglycolic acid (TDGA), and 1-naphthol (1-N) in the urine. Briefly, six new Ln-MOFs have been prepared namely $[Eu_2(tyia)_3(H_2O)_3]n$ (1) and $\{[Ln_2(tyia)_3(H_2O)_3]*3H_2O\}n$, wherein Ln = Terbium (Tb, 2), Dysprosium (Dy, 3), Samarium (Sm, 4), Gadolinium (Gd, 5) and Neodymium (Nd, 6) using 5-(triazol-1-yl) isophthalic acid (H_2tyia) and lanthanum (III) nitrate hexahydrate $[Ln(NO_3)_36H_2O]$ through hydrothermal reaction. The synthesized MOF composites showed the Ln^{3+} ions

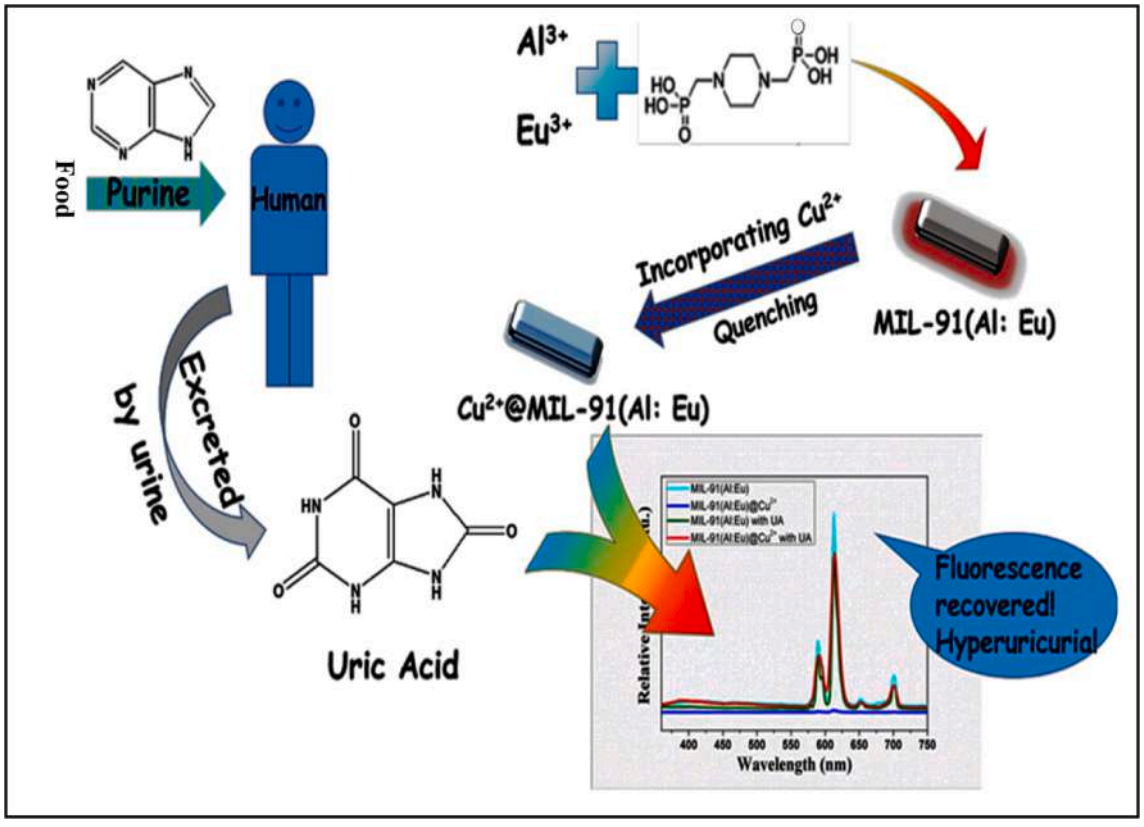

Fig. 4. Ln-MOF-based On-Off-On fluorescent biosensor for UA detection and hyperuricuria diagnosing. [Reprinted with permission from ref [63]. Copyright 2017, American Chemical Society.]

luminescence emission peak at different wavelengths along with the free ligand. As a result, the MOF-based compounds have been used as a luminescent probe for the detection of UA and other metabolites in urine samples. It has been observed that compounds' surface morphology does not alter after and before the sensing experiments, which concludes that the other chemicals present in the urine show minute effects on the emission of compounds 2, 4, 5, and 6. Finally, these compounds provide the LOD for UA, 1-N, TDGA, HA about 0.49, 5.5, 1.7, and 4.6 μM, respectively. The linear concentration range was found to be 0–64 mM. Moreover, it provides good reversibility, regeneration, and excellent selectivity. Therefore, in the future, the MOF-based 2, 4, 5, and 6 compounds can be used as a promising material for the fabrication of fluorescent biosensors for the detection of UA, other urinary metabolites, and chemicals [74].

To date, several MOF-based sensors have been developed in an organic solvent and not in practical aquatic media. A real applications sensor, it has to be precise, fast, and best with a clear demonstration, like a color shift. A recently published original work claimed that a newly premeditated Tb-MOF could give the nM sensing of UA based on the luminescent turndown phenomenon. Tan *et al.,* synthesized novel Tb-MOFs $(Me_2NH_2)_2[Tb_2(L)_2]\cdot(H_2O)_6$ [(ZJU-158-Tb, L = 1-(3,5-dicarboxylatobenzyl) − 3,5-pyrazole dicarboxylic acid)] by the solvothermal synthesis. The free ligand absorbed the photon and luminescence emission (at 435 nm) that may due to the singlet state to ground singlet state radioactive transition (π-π*). This MOF resulted in a fluorescence mechanism due to the quenching process and the synthesized Tb-MOFs showed good water stability. The introduction of UA into MOF suspension resulted in the interaction with the linker in MOF pores. This quickly quenched at 544 nm ($5D^4 \rightarrow 7F^5$, Tb^{3+}) followed by a decline in intensity by adding 0 nM to 1 nM UA concentration. Astonishingly, the ZJU-158-Eu suspension was found to be quite sensitive and it showed acceptable results for sensing of UA in the provided samples. For a moment, ZJU-158-Tb test papers have been designed for biological applications that rapidly monitored levels of artificial, or serum UA that were confirmed due to change in color. The practical test paper strategy using ZJU-158-Tb for the fast observing capability of abnormal UA has shown dark green color at a 500 μM concentration of the UA that can be observed by naked eyes. Finally, the sensitivity of ZJU-158-Tb to UA was conducted by using different solutions of UA and that showed by Stern-Volmer equation and selectivity factor, which is essential for different biomolecules ions sensing. This novel MOF platform provided the LOD of 7 nM (S/N = 3) and showed a good linear correlation between UA concentration from 0 − 100 μM to the luminescent intensity of biosensors. Besides, MOF showed a higher selectivity towards the UA in presence of metal ions (Na^+, K^+, etc.) and small biomolecules (urea, creatinine, sucrose, etc.). Concisely, the synthesized MOF provided good stability, superb luminescence, high selectivity, and sensitivity. In the future, it can be a potential substitute for futuristic UA sensing and other biosensing applications [69]. As per the literature, enzyme-based UA detection suffers from several demerits such as low selectivity, accurate pH environment, costly enzymes, long incubation time (up to 30 min), and minimal detection accuracy. Interestingly, fluorescence-based sensors offer several merits in terms of repeatability, convenience, and cost. In 2019, a novel fluorescent sensor has been synthesized from Zr- MOF (UiO-66-NH_2) followed by functional PSM (UiO-PSM) with picolinic acid (PA) through amidation reaction for direct estimation of UA.

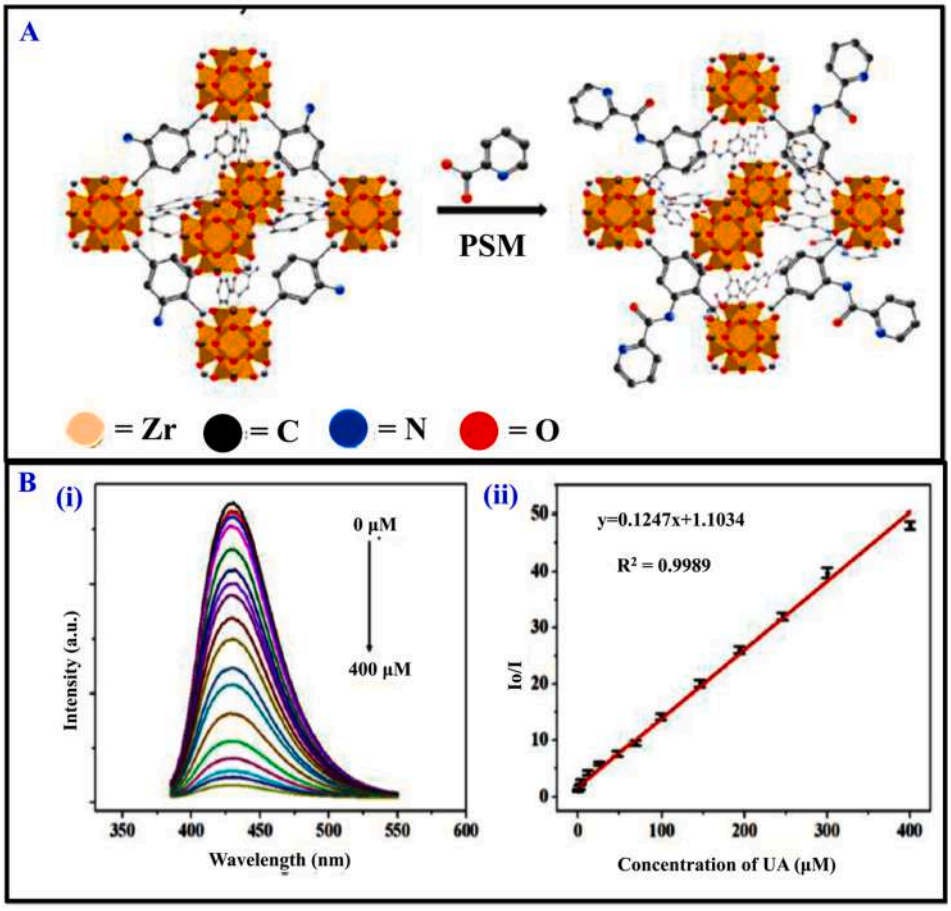

Fig. 5. (A) Synthesis process of UiO-PSM. (B-i) Fluorescence spectra after adding a range of concentrations of UA (0 μM to 400 μM) and (B-ii) fluorescence intensity ratios (I_0/I) of UiO-PSM after adding a range of concentrations of UA (0 μM to 400 μM).[Reprinted with permission from ref [27]. Copyright 2019, American Chemical Society.]

Fluorescence investigation showed high selectivity and sensitivity that may be due to the quenching mechanism of UiO-PSM, π − π interactions, and hydrogen bonding. UiO-66-NH_2 was employed because of its excellent unsaturated coordination, metal active sites, and (Zr) chemical stability. Fig. 5A shows the synthesis of novel UiO-PSM. Interestingly, in this biosensor, PSM was found to be an efficient approach to lead functional groups with activated sites into MOF to achieve high-performing fluorescent sensors. Interestingly, owing to the ligand-to-metal charge transfer, UiO-66-NH_2 provides fluorescence emission at a wavelength of 419 nm. After PSM, it shows a bright blue fluorescence (at 435 nm) as compared to the plain UiO-66-NH_2. The red shift in emission wavelength confirmed an improvement in ligand-to-metal charge transfer efficiency of MOF. A minor reduction of the fluorescence intensity of UiO-66-NH_2 was observed, which might be a presence of weak interaction among unsaturated metal sites (Zr) and UA. The size and cubic morphology of UiO-PSM crystals transformed only a little after adding UA. Notably, this biosensor showed a wide linearity in the range 0.01–400 μM ($R^2 = 0.9986$) with a LOD of 2.3 nM (S/N = 3), which was much less than the normal healthy person serum-containing UA. In addition, this method had a response time of 1 min (Fig. 5B). UiO-PSM sensors showed specific sensing of UA in the presence of glycine, glucose, adenine, L-cysteine, Na^+, K^+, urea, and ascorbic acid. The possible mechanism in the sensing of UA is based on the coordination among UA containing amino groups and Zr containing unsaturated metal sites. Additionally, the UA and UiO-PSM containing π-π interaction, coordination, and hydrogen bonding contributed to the fluorescence quenching mechanism of MOF. After the addition of UA into UiO-PSM, the fluorescence lifetime did not change and this assured the UA recognition using UiO-PSM through a static quenching mechanism. In conclusion, it can be expected that this biosensor has a great potential in the detection of UA and related biomarkers of various diseases [27].

The organic metal structure functionalization using pyrene for the recognition of UA is an alternative substitute of previously reported fluorescence sensors using non-enzymatic-ratiometric detection via conformational changes in their properties. In a recent study, Dalapati *et al.* developed the pyrene functionalized and Hf-based mixed ligand MOF with UiO-66 for UA fluorimetric sensing (Fig. 6A). A mixed ligand Hf-MOF (Hf-UiO-66-Py MOF) was developed along with incorporating 2-(pyrene-1-carboxamide) terepthalic acid (H_2L): 1, 4 - benzene dicarboxilic acid (H_2BDC) as a ligand (1:1) that showed high selectivity and sensitivity towards the UA. A non-enzymatic and ratiometric sensor showed a detection limit of 1.4 μM with a 0–30 μM sensitivity range. It offered better sensitivity for UA detection in pure aqueous solution that may due to the conformational changes from the excimer into the monomer. The presence of a free pyrene functionalized ligand played an important role in the conformation changes. The pyrene-functionalized ligand in UA sensing revealed that un-functionalized Hf-UiO-66 MOF in both conditions (presence and absence of UA) showed as a spectrum of fluorescence. This study ultimately showed that fetal bovine serum lowered fluorescence when mixed with water compared to the fixed UA level. Furthermore, a diluted serum sample with 100 μM of MOF was added and that showed a clear appearance of monomeric emission (λ_{em} = 383 nm and 400 nm) of pyrene with reduced excimer emission (λ_{em} = 512 nm) in the presence of UA, which lead to conformational changes.

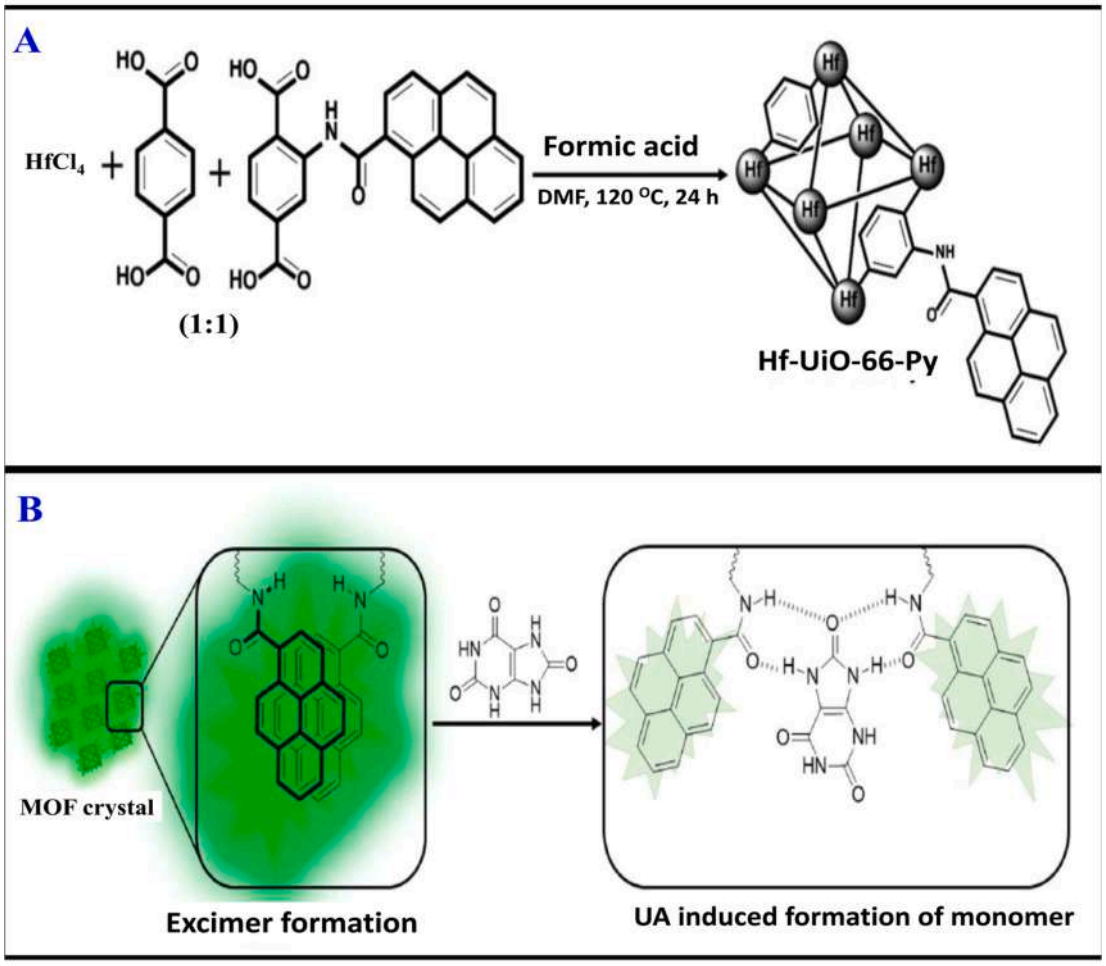

Fig. 6. Fabrication of Hf-UiO-66 MOF (A), The Plausible H-bonding interaction among the amide group of the organic linker and the UA containing complementary amide group (B). [Reprinted with permission from ref [51] Copyright 2019, American Chemical Society.]

This study concluded that the H_2L ligand was responsible for the sensing mechanism. The structural optimization demonstrated that the amide 'O' atom of preferred organic ligand and amide 'H' atom of UA resulted in the hydrogen bonding between UA and MOF. Additionally, the MOF contained large mesopores properties that helped in diffusing of the UA via a pore and that was possible due to the hydrogen-bonding interactions. The presence of a high number of H-bonding interaction sites in UA offered a rapid fluorescence response as compared to other biomolecules similar to UA. Therefore, this study suggested that the highly selective detection of UA was found, which might due to the hydrogen bonding interactions between UA and MOF ligand (Fig. 6B). This MOF demonstrated the poor fluorescence intensity into aqueous in contrast to the other solvent. Subsequently, it showed a linear correlation between the solvent polarity and fluorescent intensity observed from Hf-UiO-66 MOF. The rise in the polarity of MOF was found due to the rise in the hydrogen bonding ability of the selected solvent. It was confirmed that the higher polarity solvent decreases the pyrene excimer formation through the strong hydrogen bonding that further lead to a proportional decrease in the MOF fluorescence. Interestingly, the solvent-reliant fluorescent assured the hypothesis of hydrogen-bonding interactions during UA biosensing. Furthermore, the small decline in the excited-state lifetime values in the case of excimer, and monomer, confirmed the interaction between UA and MOF. The recovery of UA in biological fluids (spiked UA concentration: 10 μM) namely blood serum and urine was found to be 98.7% and 103%, respectively. Finally, the MOF-coated paper strip showed the drastic alteration in fluorescence from bright green to bluish-green at a 1 mM concentration of UA. Overall, this biosensor could be a new and highly sensitive alternative to diagnose various UA-associated health issues and can be used for on-site detection [51].

Several pioneering studies mentioned that the different types of Ln-MOFs (Ln = Tb, Eu) have been used for precise recognition of metal ions, inorganic and small molecules. The promising interest analyte detection can be possible using Ln-MOF that may be because of its coordinating modes and remarkable fluorescent properties. In 2020, Han and co-researchers designed Ln-MOF $Eu_2(TDA)_4(OOCCH_3)_2(H_2O)_2$ also known as Eu-TDA (TDA = 2,5-thiophenedicarboxylic acid group, $OOCCH_3$ = glacial acetic acid group) through the hydrothermal method and used for the detection of malachite green (MG) and UA (Fig. 7). It showed good thermal stability and exhibited stronger fluorescence in ethanol as compared to other organic solvents. Interestingly, Eu-MOF offered remarkably high sensitivity plus selectivity towards MG and UA along with detection limits of 0.0221 μM and 0.689 μM, respectively. Furthermore, the Eu-MOF showed quenching of fluorescence emission in the existence of MG and UA. The possible detection mechanisms such as spectral overlap, competition, and energy transfer can be involved in the detection of UA and MG using Eu-MOF. The individual quenching ability of the analyte showed LOD and provided higher selectivity in the presence of different metal ions (14 anions and 11 cations). In conclusion, Eu-MOF could be used as a substitute for highly sensitive plus selective recognition of biomarkers and chemicals such as UA and MG in the biomedical fields and the aquaculture industry [70].

Xanthine oxidase (XO) helps in the oxidation of hypoxanthine to xanthine and then to UA using oxygen as an oxidant. Therefore, it gained much consideration from researchers in the diagnosis of UA-related health issues. In this context, Zr-based MOFs (BTB-MOF) were synthesized using zirconium (IV) chloride and 1, 3, 5-tris (4-carboxyphenyl) benzene (H_3BTB) that offered stable photoluminescence in a buffer solution and pure water. Finally, the assay of xanthine and XO was carried out by monitoring the fluorescent intensity at 372 nm. BTB-MOF showed an excellent fluorescent response to xanthine and UA (an oxidation product of xanthine). Both UA and xanthine affected the BTB-MOF emission (quenching) along with many differences in efficiency. It provided a linear range concentration of 0.02–4 mg/L and a low LOD of 0.4 μg/L (0.004 U/L). In addition, it provided rapid detection within 1 min that confirmed the speedy detection of UA and their related products. Moreover, it demonstrated high selectivity in the presence of interfering species such as enzymes, and amino acids. Concisely, BTB-MOF offered high sensitivity, rapid detection, simplicity, and selectivity. In the future, BTB-MOF can be used for enzyme analysis as well as biomolecules detection [75]. Table 1 summarizes the types of luminescent/fluorescence-based biosensors for UA detection in body fluids.

3.2. Electrochemical biosensor

Electrochemical biosensor offers unique characteristics such as high precision, ease of use, remotely controlled devices that are considered to be desired tools for UA measurement. Recently, the design of advanced electrochemical biosensors has gained huge significance due to the

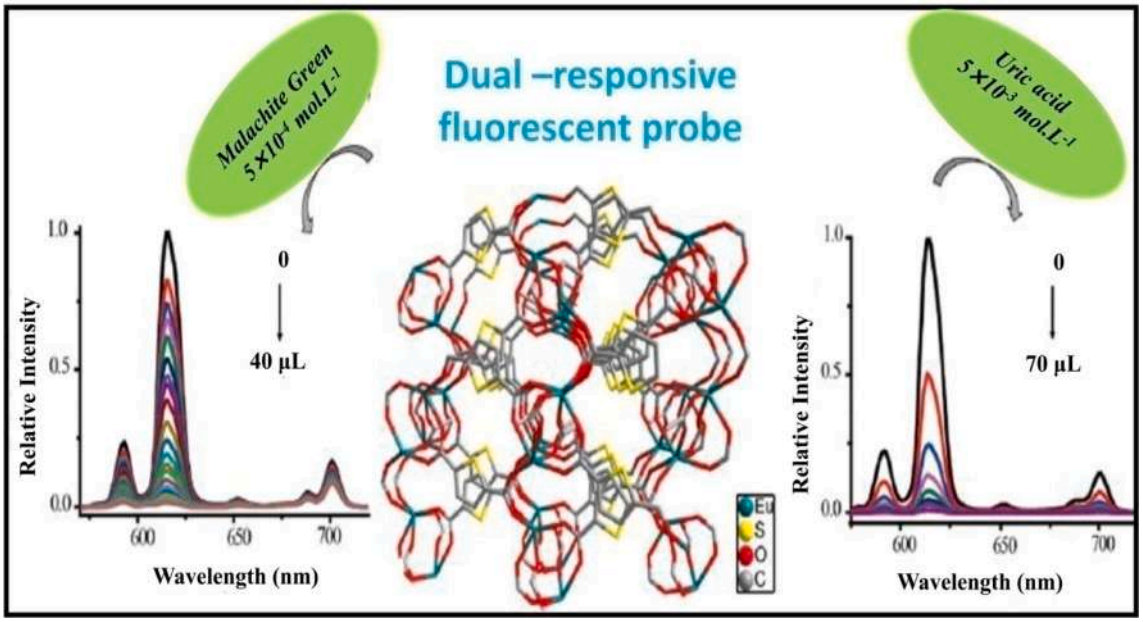

Fig. 7. A Eu-MOFs fluorescent probe for efficient detection MG and UA. [Reprinted with permission from ref [70]. Copyright 2020, American Chemical Society.]

Table 1
Summary of surface architectured MOF-based fluorescence biosensor for ultrasensitive detection of UA in clinical samples.

Sr. No.	MOF-basedcomposite	Precursor (Initial material)	Types of sensor	Sensing mechanism	Linear range	Quenching constant (K_{sv})	LOD	Clinical sample	Silent features	Ref.
	Cu^{2+}@MIL-91 (Al: Eu)	Europium nitrate	Fluorescent	On-Off-On	10–1200 μM/L	—	1.6 μM	Urine	It exhibited luminescence but after inducing UA into MOF solution showed a rebound with greater luminescence intensity, which responsible for the detection of UA.	[63]
	Ln-MOF	Ln $(NO_3)_3$*$6H_2O$	Fluorescent	On-Off	0 mM –64 mM	1.13×10^3M/L	0.49 μM	Urine	It provides high sensitivity, good selectivity, excellent reversibility, and regeneration ability.	[74]
	ZJU-158-Tb	Tb	Fluorescent	On-Off	0 μM −100 μM	8370 M^{-1}	7.0 nM	Urine	The chemical state of selected ligands influenced due to Tb-MOF interaction with UA and it resulted in "turn down sensing" for UA.	[69]
	UiO-PSM	Zirconium chloride	Fluorescent	On-Off	0.01 μM – 400 μM	1.395×10^5 L/M	2.3 nM	Serum	The resulting UiO-PSM sensor quenched the fluorescence owing to hydrogen bonding and π − π interactions.	[27]
	Hf-UiO-66-Py MOF	Halfnium tetrachloride	Fluorescent	On-Off	0 μM −30 μM	—	1.4 μM	Serum, urine	Hf-UiO-66-Py-MOF interacts with UA owing to hydrogen bonding that resulted in quenching of fluorescence followed by an assessment of UA.	[51]
	Ln-MOF	Europium (III) nitrate hexahydrate	Fluorescent	On-Off	—	4.15×10^4 M^{-1}	0.689 μM	—	The Ln-MOF-based fluorescent biosensor shows greater potential towards UA. It exhibited fluorescence quenching after the addition of UA due to energy transfer and spectral overlap.	[70]
	BTB-MOF	H_3BTB	Fluorescent	On-Off	—	0.02 – 4 mg/L	0.0004 mg/L	—	BTB-MOF showed an excellent fluorescent response to xanthine and UA (an oxidation product of xanthine).	[75]

necessity for speedy and specific quantification of analytes, viz. biochemical agents and biomedical markers. The applications of gold (Au), silver (Ag), Pt-like metals are extensively employed in electrochemical sensors, but the application of such costly metals impedes its application in biosensing. Therefore, the application of metal oxide is an excellent substitute that replaced the costly metals in recent years. In 2018, Pend and colleagues constructed nanosized and stable cerium oxide (CeO_2) and pristine graphene oxide (GO) based CeO_{2-x}/C/rGO composites (rGO: reduced GO) through pyrolysis of MOF (Ce-MOF) with the pristine GO material. The application of carbon materials such as rGO in electrochemical biosensors offers less negative potential that may due to the excellent electrical conductivity and larger surface area. The addition of metal oxide into the rGO resulted in enhanced catalytic performance and electron transfer mobility that helps speedy and accurate recognition of UA in clinical samples. It has been stated that the CeO_{2-x}/C/rGO furnishes superb catalytic characteristics towards hydrogen peroxide (H_2O_2), which may due to the co-existence of Ce^{3+} and rGO. Ultimately, the calcination temperature plays an important part in the presentation of CeO_2-x/C/rGO composites towards H_2O_2 revealing. It showed high selectivity and sensitivity towards the UA along with a wider linear range from 49.5 − 1050 μM. Additionally, the LOD of UA was found to be 2.0 μM. In this study, the UA sensing mechanism depends on the concentration of H_2O_2 due to its high catalytic property. Furthermore, voltammograms, chronoamperometry demonstrates the remarkable thermostability of developed nanocomposites, which may be due to oxygen vacancies. Higher oxygen vacancies in fabricated CeO_{2-x}/C/rGO nanocomposites favored the upgrading of the overall catalytic property towards H_2O_2 along with excellent electrical conductivity of 'C' entrapment with CeO_{2-x} and rGO furnishing electron transport in the electrochemical reaction. Finally, the excellent anti-interference ability of CeO_{2-x}/C/rGO composites towards ascorbic acid and urea in the presence of UA can further its prospects in clinical applications [67].

Yet another work reported the Ce-MOF-based porous CeO_{2-x}/C nanorods (NRs) for highly sensitive and selective sensing of UA at the low working potential. In brief, after the synthesis of CeO_{2-x}/C NRs from Ce-MOF, the uricase-loaded CeO_{2-x}/C NRs (enzyme electrode) have been immobilized on the surface of the glassy carbon electrode (GCE) through physical adsorption and cross-linking method. The raised oxygen vacancies permit the negative shifting of the working potential to the detection of H_2O_2. As per amperometric responses, the LOD, sensitivity, the linear concentration range of UA using CeO_{2-x}/C NRs were found to be 3.2 μM, 220 μA*cm^{-2}*mM^{-1} and 50–1000 μM (R^2 = 0.998), respectively, at lower working potential (-0.4 V). Additionally, the CeO_{2-x}/C NRs exhibited superior selectivity towards UA in the presence of other interferences in the human urine samples that may due to the low working potential. Importantly, the Ce^{3+} accumulation in NRs showed an excellent reduction potential towards H_2O_2. In the future, Ce-MOF-based electrochemical biosensor can be used as an excellent alternative for biosensing of UA in clinical samples [76]. As we know, the electrochemical sensor-based analysis of target molecules offers several merits such as high sensitivity, accuracy, simplicity, and less expensive. However, simultaneous estimation of UA and other biomolecules using conventionally designed solid electrodes suffer from several limitations such as overlapping of oxidation potentials. Researchers working in this area have attempted to create innovative nanocomposites as biosensing materials that can simultaneously recognize these small biomolecules. In 2018, Hu *et al.* designed Co_3O_4/Fe_3O_4/mC@g-C_3N_4 by embedding

cobalt (Co) and iron (Fe) based bimetallic (Co-Fe) nanocatalysts into the mesoporous carbon (mC) and graphitic carbon nitride (g-C_3N_4) nanosheets for simultaneous analysis of UA, ascorbic acid, and dopamine. Bimetallic Co-Fe alloy nanoparticles encapsulated in N-doped carbon matrix has been constructed through pyrolysis of melamine ground Co/Fe-MOFs (Fig. 8). The application of cobalt tetraoxide (Co_3O_4) and iron oxide (Fe_3O_4) offered high stability and enhanced the electrocatalytic property of nanocomposites. Moreover, the application of Co_3O_4 provided high selectivity to the target molecule, whereas the addition of g-C_3N_4 nanosheets offered a large surface area and high fluorescence that gives a new platform for the assessment of biomarkers. This technique furnishes a higher electrochemically active surface area (0.0963 cm^2) of Co_3O_4/Fe_3O_4/mC@g-C_3N_4 based GCE as compared to g-C_3N_4 and Co/Fe-MOF-loaded GCE and confirmed the presence of electron inactive sites and blacking groups reduced the electrochemically active surface areas. Furthermore, Co_3O_4/Fe_3O_4/mC@g-C_3N_4 increased the surface area of GCE that helped to rapid mass transfer of the interest analyte. Particularly, the sensing performance of Co_3O_4/Fe_3O_4/mC@g-C_3N_4 based GCE provided an excellent electrochemical performance that may due to the good electronic conductivity composite and the synergistic response of each component in Co_3O_4/Fe_3O_4/mC@g-C_3N_4. The differential pulse voltammetry (DPV) techniques provided a linear concentration range and LOD of UA about 5.0–100 μM ($R^2 = 0.994$) and 0.37 μM, respectively. In the case of simultaneous estimation, the linear concentration range, and LOD for UA were found to be about 5.0 μM to 100 μM and 0.18 μM, respectively. Moreover, Co_3O_4/Fe_3O_4/mC@g-C_3N_4 biosensor showed good selectivity, acceptable reproducibility, and excellent stability. Concisely, the analysis of UA, ascorbic acid, and dopamine in human urine samples showed outstanding recoveries that confirmed the practical applications of Co_3O_4/Fe_3O_4/mC@g-C_3N_4 in clinical diagnosis [77].

In 2019, the appropriate ratio of ZIFs (ZIF-8: ZIF-67) was used for the designing of bimetallic ZIFs (BMZIFs) using bimetals Zn/Co at 900 °C in an N_2 atmosphere through nitrogen (N), and Co-doped porous carbon (CNCo). In brief, Liu and co-investigators came up with ZIF-8 and ZIF-67 for the assessment of UA in the human serum sample using an electrochemical CNCo/GCE biosensor. In this biosensor, the BMZIF-templated porous carbon provided several advantages such as high surface area and pore volume along with excellent catalytic activity, high chemical stability, electrical conductivity, low cost, and easy availability. Due to this, the CNCo modified GCE biosensor provided an elevated peak current as compared to the bare GCE. The results showed an improved conductivity and sensitivity of the sensor. The LOD was 0.83 μM (S/N = 3) with a liner range of 2–110 μM ($R^2 = 0.995$). The presence of interfering substances such as glucose, ascorbic acid, and other positive and negative ions had no significant influence on the current changes. Interestingly, the modified GCE biosensor exhibited a superior reproducibility of 3.07% and repeatability with a relative standard deviation (RSD) of 3.26% in phosphate buffer saline (PBS, pH 7.0) with a 50 μM concentration of UA. Eventually, the recoveries of samples (spiked) ranged from 98.2% to 103.5% and RSDs ranged from 1.8% to 2.7%, signifying that the fabricated CNCo/GCE biosensor had a great perspective for use in real samples analysis [68]. Recently, tears containing biomarkers have received a lot of interest in sensing and controlling health. The concentration of UA in the tears is a sign of different diseases including gout, kidney disease, etc. The concentration of UA in tears, according to the literature, is between 25 and 150 μM. Nowadays, the seedy and accurate detection of UA is a critical step that affects the diagnosis and treatment. In 2018, Xiong and co-authors constructed solution-gated graphene transistors (SGGTs) based on two separate 'Au' gate electrodes that were modified with GO-chitosan (GOx-CHIT) and bovine serum albumin (BSA)-CHIT (BSA-CHIT) for UA and glucose

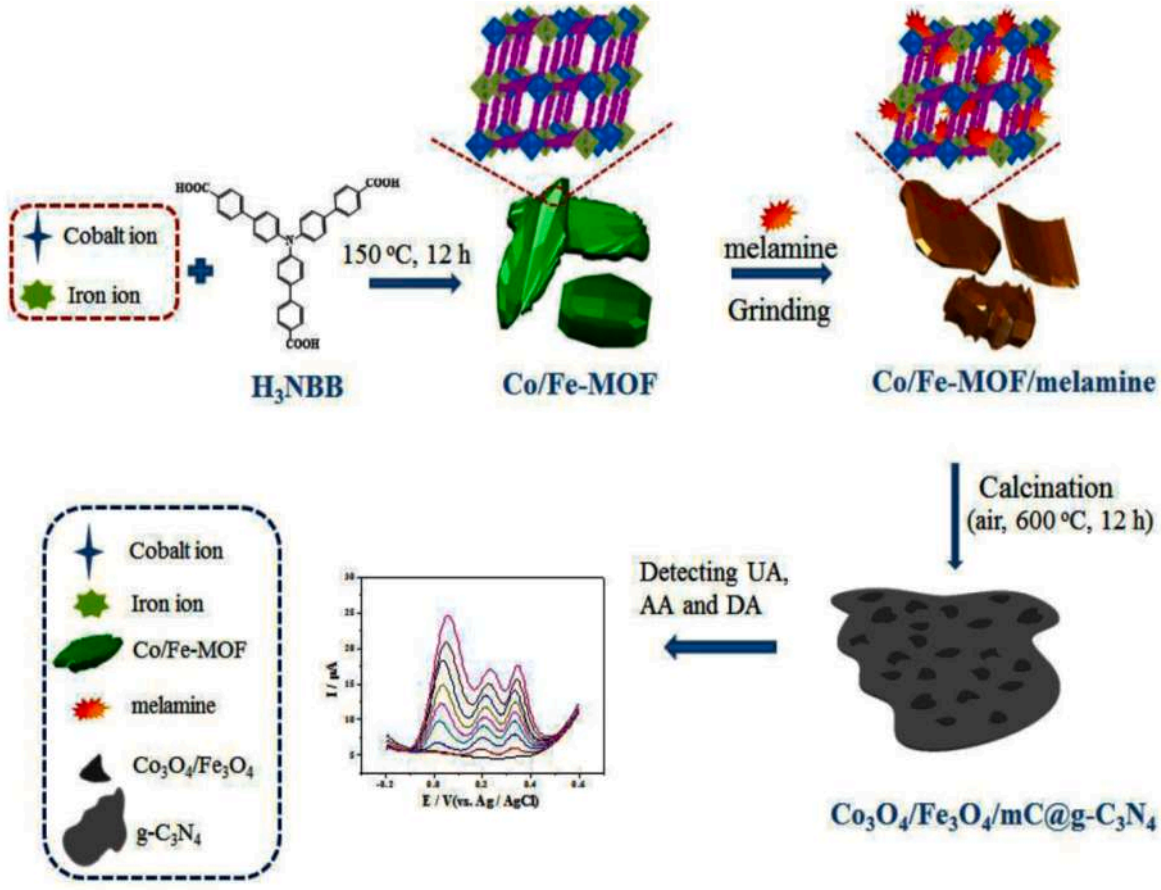

Fig. 8. Synthesis scheme of Co_3O_4/Fe_3O_4/mC@g-C_3N_4 for sensing of UA and other molecules. [Reprinted with permission from ref [77]. Copyright 2018, Elsevier.]

detection. Primarily, the sensitivity of SGGTs was boosted significantly through co-modifying the 'Au' gate with porous hollow nano-polyhedrons (Co_3O_4) obtained from ZIF-67. The GOx-CHIT/Co_3O_4/Au gate identified the current response for UA and glucose. On the contrary, BSA-CHIT/Co_3O_4 modified gate could sense the UA current response only. The direct electro-oxidation of UA on the designed gate provided a highly sensitive detection of UA. Whereas, at the designed gate, glucose suffered the oxidation, converted into H_2O_2, which helps to sense glucose. Interestingly, it provided a low LOD of 100 nM for UA and glucose. In addition, the functionalized SGGT biosensor confirmed the presence of UA and glucose in real-time sample analysis in human tears. This method showed 98.5 μM and 323.2 μM amounts of UA and glucose in tears, respectively. Overall, the Co_3O_4 hollow nanopolyhedron offers different merits such as biocompatibility, simplicity, excellent electrocatalytic performance, high sensitivity, and selectivity. This study concluded that the biosensor modification offered a new electrochemical sensing platform for UA and other biomarker detection in tears [78]. Studies indicated that MOF-derived porous carbon provided a robust structure and high specific surface area that can be an excellent candidate for biosensors. In this vein, Xu *et al.* developed ligand-derived carbon matrix (Z-1000) by carbonizing ZIF-8 that showed high electrical conductivity and improved electrochemical activity. This could be attributed to the high graphitization, nitrogen doping, and organized porous structure. ZIF-8 was synthesized using zinc nitrate and 2-methylimidazole, whereas Z-1000 was obtained from ZIF-8 by carbonization process (Fig. 9). Later, Z-1000 was applied on the surface of GCE (Z-1000@GCE). Amperometric responses of Z-1000@GCE confirmed that the present biosensor offered the linear response and low LOD for UA from 0.001 to 0.3 mM and 278 nM, respectively. It demonstrated the high selectivity for UA in the presence of ascorbic acid and dopamine. In addition, the Z-1000@GCE biosensor (n = 10) provided 1.04% of RSD for 0.1 mM UA, which assured high reproducibility. The real-time analysis of UA in human serum resulted in 95% to 102% recovery that confirmed the potential of electrochemical detection of UA in real samples. The authors of this study concluded that good sensitivity, high selectivity, excellent reproducibility, and real-time applicability of Z-1000@GCE make it promising in sensing different biomolecules in body fluids [79].

Xanthine is a precursor for UA and elevated concentrations of xanthine in biological samples confirmed the presence of different UA-related diseases. In comparison with the previously used method, the applications of an electrochemical sensor with non-enzymatic detection have gained much attention. In this context, a novel MIL-101 (Cr) porous cage with a large specific surface for loading of the Pt nanoparticles were developed for non-enzymatic electrochemical biosensing of UA and other related biomarkers such as xanthine, dopamine, and hypoxanthine. In brief, the MIL-101 (Cr) was synthesized using chromium (III) chloride hexahydrate ($CrCl_3{\cdot}6H_2O$) and H_2BDC for conjugation using the vigorous stirring method. Later, Pt-nanoparticles were incorporated followed by loading onto polished GCE. The DPV method was used for sensing XA and simultaneous detection of UA that showed reactions at Pt@MIL-101 (Cr) modified electrode for sequential accumulation of xanthine at varying concentrations. Pt@MIL-101 (Cr) showed remarkable sensitivity of 1.88 $\mu A{\cdot}\mu M^{-1}{\cdot}cm^{-2}$ and 0.42 μM LOD at 0.68 V potential. Moreover, Pt@MIL-101 (Cr) containing 3D cavities helped to reach over small pores for transmission of xanthine molecules to GCE. The linear concentration range was found to be in the range of 0.5 μM to 162 μM ($R^2 = 0.999$). This biosensor provided high conductivity and high efficiency for electrocatalytic oxidation of xanthine when combined with MIL-101 (Cr) and Pt nanoparticles in the case of UA, xanthine, dopamine, and hypoxanthine. In this study, the MOF showed a good porous surface that prevented the aggregation of nanoparticles, whereas the RSD of this biosensor was found to be 2.06% (n = 5) with good reproducibility. The real-time analysis of xanthine at three spiked (specific known concentration) human serum samples (pH 7, PBS) showed 100.80% to 203.00% recoveries of xanthine that confirmed the applicability in real sample analysis. However, there is a necessity to perform this assay directly in the real-time samples without dilution. Therefore, Pt@MIL-101 (Cr) offers huge active sites for biosensing of xanthine and simultaneously UA. In the near future, this can be a new technique for the electrochemical determination of xanthine in clinical samples [71]. Yet another work reported the determination of UA and dopamine using Co(II)-based ZIF-67 and GO electrodeposited GCE (ZIF-67-GO/GCE). The linear concentration range and LOD for UA were reported to be 0.8–200 μM ($R^2 = 0.992$) and 100 nM, respectively (S/N = 3). It is worthy to mention that the high porosity and larger specific

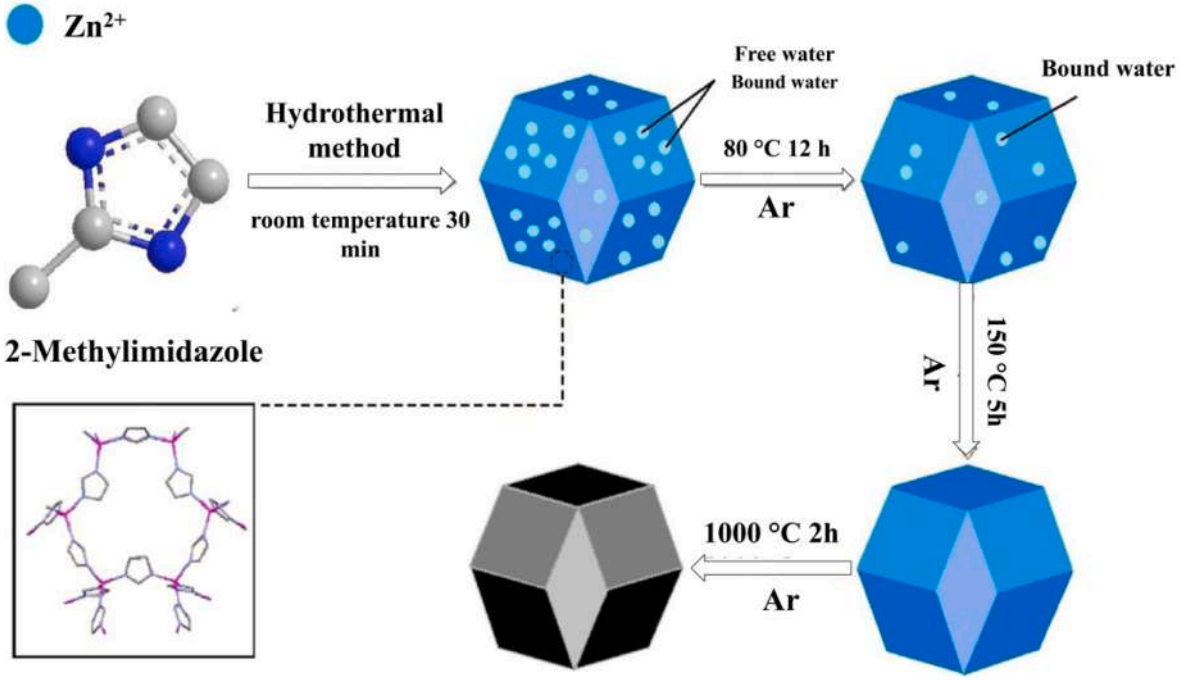

Fig. 9. Preparation of ZIF-8 and synthesis scheme of Z-1000. [Reprinted with permission from ref [79]. Copyright 2017, Elsevier.]

surface area of ZIF-67 and high electrical conductivity of GO resulted in electron transfer. ZIF-67-GO/GCE offered synergistic effects in terms of sensitivity, selectivity, stability, and reproducibility. The real-time analysis of UA and dopamine in spiked samples of human urine showed 97.6% − 103.9% and 97.3% − 100.6% recoveries for UA and dopamine, respectively. Therefore, in the future, the modified electrodes can open a new door for the simultaneous estimation of UA and dopamine in biomedical fields [80]. It was reported that the porphyrinic MOF (Por-MOF) contains specific catalytic ability of biomimetic catalysis. Yin and colleagues reported a one-step synthesis of Zr-Por-MOF/MPC using 5, 10, 15, 20-Tetrakis (4-carboxyphenyl) porphyrinato]-Fe (III) chloride as a ligand, zirconium chloride, macroporous carbon (MPC) through the solvothermal method. Zr-Por-MOF/MPC was applied onto the surface of GCE (Zr-Por-MOF/MPC@GCE). The electrocatalytic activity of Zr-PorMOF/MPC towards H_2O_2 reduction was measured using CV that confirmed the outstanding performance of Zr-Por-MOF/MPC@GCE as compared to the bare GCE, Zr-Por-MOF, and Por-MOF. The addition of MPC into Zr-Por-MOF resulted in increased specific surface area and prevented the agglomeration of Zr-Por-MOF nanocomposites. In addition, it improved the electrochemical stability of Zr-Por-MOF and reduced the electron transfer resistance. Taken as a whole, MPC offered a conductive bridge for simplistic charge transport and finally, Zr-Por-MOF/MPC provided an elevated electrocatalytic efficiency for the reduction of H_2O_2. As a result, two linear concentration ranges of 0.5–137 μM (R^2 = 0.991) and 137–3587 μM (R^2 = 0.993) with a respective sensitivity of 66 μA/mM and 16 μA/mM were reported. In addition, this method provided a rapid response within 1 s and a low LOD of 0.18 μM. This developed sensor offered high selectivity for H_2O_2 (0.1 mM) in the presence of different biomolecules with excellent stability and high reproducibility. Additionally, the simultaneous detection of UA was performed using DPV in the presence of purine derivatives. The peak current was increased linearly with an increase in UA concentration in the range of 20–410 μM (R^2 = 0.996) and a lower detection value of 160 nM. In conclusion, enzyme-free H_2O_2 Zr-Por-MOF/MPC@GCE showed a wide linearity range, high sensitivity, low detection limit, rapid response, good reproducibility, good selectivity, and excellent stability. This method could also be used for UA detection in the presence of other purine derivatives such as xanthine and hypoxanthine [81]. In recent years, the production of metal-based simplified sensing materials for sensitive and selective UA detection was discussed. In 2020, Abrori *et al.* reported MOF-67-loaded GCE for non-enzymatic electrochemical detection of UA using DPV and cyclic voltammetry (CV). The synthesis of MOF-71 was accomplished using H_2BDC and cobalt nitrate hexahydrate through the solvothermal method. The detection of UA using DPV showed a lower detection of 15.60 μM and linearity in the range of 50–1000 μM with 0.4811 $mA.mM^{-1}.cm^{-2}$ sensitivity (S/N = 3). A relatively less significant oxidation peak was observed at a lower UA concentration of 50 μM as compared to the oxidation peak obtained from PBS. This could be attributed to the release of electrons from the low concentration of UA upon contact with GCE-coated MOF-71. Fig. 10 showed the sensing mechanism of MOF-71-loaded GCE for UA oxidation, wherein UA was converted into the allantoin. The increase in UA concentration showed an increment in the UA oxidation and reduction in the oxidation peak of PBS solution. The selectivity test in the presence of glucose and urea confirmed the selectivity of MOF-71 coated GCE towards the UA. Importantly, the larger the surface area, the better was the electrical conductivity of MOF-71 due to elevated electron transfer. Therefore, in the future, MOF-71 can be preferred as a potential sensor material for non-enzymatic electrochemical biosensor for high sensitivity and selective detection of UA in clinical samples [82].

Current electrochemical sensors have significant drawbacks, including a lack of sensitivity, particularly for detecting low concentrations of UA. Therefore, the application of enzyme mimetic activity containing nanomaterials (termed nanozyme) is gaining much attention for the development of ultrasensitive biosensors. Along with nanozyme, the application of MOF offers synergistic benefits for sensing the target analyte. Recently, Wang and co-researchers developed an ultrasensitive

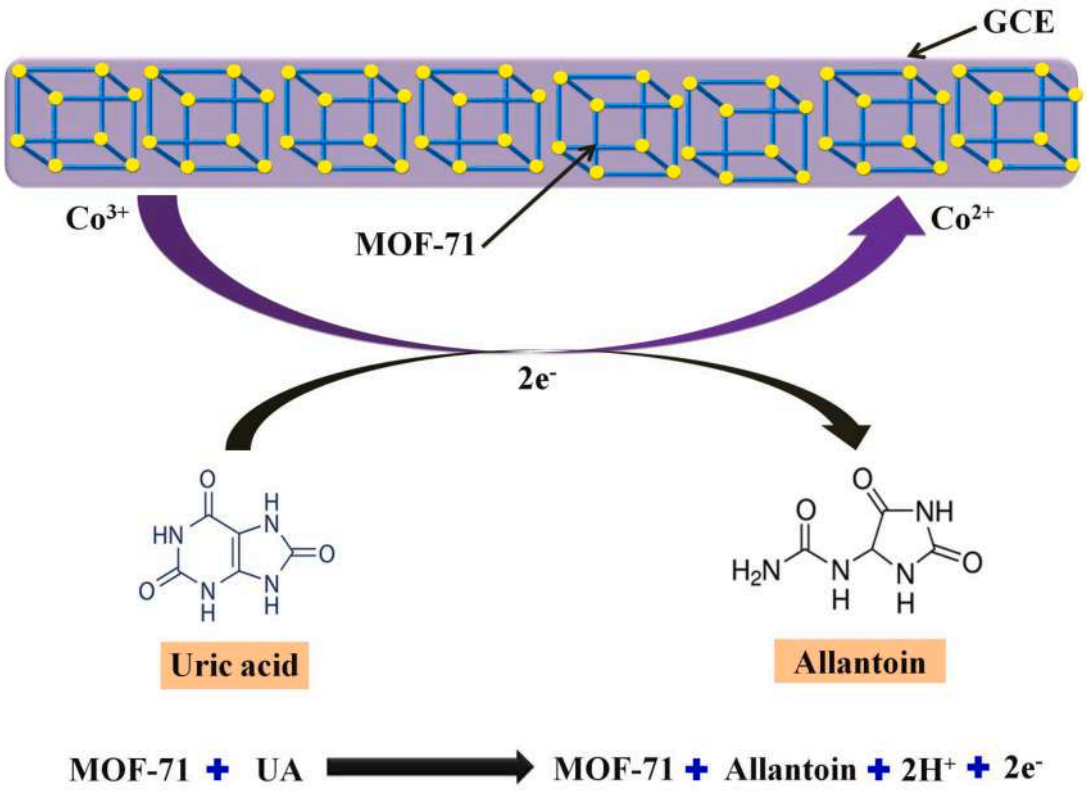

Fig. 10. Schematic presentation of sensing mechanism of MOF-71-loaded GCE for UA oxidation.

ZIF-67 based MOF through the pyrolysis method using auric chloride ($HAuCl_4$) for the estimation of UA in the human serum samples. Au/Co bimetallic nanoparticles integrated hollow nonporous carbon-based frameworks (Au/Co@HNCF) were manufactured as a nanozyme through pyrolysis of the Au (III)-etching ZIF-67. The application of Au/Co on the external surface of HNCF accomplished an elevated activity for UA oxidation and generated a superior signal in the electrochemical biosensor. This engineered Au/Co@HNCF biosensor exhibited a detection limit of 0.023 μM (S/N = 3) for all human serum samples. Additionally, the method provided an ultrahigh sensitivity of 48.4 $\mu A*\mu M^{-1} cm^{-2}$ and linearity in the concentration range of 0.1–25 μM. The logarithmic concentration region was found to be 25 μM to 2500 μM. The test results showed DPV responses within the range of 95.1% to 104.4%, which revealed that the Au/Co@HNCF based sensor had an outstanding selectivity to UA. The ordered nonporous structure of MOF and carbon material-based interfacial features showed good selectivity towards UA in the presence of other biomolecules. The intra-day and inter-day reproducibility were found to be 4.1% and 4.3%, respectively. Human serum samples were analyzed using Au/Co@HNCF biosensor and compared with the results obtained using Roche Diagnostics Cobas® 8000. It was confirmed that the MOF-based biosensor could be used practically for UA determination in clinical samples. This study indicated that Au/Co@HNCF biosensor provides several merits such as low cost, good stability, reproducibility, high selectivity, and sensitivity. Further, a MOF-centered biosensor could be a reliable tool for the diagnosis of UA-associated life-threatening issues [44].

U*ricase*-based electrochemical sensing is a very important step in the biomedical field, due to its high accuracy, selectivity, and specificity. The oxidation of UA with rapid enzymatic function furnishes H_2O_2 and allantoin. The amperometric response obtained by the catalysis of H_2O_2 is related to the UA concentration. In this context, the Cu_2O/Cu@C porous core–shell nanowire (NW) has been designed through a thermal breakdown of HKUST-1(Hong Kong University of Science and Technology), copper (II) nitrate hydrate [$Cu(NO_3)_2{\cdot}3H_2O$], and trimesic acid (H_3BTC). Later, the NWs were recycled as electrode materials to formulate novel MOF-based UA biosensors. Remarkably, they were able to control the calcination and the composite particle was enfolded with a long NW for the lower working potential. It is advantageous for the successful anti-interference aptitude of UA biosensing. Leo *et al.* immobilized *uricase* on Cu_2O/Cu@C porous core–shell NWs modified GCE through physical adsorption and crosslinking method. Carbon from the decomposition of selected organic ligand molecules in NWs promoted higher electron transfer. Furthermore, 'Cu' in the NWs exhibited good catalytic presentation towards H_2O_2 decline. Ultimately, the catalytic attributes of Cu^+ to H_2O_2 were much effective than Cu^{2+} at a lower working potential. The cathodic current increased significantly from −0.2 to −0.6 V in the presence of 2 mM of H_2O_2. Therefore, it has been considered as optimized working potential. The linear range and sensitivity were found to be 0.05 to 1.15 mM ($R^2 = 0.997$) and 330.5 μA. $mM^{-1}cm^{-2}$, respectively. Moreover, the real-time sample analysis in human urine (PBS diluted) showed 99.6% to 102.9% recoveries that confirmed the applicability of biosensors in clinical samples. Hence, biosensors based on Cu_2O/Csu@C core–shell NWs can be used to accomplish highly sensitive UA biosensing and could be a favorable method for sensing UA [42]. The literature survey reveals that the UA and other molecules like ascorbic acid, dopamine, and acetaminophen show redox behaviors at analogous potentials, making it challenging for assessment due to interfering overlapping effects. Ngo and the team designed a graphitic carbon nitride (g-C_3N_4) based ZIF-67/g-C_3N_4 composite using ZIF-67 through an ultrasound/microwave-assisted synthesis. ZIF-67/g-C_3N_4 composite suspension coated GCE (ZIF-67/g-C_3N_4/GCE) was developed for the detection of UA and acetaminophen using cetyltrimethylammonium bromide as a masking/discriminating agent (Fig. 11). ZIF-67/g- C_3N_4 composite increased the electron transfer due to the oxidation of UA and acetaminophen. ZIF-67/g-C_3N_4 demonstrated the stacking interaction among ZIF-67/g-C_3N_4 containing

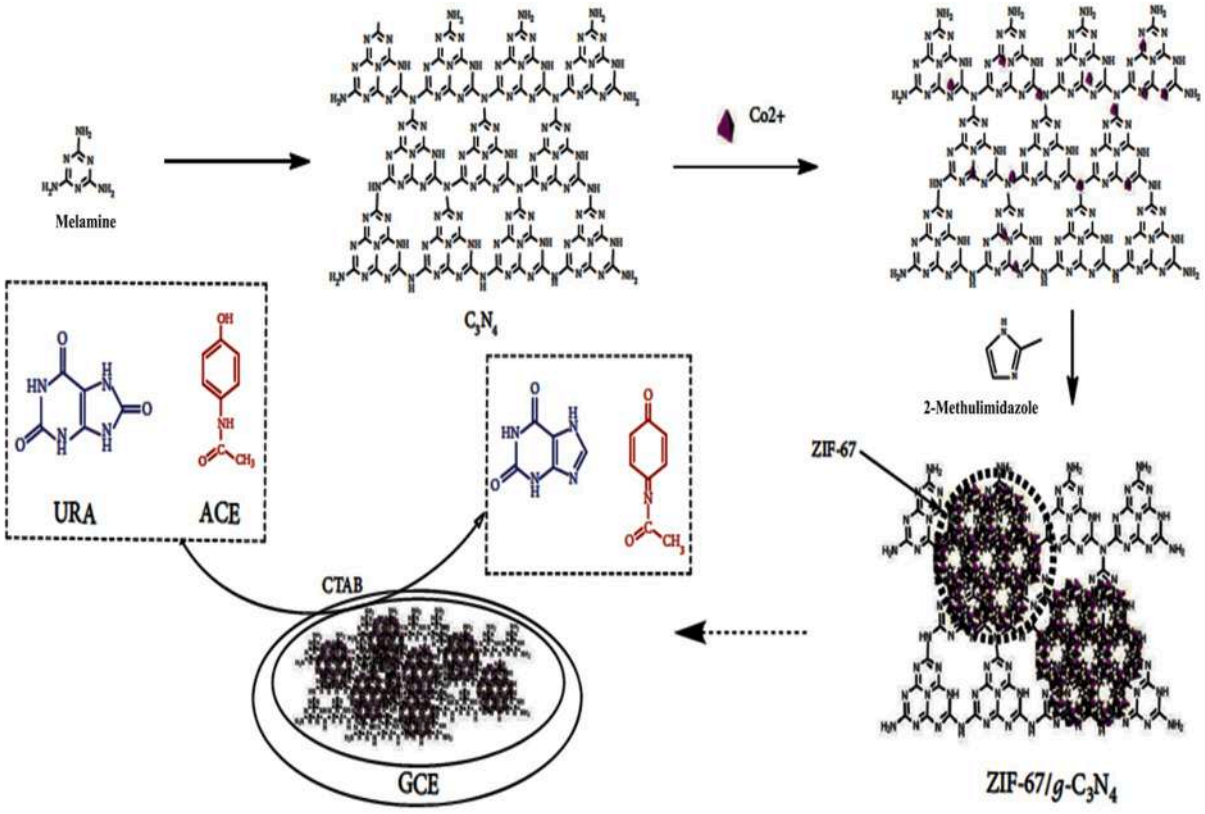

Fig. 11. Oxidation mechanism of UA (or URA) and acetaminophen (ACE) by ZIF-67/g-C_3N_4/GCE. [Reprinted with permission from ref [83] Copyright 2020, Huynh Truong Ngo et al.]

3D imidazole structure and UA/acetaminophen-containing phenyl structures resulted in the adsorption of analyte on ZIF-67/g-C_3N_4/GCE surface. Moreover, the utilization of g-C_3N_4 offered electron mobility during the redox reaction. The simultaneous detection of UA using GCE provided a linear concentration range and LOD of 0.05–0.065 μM (R^2 = 0.995) and 0.052 μM, respectively. The DPV method for analysis of human urine samples showed 90–110% recovery. In conclusion, ZIF-67/g-C_3N_4/GCE biosensor could be used as a potential tool for the detection of UA in real samples in the presence of similar substances [83].

Yet another work reported the voltammetric simultaneous detection of UA, ascorbic acid, dopamine using an electrochemical biosensor. Mesoporous silica (S'BA-15) based Ag-doped titanium dioxide (TiO_2) and stannic dioxide (SnO_2) nanocomposite [Ag-(TiO_2/SnO_2] or h-ATS) on the surface of g-C_3N_4 were prepared. Later Ag-(TiO_2/SnO_2)@g-C_3N_4 was decorated with carbonized (NC@GC) hierarchical core–shell MOF (ZIF-8@ZIF-67). The analysis of UA and other similar substances was carried out using a modified indium-tin-oxide (ITO) electrode (ITO/g-C3N4/NC@GC/h-ATS), which provided a larger surface area, high porous assembly, and synergistic effects. It demonstrated a good electrocatalytic presentation towards UA, ascorbic acid, and dopamine. It provides the linear concentration detection range (2.5–625 M) and the low detection limit (0.06 M). It shows the oxidation peak at 390 mV for UA during simultaneous detection of UA, ascorbic acid, and dopamine. Moreover, the real-time analysis of spiked serum samples showed > 98% recovery that confirmed the applicability of ITO/g-C_3N_4/NC@GC/h-ATS in clinical analysis. In total, the hierarchically modified electrode g-C_3N_4/NC@GC/h-ATS is a replacement prospect for electrochemical sensing UA and other substances in real-time [84]. Setoudeh and colleagues carried out a similar line of work wherein ZIF-8 based Co-tannic acid (TA) nanocomposite (ZIF-8@Co-TA) were synthesized for simultaneous assessment of acetaminophen, dopamine, tryptophan, and UA. In brief, the ZIF-8@K-TA was designed using ZIF-8, TA in potassium hydroxide. ZIF-8@K-TA was later mixed with cobaltous nitrate hexahydrate to form ZIF-8@Co-TA (Fig. 12). The ZIF-8@Co-TA modified electrode offered an improved catalytic activity, high-level conductivity, precise selectivity, which lead to sensitivity enhancement. The LOD of acetaminophen, dopamine, tryptophan, and UA were found to be 5.1 nM, 3.4 nM, 6.7 nM, and 1.2 nM, respectively. For all analytes, the concentration range was found to be 0.02–0.44 μM. This method showed good stability at the different conditions and acceptable repeatability for acetaminophen, dopamine, tryptophan, and UA. The real-time analysis in spiked human serum samples showed 97.3% to 103.1% recoveries that confirmed the suitability of the ZIF-8@Co-TA biosensor in clinical applications. In a nutshell, the ZIF-8@Co-TA based electrochemical sensor can be employed as an appropriate alternative in clinical investigations [85].

The LOD of UA and dopamine should be reduced even at a trace level by coordinated monitoring to ensure diagnostic precision, early avoidance, and proper cure. The new and promising scientific fields were developing composite biosensors with high signal resolution and sensitivity to simultaneous detection of dopamine and UA in clinical samples. Qu et al., designed C-Fe-O bonded MIL-88B(Fe)/carbon composite for simultaneous detection of UA and dopamine with improved sensitivity and resolution. The biosensor performance relied on the adsorption enhancement and distinguished potential regulation strategy. In brief, the Jasmine petal (JP) resultant biocarbon (JPBC) was used as electrode support and 'Fe' loaded JPBC (Fe-JPBC) was synthesized using C-Fe-O bonding that aids in the rise of its interfacial contact with MIL-88B(Fe). The C-Fe-O bond offers a strong interface between the MOF and Fe-JPBC that provided an elevated signal transmission capacity. This resulted in a novel MIL(Fe)/Fe-JPBC composite biosensor for UA and dopamine detection. Due to adsorption enhancement, the MIL-88B(Fe) demonstrated an improved analyte capture aptitude that boosted the signal and provided high sensitivity and LOD. Notably, the LOD (S/N = 3) of UA and dopamine was found to be 10.2 nM and 60.7 nM, respectively. The simultaneous estimation of UA and dopamine using MIL(Fe)/Fe-JPBC provided a low LOD of 5.6 nM and 42 nM for UA and dopamine, respectively. The linear concentration range of UA and dopamine was reported to be 0.05–3.0 μM and 0.1–2.5 μM, respectively, which confirmed that the developed sensor could identify the UA and dopamine concurrently without any mutual interference. Finally, the surface functionality of MIL-88B(Fe) offered more sensitivity and selectivity towards UA and dopamine in the presence of others analogues. The RSD of this biosensor was found to be 4.7% to 2.0% for dopamine and UA, respectively, which confirmed the reproducibility of the biosensor. Moreover, MIL(Fe)/Fe-JPBC after 15 days showed good stability as confirmed by the current responses of dopamine (95.1%) and UA (96.8%) in PBS as compared to its initial responses reading (Fig. 13). The real-time analysis of dopamine and UA in human serum samples provided 97.3% to 106.7% recovery that assured the application of MIL (Fe)/Fe-JPBC as a biosensor for detection of UA and dopamine in clinical samples [86].

In a different study, biosensing of UA and dopamine using 'N' and 'Co' doped carbon particles (NCCNPs) has been reported. Initially, NCCNPs was synthesized by carbonizing of ZIF-67 at 800 °C followed by casting on GCE (NCCNPs-GCE) for electrochemical detection of UA and dopamine. As a result, NCCNPs-GCE exhibited 0.98 μM detection limit and linearity in the concentration range of 5–192.3 μM (R^2 = 0.990) for UA. In addition, NCCNPs-GCE showed a sensitivity of 610.7 μA/mM. Interestingly, the obtained carbon materials at 800 °C contained a small amount of N-doping and high electron acceptability that played a significant role in the electrocatalytic reaction. Moreover, a large amount of Co-based biosensor offered maximum active sites for electrochemical reactions. It demonstrated excellent electrochemical performance during sensing of UA and dopamine. The highly selective amperometric responses of NCCNPs-GCE for UA (0.2 mM) and dopamine (0.2 mM) in the presence of other interfering agents such as ascorbic acid, glucose, and ethanol indicated a high selectivity towards UA and dopamine in PBS (pH 7). In the near future, fabricated NCCNPs provide new opportunities for simultaneous detection of UA and DA by electrochemical sensing [87]. In 2020, Ko and coauthors reported the 2D conductive MOFs in the form of a drop casted film on GCE for UA voltammetric detection (redox-active analyte). A conductive film of Cu_3HHTP_2 was synthesized using 'Cu' as a metal and 2, 3, 6, 7, 10, 11-

Fig. 12. Possible growth mechanism of ZIF-8@Co-TA nanocomposite. [Reprinted with permission from ref [85]. Copyright 2020, Elsevier.]

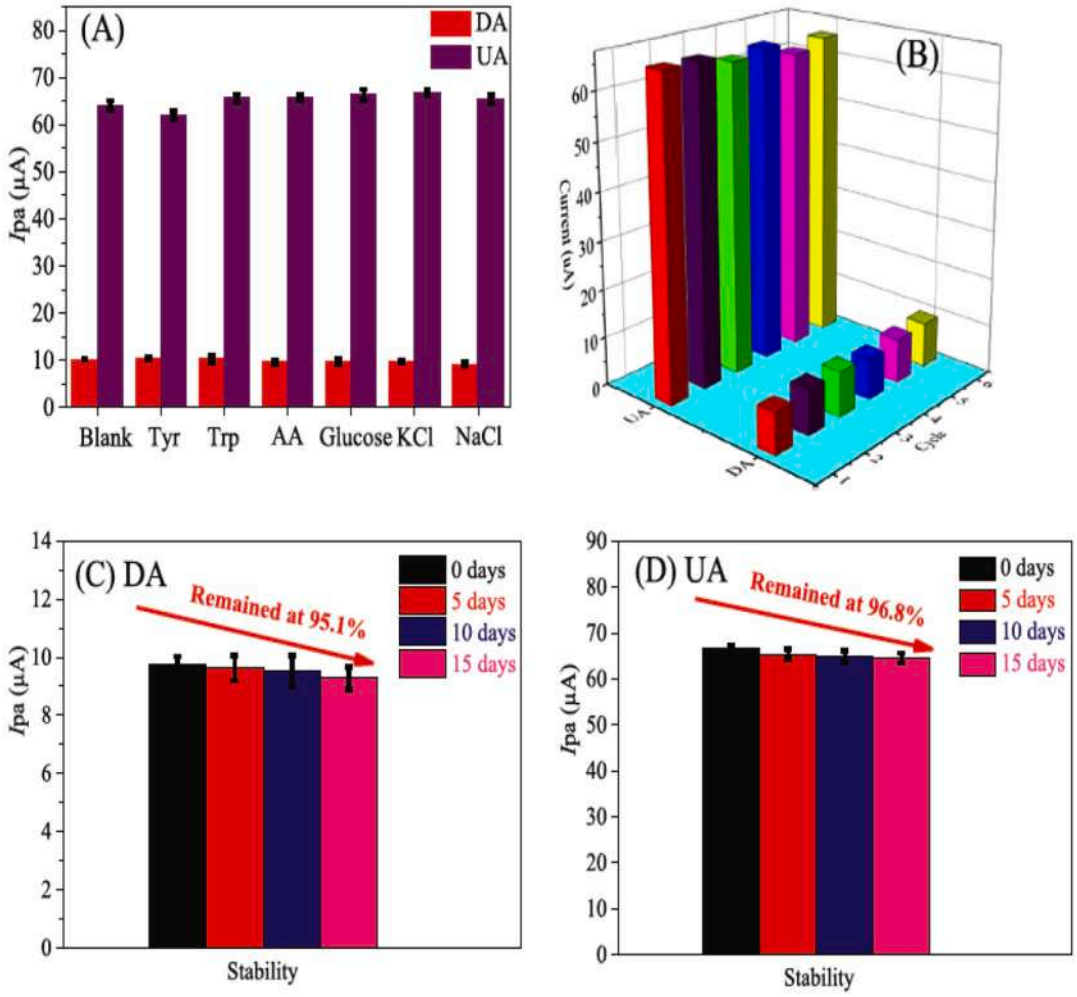

Fig. 13. The simultaneous determination of dopamine (or DA) and UA using MIL(Fe)/Fe-JPBC biosensor demonstrates the (A) Selectivity, Test condition: DA (1.0 μM), UA (1.5 μM) and interferences (20 μM) in 0.2 M of PBS at pH = 5.5. (B) Repeatability, Test condition: DA (1.0 μM) and UA (1.5 μM) in 0.2 M of PBS at pH = 5.5. Stability, Test condition. simultaneous detection of (C) DA (1.0 μM) and (D) UA (1.5 μM) in 0.2 M PBS at pH = 5.5 [Reprinted with permission from ref [86]. Copyright 2020, Elsevier]

hexahydroxytriphenylene (HHTP) as an organic ligand. The synthesized Cu_3HHTP_2 was then loaded onto the surface of GCE (Cu_3HHTP_2-GCE) and used for voltammetric sensing of UA in PBS (pH 7.4). This biosensor was used for the simultaneous detection of different biomolecules such as dopamine, serotonin, ascorbic acid, and UA. The surface active sites such as metallic nodes interact with UA via hydrogen bonding or by electrostatic interactions, and subsequently result in the peak current enhancement. As a result, DPV offers an extremely low LOD and wide linear concentration range of about 198 nM and 0.19–200 nM, respectively. In addition, this method provided less than 0.04 V difference in UA samples (100 μM, n = 3) that confirmed the reproducibility of a biosensor. In voltammetric detection, conducting MOFs are promising to develop a highly sensitive, reproducible, and stable electroanalytical device [88]. It is noteworthy to mention that the larger surface areas, controlled porosity, and countless structural topologies of MOF make them suitable candidates in the electrochemical field. Wand and co-authors developed multi-walled carbon nanotubes (MWCNTs) that incorporated manganese MOF, Mn-BDC (BDC = 1, 4-benzene dicarboxylate), through the single-step solvothermal process for simultaneous detection of UA, dopamine and ascorbic acid. MWCNTs@Mn-BDC was prepared by the addition of MWCNTs into the dispersion of p-benzene dicarboxylic acid (linker) and manganese (II) nitrate hexahydrate in N, N-dimethylformamide. Finally, the MWCNTs@Mn-BDC was dropped on the surface of GCE (MWCNTs@Mn-BDC@GCE). Notably, the MWCNTs incorporation into Mn-BDC provided a thin layer of MOF, which enhanced electrical conductivity, and improved electrocatalytic ability. As a result, MWCNTs@Mn-BDC@GCE showed a wider linear range and lower LOD about 0.02–1100 μM and 0.005 μM, respectively. Additionally, simultaneous detection of UA and other molecules confirmed that the MWCNTs@Mn-BDC@GCE exhibited higher selectivity for UA, dopamine, and ascorbic acid in the presence of citric acid, L-cysteine, glucose, and glutamic acid. Moreover, DPV measurements showed 2.1% of RSD that confirmed the reproducibility of the MWCNTs@Mn-BDC@GCE sensor (n = 6). The real-time analysis in urine showed a good recovery of the UA that assured real-time applicability for the determination of UA, ascorbic acid, and dopamine in the clinical samples. In conclusion, MWCNTs@Mn-BDC@GCE offered good sensitivity, high selectivity, excellent repeatability, and effective detection of UA in human urine. Therefore, this proposed sensor can furnish a promising approach for the recognition of UA in biological samples [89]. Table 2 summarized the various types of MOF-based electrochemical biosensors for highly sensitive and selective real-time detection of UA in clinical samples.

3.3. Colorimetric biosensor

Recently, nanomaterial-based colorimetric chemosensors have received huge attraction from researchers. This method has several

Table 2
Summary of surface architectured MOF based electrochemical biosensor for ultrasensitive detection of UA.

Sr. No.	MOF-basedcomposite	Precursor(Initial material)	Linear range	LOD	Clinical sample	Silent features	Ref.
	CeO_2-x/C/rGO	Cerium nitrate	49.8 μM to 1050 μM	2.0 μM	—	CeO_2-x/C/rGO nanocomposites interact with H_2O_2 (*uricase* catalyzed intermediates) and resulted in the peroxidase-like catalytic performance for oxidation of H_2O_2 (*uricase* catalyzed intermediates).	[67]
	CeO_{2-x}/C NRs	Ce-MOF	50 μM to 1000 μM	3.2 μM	Urine	It exhibited superior selectivity towards the UA in presence of other interferences in human urine samples.	[76]
	Co_3O_4/Fe_3O_4/ mC@g-C_3N_4	Co/Fe-MOFs	5.0 μM to 100 μM	0.18 μM	Urine	It shows high sensitivity, good selectivity, acceptable reproducibility, and excellent stability.	[77]
	CNCo/GCE	ZIF-8: ZIF-67	2.0 μM to 110 μM	0.83 μM	Serum	A simplistic electrochemical biosensor based on CNCo modified GCE developed via BMZIFs depends on ZIF-8 and ZIF-67, which induced catalytic activity towards UA detection.	[68]
	GOx or BSA -CHIT/ Co_3O_4/Au	ZIF-67	—	100 nM	Tears	The direct electro-oxidation of UA on the designed gate provides the highly sensitive detection of UA.	[78]
	Z-1000@GCE	ZIF-8	0.001 mM – 0.3 mM	278 nM	Serum	Due to good sensitivity, high selectivity, excellent reproducibility, and real-time applicability, Z-1000@GCE holds a huge potential for sensing different biomolecules in body fluids.	[79]
	Pt@MIL-101 (Cr)	Chromium (III) chloride hexahydrate	0.5 μM to 162 μM	0.42 μM	Serum	Pt@MIL-101 (Cr)/ MOFs modified GCE non-enzymatic sensor decreased their working potential due to the addition of XA and increased the signal current for oxidation mechanism with detection of UA.	[71]
	ZIF-67-GO/GCE	ZIF-67	0.8 mM to 200 mM	100 nM	Urine	The high porosity and larger specific surface area of ZIF-67 as well as the high electrical conductivity of GO resulted in electron transfer. Finally, it offers synergistic effects in terms of sensitivity and selectivity.	[80]
	Zr-Por-MOF/MPC	Por-MOF	20 μM to 410 μM	160 nM	—	In addition, it can be used for UA detection in presence of other purine derivatives such as xanthine and hypoxanthine	[81]
	MOF-71/GCE	MOF-71	0.05 mM to 1.00 mM	15.61 μM	—	The non-enzymatic UA detection using MOF-71 based electrochemical sensor offers high sensitivity and good selectivity in presence of similar substances.	[82]
	Au/Co@HNCF	Au (III)-etching ZIF-67	0.1 μM to 25 μM	0.023 μM	Serum	In Au/Co@HNCF, the addition of external 'Au' nanoparticles into internal 'Co' nanoparticles resulted in an enhanced oxidation potential of UA.	[44]
	Cu_2O/Cu@C	Copper (II) nitrate hydrate	50 mM to 1100 mM	0.4 μM	Urine	Cu_2O/Cu@C core–shell NWs exhibited as the best strategy for the superb electrocatalytic ability at a little working potential, which is a greater benefit for enhancing anti-interference capability in UA detection.	[42]
	ZIF-67/g-C_3N_4/GCE	ZIF-67	0.02 μM to 0.65 μM	0.052 μM	Urine	It provides the simultaneous estimation of UA in presence of similar molecules in urine samples that may due to the π–π stacking interaction among ZIF-67/g-C3N4 and UA.	[83]
	ITO/g-C3N4/ NC@GC/h-ATS.	ZIF-8@ZIF-67	2.5 μM to 625 μM	0.06 μM	Serum	It provides a larger surface area, high porous assembly, and synergistic effects that resulted in a good electrocatalytic presentation towards the UA and other molecules.	[84]
	ZIF-8@Co-TA	ZIF-8	0.02 μM to 0.44 μM	1.2 nM	Serum	It offers the improved catalytic activity, high-level conductivity, precise selectivity that provides a low detection limit for UA and other similar analogues.	[85]
	MIL(Fe)/Fe-JPBC	MIL-88B(Fe)	0.05 μM to 3.0 μM	5.6 nM	Serum	It provides the simultaneous estimation of UA and dopamine in real-time samples with high sensitivity and selectivity based on the strategy of adsorption enhancement and potential regulation.	[86]
	NCCNPs-GCE	NCCNPs	5 μM to 192.3 μM	0.98 μM	—	The carbonized ZIF-67 provides the NCCNPs based highly sensitive as well as a selective electrochemical biosensor for UA and dopamine detection.	
	Cu_3HHTP_2-GCE	Cu_3HHTP_2	0.19 nM to 200 nM	198 nM	—	Conductive Cu_3HHTP_2 provides the simultaneous estimation of UA along with high sensitivity and excellent reproducibility in presence of other neurochemicals.	[88]
	MWCNTs@Mn-BDC@GCE	Mn-BDC	0.02 μM to 1100 μM	0.005 μM	Human urine	The MWCNTs incorporation into Mn-BDC provides the thin layers of MOF that enhanced electronic conductivity and improved the electrocatalytic ability of the sensor for UA detection.	[89]

advantages, including its simplicity, low cost, and lack of the need for advanced devices. Besides, the researchers have reported that the application of nanozyme and *uricase* (enzyme) combination to overcome the low selectivity issue of the colorimetric biosensor. In 2019, Badoei-dalfard and co-workers developed colorimetric biosensors of Th-MOF through an ultrasound-assisted reverse micelle (UARM) system using thorium tetranitrate-pentahydrate for highly sensitive and selective sensing of UA (Fig. 14). The affinity of a nanomaterial-based artificial enzyme (nanozyme) to the substrate was found to be more sophisticated than *horseradish peroxidase* (HRP, a natural enzyme). Additionally, Th-MOF with TMB-H_2O_2 showed a tense absorbance peak that confirmed the peroxidase-like activity of Th-MOF. The oxidation reaction was found to be finished after 5 min of incubation of Th-MOF at 40°C to 60°C (pH 5.5), which confirmed that the faster rate of TMB oxidation by nanozyme in the presence of H_2O_2. Besides, linearity has been reported between the oxidized TMB and H_2O_2 concentration. The blue-colored oxidized TMB was confirmed through the naked eyes wherein the absorbance value of blue-colored oxidized TMB increased with UA concentration. Notably, the linear range and LOD of UA detection were found to be 4.0–7.0 μM and 1.15 μM, respectively. The final concentration of added UA in serum and urine samples shows 93.10% to 99.04% and 93.25% to 101.62% recoveries (n = 3), respectively. Therefore, unique peroxidase mimicking MOF nanozyme is a brilliant contestant for UA biosensing in real body fluids. In the future, it can be utilized as a prospective for UA detection, especially in the care for gout diagnostics [46].

Luan and co-authors developed the Ce-MOF using terephthalic acid as a linker. In brief, Ce-MOF was used as a chromogenic reagent that

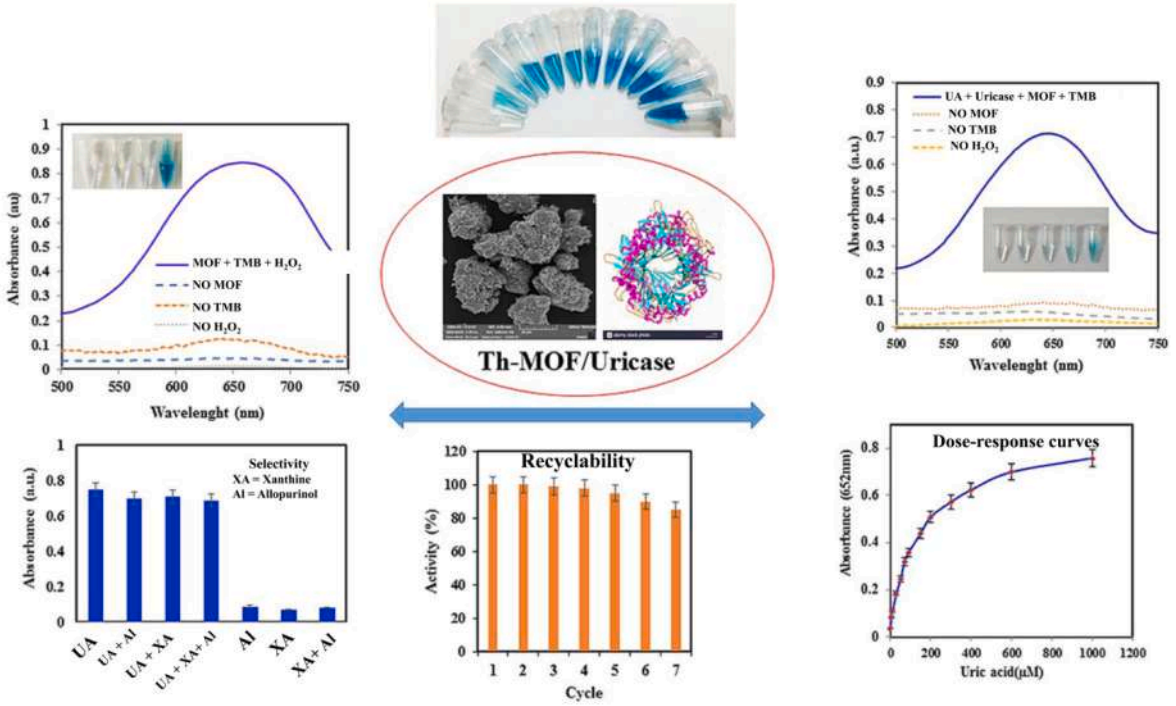

Fig. 14. Presentation of uricase-based Th-MOF colorimetric biosensor for highly sensitive and selective detection of UA. [Reprinted with permission from ref [46]. Copyright 2019, Elsevier]

offers simultaneous colorimetric and fluorescent responses. During the assay, the synthesized Ce-MOF was used for the fabrication of origami paper-based SlipChip that offers the simultaneous detection of UA and glucose level in provided serum samples. Interestingly, it showed a dual-sensing response wherein "turn on" indicated the colorimetric response and "turn off" indicated the fluorescence response. The assay demonstrated a linear concentration range from 0 to 1000 mM for UA and the LOD was found to be 39.6 μM. The clinical blood sample analysis in hyperuricemia patients confirmed relatively high accuracy. In conclusion, this Ce-MOF-based colorimetric sensor provided an excellent color stability, high selectivity, elevated sensitivity, and serum protein filtration. In the future, this Ce-MOF sensor can be used widely in clinical applications as compared to the traditionally used colorimetric method [90]. In 2021, Gao and co-investigators designed UiO-66-NH_2 using Zr(IV) as metal ions and 2-amino terephthalic acid as a ligand. Later UiO-66-NH_2 was modified using ferrocene carboxylic acid (Fc-COOH) to result in UiO-66-Fc. UA has been combined with urate oxidase that converts UA into H_2O_2. This produced H_2O_2 participated in the oxidation of substrate namely, 2, 2′-azino-bis (3-ethylbenzothiazoline-6-sulfonic acid) under the UiO-66-Fc catalysis. Finally, it resulted in chromogenic products that are directly proportional to the concentration of UA and H_2O_2. This assay showed linearity in the concentration range from 50 – 600 μM with a detection limit (LOD) of 1.18 μM. Overall, UiO-66-Fc showed the enzyme-like function and improved the catalytic performance that offers high sensitivity for UA and their metabolites. In the future, UiO-66-Fc based colorimetric sensor can open a new door for sensing disease-related biomarkers such as UA and H_2O_2 [91]. Lu *et al.* developed MIL-53 (Fe) based colorimetric sensor for the detection of UA in a real-time scale assay. Initially, MIL-53 (Fe) was synthesized using 1,4-benzene dicarboxylic acid (precursor) and iron (III) chloride hexahydrate by a simple solvothermal method. MIL-53 (Fe) contains intrinsic peroxidase-like activity that will help in the detection of UA. MIL-53 (Fe) catalyzes the oxidation of TMB (peroxidase substrate) in the presence of H_2O_2, resulting in a blue-colored product. The LOD of assay method was 1.3 μM with a linearity between the range of 4.5–60 μM ($R^2 = 0.995$). The real-time applicability of the sensor was confirmed by using UA spiked in human urine and serum samples, which resulted in 89.50% – 101.44% recoveries. Moreover, it showed high selectivity in the presence of different interfering agents such as glutathione, tryptophan, ascorbic acid, glucose, and sodium chloride. This method provided high sensitivity and selectivity, and good recovery of UA. Therefore, it can be used as an alternative for the regularly used colorimetric method for the detection of UA in real-time samples [26]. Recently, the *uricase*-free approach for the biosensing of UA in serum and urine has been reported. In 2020, Wang *et al.* have come up with UA colorimetric biosensor based on polypyrrole (PPy)-coated polyoxometalate-encapsulated 4-fold helical MOF namely Ag_5PMo_{12}@PPy as a monolithic *peroxidase* mimic (Fig. 15 A). The incorporation of polyoxometalates (POM) with MOF resulted in POMOFs with good biocompatibility, excellent performance, and high structural stability. In this study, POMOFs were assembled using Ag ions, ligands [3,5-bis((1H-imidazole-1-yl)methyl)-1H-1,2,4-triazole], and Keggin types of POMs. Ag_5PMo_{12}@PPy composite was constructed by loading PPy on the surface of Ag_5PMo_{12} via oxidative polymerization. PPy loading on the surface of Ag_5PMo_{12} boosted the peroxidase activity that may due to the synergistic effect. Fig. 15 B demonstrated that the electrons were initially excited with Ag_5PMo_{12} composite and were later transferred to PPy to prevent the recombination of electron-hole pairs. After that, the H_2O_2 has been adsorbed on the surface of Ag_5PMo_{12}@PPy. The addition of TMB adsorbed on the surface of Ag_5PMo_{12}@PPy and reacted with desorbed •OH through the process of electron transfer. During this, the TMB (colorless) was converted into the oxTMB (green). Finally, the addition of UA into this system resulted in no green color, which may due to the inhibition of catalytic oxidation of TMB. As the target UA concentration increased, the absorption peak decreased and the dark green color faded into light green and ultimately colorless, which can be visualized easily through bare eyes. Thus, the absorbance change of oxTMB is used in sensing UA levels. The sensitivity range and LOD of UA were found to be 1–50 μM ($R^2 = 0.9972$) and 0.47 μM, respectively. The RSD value of this biosensor was found to be 1.49% that confirmed the repeatability of this sensor in UA detection. The real-time analysis of UA in human serum and urine samples showed the 95%

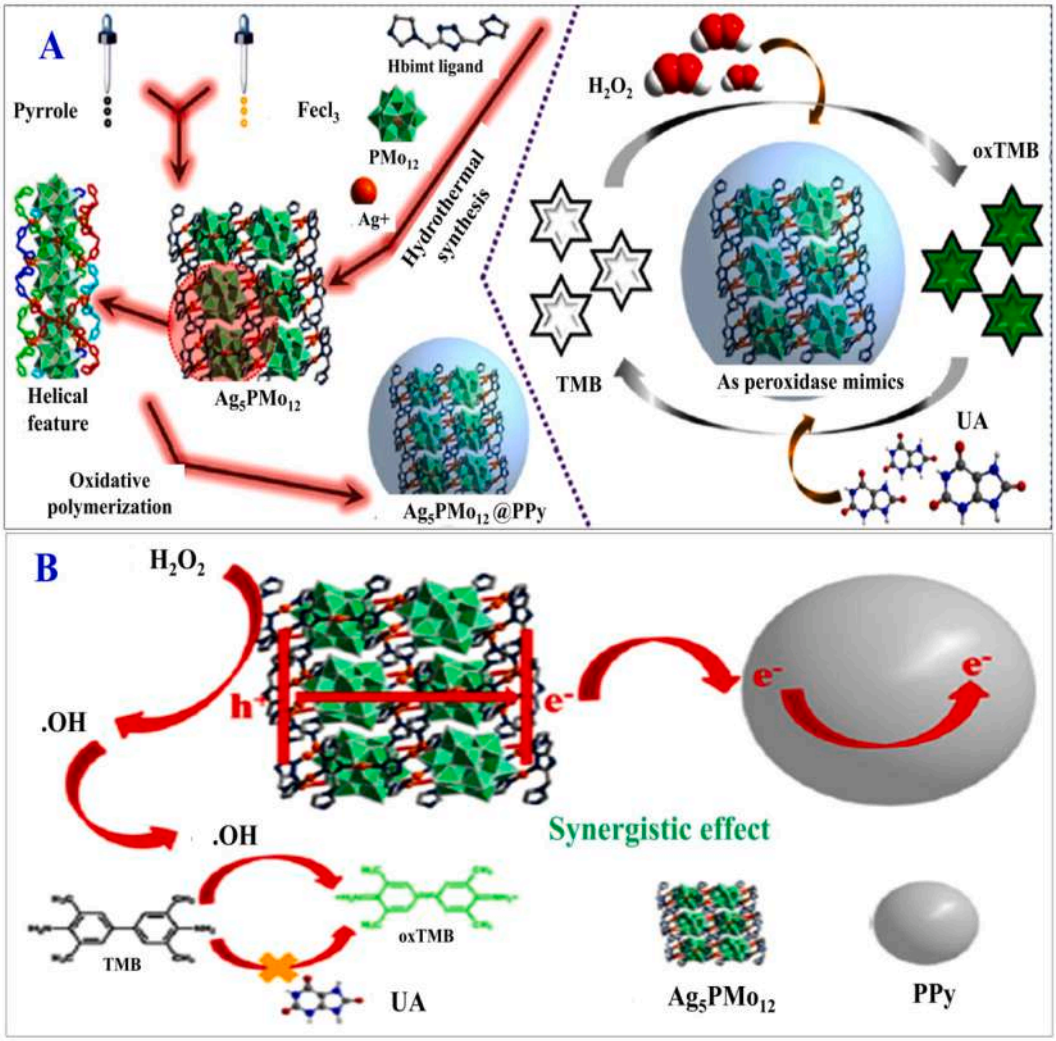

Fig. 15. Synthesis of Ag_5PMo_{12}@PPy and the corresponding colorimetric UA biosensor by utilizing Ag_5PMo_{12}@PPy as peroxidase mimics (A). Ag_5PMo_{12}@PPy toward UA colorimetric biosensing based on peroxidase-like activity (B). [Reprinted with permission from ref [92]. Copyright 2020, American Chemical Society.]

to 106.1% recovery, which authenticates the practicability in addition to the repeatability of Ag_5PMo_{12}@PPy based colorimetric sensor. Therefore, the Ag_5PMo_{12}@PPy biosensor is reliable for sensing UA in the meadow of bioanalysis along with clinical diagnosis [92].

The literature survey reported that MOFs could be used as an excellent substrate for enzyme immobilization. Possibly, it may because of their high surface area, tunable porosity, and excellent stability. In this context, Liu and investigators synthesized a stable hierarchically porous MOFs, namely HP-MOFs or HP-DUT-5 (Dresden University of Technology). In brief, DUT-5 was synthesized using 4,4′-Biphenyldicarboxylic acid (BPDC) and aluminum nitrate nonahydrate and then modified into HP-DUT-5 using Al^{3+}/BPDC/dodecanoic acid followed by immobilization of uricase: HRP with a ratio of 4:1 on the surface of HP-DUT-5 (Uricase@HRP@HP-DUT-5) for detection of UA. The cascade enzyme activity of Uricase@HRP@HP-DUT-5 biosensor was measured by UA oxidation and the chromogenic substrates, namely 4-aminophenazone and 2, 4-dichlorophenol sulfonate in Tris buffer (pH 7.5). After the addition of low to high concentrations of UA, the color changed from very light pink to deep pink within 30 min of incubation at ambient temperature. Concisely, the concentration of UA showed a proportional relationship with the absorbance of samples. The linear concentration range and LOD of UA were found to be 5–100 μM and 0.8 μM, respectively. In addition, the method resulted in 87% residual activity after 5 times that confirmed their reusability in UA detection. Uricase@HRP@HP-DUT-5 biosensor showed the high selectivity towards the UA in the presence of urea, sodium chloride, glucose, ascorbic acid, etc. Overall, the uricase@HRP@HP-DUT-5 colorimetric biosensor offers simplicity, high sensitivity, good recyclability, and high selectivity. Hence, this colorimetric sensor opens a new era for the detection of UA and other biomolecules such as glucose in clinical samples [93]. Yet, another similar line of work reported the detection of UA using mimic multi-enzyme systems in HP biomimetic MOFs colorimetric biosensor (Fig. 16). Briefly, porphyrinic MOFs composite [PCN-244(Fe)] was synthesized using zirconium chloride and Fe-TCPP [TCPP = tetrakis (4-carboxyphenyl)porphyrin]. Later, the HP-based PCN-244(Fe) namely HP-PCN-224(Fe) was synthesized using zirconium chloride and Fe-TCPP followed by the activation using hydrochloric acid and N, N'-dimethylformamide. Finally, uricase immobilized on the surface of HP-PCN-224(Fe) and obtained uricase-HP-PCN-224(Fe) biosensor used for the measurement of UA in the presence of 2, 4-dichlorophenol sulfonate and 4-aminophenazone. Interestingly, UA reacts with oxygen under the uricase catalysis that produces H_2O_2 and allantoin. Then, H_2O_2 oxidized the 2, 4-dichlorophenol sulfonate and 4-aminophenazone and resulted in a colored product. The absorbance of the obtained solution was demonstrated direct proportionality to the concentration of UA in samples. The linear concentration range and LOD for UA were found to be 5–1000 μM and 1.8 μM, respectively. In addition, it showed a high selectivity towards the UA in the presence of glutamic acid, urea,

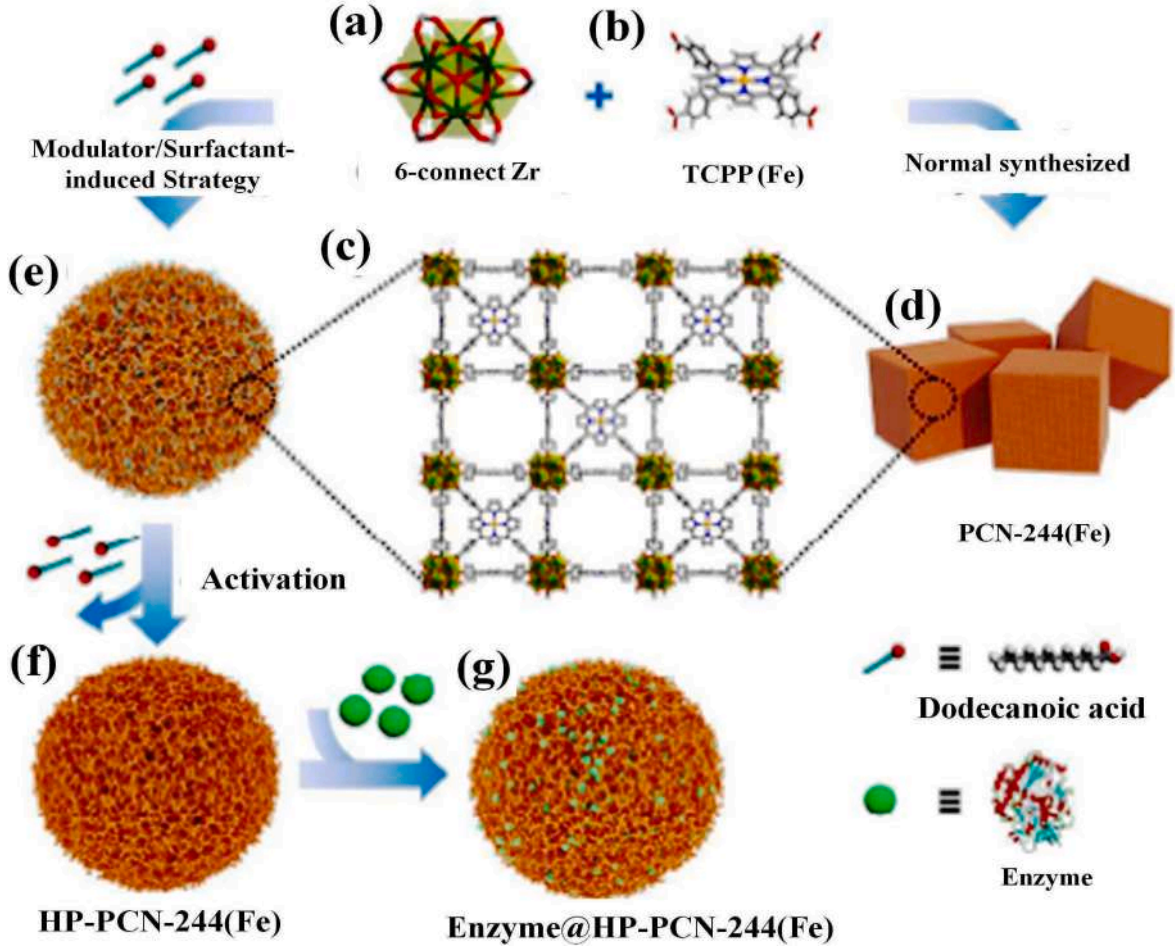

Fig. 16. Enzyme@HP-PCN-224 (Fe) biosensor for UA sensing. Scheme of the 6-connected D3d symmetric Zr6 (a) and tetratopic TCPP ligand in PCN-224(Fe) (b). Design of PCN-224(Fe) crystal structure (c). Representation of the normal synthesized PCN-224(Fe) (d). The synthesis of HP-PCN-224(Fe) with a modulator/surfactant-induced strategy (e). The representation of HP PCN-224(Fe) activation (f), and mimic multi-enzyme systems (g). [Reprinted with permission from ref [94]. Copyright 2018, American Chemical Society).

ascorbic acid, glucose, urea, and maltose, and confirmed the feasibility of synthesized colorimetric biosensor. In conclusion, this sensor offers a great potential for biosensing and biomedical applications [94].

The growth of point-of-care (POC) technology has been boosted by portable devices with quick analysis and reasonably priced methodologies for clinical diagnostics and could potentially reduce mortality scores. In 2020, Kau and coauthors reported the smartphone mediated biomimetic ZIF-8 based nanoreactor colorimetric paper namely SBMCP for detection of different biomolecules including UA. Initially, biomimetic enzyme (*Urease*- HRP)-MOFs (i.e. *Urease*- HRP-BEMs or UH-BEMs) nanoreactor was synthesized based on urease, HRP, and ZIF-8. Later, UH-BEMs were developed by the coating of previously developed BEMs on the surface of raw paper. Finally, a smartphone-based software was developed that contains the recording ability of Hue-Saturation-Value (HSV). Biosensing experiments have been conducted for detection of UA wherein UA sample drop cast on the surface of SBMCP biosensor followed by TMB addition that produces the visual color. Then, this obtained red color was captured by using a Smartphone camera followed by analysis using designed software. Interestingly, it showed the linear response within the concentration range of 0.4–1 mM ($R^2 = 0.988$). Moreover, the LOD was found to be 0.5 mM that can help to diagnose the UA-related health issues by using human plasma. Interestingly, the addition of an extremely low concentration of UA (about 0.5 mM) resulted in color changes, which can be detected by the naked eye. The spiked recovery of UA using paper biosensor was found to be 103.1% to 106.3% that confirmed the feasibility of sensing. In addition, it showed excellent selectivity in presence of different interference such as amino acids, glucose, proteins. In conclusion, this paper-based biosensor will open a new avenue in the non-invasive detection of UA and other biomolecules along with plenty of advantages in terms of high sensitivity, selectivity, and simplicity [95]. In a nutshell, MOF-based colorimetric biosensor offers plenty of meticulous benefits in terms of sensitivity, selectivity, simplicity, feasibility, recyclability, etc. that can open a new horizon for biosensing of UA in clinical samples. Table 3 summarized the various types of MOF, a precursor used, the LOD, and the linearity range of UA using surface architectured MOF-based colorimetric biosensors.

4. Summary

Abnormal levels of UA will adversely raise the risk of gout and other related health issues. UA can serve as a biomarker by detecting its concentration in the urine and serum to make that judgment of such diseases. Several identification methods for UA such as enzyme-based method, chromatographic method have been reported. Unfortunately, the complex measuring techniques and expensive instruments restrict their practical applications. A sensitive and convenient procedure for detecting UA is urgently requested for diagnosis and care. Luminescent, electrochemical, and colorimetric sensors have in recent years brought much focus to the benefits of installation, low costs, and repetitiveness. Interestingly, MOF-centric UA biosensing has received considerable attention due to its incredible advantages and its ability to provide a

Table 3
Summary of surface architectured MOF based colorimetric biosensor for ultrasensitive detection of UA.

Sr. No.	MOF-basedcomposite	Precursor(Initial material)	Linear range	LOD	Clinical sample	Silent features	Ref.
1.	Th-MOF	Thorium tetranitratepenta-hydrate	4.0 μM −70 μM	1.15 μM	Serum and urine	Th-MOF showed a peroxidase-like mechanism for oxidizing TMB in presence of H_2O_2 (*uricase* catalyzed intermediates).	[46]
2.	Uricase@HRP@HP-DUT-5	DUT-5	5 μM – 100 μM	0.8 μM	—	Uricase@HRP@HP-DUT-5 colorimetric biosensor offers high sensitivity, good recyclability, and towering selectivity.	[93]
3.	Ce-MOf	Ceric ammonium nitrate	0 mM – 1000 mM	39.6 μM	Fetal bovine serum	It provides a good performance as compared to theHRP-based detection. In addition, it showed excellent color stability, real-time applicability, and high sensitivity.	[90]
4.	UiO-66-Fc	Zr-MOF	50 μM – 600 μM	1.18 μM	—	UiO-66-Fc showed enhanced catalytic activity, Low LOD, wider linear range, and favorable reusability. It is a simple colorimetric method that can be used for the quantitative detection of UA.	[91]
5.	MIL-53(Fe)	Iron(III) chloride hexahydrate	4.5 μM – 60 μM	1.3 μM	Human urine and serum	MIL-53(Fe) based colorimetric sensor shows the peroxidase-like activity and catalyzes the TMB oxidization by H_2O_2 along with high efficiency.	[26]
6.	Ag_5PMo_{12}@PPy	$AgNO_3$	1 μM −50 μM	0.47 μM	Serum and urine	Ag_5PMo_{12}@PPy based colorimetric biosensor exhibited catalytic oxidation of colorless TMB to emit colored TMB in the presence of H_2O_2.	[92]
7.	Uricase-HP-PCN-224 (Fe)	PCN-224(Fe)	5 μM −1000 μM	1.8 μM	—	It provides the lower LOD up to μM concentration. It gives the high selectivity for UA in presence of different interfering agents.	[94]
8.	UH-BEMs	ZIF-8	0.5 mM – 1 mM	0.5 mM	Plasma	It provides the ability to detect the UA levels by the naked eye. Moreover, it offers high sensitivity and selectivity towards the UA.	[95]

speedy platform to expand molecular interaction. A nanoarchitectured MOF biosensing assay enables a lower detection limit from μM to nM for early detection of gout and hyperuricemia. Due to its tunable properties and the extremely attractive interaction between UA and chosen MOF, higher specificity and extraordinary sensitivity can be achieved. Comparative measurement of biomarkers using MOF-based biosensors such as colorimetric biosensors, fluorescent biosensors, and electrochemical biosensors can be a suitable substitute for UA biosensing. The hydrogen bonding between UA and the MOF nanosized framework containing fixed ligand is accountable for the modification of the pyrene-functional ligand molecule conformation and fluorescence emission properties. The dual transition in conformation (excimer to monomer) helps to use the MOF material for UA biosensing. The practical test papers provided by ZJU-158-Tb offer rapid monitoring for irregular UA levels of artificial urine and serum with a distinct shift in color that can even be characterized by the naked eye. Remarkably, UA can efficiently quench the fluorescence of novel UiO-PSM MOF via hydrogen bonding, coordination, and $\pi - \pi$ interactions. In this case, biosensor could detect UA within one minute, along with a limit of nM detection and a large linear UA detection range. Excellent recovery and precision in UA sensing suggested that this colorimetric biosensing system based on proven Th-MOF is suitable for disclosing UA in actual experimental samples. MOF nanozyme with peroxidase mimicking ability is a wonderful candidate for UA biological sensing in real specimens, especially in care diagnosis. The manufactured CNCo/GCE electrode offers a greater electrocatalytic activity for oxidizing the UA and a greater peak current as compared to the bare GCE electrode. It may due to the high pore volume, high surface, and highly distributed CNCo active sites. In Au/Co@HNCF, the number of catalytic sites, high activeness, organized structure, special nanoporous carbon provides the lowest detection limit for UA, which could be useful in detecting diseases. Polypyrrole-coated polyoxometalate-encapsulated 4-fold helical MOF uricase-free method for selective and sensitive colorimetric sensing of UA offers a detection limit up to μM. The substance lowers H_2O_2 at a lower operational potential due to the presence of Cu^+ and Cu in providing composite particles, which lead to an improvement of the biosensor's selectivity. Besides, the carbon and copper present in the core nanostructure of the MOF biosensor lead to an increase in the electron transfer and eventually increased biosensor sensitivity. A recently published research study suggested that the adsorption enhancement and distinguished potential regulation approach in MOF biosensor showed the simultaneous detection of UA in real-time samples with elevated sensitivity up to nM and good anti-interference potential in the presence of different analogues. Fascinatingly, the π–π stacking interaction between ZIF-67/g-C3N4 containing 3D imidazole structure and UA/acetaminophen-containing phenyl structures resulted in the adsorption of analyte on ZIF-67/g-C_3N_4/GCE surface. Overall, comparative measurements of gout biomarkers (especially UA) using experiments indicate that biosensors based on MOF are more sensitive, selective, and rapid.

5. Future prospects and challenges

Gout is a chronic disease with a gradual onset and steady growth, leading to increased levels of UA. Since the prevalence of gout in the next few decades is projected to rise exponentially, analysis technologies to sensibly, accurately, and economically diagnose gout biomarkers should be created. Furthermore, an early review of gout biomarkers levels leads to wise choices and the best treatment options resulting in an increase in the overall therapeutic efficacy. Specifically, monitoring of UA levels in different body fluids has drawn momentous interest over the last few years that may due to its clinical importance. Several approaches such as electrochemical sensors, liquid chromatography and capillary electrophoresis have majorly contributed to supervising the UA level. Despite the merits of these reported methods, they have major lacunas such as low sensitivity, time-consuming, and much expensive. As a result, the POC diagnostic policy for UA is still demanding to research scholars. In the last decade, the applications of advanced nanomaterial such as 2D carbon nanomaterial (graphene quantum dots, graphene oxide), metal nanoparticles (AgNPs, AuNPs), and metal oxides for the fabrication of different types of biosensors have gained much interest. In addition to the nanomaterials, well-defined hollow MOF synthesized using organic linker and a metal ion is also used for detection of biomolecules, gas sensing, and catalysis. It may because of their diverse chemical properties and tunable network structure. Taken as a whole, the high surface area, tunable porosity, elastic complex, and easy functionalization of MOF make them suitable in gout biosensing applications. Furthermore, the combination of MOF with other materials such as metal nanoparticles, carbon materials, polymer, could synergistically improve sensitivity in UA detection. Various studies have described the sensitivity of MOF-based biosensors for UA detection with a lower LOD up to nM. Despite these notable developments in the biosensing of UA using MOF, there is still a need to improve the overall performance of MOF biosensors in terms of sensitivity and selectivity. This could help

diagnose and manage gout at an early stage. Although momentous progress has been made in the sensing of disease biomarkers, there are some limitations for MOF performance. In the future, for further improvement of stability, and biocompatibility of MOF-based biosensors, there is a huge need to perform critical trials and assessments. On this account, the toxicity of metal salts, ligands, and MOF should be considered separately. This will help in the development of biocompatible MOF. In addition, non-toxic metals such as Zn^{2+}, Mn^{2+}, Fe^{2+}, Cu^{2+}, Ca^{2+}, Mg^{2+}, Au^{3+}, Ag^{+} can be used to reduce toxicity and enhance biocompatibility towards the biomarker. MOF toxicity is related to morphology, crystallinity, and composition. MOF-based biosensors for UA are also known to have stability issues. Further research work is a prerequisite to address these limitations for refining the overall performance of MOF-based biosensors. In the future, it may be one of the main trends for MOF-based biosensors to achieve functional MOFs with high stability, low toxicity, and high biocompatibility. The reported MOF-based biosensors offer sensitivity up to μM to nM range. In the future, the modifications using different 2 D materials in MOF-based biosensors can increase the sensitivity and selectivity of the biosensor. As a result, it can provide extremely low detection limit for UA. Furthermore, MOF can be functionalized using different affinity receptors that can improve the selectivity towards the UA only in complex samples. Accordingly, the reproducibility of MOF biosensors in UA estimation can be improved. All these improvements can help reduce the total analysis time and cost. Besides, it can improve UA detection in the clinical sample without failure. In a nutshell, with groundbreaking innovations in MOF biosensors, there is a need for cross-validation of methodologies by academic and industrial laboratories. Future longitudinal studies should involve the finding of positive cutoffs,specificity and sensitivity for detecting gout biomarkers. In conclusion, MOF-based biosensors can unlock the novel windows for the early diagnosis of gout with high sensitivity and selectivity towards the UA.

6. Conclusion

With the increase in the prevalence of gout in recent years and no satisfactory cure, early diagnosis is important to prevent complications and rapid worsening. A suitable biosensor can facilitate the early-stage diagnosis of gout. With the current innovation in the field of unconventional material and material science, MOF has advanced in a way to be exploited in manifold technologies in the arena of biomedical. Furthermore, along with versatility in structures of biosensor and functions of a biosensor, MOF-based biosensor has gained colossal attention from young researchers working in the arena of biosensing of various diseases and disorders. The biosensing plus diagnostic capability of nanoarchitectured MOF in gout can be improved through PSM. With the utilization of novel inorganic materials, the efficacy of nanoarchitectured MOF can be amplified equally in the ground of gout therapy and gout biosensing. Furthermore, the nanoarchitectured MOF-based fluorescent biosensor, electrochemical biosensor, and colorimetric biosensor could be reused several times in UA biosensing events. Additionally, MOF biosensors could be used as a reliable tool to detect UA in clinical/body fluid samples such as serum and urine. Recently, paper-based tests for on-site UA detection have been reported using MOF material-based biosensors. A paper-based test can be used for a tentative diagnosis of UA-associated hyperuricuria. In the case of MOF-based colorimetric biosensors, the UA concentration can be measured using smartphone-associated software. In addition, various metal/polymer composites-based MOF also divulged that this advanced biosensor is capable of detecting UA in clinical samples such as human urine, serum/plasma, and tear samples. In a nutshell, significant progress was made in the biosensing of UA using MOF-based highly sensitive and selective biosensors. Soon, a nanoplatform centered on MOF can be expected to be on the market in one or more biomedical fields.

Declaration of Competing Interest

The authors declare that they have no known competing financial interests or personal relationships that could have appeared to influence the work reported in this paper.

Acknowledgments

The authors are thankful to H. R. Patel Institute of Pharmaceutical Education and Research, Shirpur for providing the necessary facilities.

References

[1] L. Ma, A. Cranney, J.M. Holroyd-Leduc, Acute monoarthritis: What is the cause of my patient's painful swollen joint? Cmaj 180 (2009) 59–65.
[2] S. Senthelal, J. Li, A. Goyal, P. Bansal, M.A. Thomas, Arthritis, StatPearls [Internet] (2020).
[3] S. Bas, S. Genevay, O. Meyer, C. Gabay, Anti-cyclic citrullinated peptide antibodies, IgM and IgA rheumatoid factors in the diagnosis and prognosis of rheumatoid arthritis, Rheumatology 42 (2003) 677–680.
[4] N. Schlesinger, Diagnosis of gout: clinical, laboratory, and radiologic findings, Am J Manag Care 11 (2005) S443–S450.
[5] M.A. Martillo, L. Nazzal, D.B. Crittenden, The crystallization of monosodium urate, Current rheumatology reports 16 (2014) 400.
[6] A.K. Kundu, Gout in Indian Scenario.
[7] G. Ragab, M. Elshahaly, T. Bardin, Gout: An old disease in new perspective–A review, Journal of advanced research 8 (2017) 495–511.
[8] M.J.G. Chang-Fu Kuo, W. Zhang, M. Doherty, Global epidemiology of gout: prevalence, incidence and risk factors, Nat. Rev. Rheumatol. 11 (2015) 649–662.
[9] M. Dehlin, L. Jacobsson, E. Roddy, Global epidemiology of gout: prevalence, incidence, treatment patterns and risk factors, Nature Reviews Rheumatology 16 (2020) 380–390.
[10] C.-F. Kuo, M.J. Grainge, W. Zhang, M. Doherty, Global epidemiology of gout: prevalence, incidence and risk factors, Nature reviews rheumatology 11 (11) (2015) 649–662.
[11] Arthritis-India, Fight arthritis with knowledge and courage, http://www.arthritis-india.com/gout.html.
[12] National library of medicine, https://pubmed.ncbi.nlm.nih.gov/, PubMed.gov (PubMed).
[13] F.J. Newberry SJ, Maglione MA, Diagnosis of Gout Comparative Effectiveness Review, Agency for Healthcare Research and Quality (US), 158 (2016) 1-148.
[14] A.P.D.H. Erhan Dincer, Dennis J Levinson, Asymptomatic hyperuricemia: to treat or not to treat, Cleve Clin J Med 69 (2002) 594–608.
[15] Q. Yan, N. Zhi, L. Yang, G. Xu, Q. Feng, Q. Zhang, S. Sun, A highly sensitive uric acid electrochemical biosensor based on a nano-cube cuprous oxide/ferrocene/uricase modified glassy carbon electrode, Scientific reports 10 (2020) 1–10.
[16] J. Maiuolo, F. Oppedisano, S. Gratteri, C. Muscoli, V. Mollace, Regulation of uric acid metabolism and excretion, International journal of cardiology 213 (2016) 8–14.
[17] F. Zhang, P. Ma, X. Deng, Y. Sun, X. Wang, D. Song, Enzymatic determination of uric acid using water-soluble CuInS/ZnS quantum dots as a fluorescent probe, Microchimica Acta 185 (2018) 499.
[18] J.T. Doherty M, Nuki G, Eliseo Pascual, Fernando Perez-Ruiz, Leonardo Punzi, Alexander K So, Thomas Bardin, Gout: why is this curable disease so seldom cured?, Annals of the Rheumatic Diseases, 71 (2012) 1765-1770.
[19] S. Nangare, P. Patil, Nanoarchitectured Bioconjugates and Bioreceptors Mediated Surface Plasmon Resonance Biosensor for In Vitro Diagnosis of Alzheimer's Disease: Development and Future Prospects, Critical Reviews in Analytical Chemistry (2020) 1–31.
[20] A.B.J. Rashmi, D. Chaudhari, Rohit Srivastava, Uric acid biosensor based on chemiluminescence detection using a nano-micro hybrid matrix, Sensors and Actuators B 1 (173) (2012) 882–889.
[21] Rehab M. Hafez, Tahany M. Abdel-Rahman, Rasha M. Naguib, Uric acid in plants and microorganisms: Biological applications and genetics - A review, Journal of Advanced Research 8 (5) (2017) 475–486.
[22] Patapong Towiwat, Zhan-Guo Li, The association of vitamin C, alcohol, coffee, tea, milk and yogurt with uric acid and gout, International journal of rheumatic diseases 18 (5) (2015) 495–501.
[23] Servet Çete, Ahmet Yaşar, Fatma Arslan, An amperometric biosensor for uric acid determination prepared from uricase immobilized in polypyrrole film, Artificial cells, blood substitutes, and biotechnology 34 (3) (2006) 367–380.
[24] R.F. Dutra, K.A. Moreira, M.I.P. Oliveira, A.N. Araújo, M.C.B.S. Montenegro, J.L. L. Filho, V.L. Silva, An Inexpensive Biosensor for Uric Acid Determination in Human Serum by Flow-Injection Analysis, Electroanalysis: An International Journal Devoted to Fundamental and Practical Aspects of, Electroanalysis 17 (8) (2005) 701–705.
[25] Vanesa Sanz, Susana de Marcos, Javier Galbán, Uric acid determination using uricase and the autotransducer molecular absorption properties of peroxidase, Analytica chimica acta 607 (2) (2008) 211–218.
[26] J. Lu, Y. Xiong, C. Liao, F. Ye, Colorimetric detection of uric acid in human urine and serum based on peroxidase mimetic activity of MIL-53 (Fe), Analytical Methods 7 (2015) 9894–9899.

[27] Shumei Qu, Zheng Li, Qiong Jia, Detection of Purine Metabolite Uric Acid with Picolinic-Acid-Functionalized Metal-Organic Frameworks, ACS applied materials & interfaces 11 (37) (2019) 34196–34202.

[28] Sopan N. Nangare, Pravin O. Patil, Affinity-Based Nanoarchitectured Biotransducer for Sensitivity Enhancement of Surface Plasmon Resonance Sensors for In Vitro Diagnosis, A Review, ACS Biomaterials Science & Engineering 7 (1) (2021) 2–30.

[29] Muhamad Taufik Ulhakim, Muhammad Rezki, Kariana Kusuma Dewi, Syauqi Abdurrahman Abrori, Suksmandhira Harimurti, Ni Luh Wulan Septiani, Kiki Adi Kurnia, Widiastuti Setyaningsih, Noviyan Darmawan, Brian Yuliarto, Review-Recent Trend on Two-Dimensional Metal-Organic Frameworks for Electrochemical Biosensor Application, Journal of the Electrochemical Society 167 (13) (2020) 136509, https://doi.org/10.1149/1945-7111/abb6cc.

[30] Abhijeet Pandey, Namdev Dhas, Prashant Deshmukh, Carlos Caro, Pravin Patil, Maria Luisa García-Martín, Bharath Padya, Ajinkya Nikam, Tejal Mehta, Srinivas Mutalik, Heterogeneous surface architectured metal-organic frameworks for cancer therapy, imaging, and biosensing: A state-of-the-art review, Coordination Chemistry Reviews 409 (2020) 213212, https://doi.org/10.1016/j.ccr.2020.213212.

[31] Yajuan Cai, Xiaoyu Li, Kangbing Wu, Xiaofeng Yang, Electrochemical sensing performance of Eu-BTC and Er-BTC frameworks toward Sunset Yellow, Analytica chimica acta 1062 (2019) 78–86.

[32] Jianping Lei, Ruocan Qian, Pinghua Ling, Lin Cui, Huangxian Ju, Design and sensing applications of metal–organic framework composites, TrAC Trends in Analytical Chemistry 58 (2014) 71–78.

[33] W. Schrimpf, J. Jiang, Z. Ji, P. Hirschle, D.C. Lamb, O.M. Yaghi, S. Wuttke, Chemical diversity in a metal–organic framework revealed by fluorescence lifetime imaging, Nature communications 9 (2018) 1–10.

[34] Sophie E. Miller, Michelle H. Teplensky, Peyman Z. Moghadam, David Fairen-Jimenez, Metal-organic frameworks as biosensors for luminescence-based detection and imaging, Interface Focus 6 (4) (2016) 20160027, https://doi.org/10.1098/rsfs.2016.0027.

[35] Kui Shen, Xiaodong Chen, Junying Chen, Yingwei Li, Development of MOF-derived carbon-based nanomaterials for efficient catalysis, Acs Catalysis 6 (9) (2016) 5887–5903.

[36] Man Huang, Kan Mi, Junhao Zhang, Huili Liu, Tingting Yu, Aihua Yuan, Qinghong Kong, Shenglin Xiong, MOF-derived bi-metal embedded N-doped carbon polyhedral nanocages with enhanced lithium storage, Journal of Materials Chemistry A 5 (1) (2017) 266–274.

[37] Sergio Carrasco, Metal-organic frameworks for the development of biosensors: a current overview, Biosensors 8 (4) (2018) 92, https://doi.org/10.3390/bios8040092.

[38] Rana Dalapati, Shyam Biswas, Post-synthetic modification of a metal-organic framework with fluorescent-tag for dual naked-eye sensing in aqueous medium, Sensors and Actuators B: Chemical 239 (2017) 759–767.

[39] Yaran Du, Xiqian Li, Xueju Lv, Qiong Jia, Highly sensitive and selective sensing of free bilirubin using metal–organic frameworks-based energy transfer process, ACS applied materials & interfaces 9 (36) (2017) 30925–30932.

[40] Hong-Cai Zhou, Jeffrey R. Long, Omar M. Yaghi, Introduction to metal–organic frameworks, ACS Publications 112 (2) (2012) 673–674.

[41] Lantao Liu, Yanli Zhou, Shuang Liu, Maotian Xu, The applications of metal–organic frameworks in electrochemical sensors, ChemElectroChem 5 (1) (2018) 6–19.

[42] J. Luo, J. Cui, Y. Wang, D. Yu, Y. Qin, H. Zheng, X. Shu, H.H. Tan, Y. Zhang, Y. Wu, Metal-organic framework-derived porous Cu2O/Cu@ C core-shell nanowires and their application in uric acid biosensor, Applied Surface Science 506 (2020), 144662.

[43] D. Wang, D. Jana, Y. Zhao, Metal-Organic Framework Derived Nanozymes in Biomedicine, Accounts of Chemical Research 53 (2020) 1389–1400.

[44] K. Wang, C. Wu, F. Wang, M. Liao, G. Jiang, Bimetallic nanoparticles decorated hollow nanoporous carbon framework as nanozyme biosensor for highly sensitive electrochemical sensing of uric acid, Biosensors and Bioelectronics 150 (2020), 111869.

[45] Y. Sun, L. Zheng, Y. Yang, X. Qian, T. Fu, X. Li, Z. Yang, H. Yan, C. Cui, W. Tan, Metal–organic framework nanocarriers for drug delivery in biomedical applications, Nano-Micro Letters 12 (2020) 1–29.

[46] A. Badoei-Dalfard, N. Sohrabi, Z. Karami, G. Sargazi, Fabrication of an efficient and sensitive colorimetric biosensor based on Uricase/Th-MOF for uric acid sensing in biological samples, Biosensors and Bioelectronics 141 (2019), 111420.

[47] S. Abednatanzi, P.G. Derakhshandeh, H. Depauw, F.-X. Coudert, H. Vrielinck, P. Van Der Voort, K. Leus, Mixed-metal metal–organic frameworks, Chemical Society Reviews 48 (2019) 2535–2565.

[48] J. Klinowski, F.A.A. Paz, P. Silva, J. Rocha, Microwave-assisted synthesis of metal–organic frameworks, Dalton Transactions 40 (2011) 321–330.

[49] H. Al-Kutubi, J. Gascon, E.J. Sudhölter, L. Rassaei, Electrosynthesis of metal–organic frameworks: challenges and opportunities, ChemElectroChem 2 (2015) 462–474.

[50] S.G. Intasa-ard, K.J. Imwiset, S. Bureekaew, M. Ogawa, Mechanochemical methods for the preparation of intercalation compounds, from intercalation to the formation of layered double hydroxides, Dalton Transactions 47 (2018) 2896–2916.

[51] Rana Dalapati, Shyam Biswas, A Pyrene-Functionalized Metal-Organic Framework for Nonenzymatic and Ratiometric Detection of Uric Acid in Biological Fluid via Conformational Change, Inorganic chemistry 58 (9) (2019) 5654–5663.

[52] Rui Xin, Xiao-Yang Yu, Wei-Ping Gao, Na Wang, Jia-Jun Yang, Xiao-Shu Qu, Xiao Zhang, Hydrothermal syntheses, crystal structures and luminescence properties of Cd (II) coordination polymers based on 2-(pyridine-2-yl)-1H-imidazole-4, 5-dicarboxylic acid, Inorganic Chemistry Communications 35 (2013) 38–41.

[53] Hou Wang, Xingzhong Yuan, Guangming Zeng, Yan Wu, Yang Liu, Qian Jiang, Shansi Gu, Three dimensional graphene based materials: Synthesis and applications from energy storage and conversion to electrochemical sensor and environmental remediation, Advances in colloid and interface science 221 (2015) 41–59.

[54] Wei-Xia Xu, Jun Li, Rui-Ping Liu, Wei-Xia Zhou, Wang-Yang Ma, Feng-Xing Zhang, A novel 1D linear zinc (II) coordination polymer based 2, 2′-bipyridine-4, 4′-dicarboxylic acid: synthesis, crystal structure and photoluminescence property, Inorganic Chemistry Communications 28 (2013) 12–15.

[55] Liangliang Zhang, Zixi Kang, Xuelian Xin, Daofeng Sun, Metal–organic frameworks based luminescent materials for nitroaromatics sensing, CrystEngComm 18 (2) (2016) 193–206.

[56] Shivani Sharma, Sujit K. Ghosh, Metal–organic framework-based selective sensing of biothiols via chemidosimetric approach in water, ACS omega 3 (1) (2018) 254–258.

[57] Ying Wang, Yaqin Hu, Qunye He, Jianhua Yan, Hongjie Xiong, Nachuan Wen, Shundong Cai, Dongming Peng, Yanfei Liu, Zhenbao Liu, Metal-organic frameworks for virus detection, Biosensors and Bioelectronics 169 (2020) 112604, https://doi.org/10.1016/j.bios.2020.112604.

[58] Banglin Chen, Shengchang Xiang, Guodong Qian, Metal− organic frameworks with functional pores for recognition of small molecules, Accounts of chemical research 43 (8) (2010) 1115–1124.

[59] P. Shi, Y. Zhang, Z. Yu, S. Zhang, Label-free electrochemical detection of ATP based on amino-functionalized metal-organic framework, Scientific reports 7 (2017) 1–7.

[60] Shamim Ahmed Hira, Saravanan Nagappan, Dicky Annas, Yedluri Anil Kumar, Kang Hyun Park, NO2-functionalized metal–organic framework incorporating bimetallic alloy nanoparticles as a sensor for efficient electrochemical detection of dopamine, Electrochemistry Communications 125 (2021) 107012, https://doi.org/10.1016/j.elecom.2021.107012.

[61] Zana Hassan Rada, Hussein Rasool Abid, Hongqi Sun, Jin Shang, Jiaye Li, Yingdian He, Shaomin Liu, Shaobin Wang, Effects of-NO2 and-NH2 functional groups in mixed-linker Zr-based MOFs on gas adsorption of CO2 and CH4, Progress in Natural Science: Materials International 28 (2) (2018) 160–167.

[62] Yichao Lin, Chunlong Kong, Liang Chen, Amine-functionalized metal–organic frameworks: structure, synthesis and applications, RSC advances 6 (39) (2016) 32598–32614.

[63] Xiao Lian, Bing Yan, Phosphonate MOFs composite as off–on fluorescent sensor for detecting purine metabolite uric acid and diagnosing hyperuricuria, Inorganic Chemistry 56 (12) (2017) 6802–6808.

[64] Ji-Na Hao, Bing Yan, Ag+-sensitized lanthanide luminescence in Ln 3+ post-functionalized metal–organic frameworks and Ag+ sensing, Journal of Materials Chemistry A 3 (9) (2015) 4788–4792.

[65] Ye Lu, Bing Yan, Jin-Liang Liu, Nanoscale metal–organic frameworks as highly sensitive luminescent sensors for Fe 2+ in aqueous solution and living cells, Chemical Communications 50 (69) (2014) 9969–9972.

[66] Ji-Na Hao, Bing Yan, Recyclable lanthanide-functionalized MOF hybrids to determine hippuric acid in urine as a biological index of toluene exposure, Chemical Communications 51 (77) (2015) 14509–14512.

[67] Bangguo Peng, Jiewu Cui, Yan Wang, Jiaqin Liu, Hongmei Zheng, Li Jin, Xinyi Zhang, Yong Zhang, Yucheng Wu, CeO 2–x/C/rGO nanocomposites derived from Ce-MOF and graphene oxide as a robust platform for highly sensitive uric acid detection, Nanoscale 10 (4) (2018) 1939–1945.

[68] Longlong Liu, Liu Liu, Yuli Wang, Bang-Ce Ye, A novel electrochemical sensor based on bimetallic metal–organic framework-derived porous carbon for detection of uric acid, Talanta 199 (2019) 478–484.

[69] Li Tan, Tianen Fan, Tifeng Xia, Yuanjing Cui, Yu Yang, Guodong Qian, A luminescent terbium metal-organic framework for highly sensitive and selective detection of uric acid in aqueous media, Journal of Solid State Chemistry 272 (2019) 55–61.

[70] Li-Juan Han, Ya-Jie Kong, Guo-Zheng Hou, Hua-Chong Chen, Xing-Min Zhang, He-Gen Zheng, A Europium-based MOF Fluorescent Probe for Efficiently Detecting Malachite Green and Uric Acid, Inorganic Chemistry 59 (10) (2020) 7181–7187.

[71] L. Zhang, S. Li, J. Xin, H. Ma, H. Pang, L. Tan, X. Wang, A non-enzymatic voltammetric xanthine sensor based on the use of platinum nanoparticles loaded with a metal-organic framework of type MIL-101 (Cr), Application to simultaneous detection of dopamine, uric acid, xanthine and hypoxanthine, Microchimica Acta 186 (2019) 9.

[72] K.-Y.A. Lin, Y.-T. Liu, S.-Y. Chen, Adsorption of fluoride to UiO-66-NH2 in water: stability, kinetic, isotherm and thermodynamic studies, Journal of colloid and interface science 461 (2016) 79–87.

[73] R. Devi, C. Pundir, Construction and application of an amperometric uric acid biosensor based on covalent immobilization of uricase on iron oxide nanoparticles/chitosan-g-polyaniline composite film electrodeposited on Pt electrode, Sensors and Actuators B: Chemical 193 (2014) 608–615.

[74] Z.-X. Zhu, C.-J. Wang, D. Luo, C. Liu, D.-N. Liu, Y.-M. Xiao, S. Chen, Y.-Y. Wang, Six new lanthanide metal–organic frameworks as luminescent sensors for the detection of 1-N, TDGA, UA, and HA in urine, Journal of Coordination Chemistry 72 (2019) 3526–3543.

[75] L. Chang, X.-Y. Yao, Q. Liu, D. Ning, Q. Wang, X.-M. Du, W.-J. Ruan, Y. Li, MOF based fluorescent assay of xanthine oxidase for rapid inhibitor screening with real-time kinetics monitoring, Talanta 183 (2018) 83–88.

[76] J. Luo, J. Cui, Y. Wang, D. Yu, Y. Qin, H. Zheng, Y. Hong, Y. Zhang, Y. Wu, MOF-Derived Porous CeO 2–x/C Nanorods and Their Applications in Uric Acid Biosensor, Nano 13 (2018) 1850085.

[77] B. Hu, Y. Liu, Z.-W. Wang, Y. Song, M. Wang, Z. Zhang, C.-S. Liu, Bimetallic-organic framework derived porous Co3O4/Fe3O4/C-loaded g-C3N4 nanocomposites as non-enzymic electrocatalysis oxidization toward ascorbic acid, dopamine acid, and uric acid, Applied Surface Science 441 (2018) 694–707.
[78] C. Xiong, T. Zhang, W. Kong, Z. Zhang, H. Qu, W. Chen, Y. Wang, L. Luo, L. Zheng, ZIF-67 derived porous Co3O4 hollow nanopolyhedron functionalized solution-gated graphene transistors for simultaneous detection of glucose and uric acid in tears, Biosensors and Bioelectronics 101 (2018) 21–28.
[79] J. Xu, J. Xia, F. Zhang, Z. Wang, An electrochemical sensor based on metal-organic framework-derived porous carbon with high degree of graphitization for electroanalysis of various substances, Electrochimica Acta 251 (2017) 71–80.
[80] J. Tang, S. Jiang, Y. Liu, S. Zheng, L. Bai, J. Guo, J. Wang, Electrochemical determination of dopamine and uric acid using a glassy carbon electrode modified with a composite consisting of a Co (II)-based metalorganic framework (ZIF-67) and graphene oxide, Microchimica Acta 185 (2018) 1–11.
[81] D. Yin, J. Liu, X. Bo, M. Li, L. Guo, Porphyrinic metal-organic framework/macroporous carbon composites for electrocatalytic applications, Electrochimica Acta 247 (2017) 41–49.
[82] S.A. Abrori, N.L.W. Septiani, F.N. Hakim, A. Maulana, I. Anshori, B. Yuliarto, Non-Enzymatic Electrochemical Detection for Uric Acid Based on a Glassy Carbon Electrode Modified With MOF-71, IEEE Sensors Journal 21 (2020) 170–177.
[83] Huynh Truong Ngo, Le Thi Hoa, Nguyen Tan Khanh, Tran Thi Bich Hoa, Tran Thanh Tam Toan, Tran Xuan Mau, Nguyen Hai Phong, Ho Sy Thang, Dinh Quang Khieu, ZIF-67/g-C3N4-Modified Electrode for Simultaneous Voltammetric Determination of Uric Acid and Acetaminophen with Cetyltrimethylammonium Bromide as Discriminating Agent, Journal of Nanomaterials 2020 (2020) 1–13.
[84] S. Krishnan, L. Tong, S. Liu, R. Xing, A mesoporous silver-doped TiO 2-SnO 2 nanocomposite on gC 3 N 4 nanosheets and decorated with a hierarchical core–shell metal-organic framework for simultaneous voltammetric determination of ascorbic acid, dopamine and uric acid, Microchimica Acta 187 (2020) 1–9.
[85] N. Setoudeh, S. Jahani, M. Kazemipour, M.M. Foroughi, H.H. Nadiki, Zeolitic imidazolate frameworks and cobalt-tannic acid nanocomposite modified carbon paste electrode for simultaneous determination of dopamine, uric acid, acetaminophen and tryptophan: Investigation of kinetic parameters of surface electrode and its analytical performance, Journal of Electroanalytical Chemistry 863 (2020), 114045.
[86] Z. Qu, Y. Muhammad, W. He, J. Li, Z. Gao, J. Fu, S.J. Shah, H. Sun, J. Wang, Z. Huang, Designing C-Fe-O bonded MIL-88B (Fe)/jasmine petal-derived-carbon composite biosensor for the simultaneous detection of dopamine and uric acid, Chemical Engineering Journal 404 (2021), 126570.
[87] H. Guo, M. Wang, L. Zhao, N. Youliwasi, C. Liu, The effect of Co and N of porous carbon-based materials fabricated via sacrificial templates MOFs on improving DA and UA electrochemical detection, Microporous and Mesoporous Materials 263 (2018) 21–27.
[88] M. Ko, L. Mendecki, A.M. Eagleton, C.G. Durbin, R.M. Stolz, Z. Meng, K.A. Mirica, Employing conductive metal–organic frameworks for voltammetric detection of neurochemicals, Journal of the American Chemical Society 142 (2020) 11717–11733.
[89] M.-Q. Wang, C. Ye, S.-J. Bao, Y. Zhang, Y.-N. Yu, M.-W. Xu, Carbon nanotubes implanted manganese-based MOFs for simultaneous detection of biomolecules in body fluids, Analyst 141 (2016) 1279–1285.
[90] X. Luan, Y. Pan, D. Zhou, B. He, X. Liu, Y. Gao, J. Yang, Y. Song, Cerium metal organic framework mediated molecular threading for point-of-care colorimetric assays, Biosensors and Bioelectronics 165 (2020), 112406.
[91] Pengfei Gao, Yaoyao Feng, Mengfan Wang, Nan Jiang, Wei Qi, Rongxin Su, Zhimin He, Ferrocene-Modified Metal-Organic Frameworks as a Peroxidase-Mimicking Catalyst, Catalysis Letters 151 (2) (2021) 478–486.
[92] Ying-Ying Wang, Hai-Feng Zhang, Dong-Hui Wang, Ning Sheng, Gong-Guo Zhang, Ling Yin, Jing-Quan Sha, Development of a Uricase-Free Colorimetric Biosensor for Uric Acid Based on PPy-Coated Polyoxometalate-Encapsulated Fourfold Helical Metal-Organic Frameworks, ACS Biomaterials Science & Engineering 6 (3) (2020) 1438–1448.
[93] Xiao Liu, Wei Qi, Yuefei Wang, Rongxin Su, Zhimin He, A facile strategy for enzyme immobilization with highly stable hierarchically porous metal–organic frameworks, Nanoscale 9 (44) (2017) 17561–17570.
[94] Xiao Liu, Wei Qi, Yuefei Wang, Daiwu Lin, Xuejiao Yang, Rongxin Su, Zhimin He, Rational design of mimic multienzyme systems in hierarchically porous biomimetic metal–organic frameworks, ACS applied materials & interfaces 10 (39) (2018) 33407–33415.
[95] Xiaoxue Kou, Linjing Tong, Yujian Shen, Wangshu Zhu, Li Yin, Siming Huang, Fang Zhu, Guosheng Chen, Gangfeng Ouyang, Smartphone-assisted robust enzymes@ MOFs-based paper biosensor for point-of-care detection, Biosensors and Bioelectronics 156 (2020) 112095, https://doi.org/10.1016/j.bios.2020.112095.

International Journal of Biological Macromolecules 166 (2021) 839–850

Contents lists available at ScienceDirect

International Journal of Biological Macromolecules

journal homepage: http://www.elsevier.com/locate/ijbiomac

A halotolerant hyaluronidase from newly isolated *Brevibacterium halotolerans* DC1: Purification and characterization

Sandip P. Patil [a], Leena P. Shirsath [a], Bhushan L. Chaudhari [b,*]

[a] Department of Microbiology and Biotechnology, R. C. Patel Arts, Commerce and Science College, Shirpur 425 405, India
[b] Department of Microbiology, School of Life Sciences, Kavayitri Bahinabai Chaudhari North Maharashtra University, Jalgaon 425 001, India

ARTICLE INFO

Article history:
Received 18 August 2020
Received in revised form 9 October 2020
Accepted 30 October 2020
Available online 2 November 2020

Keywords:
Hyaluronidase
Halotolerant
Brevibacterium halotolerans
Hyaluronic acid

ABSTRACT

An enzyme hyaluronidase (hyase) producing halotolerant bacterium was isolated from dental caries and identified as *Brevibacterium halotolerans* DC1. Higher growth and hyase production were observed in nutrient broth fortified with hyaluronic acid at pH 7.0, temperature 37 °C, 120 rpm upon 48 h of incubation. Hyase was purified using salt precipitation, DEAE cellulose ion exchange, and Sephadex G-100 gel filtration chromatography. The enzyme was purified to 13-fold with 67.19% recovery of activity and 26.37 U/mg of specific activity. SDS-PAGE and zymography revealed it to be near to homogeneity showing a relative molecular weight of about 43 kDa that was confirmed by MALDI-TOF MS. This hyase was very active and stable at pH 7.0 and temperature 40 °C. The presence of metal ions Ca^{2+} and Mg^{2+} increased its activity while Zn^{2+} and Cu^{2+} severely inhibited it. Being stable at 2 M NaCl, hyase exhibited its halotolerant nature. This enzyme showed wide substrate specificity where hyaluronic acid (HA) was the best substrate. The kinetic studies revealed that K_m and V_{max} were 91.3 μg/mL and 306.2 μg/mL/min respectively. This is the first report of hyaluronidase from a halotolerant *Brevibacterium* spp. which can find applications under high salinity.

1. Introduction

The hyaluronidase (hyase) is a glycosidase enzyme that predominantly degrades a polymeric substrate hyaluronic acid (HA), with restricted ability to degrade Chondroitin, Chondroitin sulfate, Dermatan sulfate and other related glycosaminoglycans [1]. The worldwide interest in hyase research has been increased tremendously owing to its great importance in medical, physiological, biological and commercial field [2]. These enzymes are widely distributed in mammalian tissues and organs, the venoms (snakes, lizards, fishes, bees, wasps, scorpions, and spiders), body fluids (blood, tears, seminal fluid), invertebrate animals (leeches, crustaceans), and microorganisms including bacteria, yeast and fungi [3]. For many years, hyases are widely utilized in many streams like orthopaedia, oncology, surgery, ophthalmology, gynecology, dermatology and internal medicine [4]. The isolation and identification of new hyaluronidases with novel properties continues since 1940; due to comprehension of its crucial role in biological processes including fertilization [5], cell migration and differentiation, embryonic development, wound healing [6], inflammation, growth and metastasis of tumor cells [7].

Bacterial hyaluronidases (hyaluronate lyase, EC 4.2.2.1) are the glycosidase enzymes that specifically cleave the β,1-4 glycosidic linkage in substrate hyaluronic acid (HA) [1]. Many pathogenic bacteria can establish and spread infections at the mucosal or skin surface by producing the enzyme hyase as their potential virulence factor [8]. The microorganisms capable of producing enzyme hyase include various species of *Streptococcus*, *Staphylococcus*, *Peptostreptococcus*, *Propionibacterium*, *Streptomyces* and *Clostridium* [9–12]. While it has also been reported in different species of *Candida*, including *C. albicans, C. krusei, C. tropicalis, C. parapsilosis,* and *C. guilliermondii* [13]. The causative agent of syphilis - *Treponema pallidum* and *Treponema pertenue* are also reported to produce hyase [14]. The veterinary pathogens, *S. uberis* and *S. dysgalactiae* that cause mastitis have also shown the synthesis of enzyme hyase [15,16]. Recently, hyases were reported as important virulence factors of Group B *Streptococcus* (GBS) involved in ascending vaginal infections in pregnant women leading to increased fetal injuries, preterm birth defects and fetal demise [17,18].

The hyase production process is greatly influenced by various physical parameters (pH, temperature, incubation period, inoculum size and agitation rate) and nutritional parameters (carbon and nitrogen sources). The optimization of these physical and nutritional parameters for hyase production plays a crucial role in improving the yield of an enzyme [19]. The purification of extracellular microbial hyase from heterogeneous protein mixture could be accomplished by salt precipitation (Ammonium sulfate), solvent precipitation (Acetone, Ethanol) followed

* Corresponding author at: Department of Microbiology, School of Life Sciences, Kavayitri Bahinabai Chaudhari North Maharashtra University, Post Box - 80, Umavinagar, Jalgaon 425 001, India.
E-mail address: blchaudhari@nmu.ac.in (B.L. Chaudhari).

https://doi.org/10.1016/j.ijbiomac.2020.10.240
0141-8130/

Optimising the fixation of reactive dyes

By **Tushar A. Shinde**, **Dr Sachin M. Munde**, **Dr Leena N. Patil**, **Swapnil Mali**, **Dr Sandip P. Patil** and **Dr K. K. Gupta**

Abstract

Today, there are more than 10,000 dyes commercially available around the world and around 800,000 tonnes of dyes are produced annually. Dyes themselves have many varieties based on their structure, such as acidic, basic, azo, metal complex, vat and reactive dyes.

The reactive dyeing process requires large quantities of salt, such as sodium chloride, sodium sulphate and Glauber salt. It requires 50-100 gm/litre (gpl) of the salts to promote adequate exhaustion. It additionally uses large quantities of water for rinsing the dyed fabric, resulting in an average of 2,000-3,000 ppm of effluent. There have been recent attempts to lower levels of sodium chlorite in this process because many dyes are discharging at high levels; many dye manufacturers have developed a line of fibre-reactive dyes that require less salt to promote exhaustion. For the reactive dyeing of cotton fabric, we optimised (decreased and increased) the concentration of salt by 1%, 3% and 4% to observe the subsequent wash fastness, rub fastness and colour strength.

Keywords

- Colour strength
- Exhaustion
- Reactive dyes
- Rinsing
- Dyestuff

1. Introduction

In the reactive dyeing process, a covalent bond forms in between the dye molecule and the cotton polymer. The textile material attaches itself to the substrate via a chemical reaction that creates a covalent bond between the molecule of dye and the fibre. The first fibre reactive dyes were designed especially for cellulosic fibres and are mostly still used today; for protein and polyamide fibres, reactive dyes are commercially available. These dyes contain reactive groups that can be applied to a fibre in a weakly alkaline medium in a dye bath to encourage a chemical bond with the fibre. Reactive dyes can also be used to dye silk, wool and nylon (-NH2 group). In the latter case, they are applied under weakly acidic conditions, and a reaction occurs in an alkaline condition (pH>10).

For this project, we used a different concentration of the exhausting agent for the dyeing of cotton fabric with reactive dye, and the maximum fixation of various reactive dyes is used. It is our aim to achieve a specific depth of shade with a certain concentration of salt. It is important to see the effect of the concentration of salt on the exhaustion and dyeing of reactive dye, because salt plays a vital role as the catalyst that facilitates dyeing action. Salt has an extremely high affinity towards water. Broadly speaking, salt is necessary for three things: it drives the dye into the textile during the dyeing process; it helps to achieve the maximum exhaustion of dye molecules during the dyeing process in textiles; and it is used as an electrolyte for migration, absorption and fixation of the dyestuff to the cellulose material.

Johann Glauber was the first to produce Glauber salt, which he derived from Hungarian spring waters. The naturally-occurring salt is called mirabilite. Glauber's salt is a common name for sodium sulphate dehydrate (Na2SO4. 10H2O) and it occurs as white or colourless monoclinic crystals. Upon exposure to dry air, it forms a powdery anhydrous sodium sulphate. Glauber salt is water soluble, has a salty, bitter taste and is sometimes used in medicine as a mild laxative. It is also used in dyeing.

2. Materials and method

Fabric

The material used for the experiment was a 100% cotton terry towel double pile, procured from Deesan Dyeing Unit Shirpur, India. This terry towel is ready for dyeing (RFD).

Dye

Reactive dyes:

A. Company A: Colourtex, red XD2B
B. Company B: Jakazol, red TRL
C. Company C: Huntsman, red EC2BL

Machine

The following machinery was used in the project: a soft flow Thies dyeing machine (bulk scale); a spectrophotometer; a weighing balance; a fastness to crocking machine; a dryer; and an AHIBA dyeing machine (lab scale).

OA HOST

Nano Biomed Eng

2021, 13(2): 179-190. doi: 10.5101/nbe.v13i2.p179-190.

Research Article

Fabrication of N-Doped Graphene@TiO_2 Nanocomposites for Its Adsorption and Absorbing Performance with Facile Recycling

Pravin Onkar Patil[1], Sopan Namdev Nangare[1], Pratiksha Pramod Patil[1], Ashwini Ghanashyam Patil[2], Dilip Ramsing Patil[2], Rahul Shankar Tade[1], Arun Madhukar Patil[2], Prashant Krishnarao Deshmukh[3], Sanjay Baburao Bari[1]

[1]H.R. Patel Institute of Pharmaceutical Education and Research, Karvand Naka, Shirpur, Dist- Dhule, Maharashtra, 425405 India.
[2]R.C. Patel Arts, Science, and Commerce College, Shirpur, Maharashtra, 425405 India.
[3]Dr. Rajendra Gode College of Pharmacy, Malkapur, Dist- Buldhana, Maharashtra, 443101 India.

Corresponding author. E-mail: rxpatilpravin@yahoo.co.in

Received: Dec. 11, 2020; **Accepted:** Mar. 29, 2021; **Published:** May 26, 2021

Citation: Pravin Onkar Patil, Sopan Namdev Nangare, Pratiksha Pramod Patil, Ashwini Ghanashyam Patil, Dilip Ramsing Patil, Rahul Shankar Tade, Arun Madhukar Patil, Prashant Krishnarao Deshmukh, and Sanjay Baburao Bari,Fabrication of N-Doped Graphene@TiO_2 Nanocomposites for Its Adsorption and Absorbing Performance with Facile Recycling. *Nano Biomed. Eng.*, 2021, 13(2): 179-190.
DOI: 10.5101/nbe.v13i2.p179-190.

Abstract

The present work aims to synthesize nitrogen-doped reduced graphene oxide-titanium dioxide nanocomposite (N-rGO@TiO_2) using a simple, eco-friendly method and its applications in spectroscopic detection of heavy metal ions such as lead (Pb^{2+}), mercury (Hg^{2+}), and chromium-VI [Cr(VI)] in potable water. Initially, TiO_2 nanoparticles loaded N doped rGO sheets were fabricated by an ecological method using *Gossypium hirsutum* (cotton) seeds extract as a green reducing agent. Then, the N-rGO@TiO_2 nanocomposites were subjected for characterizations such as spectroscopic techniques, particle size analysis, zeta potential analysis, and spectroscopic sensing. Notably, the results of this study confirmed that N-rGO@TiO_2 exhibited countless stupendous features in terms of sensing of an analyte. Briefly, the UV-visible spectroscopy and Fourier transform infrared (FTIR) spectroscopy confirmed the successful synthesis of N-rGO@TiO_2. The SEM images showed the wrinkled, folded, and cross-linked network structures that confirmed the surface modification and nitrogen doping in the rGO sheet and synthesis of N-rGO@TiO_2. The EDAX study confirmed the elemental composition of the N-rGO@TiO_2 nanocomposite. Finally, due to the larger surface area, porous nature, high electron mobility, etc. the N-rGO@TiO_2 probe provides the lower detection limit for Pb^{2+}, $Hg^{2+,}$ and Cr (VI) as low as 50 nM, 15 µM, and 25 nM, respectively. Concisely, our study affirms the admirable sensitivity of N-rGO@TiO_2 nanocomposite to the Pb^{2+}, $Hg^{2+,}$ and Cr (VI) in potable water can provide better environmental remediation.

Keywords: Graphene oxide, N-rGO@TiO_2, Nanocomposite, Cotton-seed, Heavy metals, Biodegradable, Sensing

Introduction

Over the past two decades, graphene-based materials are gaining tremendous attention from a scientific fraternity in various fields [1-3]. It may because of its astonishing properties and potential to revolutionize the scientific sector [3-5]. Graphene can be used to fabricate several dimension materials such as 1D nanostructure [6], 2D layer stacked films [7], 3D graphene hydrogel [7-9], and aerogel [10-13], etc. Out

of various properties, graphene exhibited a high surface area in contrast to carbon nanotubes (CNTs) [14]. Also, it significantly enhances the electrochemical activity of various metal oxides such as titanium dioxide (TiO_2), zinc oxide (ZnO), etc). Several reports mentioned that the graphene in combination with photocatalysts resulted in the enhancement of the adsorption of pollutants [15-17]. Interestingly, several scientific groups are working on the conversion of graphene into a different unique form of graphene. On this account, the further modification of graphite (graphene) through oxidation gives the utmost graphene oxide (GO) [13, 18] and other structural models [13, 19-21]. Herein, GO exhibited abundant oxygen functionalities including carboxyl, epoxy and hydroxyl [22-24]. This GO containing oxygen functionalities, structural defects [25, 26] can be used for a range of applications. Further continuous development in GO leads to the synthesis of reduced GO (rGO). On this account, several methods have been reported for the rGO but they have some demerits such as influences of original electronic properties of graphene. Majorly reported methods can lead to ion doping and there is a chance of the presence of aggregate in nanocomposites. Besides, the uses of chemical reducing agents for the synthesis of rGO are hazardous, potentially explosive, and highly toxic to human health plus environments. Therefore, there is a need to stay away from the use of such toxic chemical agents. On this account, several eco-friendly green reducing agents (biomolecules, plant extracts and microbes) have been reported for the synthesis of rGO that acts as a capping agent and reducing agent [27]. Plenty of plant metabolites have been utilized for the fabrication of rGO for example plant extracts containing amino acids, vitamins, saccharides, microorganisms, proteins, etc. [28, 29]. Briefly, Zhang *et al.* reported vitamin C as a reductant for GO in combination with L-tryptophan [30]. Gou and co-workers confirmed that GO can be reduced using L-cysteine (amino acid) [31]. In a similar line, Dong *et al.* reported the synthesis of rGO using reducing sugar (fructose, glucose) [32]. Overall, these novel green synthesis approaches are based on several methods such as solvothermal, hydrothermal, electrochemical, microwave, and UV irradiation approaches [24]. It means the broader interest in green chemistry and environmentally sustainable synthesis of GO could be contributing to many new approaches for reducing GOs as excellent alternatives to traditional chemical processes.

From its inception, titanium dioxide (TiO_2) is extensively used in various pharmaceutical formulations such as toothpaste, ointments, paints and sunscreens. Furthermore, TiO_2 has attracted significant attention in material chemistry and it has been well investigated by the research scholars. It may because of its strong redox ability, long-term stability against photo-corrosion and chemical corrosion, relative non-toxicity, and excellent optical plus electrical properties [27, 28, 33]. On the other hand, the photocatalytic potential of TiO_2 is restricted owing to its low photocatalytic sensitivity in the UV region and the fast recombination of photogenerated electron-hole pairs [29, 31]. In this line, the photocatalytic performance of TiO_2 can be increased by optimizing optical absorption and charge transfer characteristics. It is worth mentioning that the photocatalytic performance of TiO_2 can be improved when combining with types of graphene-based nanocomposites [34-36].

In the last few years, several heteroatoms including boron (B), phosphorus (P), sulfur (S), and nitrogen (N) have been successfully explored in sensing applications. The heteroatom doped nanocomposites lead to an improvement in overall required characteristics of novel synthesized material for sensing of different interest analyte [37, 38]. Among these above mentioned heteroatoms, the doping of N is of notable interest as of its electron-rich nature, comparable size to that of carbon and high electronegativity of 'N', which might provide an appropriate location to fit into the graphene lattice. The finally obtained 'N' doped graphene composites can be used for various applications [39-43]. In the line of doping-based sensing, the majority of investigations have been focused on N-doping only. Remarkably, it is well known to induce favorable changes like increasing conductivity into the carbon material [38, 44] and high activity in the redox reactions in fuel cells [45]. As per literature, the synthesis of N-doped carbon material can be achieved through several pathways including post-treatment of carbon with ammonia [46], amines, or urea [47] and also it can be synthesized using more direct approaches using acetonitrile [48], pyrrol [49], polyacetonitrile [2, 50] as starting compounds.

As we know, the numbers of heavy metals naturally present in the environment that is in the normal range. unfortunately, during development in a different sector, the amount of heavy metals in nature is rising rapidly. it may due to various manufacturing and smelting activities. in addition to that, old infrastructure water

sources, pollution from vehicles, polluted paint, different fertilizers, plastic, etc. are also helped to raise the level of heavy metals [51]. It is worth mentioning that most developed and under developing countries are suffering from issues of heavy metal pollution [52]. Nowadays, it becomes a major problem. in addition to that, presently we are suffering good quality water shortages due to water contamination. in this framework, the various pollutants including heavy metals are harmful to human beings plus the environment. it majorly affects the quality of the naturally available water. besides, because of the presence of such heavy metals, it causes many health issues such as gastrointestinal diseases, muscular diseases, tumors, reproductive diseases, neurological diseases, genetic disorders, etc [51]. therefore, there is a need to detect the level of heavy metals in potable water and separate it. numbers of research groups are working on the detection and separation of such water contaminants. nevertheless, most of the approaches are suffering from some hurdles such as sensitivity, selectivity. also, the chemically synthesized materials for sensing pollutants are limited its applications due to the use of toxic chemicals for the synthesis of such nanocomposites [51, 53-55].

In this attempt, we have synthesized N-rGO@TiO_2 nanocomposites for sensing heavy metal ions. Initially, we synthesized N-rGO@TiO_2 via fixing of TiO_2 nanoparticles on GO sheets by a simple, green, eco-friendly, single-step method wherein cottonseeds extract is used as a green reducing agent. Finally, the spectroscopic detection of heavy metal ions from the potable water was investigated using stable N-rGO@TiO_2 nanocomposite. As a result, the N-rGO@TiO_2 nanocomposites based spectroscopic detection of Pb^{2+}, Hg^{2+}, and Cr (VI) ions exhibited a good ability to detect these heavy metal ions in potable water efficiently. Taken as a whole, N-rGO@TiO_2 could be a simple, rapid and economic method for heavy metal detection in water. In the future, our present work can encourage the N-rGO@TiO_2 based future applications to remove Pb^{2+}, Hg^{2+}, and Cr (VI) ions from potable water.

Experimental

Materials

Graphite flakes (particle size 8 μm, 99.9995%) were gifted by Asbury Carbons, New Jersey, USA. All of the chemicals utilized in this present work were of analytical grade and applied as received without further purification. Green source, cotton-seed was collected from the cotton processing center, Shirpur (MS), India.

Synthesis of graphene oxide

Initially, GO was synthesized using a modified Hummers method followed by slight modification [56]. In brief, sulfuric acid (H_2SO_4) and phosphoric acid (H_3PO_4) in the ratio of 27 mL:3 mL were mixed properly followed by stirring for 15 min using a magnetic stirrer at 200 rpm. Subsequently, 0.225 g of graphite powder was added into the above mixture with constant stirring. After that, 1.32 g of potassium permanganate ($KMnO_4$) was added slowly into the previous graphite powder mixture followed by stirring up to 6 hrs until the color of the mixture became dark green. Then, hydrogen peroxide (H_2O_2, 0.675 mL) was dropped slowly followed by stirring for 10 min to eliminate the excess of $KMnO_4$. After completion of the reaction, the obtained mixture was cooled at room temperature. Furthermore, this mixture was purified three times by using hydrochloric acid (HCl) and DDW (1:3 ratio) and centrifuged using a cold centrifuge at 7000 rpm (for 20 min at 25 °C). Finally, the obtained product was dried at 60 °C for 24 h.

Synthesis of N-rGO@TiO_2 nanocomposite

Firstly, the following steps were implemented for the preparation of the N-rGO@TiO_2 nanocomposite. Initially, GO (75 mg) was dispersed into 10 mL of DDW followed by continuous stirring at room temperature (200 rpm). Then, sonication of nanocomposites was completed for 30 min. After that, the collected cotton seed powder (50 mg) was added into 50 mL of DDW and refluxed for 1 h. After that, the seed extract was filtered and further concentrated by centrifugation (7500 rpm for 30 min) using a cold centrifuge (Refrigerated Centrifuge, Elteck Overseas Pvt., India). The obtained concentrated filtrate was used for further phytochemical testing and the nanocomposite synthesis process. Simultaneously, TiO_2 dispersion was prepared by dispersing 50 mg TiO_2 into 10 mL DDW followed by sonication for 30 min. After that, cotton seed extract GO and TiO_2 dispersions were mixed (2:6:2) and heat on a water bath for 6 h (90 °C). Consequently, the obtained composite was freeze-dried using a laboratory freeze dryer (Freezone12, Labconco, MO, USA). The N-rGO@TiO_2 composite was

prefreezed at –30 °C for 12 h. After that, the primary drying of N-rGO@TiO_2 composites was performed at –53 °C and 0.016 mbar for 24 h. Then, the secondary drying of N-rGO@TiO_2 composites was performed at 10 °C for 8 h followed by drying at 25 °C for 4 h with a gradual increase in temperature at 1 °C/min. Finally, the temperature of the cold trap was maintained at –53 °C until the completion of the drying process. This resulted in N-rGO@TiO_2 composite powder was further used for subsequent evaluation studies.

Characterization of N-rGO@TiO_2 nanocomposite

The synthesized GO and N-rGO@TiO_2 nanocomposite was characterized by various spectroscopic techniques. Initially, the UV-visible spectra of GO and nanocomposite were recorded between 800-400 nm through UV 1800 spectrophotometer (Shimadzu, Japan) using a quartz cuvette. The functional groups of GO and N-rGO@TiO_2 nanocomposites were examined using an IR spectrophotometer (DRS 8000 IR spectrophotometer Shimadzu 8400s, Japan) and scanned over a wave range of 4000-400 cm^{-1}. The morphology and elemental analysis of GO and N-rGO@TiO_2 nanocomposite were examined under a scanning electron microscope (SEM) with 15 kV acceleration voltage and interpretation was carried out on Bruker, 1530-2 FESEM/EDX, Germany. The particle size analysis, as well as zeta potential of synthesized GO and N-rGO@TiO_2 nanocomposite, were measured using Nanoplus 3 Particulate System (Micromeritics, USA). Composite shape, size, were analyzed by using High-Resolution Transmission Electron Microscope (HR-TEM, Jeol/JEM 2100) using the LaB6 light source at 200 kV.

Spectroscopic sensing of heavy metal ions by N-rGO@TiO_2 nanocomposite

Sensing of Pb^{2+} by N-rGO@TiO_2 nanocomposites

The selective detection of Pb^{2+} was performed by UV visible spectroscopic method. Typically, a stock solution of 1 mM lead (II) chloride ($PbCl_2$) in water was prepared in DDW. After that, 1 mL of 10 nM, 25 nM, 50 nM, 250 nM, 500 nM, 1000 nM, 2500 nM, 5×10^3 nM, 75×10^2 nM and 1×10^4 nM concentrations of Pb^{2+} were added into separate vials. Simultaneously, N-rGO@TiO_2 nanocomposite solution (1 mg/mL) was prepared in DDW. Then, 2 mL of N-rGO@TiO_2 nanocomposite solution was added above different test tubes. Similarly, the real-time sensing of the Pb^{2+} in spiked sample was performed using N-rGO@TiO_2 nanocomposites. In that, 100 nM concentration of Pb^{2+} was added into vials containing 2 mL of N-rGO@TiO_2 nanocomposite. After thorough shaking, the color change in the test tube solution was observed by the naked eye followed by a recording of UV-Vis absorption spectra from 800-200 nm.

Sensing of Hg^{2+} by N-rGO@TiO_2 nanocomposites

The absorption spectra of the N-rGO@TiO_2 nanocomposite were recorded by adding different concentrations of Hg^{2+}. In brief, the different concentration (10 μM, 15 μM, 50 μM, 100 μM, 250 μM, 500 μM, 1000 μM) of $HgCl_2$ were prepared. Then, 1 mL of this solution was added into 2 mL of N-rGO@TiO_2 nanocomposite solution followed by shaking and subjected to 2 min as a resting time. The changes in the N-rGO@TiO_2 nanocomposite absorbance band with the addition of diverse concentrations of Hg^{2+} were monitored by recording absorption spectra from 800 nm-200 nm. For detection, the different Hg^{2+} concentrations were added separately into the N-rGO@TiO_2 nanocomposite solution followed by mixing and allowed to rest. Finally, real-time sensing of Hg^{2+} was performed in a spiked sample using N-rGO@TiO_2 nanocomposites. In that, 75 μM concentration of Hg^{2+} was added into vials containing 2mL of N-rGO@TiO_2 nanocomposite. The color changes in vials were observed with the naked eye followed by a recording of UV-Vis absorption spectra from 800-200 nm.

Sensing of Cr (VI) by N-rGO@TiO_2 nanocomposites

The detection of Cr (VI) was performed using N-rGO@TiO_2 through UV visible spectroscopic method. Firstly, the stock solution of 1 mM $K_2Cr_2O_7$ was prepared in DDW. Simultaneously, N-rGO@TiO_2 nanocomposites solution (1 mg/mL) was prepared in DDW. Herein, 1 mL of 10 nM, 25 nM, 50 nM, 250 nM, 500 nM, 2500 nM, 5×10^3 nM, 75×10^2 nM, and 1×10^4 nM were added in separate vials. Then, 2 mL of N-rGO@TiO_2 nanocomposites solution was added into previously prepared vials. Real-time sensing of Cr (VI) in a spiked sample was performed using N-rGO@TiO_2 nanocomposites. In that, 50 nM concentration of Cr (VI) was added into vials containing 2 mL of N-rGO@TiO_2 nanocomposite. After thorough shaking, the color changes in the solution were observed by recoding UV-Vis absorption spectra from 800 - 200 nm.

Results and Discussion

The phytoconstituents screening of cotton-seed extract was showed the presence of carbohydrates, proteins, amino acids, tannins, phenols, alkaloids, and flavonoids, etc [57]. Due to the presence of phytoconstituents, the green synthesis of rGO-based nanocomposites can be possible [58].

UV-vis absorption study

The UV absorption spectra of GO and N-rGO@TiO_2 nanocomposite are depicted in Fig. 1. In brief, Figure 1A demonstrates that the GO dispersion exhibited an intense absorption peak at 232 nm (λ_{max}) which corresponds to π-π* transitions of an aromatic ring containing C-C bonds and slightly low intense shoulder peak at 300 nm due to graphene, n-π transitions of C-O bonds, respectively. Based on this, it confirmed the synthesis of GO. The UV Visible spectrum was conducted to investigate the optical absorption capability of the N-rGO@TiO_2 nanocomposite, as shown in Fig. 1. The TiO_2 dispersion exhibited the characteristic absorption at around 350 nm in the UV region. However, a gradual red-shift to longer wavelengths was observed for the N-rGO@TiO_2 nanocomposite fabricated using the one-pot method. The red-shift absorption was attributed due to the construction of the Ti-O-C bond, which reduces the band-gap energy of the N-rGO@TiO_2 nanocomposites. On the other hand, it gets hybridized with O 2p and C 2p atomic orbital under high pressure and temperature. Also, the introduction of 'N' into the graphene nanosheet resulted in the high absorption intensity as compared to the plain TiO_2 [59]. So, it confirmed that the shift in the absorption in the UV-Vis range of N-rGO@TiO_2 is due to N-doping.

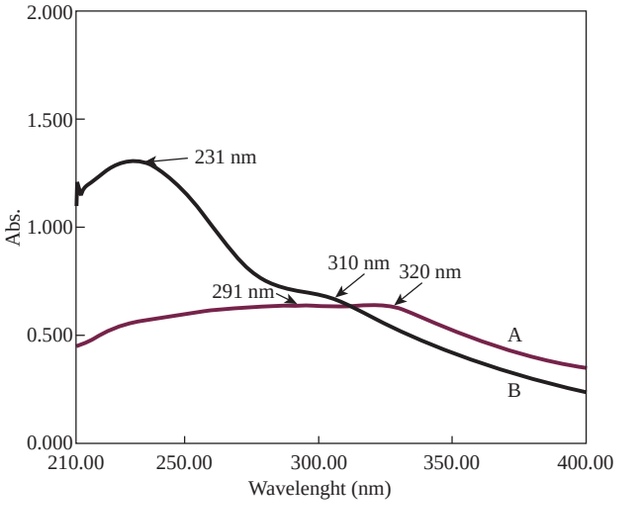

Fig. 1 UV visible spectra of **(a)** GO and **(b)** N-rGO@TiO_2 nanocomposite.

FTIR analysis

FTIR analysis GO and N-rGO@TiO_2 are depicted in Fig. 2. Figure 2A shows a broad-band around 3300 cm^{-1} that confirmed the stretching vibrations of O-H groups in GO. The various prominent vibrational bands (cm^{-1}) for GO were observed at ~2900 cm^{-1}, 2800 cm^{-1}, 1730 cm^{-1}, 1400 cm^{-1}, 1200 cm^{-1}, and 1030 cm^{-1}, which have been assigned to symmetrical C-H stretching, unsymmetrical C-H stretching, C=O stretching, O-H bending, C-O-C stretching and C-O stretching, respectively [60]. Therefore, we conclude that the flourishing synthesis of GO. Figure 2B confirmed that the FTIR spectrum of N-rGO@TiO_2 nanocomposite shows a band at ~3561 cm^{-1}, 3120 cm^{-1}, 2947 cm^{-1} that confirmed the N-H stretching vibrations, O-H stretching, C-H stretching, respectively. Furthermore, the peaks at 1670 cm^{-1} and 1556 cm^{-1} which are correspond to the C=N and C=O stretching and vibration mode. The peak corresponds to C=O stretching, vibration in GO was decreased due to the reduction of oxygen functionalities. The peak at 1228 cm^{-1} and 1041 cm^{-1} was observed due to C-O stretching vibration. Two peaks were also observed for Ti-O-C and Ti-O-Ti at 673 cm^{-1} and 497 cm^{-1}, respectively [61]. It may due to the interaction of TiO_2 with rGO sheets. Therefore, based on the FTIR, we conclude that the synthesis of N-rGO@TiO_2 nanocomposite. Herein, FTIR spectra of GO confirmed that the presence of oxygen functionalities such as –COOH, –OH, etc. when TiO_2 nanoparticles mixed with GO, the nanoparticle get fixed on the surface of the GO sheet due to the bonding between TiO_2 and GO that form the new bonds such as –COO–. After

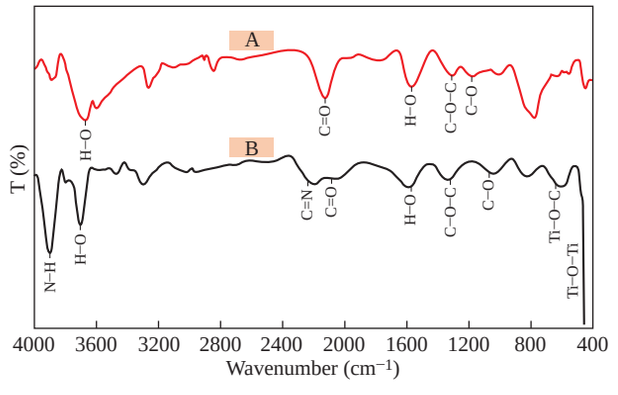

Fig. 2 IR spectra of **(a)** GO and **(b)** N-rGO@TiO_2 nanocomposites.

the successful reduction of GO in nanocomposites, the free nanoparticles are entrapped into the 3 D structure of nanocomposites via physical entrapment. Finally, it gives the 3D self assemble nanosized, stable hydrogel [62].

Scanning electron microscopy and high-resolution transmission electron microscopy

Generally, the SEM is used to confirm the surface morphology of materials. Based on this, it facilitates the verification of synthesis of nanocomposites. Herein, Figure 3(a) and Figure 3(b) shows a wrinkled and typical crumpled surface. Also, the sheets are stacked together and form a typical multi-layer structure of GO. Normally, the wrinkled arrangement of GO sheets offers a great rough surface. Besides, due to such unique nature of GO sheets, it offers more surface for doping of heteroatoms [61]. Figure 3(c) and Figure 3(d) show the SEM images of the N-rGO@TiO_2 nanocomposite that confirms the surface morphological microstructures of the N-rGO@TiO_2 nanocomposite. As per Figure 1A and B, the GO sheets show wrinkled and folded form, whereas nanocomposites showed cross-linking of TiO_2 nanoparticles on the surface of the GO sheet that formed the network structures in N-rGO@TiO_2 nanocomposite. The HR-TEM image of the N-rGO@TiO_2 nanocomposite is shown in Fig. 3(e). The TEM analysis demonstrates that the spherical shapes TiO_2 nanoparticles are distributed and attached on the surface of the rGO sheet. The size distribution of TiO_2 nanoparticles in N-rGO@TiO_2 nanocomposite was found to be 42 nm to 115 nm. Besides this, the anchoring of TiO_2 was found on the sheet of the rGO, it might because of the chemical bonding and physical entrapment of nanoparticles into the mixture of graphene. The morphology of 'N' doped nanocomposite showed the stacked layer of graphene thin layers that resulted in the multilayered graphene nanosheet. Notably, the curled edge and fold appearance in nanocomposite was credited to the defect structure, which may be caused due to the 'N' doped graphene sheet [59]. Overall, the SEM and HRTEM images confirmed the rough surface of the N-rGO@TiO_2 nanocomposite. It may because of the attachment of TiO_2 nanoparticles on the stable dispersion of the nanosized rGO sheet. The formation of nanocomposites meant that the restored conjugated arrangement of GO sheets reduces and functionalized using CSE in an aqueous medium. Overall, it indicates partial overlapping and aggregation of flexible GO sheets via π-π stacking interaction resulted in 3D graphene porous network. During the synthesis of the nanocomposite, the GO containing oxygen functional groups might be notably reduced during synthesis process. Interestingly, the π-π intrinsic interaction between rGO is slowly restored in nanocomposites. Furthermore, the slight overlapping and coalescing of flexible nanosized rGO converted into the 3D porous nanostructure. During the synthesis of the composite, the nanoparticle completely decorates the rGO

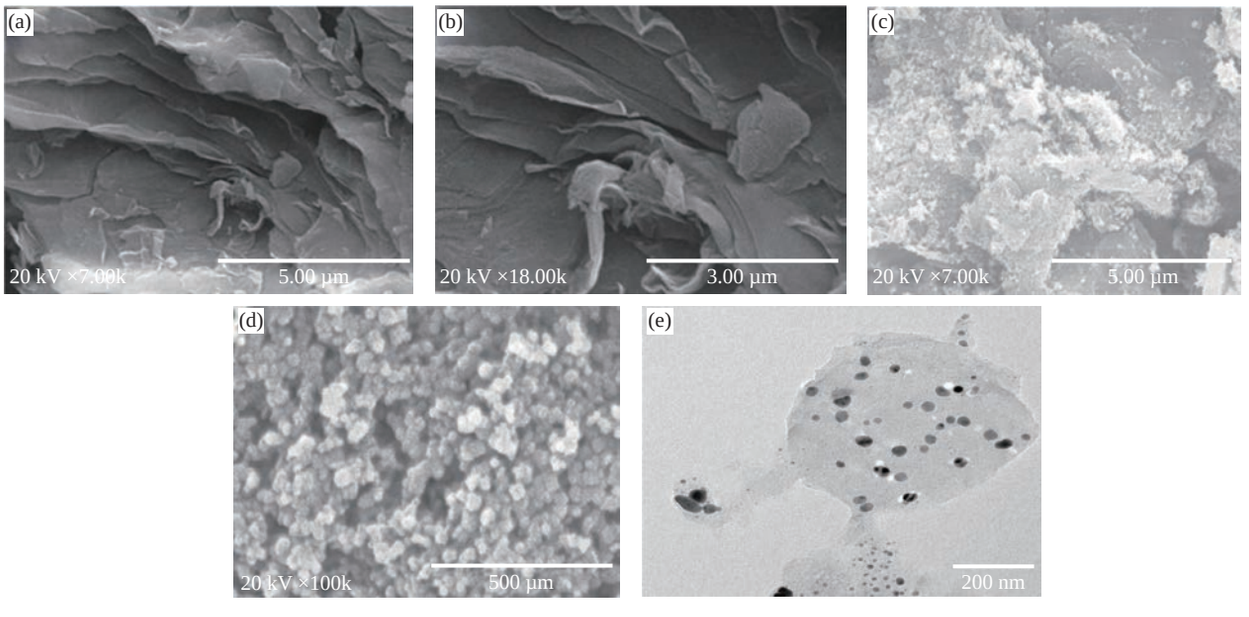

Fig. 3 The SEM images of **(a)** and **(b)** GO, and **(c)** and **(d)** N-rGO@TiO_2 nanocomposites; the HRTEM image of **(e)** N-rGO@TiO_2 nanocomposite.

sheets. It helps to avoid the aggregations of graphene nanosheets. Automatically, it improves the volume and surface areas of nanocomposites. Fascinatingly, TiO_2 nanoparticles also provide the bridge to connect the RGO nanosheets via chemical bonding, and finally, it is converted into the pores with smaller size. Simultaneously, π-π intrinsic conjugation gets weakened in rGO and it provides a high quantity of TiO_2 anchoring on the surface of 3D graphene sheet [63].

Elemental analysis by EDAX

The elemental composition of nanocomposites plays an important role for to achieve the highly sensitive detection of the analyte. In this context, the EDAX provides the details of elements present in the composition. In this report, Figure 4(a) demonstrates the EDX spectra of GO, which confirmed the presence of carbon (C) and oxygen (O) at about 34.31 wt% and 64.69 wt%, respectively. As per literature, the presence of 'O' confirmed the different 'O' functionalities are present on the surface of the GO sheet. It provides the bonding among different metal ions, which helps to sense the interest analyte. Besides, it also acts as an intermediate for nanocomposite synthesis. The doping of 'N' in nanocomposite can confirm based on the percent composition of 'N' present in the final formulation. In this report, Figure 4(b) provides the EDAX spectrum of N-rGO@TiO_2 nanocomposites. In brief, EDAX spectra of N-rGO@TiO_2 confirmed that the 1.45 wt% of 'N' and 43.77 wt% of 'C' were present in the nanocomposite. The analysis of EDAX spectra showed a significant decrease in 'O' about 38 wt%. It may due to the doping of 'N' on the GO sheets. Furthermore, the content of 'Ti' was found to be 16.78 wt%. Therefore, based on the existing elements such as N, C, O, Ti, confirmed the complete formation of N-rGO@TiO_2 nanocomposite.

Particle size and zeta potential analysis

Particle size analysis is performed to confirm the distribution (or average diameters) of nanomaterials, whereas zeta potential provides the information about the stability of nanocomposite. Figure 5(a) demonstrates the particle size distribution of synthesized GO. Herein, the average diameter of GO was found to be 81.2 nm (Figure 5(a)). The polydispersity index of GO dispersion was found to 0.42, which confirmed the uniform distribution of GO nanosized sheets in dispersion. The zeta potential

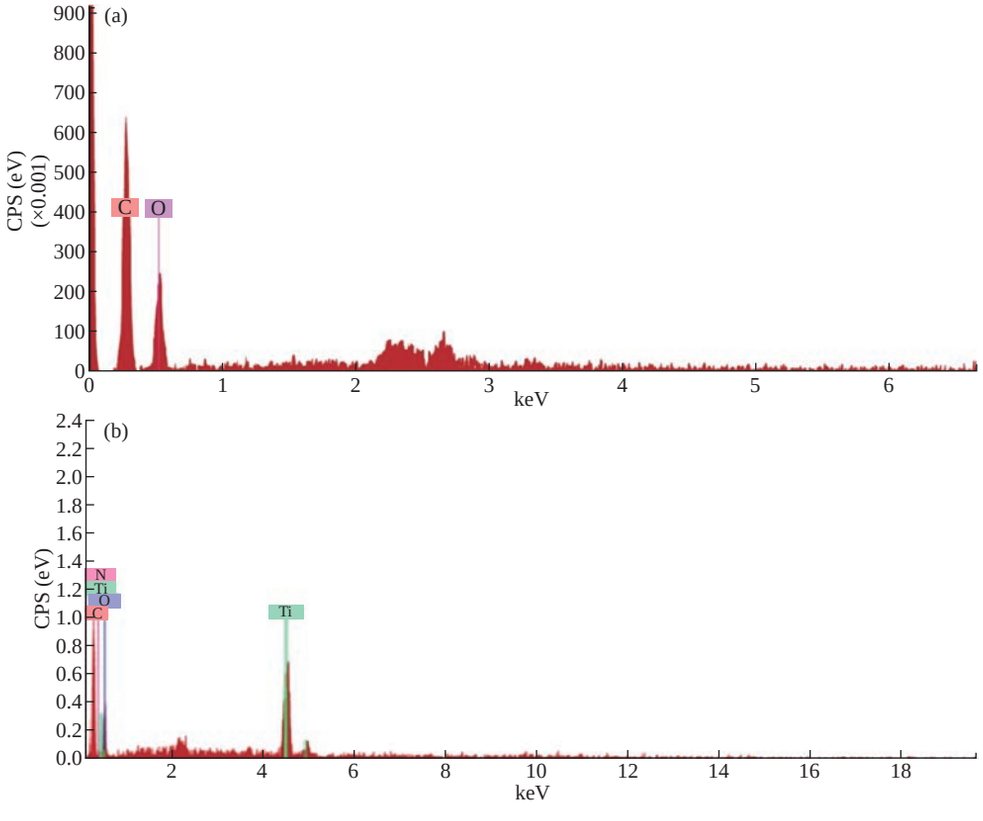

Fig. 4 EDX spectra of **(a)** GO and **(b)** N-rGO@TiO_2 nanocomposites.

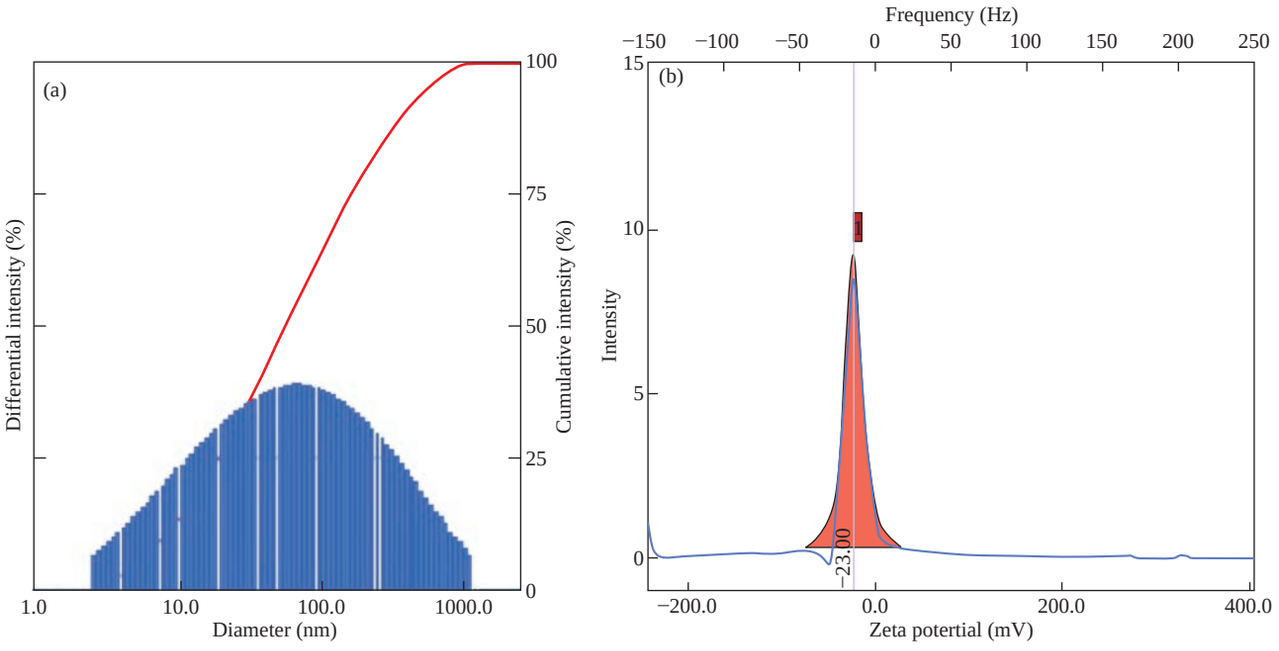

Fig. 5 (a) Particle size and **(b)** zeta potential of GO.

analysis of GO dispersion was found to be -23.00 mV (Figure 5(b)). Therefore, it confirmed the uniform distribution and stability of nanosized GO sheets in dispersion. Figure 6(a) provides the particle size distribution of the N-rGO@TiO_2 nanocomposite. The average particle size of the N-rGO@TiO_2 nanocomposite was found to be 357.6 nm that assured the synthesis of the N doped nanosized composite. The polydispersity index of nanocomposite was found to be 0.51 that confirmed the uniform distribution of nanocomposite in water. The zeta potential analysis of N-rGO@TiO_2 is depicted in Fig. 6(b). The nanosized composites showed a positive zeta potential of about +29.55 mV, which confirmed the stability of the nanocomposite and successful doping of N into the rGO sheet. Overall, based on these findings, it confirmed that the N-rGO@TiO_2 composite exhibited the nanosized distribution and high stability in dispersion.

Spectroscopic sensing of Pb^{2+}, Hg^{2+}, and Cr (VI) by N-rGO@TiO_2 nanocomposites

In this study, the synthesized N-rGO@TiO_2 nanocomposite was checked for the spectral as well as optical detection of the above mentioned heavy metal

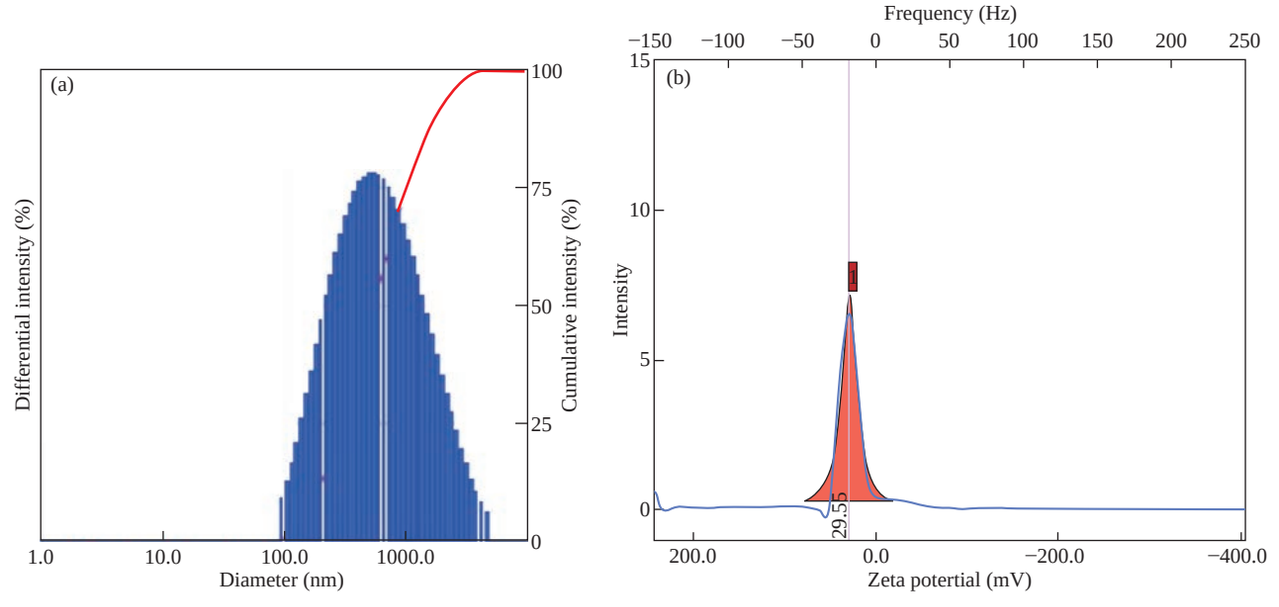

Fig. 6 (a) Particle size and **(b)** zeta potential of N-rGO@TiO_2 nanocomposite.

ions. The details of the sensing study are discussed in the respective subsection.

Sensing of Pb^{2+}

The synthesized N-rGO@TiO_2 nanocomposite was tested for the spectral and optical detection of Pb^{2+} ions. In brief, the detection of Pb^{2+} ions by N-rGO@TiO_2 nanocomposite revealed that the UV-visible spectra absorption peaks decreased with an increasing concentration of Pb^{2+} ions are shown in Fig. 7. The changes in the UV spectra of the N-rGO@TiO_2 nanocomposite solution help to calculate the nM concentration of Pb^{2+} ions (r^2 = 0.0074x + 0.08). In this study, nanocomposites intensity dramatically decreased with an increasing amount of Pb^{2+} ions. The sudden change was observed at 50 nM concentration. Therefore, the detection limit of Pb^{2+} was found to be 50 nM. After the addition of 1×10^4 nM concentration of Pb^{2+} ions into the N-rGO@TiO_2 composite solution, the characteristic peak completely disappeared. It may due to the loss of characteristic properties of nano-region after the strong aggregation of N-rGO@TiO_2 aerogel at this high concentration of Pb^{2+}. The spiked sample analysis was showed the 100 nM concentration of Pb^{2+} in the waste-water. Overall, upon addition of Pb^{2+} ions in the N-rGO@TiO_2 solution turned colorless that induced by aggregation of N-rGO@TiO_2 aerogel, which was detected visually and also confirmed by UV spectroscopy.

Sensing of Hg^{2+}

The N-rGO@TiO_2 nanocomposite was tested for the spectroscopic determination of Hg^{2+}. Because of the formation of an intense UV absorption band of N-rGO@TiO_2 nanocomposite, it is much straightforward to monitor changes in the UV absorption band during the determination of Hg^{2+} (Fig. 8). A significant decrease in the absorption peak with a red-shift on the UV band of the N-rGO@TiO_2 nanocomposite was observed upon increasing the concentration of Hg^{2+} ions. Thus, the Hg^{2+} with a concentration of 15 μM was taken as a limit of detection for N-rGO@TiO_2 nanocomposite (r^2 = 0.022x + 0.09). After the addition of 1000 μM concentration of Hg^{2+} into the nanocomposite, the UV absorption peak was completely disappeared. The spiked sample analysis confirmed the presence of 75 μM Hg^{2+} ions in the wastewater. The red-shift and significant decrease in the absorption peak intensity were caused due to the redox interaction between the Hg^{2+} ions and the N-rGO@TiO_2 nanocomposite. The red-shift in the UV absorption band can be attributed to the adsorption of Hg^{2+} onto the N-rGO@TiO_2 nanocomposite surface and thereby formed a combination. Finally, the addition of Hg^{2+}, N-rGO@TiO_2 nanocomposite was turned colorless.

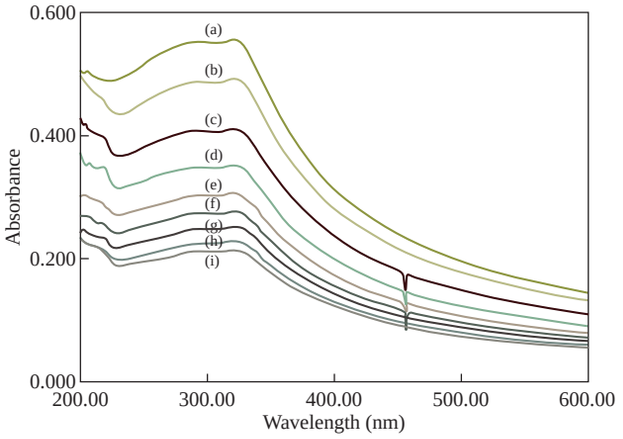

Fig. 7 Spectroscopic sensing of Pb^{2+} by N-rGO@TiO_2 nanocomposite: **(a)** 0 nM, **(b)** 50 nM, **(c)** spiked sample (100 nM), **(d)** 250 nM, **(e)** 500 nM, **(f)** 1000 nM, **(g)** 2500 nM, **(h)** 5×10^3 nM, and **(i)** 75×10^2 nM of $PbCl_2$ with N-rGO@TiO_2 nanocomposite.

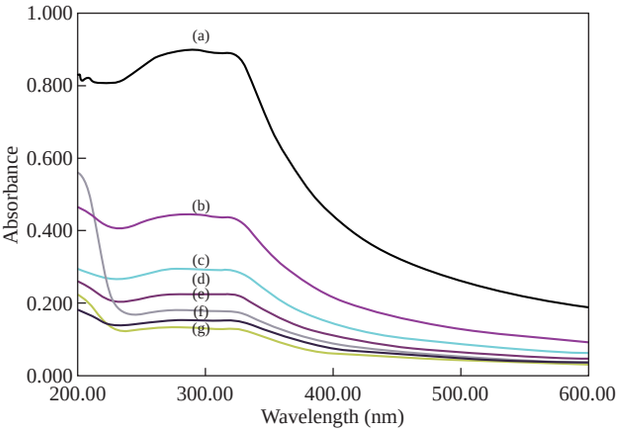

Fig. 8 UV absorption spectral changes observed for N-rGO@TiO_2 nanocomposite upon the addition of Hg^{2+}ions: **(a)** 0 μM, **(b)** 15 μM, **(c)** 50 μM, **(d)** 75 μM, **(e)** 100 μM, **(f)** 250 μM, and **(g)** 500 μM of Hg^{2+}ions with N-rGO@TiO_2 nanocomposite.

Sensing of Cr (VI)

The detection of Cr (VI) ion by the N-rGO@TiO_2 nanocomposite was performed by the UV spectroscopically. Figure 9 shows the UV absorption spectra of N-rGO@TiO_2 nanocomposite get increased with a decreased the concentration of Cr (VI) ions. It means the intensity of the UV absorption peak of the N-rGO@TiO_2 nanocomposite is inversely proportional to the concentration of Cr (VI). Finally, the peak that disappeared was at the highest concentration of Cr

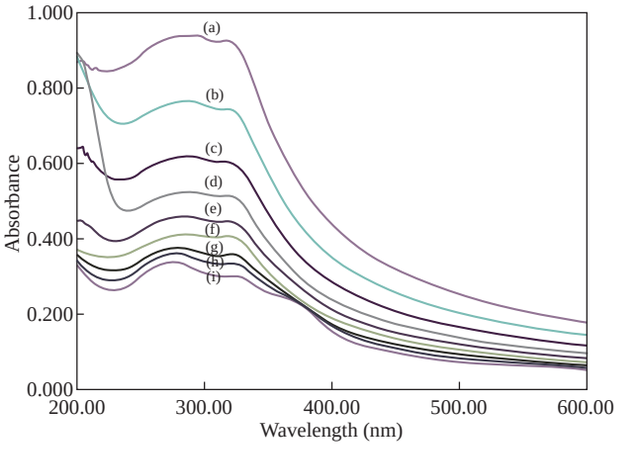

Fig. 9 Spectroscopic sensing of Cr (VI) using N-rGO@TiO_2 nanocomposites: **(a)** 0 nM, **(b)** 25 nM, **(c)** spiked sample (50 nM), **(d)** 100 nM, **(e)** 250 nM, **(f)** 500 nM, **(g)** 2500 nM, **(h)** 5×10^3 nM, and **(i)** 75×10^2 nM of $K_2Cr_2O_7$ solution with N-rGO@TiO_2 nanocomposite.

(VI) ions. The change in the UV spectra of N-rGO@TiO_2 nanocomposite occurs at 25 nM concentration of Cr (VI) ions. It exhibited a prominent peak at 283 nm (r^2 = 0.0014x + 0.05). The intensity of this peak was significantly decreased with increasing concentration of Cr (VI). The sudden changes of the peak at 25 nM concentration of Cr (VI) were considered as a limit of detection. After the addition of 1×10^4 nM concentration of Cr (VI) ions into the N-rGO@TiO_2 nanocomposite solution, the characteristic UV absorption peak was completely disappeared. The spiked sample analysis showed the 50 nM concentration of Cr (VI) was present in the wastewater. Overall, due to the strong adsorption of Cr (VI) on the N-rGO@TiO_2 nanocomposite, it provides excellent sensing ability. Finally, the addition of Cr (VI) ion in the solution of N-rGO@TiO_2 nanocomposite was turned colorless, which can be determined visually and can be confirmed by UV spectroscopy.

As per the literature, the addition of TiO_2 nanoparticles in graphene-based materials enhances the catalytic activity of nanoparticles. It may due to the high surface area and electron mobility of graphene. Moreover, it showed a high affinity towards the interest analyte. In addition, it provides a higher charge separation as well as higher charge transport potential. The main sensing mechanism of this nanocomposite is still unknown, but several possible mechanisms have been reported by previously published literature. In brief, the addition of rGO helps to the adsorption of heavy metals on the surface of nanocomposites via strong electrostatic interaction plus π-π stacking. Concisely, the graphene-based nanocomposite containing π domains is the major part of the driving force to the sensing of heavy metal ions. Furthermore, the synthesized nanocomposites were in 3D form. Owing to the 3D structure, it offers a high surface area and a more porous nature as compared to the 2D materials. It may provide the higher binding sites for sensing of heavy metals [63]. Notable, the N contains the same atomic radius as graphene containing carbon. Due to the same atomic radius of 'N', it can be easily doped into carbon grid nanocomposites. Accordingly, the efficient doping of 'N' into nanocomposites also helps to improve the sensing ability and that resulted in the lowest detection limit for heavy metal ions. Also, it improves the stability and magnetic properties of graphene nanocomposites [64]. In addition to that, the N doped graphene nanocomposites provide a higher surface area and subsequently provide more site for adsorption of heavy metal ions on the surface of nanocomposites. The combination of TiO_2 and graphene followed by 'N' doping resulted in high electron mobility of the catalyst plus a larger specific surface area. This also helps to absorb and degrade the analyte [59]. Overall, the synthesized 3D, porous N-rGO@TiO_2 nanocomposites demonstrate good sensing ability and excellent performance, which are much essential in the protection of the ecosystem.

Conclusions

In summary, the green synthesis of N-rGO@TiO_2 nanocomposite is a single-step, facile, economical and less time-consuming method. The *Gossypium hirsutum* seeds are a good source of 'N' containing amino acid and proteins, which provide the N doping. They also reduce the Go and stabilize the nanocomposites. Concisely, the reported method simultaneously resulted in the eco-friendly synthesis of the N-rGO@TiO_2 nanocomposite. This nanocomposite accomplished an exceptional probe for the detection of Pb^{2+}, $Hg^{2+,}$ and Cr (VI) with 50 nM, 15 µM and 25 nM lower detection limits, respectively. In addition, the analysis of heavy metals (Pb^{2+}, Hg^{2+}, Cr (VI)) in spiked samples using synthesized N-rGO@TiO_2 nanocomposites provided an excellent result. Besides, the application of a simple spectroscopic method with eco-friendly nanocomposites can provide an alternative cost-effective tool to conventional and expensive methods for heavy metal detection in water. Overall, the findings of these investigations confirmed that the N-rGO@TiO_2 nanocomposite exhibited better Pb^{2+}, Hg^{2+} and Cr

(VI) sensing ability in water through the spectroscopic method. In the future, these nanocomposites could provide better environmental remediation.

Acknowledgments

The authors are thankful to Kavayitri Bahinabai Chaudhari North Maharashtra University (KBCNMU), Jalgaon for providing funding through the Vice-Chancellor Research Motivation Scheme (VCRMS, NMU/HA/VCRMS/Budget-2016-17/ Pharmacy-10/84/2017).

Conflict of Interests

The authors declare that no competing interest exists.

References

[1] A.K. Geim, K.S. Novoselov, The rise of graphene. *Nature Materials*, 2007, 6: 183-191.

[2] Y. Kopelevich, P. Esquinazi, Graphene physics in graphite, *Advanced Materials*, 2007, 19: 4559-4563.

[3] R. Tade, S.N. Nangare, and P.O. Patil, Fundamental aspects of graphene and its biosensing applications. *Functional Composites and Structures*, 2021, 3: 012001.

[4] X. Li, X. Wang, L. Zhang, et al., Chemically derived, ultrasmooth graphene nanoribbon semiconductors. *Science*, 2008, 319: 1229-1232.

[5] C. Stampfer, E. Schurtenberger, F. Molitor, et. al., Tunable graphene single electron transistor. *Nano Letters*, 2008, 8: 2378-2383.

[6] D.A. Dikin, S. Stankovich, E.J. Zimney, et al., Preparation and characterization of graphene oxide paper. *Nature*, 2007, 448: 457-460.

[7] Y. Xu, K. Sheng, C. Li, et al., Self-assembled graphene hydrogel via a one-step hydrothermal process. *ACS Nano*, 2010, 4: 4324-4330.

[8] H. Bai, K. Sheng, P. Zhang, et al., Graphene oxide/ conducting polymer composite hydrogels. *Journal of Materials Chemistry*, 2011, 21: 18653-18658.

[9] Y. Xie, S. Xu, Z. Xu, et al., Interface-mediated extremely low thermal conductivity of graphene aerogel. *Carbon*, 2016, 98: 381-390.

[10] L. Xu, G. Xiao, C. Chen, et al., Superhydrophobic and superoleophilic graphene aerogel prepared by facile chemical reduction. *Journal of Materials Chemistry A*, 2015, 3: 7498-7504.

[11] M.A. Worsley, P.J. Pauzauskie, T.Y. Olson, et al., Synthesis of graphene aerogel with high electrical conductivity. *Journal of the American Chemical Society*, 2010, 132: 14067-14069.

[12] J.L. Vickery, A.J. Patil, and S. Mann, fabrication of graphene-polymer nanocomposites with higher-order three-dimensional architectures. *Advanced Materials*, 2009, 21: 2180-2184.

[13] W. Gao, L.B. Alemany, L. Ci, et al., New insights into the structure and reduction of graphite oxide. *Nature chemistry*, 2009, 1: 403-408.

[14] J. Liu, H. Bai, Y. Wang, et al., Self-assembling TiO_2 nanorods on large graphene oxide sheets at a two-phase interface and their anti-recombination in photocatalytic applications. *Advanced Functional Materials*, 2010, 20: 4175-4181.

[15] E. Gao, W. Wang, M. Shang, et al., Synthesis and enhanced photocatalytic performance of graphene-Bi_2WO_6 composite. *Physical Chemistry Chemical Physics*, 2011, 13: 2887-2893.

[16] Y.H. Ng, A. Iwase, A. Kudo, et al., Reducing graphene oxide on a visible-light $BiVO_4$ photocatalyst for an enhanced photoelectrochemical water splitting. *The Journal of Physical Chemistry Letters*, 2010, 1: 2607-2612.

[17] T. Ramanathan, A. Abdala, S. Stankovich, et al., Functionalized graphene sheets for polymer nanocomposites. *Nature Nanotechnology*, 2008, 3: 327-331.

[18] T. Szabó, O. Berkesi, P. Forgó, et al., Evolution of surface functional groups in a series of progressively oxidized graphite oxides. *Chemistry of Materials*, 2006, 18: 2740-2749.

[19] X. Li, H. Wang, J.T. Robinson, et al., Simultaneous nitrogen doping and reduction of graphene oxide. *Journal of the American Chemical Society*, 2009, 131: 15939-15944.

[20] F. Kim, L.J. Cote, and J. Huang, Graphene oxide: Surface activity and two−dimensional assembly. *Advanced Materials*, 2010, 22: 1954-1958.

[21] K.A. Mkhoyan, A.W. Contryman, J. Silcox, et al., Atomic and electronic structure of graphene-oxide. *Nano letters*, 2009, 9: 1058-1063.

[22] M. Agharkar, S. Kochrekar, S. Hidouri, et al., Trends in green reduction of graphene oxides, issues and challenges: A review. *Materials Research Bulletin*, 2014, 59: 323-328.

[23] S. Thakur, N. Karak, Alternative methods and nature-based reagents for the reduction of graphene oxide: A review. *Carbon*, 2015, 94: 224-242.

[24] J. Gao, F. Liu, Y. Liu, et al., Environment-friendly method to produce graphene that employs vitamin C and amino acid. *Chemistry of Materials*, 2010, 22: 2213-2218.

[25] Y. Wang, Z. Shi, and J. Yin, Facile synthesis of soluble graphene via a green reduction of graphene oxide in tea solution and its biocomposites. *ACS Applied Materials & Interfaces*, 2011, 3: 1127-1133.

[26] C. Zhu, S. Guo, Y. Fang, et al.,, Reducing sugar: new functional molecules for the green synthesis of graphene nanosheets, *ACS Nano*, 2010, 4: 2429-2437.

[27] P. Zhang, T. Tachikawa, M. Fujitsuka, et al., Efficient charge separation on 3D architectures of TiO_2 mesocrystals packed with a chemically exfoliated MoS_2 shell in synergetic hydrogen evolution. *Chemical Communications*, 2015, 51: 7187-7190.

[28] Y. Agrawal, G. Kedawat, P. Kumar, et al., High-performance stable field emission with ultralow turn on voltage from rGO conformal coated TiO_2 nanotubes 3D arrays. *Scientific Reports*, 2015, 5: 11612.

[29] A.L. Linsebigler, G. Lu, and J.T. Yates Jr, Photocatalysis on TiO_2 surfaces: principles, mechanisms, and selected results. *Chemical Reviews*, 1995, 95: 735-758.

[30] W. Han, C. Zang, Z. Huang, et al., Enhanced photocatalytic activities of three-dimensional graphene-based aerogel embedding TiO_2 nanoparticles and loading MoS_2 nanosheets as Co-catalyst. *International Journal of Hydrogen Energy*, 2014, 39: 19502-19512.

[31] F. Wu, W. Liu, J. Qiu, et al., Enhanced photocatalytic degradation and adsorption of methylene blue via TiO_2 nanocrystals supported on graphene-like bamboo charcoal. *Applied Surface Science*, 2015, 358: 425-435.

[32] L.L. Tan, W.J. Ong, S.P. Chai, et al., Visible-light-active

oxygen-rich TiO_2 decorated 2D graphene oxide with enhanced photocatalytic activity toward carbon dioxide reduction. *Applied Catalysis B: Environmental*, 2015, 179: 160-170.
[33] W. Yan, F. He, S. Gai, et al., A novel 3D structured reduced graphene oxide/TiO_2 composite: Synthesis and photocatalytic performance. *Journal of Materials Chemistry A*, 2014, 2: 3605-3612.
[34] W. Wang, J. Yu, Q. Xiang, et al., Enhanced photocatalytic activity of hierarchical macro/mesoporous TiO_2-graphene composites for photodegradation of acetone in air. Applied Catalysis b: Environmental, 2012, 119: 109-116.
[35] M. Aleksandrzak, P. Adamski, W. Kukułka, et al., Effect of graphene thickness on photocatalytic activity of TiO_2-graphene nanocomposites. *Applied Surface Science*, 2015, 331: 193-199.
[36] K. Fujisawa, R. Cruz-Silva, K.S. Yang, et al., Importance of open, heteroatom-decorated edges in chemically doped-graphene for supercapacitor applications. *Journal of Materials Chemistry A*, 2014, 2: 9532-9540.
[37] M. Khandelwal, A. Kumar, One-pot environmentally friendly amino acid mediated synthesis of N-doped graphene–silver nanocomposites with an enhanced multifunctional behavior. *Dalton Transactions*, 2016, 45: 5180-5195.
[38] K. Gong, F. Du, Z. Xia, et al., Nitrogen-doped carbon nanotube arrays with high electrocatalytic activity for oxygen reduction., *Science*, 2009, 323: 760-764.
[39] K.A. Kurak, A.B. Anderson, Nitrogen-treated graphite and oxygen electroreduction on pyridinic edge sites. *The Journal of Physical Chemistry C*, 2009, 113: 6730-6734.
[40] P.H. Matter, E. Wang, M. Arias, et al., Oxygen reduction reaction catalysts prepared from acetonitrile pyrolysis over alumina-supported metal particles. *The Journal of Physical Chemistry B*, 2006, 110: 18374-18384.
[41] P.H. Matter, L. Zhang, and U.S. Ozkan, The role of nanostructure in nitrogen-containing carbon catalysts for the oxygen reduction reaction. *Journal of Catalysis*, 2006, 239: 83-96.
[42] T. Iijima, K. Suzuki, Y. Matsuda, Electrodic characteristics of various carbon materials for lithium rechargeable batteries. *Synthetic Metals*, 1995, 73: 9-20.
[43] Y. Wu, S. Fang, and Y. Jiang, Carbon anode materials based on melamine resin. *Journal of Materials Chemistry*, 1998, 8: 2223-2227.
[44] F. Jaouen, M. Lefèvre, J.P. Dodelet, et al., Heat-treated Fe/N/C catalysts for O_2 electroreduction: Are active sites hosted in micropores? *The Journal of Physical Chemistry B*, 2006, 110: 5553-5558.
[45] S. Lim, H. Elim, X. Gao, et al., Electronic and optical properties of nitrogen-doped multiwalled carbon nanotubes. *Physical Review B*, 2006, 73: 045402.
[46] S. Glenis, A. Nelson, and M. Labes, Formation of nitrogen doped carbon during arc-discharge of carbon rods in the presence of pyrrole. *Journal of Applied Physics*, 1996, 80: 5404-5407.
[47] S. Lim, H. Elim, X. Gao, et al., Electronic and optical properties of nitrogen-doped multiwalled carbon nanotubes. *Physical Review B (Covering condensed matter and material physics)*, 2006, 73: 045402.
[48] L. Li, E. Liu, Y. Yang, et al., Nitrogen-containing carbons prepared from polyaniline as anode materials for lithium secondary batteries. *Materials Letters*, 2010, 64: 2115-2117.
[49] W.S. Hummers Jr, R.E. Offeman, Preparation of graphitic oxide. *Journal of the American Chemical Society*, 1958, 80: 1339-1339.
[50] Y. Wu, S. Fang, and Y. Jiang, Effects of nitrogen on the carbon anode of a lithium secondary battery. *Solid State Ionics*, 1999, 120: 117-123.
[51] A.M. Massadeh, A.W.O. El-Rjoob, and S.A. Gharaibeh, Analysis of selected heavy metals in tap water by inductively coupled plasma-optical emission spectrometry after pre-concentration using chelex-100 ion exchange resin. *Water, Air, & Soil Pollution*, 2020, 231: 1-14.
[52] A. Mahar, P. Wang, A. Ali, et al., Challenges and opportunities in the phytoremediation of heavy metals contaminated soils: A review. *Ecotoxicology and Environmental Safety*, 2016, 126: 111-121.
[53] R. Karkra, P. Kumar, B.K. Bansod, et al., Analysis of heavy metal ions in potable water using soft computing technique. *Procedia Computer Science*, 2016, 93: 988-994.
[54] M.B. Gumpu, S. Sethuraman, U.M. Krishnan, et al., A review on detection of heavy metal ions in water–an electrochemical approach. *Sensors and Actuators B: Chemical*, 2015, 213: 515-533.
[55] A. Odobašić, I. Šestan, and S. Begić, Biosensors for determination of heavy metals in waters. *Biosensors for Environmental Monitoring*, Intech Open, 2019.
[56] N. Zaaba, K. Foo, U. Hashim, et al.,Synthesis of graphene oxide using modified hummers method: Solvent influence. *Procedia Engineering*, 2017, 184: 469-477.
[57] R. Chandrashekhar, B. Ram, and N.L. Bhavani, Quantitative analysis of phytochemical compounds in the cotton (*Gossypium*) seed xetracts; an important iommercial crop plant. *Bulletin of Pure & Applied Sciences-Botany*, 2019, 38: 56-62.
[58] J.H. Patil, M.P. More, M.R. Mahajan, et al., Green synthesis of graphene based manocomposite for sensing of heavy metals. *Journal of Pharmaceutical and Biological Sciences*, 2019, 7: 56-62.
[59] J. Liu, K.Y. Chen, J. Wang, et al., Preparation and photocatalytic properties of N-doped graphene/TiO_2 composites. *Journal of Chemistry*, 2020, 2020: 2928189.
[60] S.R.B. Nazri, W.W. Liu, C.S. Khe, et al., Synthesis, characterization and study of graphene oxide. AIP Conference Proceedings, AIP Publishing LLC, Dec. 6, 2018, 2045:020033.
[61] S. Ida, P. Wilson, B. Neppolian, et al., Tuning the type of nitrogen on N-RGO supported on N-TiO_2 under ultrasonication/hydrothermal treatment for efficient hydrogen evolution–A mechanistic overview. *Ultrasonics Sonochemistry*, 2020, 64: 104866.
[62] Y. Li, J. Yang, S. Zheng, et al., One-pot synthesis of 3D TiO_2-reduced graphene oxide aerogels with superior adsorption capacity and enhanced visible-light photocatalytic performance. *Ceramics International*, 2016, 42: 19091-19096.
[63] X. Shi, J. Chen, and W. Wang, Effects of TiO_2 content on the microstructure, mechanical properties and photocatalytic activity of three dimensional TiO_2-Graphene composite prepared by hydrothermal reaction. *Materials Research Express*, 2016, 3: 075602.
[64] N.N. Malinga, A.L. Jarvis, Synthesis, characterization and magnetic properties of Ni, Co and FeCo nanoparticles on reduced graphene oxide for removal of Cr (VI). *Journal of Nanostructure in Chemistry*, 2020, 10: 55-68.

International Journal of Biological Macromolecules 175 (2021) 270–280

Contents lists available at ScienceDirect

International Journal of Biological Macromolecules

journal homepage: http://www.elsevier.com/locate/ijbiomac

Inhibitory kinetics and mechanism of pentacyclic triterpenoid from endophytic *Colletotrichum gigasporum* against pancreatic lipase

Ravindra Patil [a], Samadhan Patil [a], Vijay Maheshwari [b], Mohini Patil [a,*]

[a] Department of Microbiology and Biotechnology, R. C. Patel Arts, Commerce and Science College, Shirpur 425405, MS, India
[b] Department of Biochemistry, School of Life Sciences, North Maharashtra University, Jalgaon 425001, MS, India

ARTICLE INFO

Article history:
Received 21 December 2020
Received in revised form 4 February 2021
Accepted 4 February 2021
Available online 06 February 2021

Keywords:
Pentacyclic triterpenoids
Pancreatic lipase inhibitor
Colletotrichum gigasporum
Withania somnifera
Plasma triglyceride
Orlistat

ABSTRACT

The burden of obesity is increasing all over the world. Except for Orlistat, no effective anti-obesity drug is currently available. Therefore, a search for the new anti-obesity compound is need of time. This study demonstrates macromolecular interaction and inhibitory effect of pentacyclic triterpenoids (PTT) on pancreatic lipase (PL). In the present study PTTs from endophytic *Colletotrichum gigasporum* were found to show significant inhibitory activity against PL with IC_{50} of 16.62 ± 1.43 μg/mL. The PTT isolated through bioassay-guided isolation showed a dose-dependent ($R^2 = 0.915$) inhibition against porcine PL and the results were comparable with the standard (Orlistat). Based on inhibition kinetic data, the gradual increase in $K_{m\ (app)}$ with increasing PTT concentration indicated that the mode of interaction of PTT with PL was a competitive type, and it directly competed with the substrate (*p*NPB) for the active site of PL. *In vivo* studies in Wistar rats at the oral dose (100 mg/kg body weight) of PTT significantly decreased ($p < 0.05$) incremental plasma triglyceride levels as compared to group B and TG absorption was down-regulated up to 49.18% *vis a vis* group D animals. The isolated PTT was identified as lupeol based on chromatographic and spectral data. The endophytic isolate was identified as *Colletotrichum gigasporum* based on morphology and ITS gene sequencing. The present study indicated that PTT had the potential to be used as a natural PL inhibitor in the treatment of obesity and the isolated endophyte can be a valuable bioresource for it.

1. Introduction

Obesity has been a major health concern worldwide in recent decades. Excessive energy intake, physical inactivity, and low energy expenditure are important contributors leading to the accumulation of fat in the body. Diverse gastrointestinal lipases including pancreatic lipase (PL) play important role in lipid digestion. Among all, PL is the most important lipolytic enzyme in humans that carry out the hydrolysis and absorption of over 70% of total dietary fats [1]. Because of its key role in lipid metabolism, PL has been the key target for synthetic anti-obesity drugs including Orlistat. Several studies have been conducted in the search of potent PL inhibitors of synthetic and natural origin compounds in the past few decades [2].

However, prolonged application of synthetic drugs has various side effects such as liver toxicity, oily stools, fecal urgency, flatulence, and abdominal distention [3]. Therefore, there is a need to explore natural products for new, effective, and safe anti-obesity compounds.

Natural products from ethnomedicinal plants and microorganisms have provided effective therapeutic drugs and lead compounds for the treatment of many metabolic diseases. The World Health Organization (WHO) estimates that 80% of the people of developing countries rely on traditional medicines, mostly plant-derived drugs for their primary health needs. Several studies have demonstrated that natural products of plant and microbial origin hold the promise for new PL inhibitors with minimum adverse effects. For example, inhibitors like platycodin D from the fresh roots of *Platycodon grandiflorum* has shown potent PL Inhibitory potential in an *in vivo* study [4]. PL inhibitors with various scaffolds (such as flavonoids, panclicins, triterpenoids, phenolics, β-lactones, and triacylglycerol analogs) have been identified from microbial, plants, and marine sources [5].

Medicinal plants harbor a hidden treasure of diverse microbial communities- the endophytes in their internal tissues. Endophytes include both; fungi and bacteria but fungi being more ubiquitous, diverse, versatile, and widespread microorganisms that colonize the plants growing in various geo-climatic conditions [6]. The endophytic microflora of medicinal plants is a cheap source of diverse bioactive compounds with varied bioactivities [7]. Endophytes have the unique property that they can produce the same and rare secondary metabolites as their plant host. For example, the bark of *Terminalia arjuna* (Combretaceae), a widely studied Indian medicinal plant known for its antioxidant and cardioprotective role, was found to be rich in many

* Corresponding author.
E-mail address: mohini_rpatil@rediffmail.com (M. Patil).

https://doi.org/10.1016/j.ijbiomac.2021.02.036
0141-8130/

Research Article

Microbial transformation of crop residues into a nutritionally enriched substrate and its potential application in livestock feed

Ravindra H. Patil[1] · Mohini P. Patil[1] · Vijay L. Maheshwari[2]

Received: 30 November 2019 / Accepted: 22 May 2020

Abstract
Bioconversion of three different agro-residues (groundnut shells, pigeon pea husk and wheat straw) was studied using endophytic fungi with a view to increasing the nutritive value and to evaluate its feasibility as poultry feed. An endophytic fungal isolate obtained from *Celastrus paniculatus,* effectively biotransformed selected agro-residues in solid state fermentation. After 21 days incubation, isolate CPL-1significantly altered the nutritional values of all tested agro-residues. Cellulose, hemicellulose, and lignin content were significantly reduced ($P < 0.05$) whereas, total carbohydrates were significantly increased in the biotransformed waste as compared to untreated residues. Of the three agro-residues studied, the groundnut shells were found to have maximum carbohydrate content (13.92 ± 0.7 g/100 g) after the treatment. Similarly, the total crude protein and total nitrogen contents of the treated waste were also significantly improved ($P < 0.05$) as a function of treatment with the isolate CPL-1 with their highest contents (24.95 ± 1.4 and 15.53 ± 1.2 g/100 g, respectively) recorded in the treated groundnut shells. The isolate CPL-1 was identified as *Colletotrichum* spp. based on the morphology. The tannins and phytate contents were found to be significantly lower ($P < 0.05$) in the processed wastes. Application of treated agro-residues in poultry diets revealed that the biotransformed groundnut shells and pigeon pea waste can be added up to 20 and 10%, respectively to the commercial poultry diet used in the study without any adverse effects. The results showed that the treated residues of groundnut shells can be used as a partial substitute to the conventional poultry diets as they are rich in enzyme phytase and other nutrients and have good digestibility.

Keywords Bioconversion · Agro-residues · Endophytic fungi · Crude protein · Poultry diet

1 Introduction

Feed is the most important factor in the poultry business which constitutes around 70% of the total production cost [1]. A number of ingredients are used to formulate the poultry diet. It mainly uses maize and soybean meal as the carbon and protein source, respectively. Several countries use other grains such as wheat, sorghum, canola and sunflower meal as well as animal-derived protein ingredients like fish and meat meal [2]. Mineral supplements play a vital role in the development of poultry. Poultry, being the monogastric animal, cannot fully assimilate the inorganic supplements which are provided in the form of calcium and phosphorus supplements that includes dicalcium phosphate, rock phosphate and bone meal [3]. The increasing cost and decreasing feed production are the major hurdles in the progress of poultry industry in the developing countries. Moreover, diversion of food grains such as maize and sorghum from feed market to ethanol production has dramatically increased their cost globally [4, 5]. Therefore, there is the urgent need to use alternative feedstuffs and look into the possibilities of bioconversion of agro-residues into feed in a sustainable way. Globally, 140 billion metric tons of lignocellulose biomass

✉ Ravindra H. Patil, ravi_nmu@yahoo.co.in | [1]Department of Microbiology and Biotechnology, R. C. Patel Arts, Commerce and Science College, Shirpur 425405, India. [2]Department of Biochemistry, School of Life Sciences, North Maharashtra University, Jalgaon 425001, India.

Published online: 29 May 2020

Research Article

Green synthesis of silver nanoparticles using *Eulophia herbacea* (Lindl.) tuber extract and evaluation of its biological and catalytic activity

Jayashri S. Pawar[1] · Ravindra H. Patil[1]

Received: 11 September 2019 / Accepted: 4 December 2019

Abstract
The present work is a report on phytosynthesis of silver nanoparticles (AgNPs) carried out using an aqueous extract of the tuber of *Eulophia herbacea* Lindl. (Orchidaceae) and evaluation of its antimicrobial and catalytic potential. The extract efficiently reduced aqueous silver ions and generated stable and bioactive nanoparticles. The maximum reduction of $AgNO_3$ was achieved when 1 mM $AgNO_3$ was incubated with 2% w/v extract for 5 h. The biosynthesized AgNPs exhibited surface plasma resonance at 447 nm. The zeta potential was − 15 mV. Scanning electron microscopy study showed that the average particle size of the AgNPs was 11.70 ± 2.43 nm and that they were non-agglomerated. An Energy Dispersive X-ray study provided support for the presence of elemental silver. X-ray diffraction studies confirmed that the AgNPs were crystalline and had a face-centered cubic geometry. The AgNPs showed excellent antibacterial and antifungal activity against common human pathogens. This activity was comparable with that of standard antibiotics. The catalytic potential of the AgNPs was studied through the reduction of methylene blue and congo red. The results showed that the AgNPs synthesized using the present method are biologically and catalytically active.

Keywords *Eulophia herbacea* · Silver nanoparticles · Antimicrobial activity · Antifungal activity · Synergistic effect · Dye reduction

1 Introduction

There is growing interest in greener synthesis of metal nanoparticles. Plant extracts have been used for nanoparticles synthesis as the process involved is simple, eco-friendly and cost-effective. Moreover, this process is reproducible and easily scaled up [1]. In comparison with microbial synthesis, phytosynthesis is rapid. It does not require aseptic conditions, and it yields stable nanoparticles [2, 3].

Indian traditional systems of medicine recommend the use of medicinal and aromatic plants for curing various human illnesses. Plant extracts containing phytoconstituents are biologically and pharmacologically active. Plant metabolites are known to be excellent reducing and capping agents that can be used to synthesize nanoparticles effectively within a short time [4–6].

The tubers of *Curcuma longa* [4, 7], sweet potato [8], *Dioscorea bulbifera*, *Dioscorea batatas*, *Dioscorea oppositifolia*, etc. are rich with different reducing and capping agents that generate stable metal nanoparticles [9–11].

Silver is known for its antimicrobial and medicinal properties [12, 13]. However, the antimicrobial effect of silver ions and its salts is limited and of short duration. These limitations can be overcome by using silver nanoforms, which are inert, stable and act as antimicrobial agents effectively [9, 14, 15].

Numerous mechanisms are involved in the microbicidal effect of silver nanoparticles (AgNPs) [16]: (a) AgNPs produce structural changes in the cell membrane by deposition on it

✉ Ravindra H. Patil, ravi_nmu@yahoo.co.in; Jayashri S. Pawar, jayashripatil59@gmail.com | [1]Department of Microbiology and Biotechnology, R. C. Patel Arts, Commerce and Science College, District Dhule, Shirpur, Maharashtra 425 405, India.

Published online: 09 December 2019

Journal Homepage: -www.journalijar.com

INTERNATIONAL JOURNAL OF ADVANCED RESEARCH (IJAR)

Article DOI:10.21474/IJAR01/12762
DOI URL: http://dx.doi.org/10.21474/IJAR01/12762

RESEARCH ARTICLE

SYNTHESIS AND CHARACTERIZATION STUDY OF HgXCr2-X S4 COMPOSITE THIN FILMS PREPARED BY CHEMICAL BATH DEPOSITION TECHNIQUE

Harishchandra B. Patil[1], Rajendrakumar B. Ahirrao[2] and Vijay N. Pawar[3]

1. Assistant Professor, P. G. Physics Depertment, R.C. Patel College, Shirpur, Maharashtra, India.
2. Assistant Professor, Physics Department, Uttamrao Patil College, Dahiwel, Maharashtra, India.
3. Associate Professor, Physics Department, Sidharth College, Fort, Mumbai, Maharashtra, India.

Manuscript Info

Manuscript History
Received: 20 February 2021
Final Accepted: 24 March 2021
Published: April 2021

Key words:-
CBD, X-Ray Diffraction, Scanning Electron Microscopy, Optical Properties, Electrical Properties

Abstract

The ternary thin films of composite $Hg_xCr_{2-x}S_4$ (x = 0.6) have been deposited by simple chemical bath deposition (CBD) technique on glass substrate. The thin films have been deposited at optimized conditions pH at 10 ± 0.1, bath temperature 65^0C, deposition time 120 minutes. The films were uniform and adherent to glass substrates. They were characterized by structural, optical, and electrical measurement techniques. According to their X-ray diffraction patterns $Hg_xCr_{2-x}S_4$(x = 0.6) films are crystalline with band gap of 2.4 eV. Scanning electron micrographs showed that the substrates were well covered with films; no cracks or pinholes were observed. The electrical resistivity of the films is found to be 1.3703 x 10^3 Ω-cm to 2.1243 x 10^3 Ω-cm at temperature range 303^0k to 423^0K. According to thermoelectric power measurements $Hg_xCr_{2-x}S_4$(x = 0.6) thin films are of n-type nature.

Introduction:-

The nanocrystalline $Hg_xCr_{2-x}S_4$(x = 0.6) (HGS) thin films, have been of interest due their semiconducting nature and considerable application in the field of electronics and electro-optical devices [1,2] magneto-optical devices and in magnetocapacitive as well as magnetoelectric devices [3-11]. Based on this concept, intensive research has been performed in the past to study the synthesis and characterization of these thin films. The characteristics of these films provides an overview of several capabilities based on photon, electron, and ion methods that can be effectively used to understand the structural, chemical, and electronic characteristics of a wide range of materials. The type or types of information required determines the characterization methods needed to investigate thin film. XRD is an excellent technique for studying thin films with a crystalline structure, such as those composed of inorganic/solid-state materials. XRD is a technique used to determine the crystalline structure and atomic spacing of a thin film, and the produced spectral pattern is compared against known references. XRD fires collimated X-rays at a crystalline sample, and the light becomes diffracted according to Braggs law by the crystal planes within the thin film. The X-rays are produced by a cathode source and are monochromated. Upon hitting the planes of the thin film, constructive interference is created, causing the sample to be scanned through an angle of 2θ and allowing all of the dimensions of the film to be observed is a tool used to characterize the morphology and composition of thin films. Electrons are fired from an electron gun and pass through the thin film. The energies of the electrons are concentrated and focused on using a series of lenses. The electron beam then passes through a pair of scanning coils and deflector plates in the final lens. After the electrons are focused, they are then directed towards the thin film. When the electrons interact with the sample, their energy diminishes due to scattering and absorption. The exchange of energy between the

Corresponding Author:- Harishchandra B. Patil
Address:- Assistant Professor, P. G. Physics Depertment, R.C. Patel College, Shirpur, Maharashtra, India.

electrons and the sample causes high energy electrons to reflect through elastic scattering. Secondary electrons are also released by inelastic scattering and the emission of electromagnetic radiation, both of which are detected. The image is a distribution of the signal intensity, which is digitally captured and allows for the structure of the thin film to be determined. The doping of nanocrystalline semiconductors with trivalent magnetic material Cr^{3+} results in new optical, electrical and structural properties. Mercury chromium sulfide is a metal chalcogenide semiconductor of the group II-VI semiconductors having an insulating and high density with excellent structure [12-13]. The chromium (III) is quite stable against oxidation in sulfides, removing mercury from the material remains a significant challenge [14]. The formation of solid phase from a solution involves two steps as nucleation and particle growth. The size of particles of a solid phase is independent upon the relative rates at which these two competing processes take place. For any precipitate, there is some minimum number of the ions or molecules required to produce a stable phase in contact with a solution, called as nucleus. The formation of nucleation is necessary for a precipitate formation. The concept of nucleation in solution is that the clusters of molecules formed undergo rapid decomposition and particles combine to grow up to a certain thickness of the film. Depending upon deposition conditions such as bath temperature, stirring rate, pH, solution concentration etc. the film growth can take place by ion-by-ion condensation of materials or by adsorption of colloidal particles from the solution on the substrate. CBD is one of the convenient processes in which compound ternary semiconductor thin films of typically 0.02^{-1} μm thickness are deposited on the substrate immersed in dilute baths containing metal ions and in a source of sulfides or selenide ions. In the process, metal ions in the solution reacted with slowly released sulfide ions to form a solid film on the substrate. This technique is suitable for coating surfaces of any morphology and geometry. The HGS films are of particular interest for the fabrication of large area photodiode arrays, solar selective coatings, solar cells, photoconductors, sensors etc. Mercury sulphides is a direct band gap (~ 2.45eV) semiconducting material for applications as IR detection [15-17], ultrasonic transducers, image sensors, electronic imaging materials and photoelectric conversion devices [18]. The thin films of HgS can also be used in storage cell with CdSe, solid state solar cells, photoelectrochemical cells and photodetectors [19-20]. Deposition of these films by vacuum evaporation, sputtering and chemical methods such as chemical vapour deposition, spray pyrolysis, electrodeposition, anodization, electro conversion, electroless, dip growth, successive ionic adsorption and reaction, chemical bath deposition and solution-gas interface techniques are well known [21-27].Using this deposition methods, a large number of binaries such as CdS, CdSe, Bi_2S_3, Bi_2Se_3, PbS, PbSe, As_2S_3, Sb_2S_3, Ag_2S, CuS, ZnS etc. and ternaries such as CdZnS, CdSSe, $CuInS_2$, $CuInSe_2$, PbHgS, CdPbSe etc. have been deposited as thin films. The so prepared thin films are pin hole free and uniform deposits are easily obtained since the basic building blocks are ions instead of atoms.

The aim of our work is to investigate the growth procedure with respect to the feasibility of HGS crystalline thin films from alkaline medium at mild reaction conditions. A di-sodium salt of ethylene-diamine tetra- acetic acid (EDTA) was used as a complexing agent to form homogeneous HGS thin films. Highly reflecting, uniform and adherent HGS thin films with faint black colour were obtained. The structural, optical and surface morphological properties of the HGS films were investigated. [28-30]. [32-34].

Experimental Method

Commercial glass substrates were degreased in sulfuric acid (H_2SO_4) for 30 min and then immersed in isopropanol ultrasonically for 20 min. Finally, they have cleaned again ultrasonically with distilled water for 10 min and dried in air. The composite HGS thin films were deposited on this glass substrate using chemical bath deposition (CBD) technique in an alkaline medium. The AR grade $HgCl_2$, CrO_3 and NH_2-CS-NH_2 are the initial precursors are used. In the procedure; 10mL (0.1M) solution of $HgCl_2$ was taken in a 100mL beaker and 20mL (0.1 M) chromic oxide (Cr_2O_3) was mixed in it. For a fabrication of the complex, 10mL (0.1 M) Na_2EDTA (ethylene-diamine-tetra-acetic acid) was added into the mixture of $HgCl_2$ and Cr_2O_3. By adding drop-wise ammonium hydroxide solution (7%) the pH of resultant solution was adjusted to 10. At the last 30mL (0.1M) solution of thiourea was added into the above-mentioned mixture. The slow-release metal and chalcogenide ions in the solution condense onto the substrates resulting in thin film formation. The glass beaker containing resultant solution was kept in an oil bath at 65ºC for two hours. Finally, deposited samples were taken out of the solution, cleaned with distilled water and dried in air. The prepared thin films were preserved in an air-tight container for further characterization. The so deposited composite HGS films exhibits black yellowish colour. After deposition time, the glass substrates with composite HGS films were removed from the bath and washed with doubly distilled water, dried in air and preserved in an airtight plastic container for further characterization. To obtain good quality films, the amount of complexing agent, the deposition time, temperature, concentration of reactants and pH of the solution were optimized.

Characterization techniques

The thickness of the HGS films was determined by weight difference method using a sensitive microbalance. Structural analysis of the films was carried out using Rigaku (D. Max. C X-ray diffractometer and Ni filter). UV-Visible absorption analysis was done using UV-Vis-NIR spectrophotometer (Jasco-V 570). SEM measurements were carried out with a 250 MK^{-3} Cambridge sterioscan, operated at 15 kV. The optical absorption studies were carried out using Systronic spectrophotometer in the wavelength range 350– 850 nm. To study the electrical characteristics of the films, resistivity measurements were carried out using dc Four-probe method in the temperature range 300–500 K. The type of electrical conductivity was determined from thermoemf measurements.

Resalts and Discussion: -

Reaction Mechanism

The chemical bath process mechanism performed by slow release of S^{2-} and controlled free ions of Hg^{2+} and Cr^{3+} react with each other to get HGS nuclei product on glass substrate in the form of precipitated material. EDTA is an amino-derived organic-compound known to be a strong hexdentate chelanting agent [35]. It affects the adsortion and desortion processes [36] also forms a complex with metal ions and dissociates reversibly at a low rate. The chemical reaction for the formation of composite $Hg_xCr_{2-x}S_4$ (x = 0.6) by CBD is given by -

In an aqueous solution, Na_2EDTA finally dissociates as-

$$Na_2EDTA \rightarrow 2\,Na^{+} + EDTA^{4-} \quad (1)$$

By dropwise addition of Na_2EDTA to the solution of Hg^{+2} and Cr^{+3} to form a complex as

$$Hg^{+2} + EDTA^{4-} \rightarrow [\text{Hg-EDTA}]^{2-} \quad (2)$$

$$2C_r^{+3} + 2EDTA \rightarrow 2[C_r\text{-EDTA}]^{-} \quad (3)$$

By reaction of thiourea in an alkaline medium releases water and sulphide ions as

$$(NH_2)_2\,CS + NH_4^{+} + OH^{-} \rightarrow CH_2N_2 + H_2O + HS^{-} \quad (4)$$

On hydrolysis of ammonia [30], $NH_3 + H_2O \rightarrow NH^{+}_4 + OH^{-}$, (5)

$$K_{hyd} = 1.8 \times 10^{-5}$$

$$HS^{-} + OH^{-} \rightarrow H_2O + S^{2-} \quad (6)$$

On reaction of Hg-EDTA complex or Cr-EDTA complex followed by sulphides (S^{2-}) ions to forms HGS

$$[H_g(Na_2EDTA)]^{2+} + [2C_r(Na_2EDTA)]^{3+} + 4S^{2-} \rightarrow H_gC_{r2}S_4 + 3Na_2EDTA \quad (7)$$

[The solubility product $K_{sp} = 2 \times 10^{-55}$]

The reaction (2), (3) and (6) releases the Hg^{2+}, Cr^{3+} and S^{2-} ions and they condense ion-by-ion on the surface of substrate to form HGS thin films.

Characterization using XRD

The X-ray diffractogram for the as-grown $Hg_xCr_{2-x}S_4$ (x = 0.6) thin film samples were obtained in the 2θ range from 20^0 to 80^0. The X-ray diffraction (XRD) pattern of the films shows crystalline nature with planes having cubic orientations with growth along (2 2 0) plane (JCPDS Card no. 03-065-7116). The use of complexing agents is very common in the preparation of thin films through CBD process. It is very clear that the quality of thin films depends on the nature of the complexing agent. In the XRD pattern (Fig.1.) very few peaks (three) could be detected;for the HGS thin films deposited in the presence of ammonia and ethylenediaminetetraacetic acid (EDTA) as the complexing agent [36].The deposition time also affects the detection of peaks. The XRD data is given in table-1. The grain size in the film is estimated using Debye-Scherrer's formula.

$$D = \frac{0.94\lambda}{\beta cos\theta}$$

Where β is full width at half maximum (FWHM) in radians, λ is wavelength of the X-ray and θ is the Bragg's angle. The HGS films crystallizes in the normal cubic spinel structure with the space group mF-d3 (No. 227). The value of lattice constant found to be a = b = c =10.23800Å. The average grain size for x = 0.6 is found to be 173 nm.

Table- I: Comparison of observed d values with standard d values of HGS thin films.

Planes (h k l)	2 Theta (degree)		d-spacing values d (^{0}A)	
	Standard	Observed	Standard	Observed
2 2 0	24.570	24.560	3.6200	3.6260
4 2 2	43.251	43.160	2.0900	2.0898
5 3 1	52.843	52.840	1.7310	1.7305

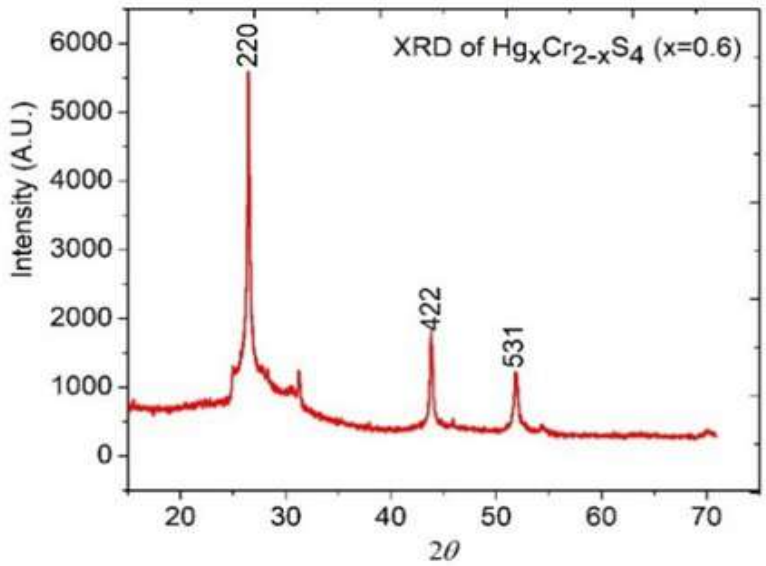

Fig. 1:- XRD pattern for $Hg_xCr_{2-x}S_4$ (x = 0.6) thin film.

Characterization using SEM

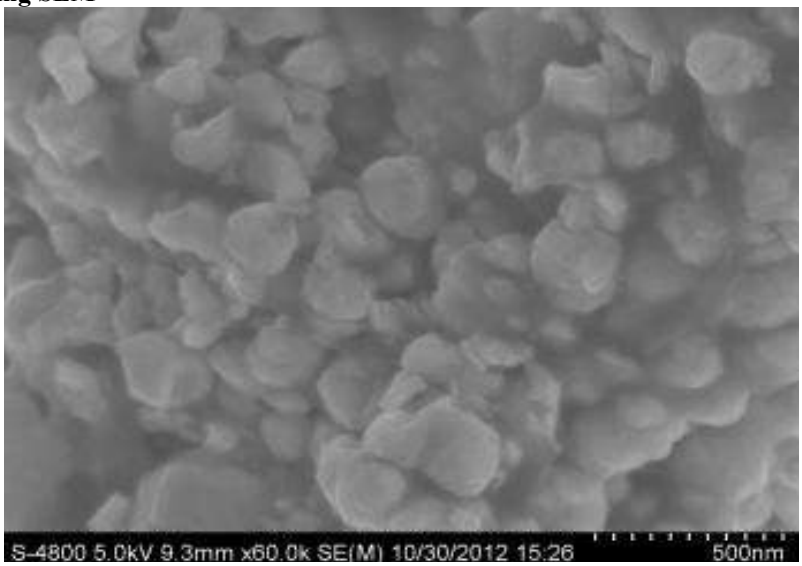

Fig. 2:- SEM image for $Hg_xCr_{2-x}S_4$ (x = 0.6).

The effect of Cr^{3+} ion in thin film $Hg_xCr_{2-x}S_4$ (x = 0.6) can be studied by SEM. The SEM micrograph of deposited samples is shown in figure 2. The SEM image showed that surface is not smooth and grains are appeared spherical shaped. The grown $Hg_xCr_{2-x}S_4$ (x = 0.6) appears to be porous fibrous group of regularly arranged matrix over which regular fine particles spread with some voids. The grain size of material of films using Cottrell method [37] was found to be in the range 160-170 nm. The surface roughness increased with addition of Cr^{3+} ion.

Characterization using UV-Vis spectrophotometer

Figure 3 depicts the optical absorption spectra of the $Hg_xCr_{2-x}S_4$ (x = 0.6) thin film. At the low optical energy; absorption is minimum and increases with increase in energy. Figure shows the variation of absorbance (αt) with incident photon wavelength. The figure shows that absorption decreases with increasing wavelength also red shift of optical absorption edge. The data were analysed from the following classical relation for near edge optical absorption in semiconductors [38]:

$$\alpha = \frac{A(h\gamma - Eg)^n}{h\gamma}$$

Where A is a constant and n = 2 for indirect band gap and n = $\frac{1}{2}$ for direct band gap. The plots of $(\alpha h\nu)^2$versus hν of the HGS films shown in Fig. 4. Since the plots of $(\alpha h\nu)^2$ versus hν are almost linear, the direct nature of the optical transition in HGS film is confirmed. Extrapolation of these curves to zero absorption coefficient gave the optical energy gap as 2.4 eV which is in good agreement with the values reported by other researchers [39-40]. The decrease in band gap energy value with increase of thickness is commonly observed phenomenon in semiconducting thin films.

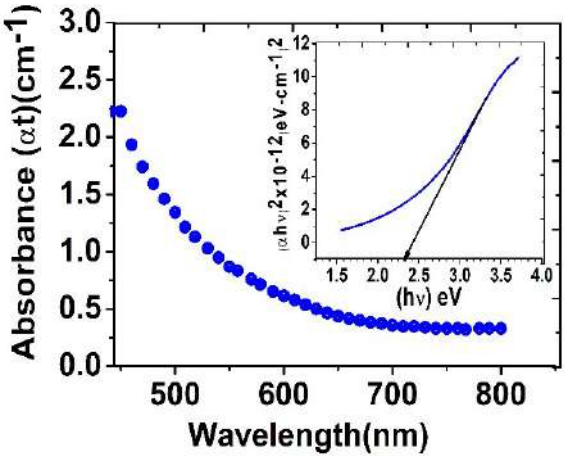

Fig.3:- The variation of absorbance (αt) with incident photon wavelength λ.Fig.4. (Inset figure) Plots of $(\alpha h\nu)^2$ hν thin films deposited on glass substrate**.**

Electrical properties

Electrical resistivity

The two-point dc probe method of dark electrical resistivity measurement was used to study the variation of electrical resistivity with temperature. The variation of log ρ with reciprocal temperature (K^{-1}) is depicted in Fig. 5. It is observed that the resistivity of film was decreased with increase in temperature, indicating a semiconducting electrical behaviour. The electrical resistivity depends on the structure of the films and working temperature. An increase in temperature affects the structure of films due to increase of grain size and removal of defects on the surface of films. The electrical resistivity of $Hg_xCr_{2-x}S_4$ (x = 0.6) was measured in the temperature range 303^0k to 423^0K and was observed to be 1.3703 x 10^3 Ω-cm to 2.1243 x 10^3 Ω-cm [40]. The plot of Log (ρ) Vs '1000/T' is almost straight line, indicating that conduction in the film is through thermally activated process. The activation energies were calculated using the relation: $\rho = \rho_0 e^{\frac{E_a}{KT}}$ (10)

where ρ is the resistivity at temperature T, ρ_0 a constant, K the Boltzmann constant, T the absolute temperature and Ea the activation energy. The activation energy represents the location of trap levels below the conduction band. The slope of the straight line gives information about activation energy and is observed to be 0.254eV for low temperature regime and 0.542 eV for high temperature regime.

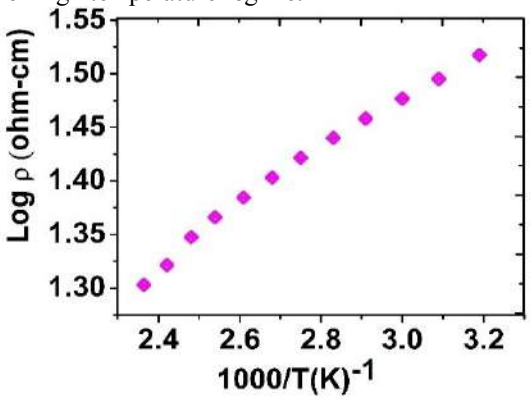

Fig. 4:- Variation of dark electrical resistivity (log ρ) with reciprocal temperature (1000/T) of $Hg_xCr_{2-x}S_4$ (x = 0.6) thin film deposited on glass substrate.

Thermoemf measurement

In the thermoemf measurement the temperature difference causes the transport of carriers from the hot end to the cold end and thus creates an electric field, which gives the thermal voltage. This thermally generated voltage is directly proportional to the temperature difference created across the semiconductor. The polarity of the induced emf for $Hg_xCr_{2-x}S_4$ (x = 0.6) film indicates an n-type electrical conductivity.

Conclusions:-

A chemical bath deposition method was used in the deposition of $Hg_xCr_{2-x}S_4$ (x = 0.6) films. The X-ray diffraction studies showed that the compositions of the deposited films correspond to $Hg_xCr_{2-x}S_4$ (x = 0.6). X-ray diffraction study reveals crystalline nature with cubic structure of the film. From electrical resistivity data, it is clear that the films were semiconducting in nature. The $Hg_xCr_{2-x}S_4$ (x = 0.6) films exhibited direct band gap transition with band gap energy of 2.4 eV. The n-type conductivity of these materials was confirmed from TEP measurements.

The study of optical Properties that present composition may be used in the application of p-n junction formation, solar cell design and photovoltaic applications. An increase in electrical resistivity with increasing temperature is attributed to the removal of defects on the surface of films**.**

Acknowledgement:-

The authors are indebted to the UGC-DAE Consortium for Scientific Research, Indore Centre for characterization of $HgCr_2S_4$ sample. The author is thankful to authority of R. C. Patel Arts, Science and Commerce College, Shirpur for their valuable guidance.

References:-

1. C. D. Lokhande, et al, Thin Solid Films, 302 (1997) 1.
2. G. Hodes, et al, Chemical Solution Deposition of Semiconductor Films, Marcel Dekker, New York, Base, l (2003).
3. R.S. Mane, et al, Vacuum, 80 (2006) 962**.**
4. R. S. Mane, et al, Nanotechnology**,** 17 (2006) 5393.
5. P. Hoschl, et al,J. Crystal Growth, 52 (1981) 669.
6. M.N. Spallart, et al, J. Electrochem. Soc., 137 (1990) 3434.
7. S. Faria, U S Patent Specification 4,374,917 (to GTE Products Corporation) 22 February (1983).
8. K. Sood, et al, Thin Solid Films 48 (1978) 73.
9. L.A. Rodriguez, et al, Solar Energy Mater., 19 (1989) 421.
10. D. C. Cameron, et al, Thin Solid Films, 58 (1979) 69.
11. S. M. Mahdavi, et al, ScientiaIranica**,**15 (2008) 360.
12. M. Jelonek, et al, Phys. Status Solidi A, 57 (1980) 11.
13. R. S. Mane, et al, Nanotechnology**,** 17 (2006) 5393.
14. Wustrow, et al, ASC publication, 57, 14, (2018) 8634–8638
15. R.S. Mane, et al, Materials Chemistry and Phy., 65 (2000) 1.
16. K.M. Gadave, et al, J. Pure Appl. Phys., 30 (1992) 299.
17. N. Tokyo, *J. Appl. Phys*., 46 (1975) 4857.
18. S.S. Kale, et al, Mater. Chem. Phys., 59 (1999) 242.
19. C. Suryanarayana, Bull. Mater. Sci., 17 (1994) 307.
20. G. Hodes, et al, Adv. Electrochem Eng.,13 (1985) 113.
21. C. Ghosh, et al, Thin Solid Films 60 (1979) 61.
22. B.B. Nayak, et al, Thin Solid Films 92 (1982) 309.
23. Y.Ma. et al, J. Electrochem. Soc. 124 (1977) 1430.
24. N.R. Pavaskar, et al, J. Electrochem. Soc.124 (1977) 743.
25. S.H. Pawar, et al, Thin Solid Films 110 (1983) 165.
26. S.H. Pawar, et al, Ind. J. Pure Appl. Phys. 21 (1983) 665.
27. S.H. Pawar, et al, Mater. Chem. Phys. 11 (1984) 461.
28. P.K. Nair, et al, J. Phys. D 22 (1989) 829.
29. C.V. Suryanarayana, Bull. Electrochem. 2 (1986) 57.
30. C.D. Lokhande, Mater. Chem. Phys. 27 (1991) 1.
31. J.G. Ibanez, et al, J. Chem. Edu. 74 (1997) 1205.

32. C.D. Lokhande, et al, Proceedings of the Workshop on Solid State Energy Conversion, Shivaji University, Kolhapur, 1985.
33. S.J. Lade, etal, Trans SAEST, 32 (1997) 72.
34. V. Tsurkan, et al, Eur. Phys., J.B 15 (2000) 401.
35. S. J. Lade, and C. D. Lokhande, Mat. Chem. Phys. 49, 160 (1997).
36. D. M. Zhou, et al, J. Environ. Sci. - Chi. 13, 153 (2001).
37. Cottrell, (1995), Introduction to metallurgy, Arnold press, London, 2: 173-184.
38. X.MathewandP.J. Sebastain, Solar Energy mater. Solar Cells, 59 (1999) 85.
39. R.S. Mane, et al, Vacuum, 80 (2006) 962.
40. R. S. Mane, etal, Mater. Res. Bulle., 34 (1999) 2035.
41. R.S. Mane, et al, Materials Chemistry and Phy., 65 (2000) 1.

Annabhau Sathe's Contribution in Social Reformation in Maharashtra

Dr. Ramesh D.Jadhav [1] Dr. Shaikh Faruk Ismail [2]
[1]HOD, History, R.C. Patel Arts, Commerce and Science College , Shirpur.
[2]Principal, Maulana Abdul Kalam Azad Urdu, High School & Jr. College, Shirpur.

Abstract:

India is a country where several attempts have been performed for social upliftment and economical transformation of downtrodden and marginalized sections of society. Multiple vibrant movements emerged and worked out for social reformation. It wouldn't be an exaggeration if commented that Maharashtra was at pioneer position at social renaissance. Dozens dedicated ceaselessly and Annabhau Sathe represents such a galiaxy of reformers. The present paper examines his role in bringing social change among lives of masses .His efforts in action and word prescribe his sentiency towards social cause and its need to transformation. Of course , his literary share in Marathi Literature demonstrates unrest against exploitation and injustice of labour class. His fascination for Marxism and involvement in communist activities proves his conflict for rights of Proletariat.Thoughts of Karl Marx and Dr Babasaheb Ambedkar influenced his actions and writings so deeply that he remained a staunch supporter of movements for labour , untouchables and marginalized communities.

Keywords:

social reformation in Maharashtra-Annabhau Sathe's literary contribution-fight for common people through literature and different activities-impact of Karl Marx' s historical materialism and class conflict -influence of Dr Ambedkar on his literary works and activities.

Objectives:

Research Paper is set with following objectives :

1. To be acquainted with the subject matter of all forms of literature written by Annabhau.
2. To comprehend his interest in Marxism and involvement in communist activities.
3. To know and understand impact of Marx and Dr Ambedkar in Anna's writings and activites.

Introduction :-

Maharashtra is a progressive state in India. It is land of saints, social reformers and educational leaders. Sant Gyaneshwar, Sant Namdev, Sant Tukaram and many such saints dedicated their lives for social awareness and intellectual enlightenment of masses. Likewise, social formation ranging from Shahu-Fule- Ambedkar continuous even today. And in this legacy a of social reformation names of Annabhau Sathe appears luminously. The present paper is an attempt to examine his continuation in social reformation and how he paid exclusive attention towards rights of marginalized sections, deprived classes and their economically backward conditions. His role in shaping labour movement is crucial and relevant.

Research Methodology :-

Primary and secondary sources are used in the research paper. Library and historical methods are used in order to understand Anna's contemporary circumstances. A book and a research articles are majorly used.

CONTENTS

SR. NO.	CHAPTER	PAGE NO
1	लोकशाहीर अण्णाभाऊ यांचे संयुक्त महाराष्ट्र चळवळीतील योगदान **डॉ. मीना गायकवाड**	1-5
2	Class And Caste Struggle In Annabhau Sathe's Literature **Lakshmanbye Rewajee**	6-9
3	Annabhau Sathe : A Brief Review **Dr. Anuradha Devidas Kshirsagar**	10-13
4	साहित्यसम्राट अण्णा भाऊ साठे यांच्या रशियाच्या प्रवासातील मानवतावादी दृष्टीकोन सह. प्रा. डॉ. राजाराम केसबा पाटील	14-17
5	Annabhau Sathe - A Social Reformer **Ramma Trishnee**	18-22
6	The Women Characters in Annabhau Sathe's Literature **Poojyata Sivram**	23-26
7	Annabhau Sathe's Contribution in Social Reformation in Maharashtra [illegible]	27-29
8	अण्णाभाऊंच्या कादंबऱ्या व कथासंग्रहातील सामाजिक क्षेमकुशलता **डॉ. बापू चिंधा राऊत**	30-33
9	अण्णाभाऊ साठे जी के उपन्यासों में सती विमर्श ('रत्ना' उपन्यास के विशेष संदर्भ में) **श्रीमती.संगीता विष्णु भोसले**	34-37
10	साहित्यरत्न, लोकशाहीर अण्णाभाऊ साठे यांचे क्रांतिकारत्व... **प्रा. डॉ. विशाल प्रकाश लिंगायत**	38-42
11	राष्ट्रनिर्मितीत अण्णाभाऊ साठे यांचे योगदान **डॉ. जनार्दन परकाळे**	43-46
12	साहित्यरत्न अण्णा भाऊ साठे याच्या साहित्यातील समाजवाद **डॉ. चंद्रकांत धनाजी कांबळे**	47-52
13	लोकशाहीर अण्णाभाऊ साठे यांच्या साहित्याला आलेल्या बाजाचे स्वरूप : एक सामाजिक अभ्यास **प्रा. डी. के. रसाळ व प्रा. डॉ. विष्णु वी. वाघमारे**	53-56
14	लोकशाहीर अण्णाभाऊ साठे जी की 'श्मशानातील सोने' कहानी में मनुष्य जीवन की विडंबना का यथार्थ चित्रण **प्रा. डॉ. सुचिता जगन्नाथ गायकवाड**	57-59
15	अण्णांच्या कथा कादंबरीत उपेक्षित नायक – नायिकेचा वास्तवादी जीवनवाद प्रा. डॉ. भारती चव्हाण	60-64
16	फकिरा कादंबरीतून व्यक्त होणारे अण्णा भाऊ **प्रा. डॉ. सुनिल सुखदेव लोखंडे**	65-67
17	अण्णाभाऊ साठेयांच्या साहित्यातील वैज्ञानिक दृष्टीकोन **प्रा. सुहास मुरलीधर उघडे**	68-70
18	अण्णाभाऊ साठे: संयुक्त महाराष्ट्र चळवळीतील क्रांतिकारी व्यक्तिमत्वाचा वेध **प्रा. प्रेमचंद गुंडू गायकवाड**	71-73
19	जनवादी साहित्यकार: अण्णाभाऊ साठे **प्रा. महेश तानवडे व डॉ. पंडित वन्ने**	74-76
20	फकीरा कादंबरीतील लोकजीवन: भौगोलिक दृष्टीकोन **डॉ. हरिश्चंद्र भानुदास तिपे**	77-79
21	[illegible] **प्रा. डॉ. मधुकर श्रीरंग पवार**	80-81
22	अण्णाभाऊ साठे यांच्या कथांमधील स्त्रीजाणीव **डॉ. शकील शेख**	82-85

खानदेश वैभव

काल आणि आज

(प्राचार्य डॉ. भी. ना. पाटील सेवापूर्ती संशोधनपर ग्रंथ)

- संपादक -

प्रा. डॉ. प्रशांत देशमुख | प्रो. डॉ. वासुदेव वले
प्रा. डॉ. जे. डी. गोपाळ | प्रा. दिपक सिरसाट

Prashant

CONTENT

१५ ते १८ व्या शतकातील काही मराठी हस्तलिखितांचा अभ्यास
Sunila Gondhalekar 3

साताऱ्याच्या छत्रपतींच्या दरबारातील जाबता कलमदाने व जाबता जासूद
डॉ. रमेश धनराज जाधव 8

सिंधुदुर्ग जिल्ह्यातील कातळशिल्पे- शोध, संशोधन आणि संरक्षण.
ऋत्विज आपटे, सुधीर रिसबूड 12

संत निळोबारायांच्या विरहिणी - एक अभ्यास
विवेक नामदेव चव्हाण 19

मल्हार दादाजी बरवे यांचा 'कोठुरे'या गावाशी असलेल्या संबंधाचे
प्राथमिक साधनांद्वारे अध्ययन ..... डॉ. अंजली वसंतकुमार सोईतकर 24

रत्नागिरी जिल्ह्यातील कातळशिल्पे :
नवीन संशोधन व संवर्धनाची दिशा ..... डॉ. तेजस मदन गर्गे 29

Cannons in Colonial Mumbai: An Appraisal
Arti Aley, Anuja Patwardhan& Tejas Garge 44

Persian Mosque of Bombay, with 'Kashikari'
and Inscriptions ..... Prasad G. Barve 57

Preliminary Results from Two Seasons of
Excavations at Koloshi, a Prehistoric Cave
ite in Konkan, Western Maharashtra
.....-Tejas Garge, Parth Chauhan,
udhir Risbud & Rutwij Aapte 65

ṣema Gaṇapati: A Study ....
..... Dr. Manjiri Bhalerao 78

Publisher
Tilak Maharashtra Vidyapeeth Vidyapeeth Bhavan,
Gultekdi, Pune - 411037.

ISSN - 0076-2571

MARCH 2021

Maharatt

Peer Review Jo

Tilak Maharashtra Vidyapeeth, P

Tilak Maharashtra Vidyapeeth, Pune

Shri Balmukund Lohia Centre of Sanskrit & Indological Studies

and

Directorate of Archaeology & Museums, Government of Maharashtra, M

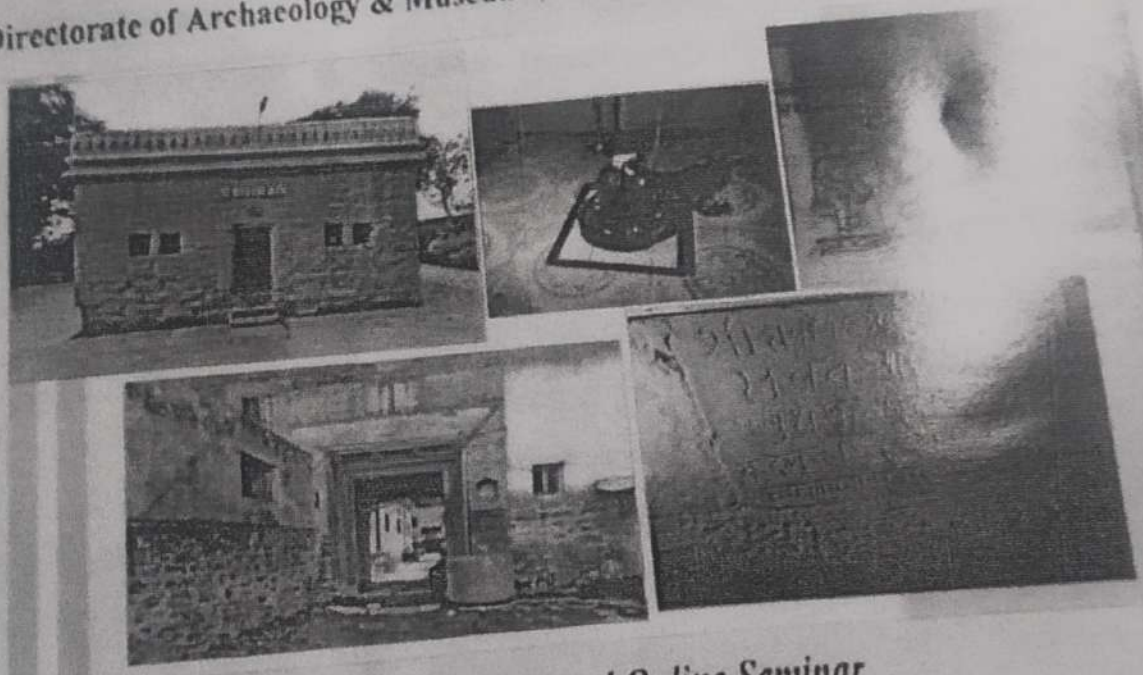

One day National Online Seminar

महाराष्ट्राच्या इतिहासातील नवीन संशोधन

19th November 2020

Conference Proceeding

महात्मा गांधीजींचे सत्य व अहिंसेसंबंधी विचार

प्रा.डी.आर.कोळी / प्रा.डॉ.आर.डी.जाधव

• **प्रास्ताविक** :-स्वातंत्र्यपूर्व भारतात विशेषत: ब्रिटीशांची सत्ता प्रस्थापित झाल्यानंतर भारतात अनेक महान व्यक्ती होऊन गेल्यात. त्यात आधुनिक भारताचे जनक राजाराममोहन रॉय, स्वामी दयानंद सरस्वती, महात्मा जोतिराव गोविंदराव फुले, सावित्रीबाई फुले, महर्षि विठ्ठल रामजी शिंदे, लोकमान्य बाळ गंगाधर टिळक, गोपाळ कृष्ण गोखले, न्यायमूर्ती महादेव गोविंद रानडे, दादाभाई नौरोजी, महर्षि धोंडो केशव कर्वे, स्वा.विनायक दामोदर सावरकर, नेताजी सुभाषचंद्र बोस, स्वतंत्र भारताचे पहिले पंतप्रधान पंडित जवाहरलाल नेहरु, सरदार वल्लभभाई पटेल, सरहद्द गांधी खान अब्दुल गफार खान, विनोबा भावे, साने गुरुजी आदी. परंतु या सर्वात महात्मा मोहनदास करमचंद गांधी यांचे नाव भारतातच नव्हे तर जगात अद्वितीय असे आहे. महात्मा गांधी हे एक मूल्यात्मक, आदर्शवादी, अध्यात्मवादी आणि मानवतावादी विचारवंत म्हणून त्यांची जगात ख्याती आहे. मानवतावाद हा त्यांच्या कार्याचा केंद्रबिंदु राहिलेला आहे. साध्य आणि साधन सूचिता हा त्यांच्या विचारांचा गाभा असून अन्यायाचा प्रतिकार सत्य, अहिंसा, सत्याग्रहाच्या मार्गाने करता येतो. हे त्यांनी आपल्या विचार व कृतीतून जगाला दाखवून दिले. भारताला ब्रिटीशांच्या गुलामगिरीतून अहिंसात्मक मार्गाने लढा देवून १५ ऑगष्ट १९४७ रोजी स्वातंत्र्य मिळवून दिले. त्यात त्यांच्या सत्य व अहिंसा या विचारांचे योगदान मोलाचे आहे.

महात्मा गांधी यांचे पूर्ण नाव मोहनदास करमचंद गांधी होते. त्यांचा जन्म दि.२ ऑक्टोबर १८६९ रोजी गुजराथ राज्यातील पोरबंदर येथे झाला. त्यांच्या घरातील धार्मिक संस्कृतीचा परिणाम गांधीजींवर झालेला दिसतो. भारतातील शिक्षण पूर्ण झाल्यावर ते उच्च शिक्षणासाठी इंग्लडला गेले. इ.स.१८९१ साली बॅरिस्टर झाल्यावर भारतात आले. इंग्लडमध्ये असतांना गांधीनी श्रीमद भागवत गीतेचा अभ्यास केला. तसेच कुराण, बायबल इ. सर्व ग्रंथाचाही अभ्यास केला. इ.स. १८९३ साली महात्मा गांधीजी दक्षिण अफ्रिकेत गेले. दक्षिण अफ्रिकेत राहणाऱ्या भारतीय लोकांना सत्य व अहिंसेच्या मार्गाने लढा देऊन ब्रिटीशाच्या गुलामगिरीतून न्याय मिळवून देण्यात त्याना यश मिळाले. इ.स.१९१५ साली गांधीजी भारतात आले. पुढील आपले आयुष्य त्यांनी भारतीय स्वातंत्र्य चळवळीसाठी समर्पित केले. गोपाळ कृष्ण गोखले हे त्यांचे राजकीय गुरु होते. त्यांच्या सूचनेनुसार त्यांनी संपूर्ण भारताचे भ्रमण केले. भारतातील दारिद्रय, खेड्यांची बिकट परिस्थिती, उपासमारी, बेरोजगारी इ.प्रश्नांमुळे त्यांचे मन व्यथित झाले. या परिस्थितीला जबाबदार असणाऱ्या ब्रिटीश राजवटीला या देशातून हद्दपार केले पाहिजे असा त्यांनी निर्धार केला. परंतू ब्रिटीशांचे साम्राज्य या काळात जगात पसरलेले होते. बलवान असे होते. अशा या साम्राज्यापुढे आपला निभाव लागणे शक्यच नाही. यावर मार्ग म्हणून त्यांनी सत्य व अहिंसा या मार्गाने भारताला स्वातंत्र्य मिळविण्याचे ठरविले. या महामानवावर गोपाळ कृष्ण गोखले, जॉन रस्कीन, टॉलस्टॉय यांच्या विचारांचा प्रभाव आहे. गांधीजींनी आपले विचार 'हरिजन' व 'यंग इंडिया' या वृत्तपत्रांतून व्यक्त केले आहेत. त्यांनी आपल्या कार्यमग्न जीवनातून वेळ काढून महत्वपूर्ण ग्रंथांची रचना केलेली आहे. त्यात हिंद स्वराज्य, गीताबोध, आत्मकथा, माझे समालकोन सर्वोदय, मंगल प्रभात, ब्रम्हचर्य, ग्रामसेवा, राष्ट्रवाणी, खादी, आत्मशुध्दी, गीताई, धर्मनिती, निती धर्म, आरोग्याची गुरुकिल्ली, आश्रमवासीयां कडून, सत्यवीराची कथा, रामनामाचे महत्व, सत्याग्रह, अनासक्तियोग इ.

महात्मा गांधीजी हे एक आदर्शवादी व आधात्मवादी विचारवंत होते. सत्य व अहिंसा ही गांधी विचारांची मुलतत्वे आहेत. महात्मा गांधीजींचा मानवाच्या माणुसकीवर विश्वास होता. म्हणून त्यांनी आपल्या विचार व कृतीने शस्त्राच्या विरुध्द अहिंसेने,अन्यायाच्या विरोधात सत्याने व अन्याय विरोधात न्यायाने लढा दिला. म्हणून प्रस्तूत शोध निबंधातून महात्मा गांधीजींच्या सत्य व अहिंसेसंबंधी विचारांना अभ्यास करावयाचे ठरविले आहे.

• <u>सत्य व अहिंसेची व्याप्ती</u> :-

मानवी जीवनाच्या प्रारंभापासून ते आजपर्यंत स्थापन झालेल्या प्रत्येक धर्माच्या प्रनेत्यांनी आपल्या धर्मग्रंथातून व प्रचारातून सत्य, अहिंसा, प्रेम, भूत, दया इत्यादी नीती तत्वांचा तळमळीने पुरस्कार केला आहे. परंतू या नितीतत्वाची व्याप्ती मनुष्यांच्या वैयक्तिक जीवनापुरतीच मर्यादीत होती. लौकीक व्यवहारात एखादी व्यक्तीच सत्य व अहिंसा तत्वाचे आचरण करत होती. बहुसख्य समाज हा वर्षानुवर्ष सामाजिक दडपणाखाली आपले जीवन व्यतित करीत होता. परंतू विसाव्या शतकातील पूर्वार्धात महात्मा गांधींनी या नीती तत्वाचा पुनरुच्चार प्रथम आफ्रिकेत व नंतर भारताच्या स्वतंत्र्य आंदोलनात केला. सर्व

213

Impact Factor-7.675 (SJIF) ISSN-2278-9308

B.Aadhar

Peer-Reviewed Indexed

Multidisciplinary International Research Journal

October - 2020

ISSUE No - [illegible]

Ideology of Mahatma Gandhi

Jawahar Education Society's Vaidyanath College Parli- Vaijnath,
Dist. Beed

This journal is indexed in :

- Scientific Journal Impact Factor (SJIF)
- Cosmos Impact Factor (CIF)
- International Impact Factor Services (IIFS)

Aadhar Publication

Amravati(M.S)

For Details Visit- -www.aadharsocial.com

VOLUME - IX, ISSUE - III - JULY - SEPTEMBER 2020
AJANTA - ISSN 2277 - 5730 - IMPACT FACTOR - 6.399 (www.sjifactor.com)

२. छत्रपती शाहू महाराजांच्या काळातील आज्ञापत्रे

प्रा. डॉ. रमेश धनराज जाधव
इतिहास विभाग प्रमुख, आर.सी.पटेल कला, वाणिज्य व विज्ञान महाविद्यालय, शिरपूर, जि. धुळे.

प्रस्तावना

मोघल बादशाह औरंगजेबाने नोव्हेंबर १६८९ मध्ये महाराष्ट्राची राजधानी रायगड ताब्यात घेतल्या नंतर शाहू [illegible] न परिणाम कैद केले होते परंतु छत्रपती शाहू महाराजांची ८ मे १७०७ मोगलांच्या कैदेतून सुटका झाली स्वराज्यात आल्यामुळे महाराणी ताराबाई-शाहू महाराज [illegible] संघर्ष निर्माण झाला आणि त्यातूनच १७०८ सालीखेडची लढाई झाली त्यात महाराणी ताराबाईचा पराभव झाला. त्यामुळे शाहू महाराजांनी आपला मोर्चा साताऱ्याकडे वळविला. शाहूंची वाढ भक्कम झालेली पाहून सातारा लढविण्याची कामगिरी प्रतिनिधींकडे सोपवून महाराणी ताराबाई पन्हाळ्याकडे निघून गेल्या आणि त्यामुळे छत्रपती शाहूमहाराजांनी सातारा राजधानी आपल्या ताब्यात घेवून १२ जानेवारी १७०८ रोजी स्वतःस राज्याभिषेक करुन मराठा साम्राज्याचा वारस घोषित केले.[1]

छत्रपती राजारामाच्या काळात तत्कालीन राजकीय परिस्थितीनुसार राजकीय व लष्करी अनुषंगाने वतने देण्यास सुरुवात केली. छत्रपती शाहू महाराजाना सत्ता प्राप्तानतर (१७०८) मराठा राज्यातील विविध ठिकाणी असलेले सरदार, सरंजामदार, दिमतीस असलेले कारभारी यांना मोकासे, इनामे, वर्षासने आणि आज्ञापत्रे देण्यास सुरुवात केली.

उद्देश

१. छत्रपती शाहू महाराजांच्या काळातील आज्ञापत्रे यांची माहिती मिळविणे.

२. आज्ञापत्रे देण्याच्या उद्देशाची माहिती मिळविणे.

३. आज्ञापत्रे कोणकोणत्या व्यक्तीस दिली होती यांची माहिती मिळविणे.

संशोधन पद्धती

प्रस्तुत शोधनिबंधासाठी विश्लेषणात्मक संशोधन पद्धतीचा वापर केला असून उपलब्ध असणारी संदर्भग्रंथे त्यांत प्रामुख्याने मराठी रियासत, वैद्य दप्तरातून निवडलेले कागद- खंड-२, विधार्भातील लेख संग्रह खड १, पेशवेदप्तरातील सनदा पत्रातील माहिती या संदर्भग्रंथाचा उपयोग करुन प्रस्तुत शोधनिबंध मांडण्याचा प्रयत्न केला आहे.

विषय विवेचन

सनद याचा अर्थ अधिकारपत्र किंवा देणगीपत्र असा होत असला तरी त्यापेक्षाही व्यापक असल्याने त्याचे स्पष्टीकरण करणे जरुरीचे असून योग्यही आहे.[3] छत्रपती शिवाजी महाराजांना अष्टप्रधान मंडळाची नेमणूक का करावी लागली. याचे

ISSN 2277 - 5730

AN INTERNATIONAL MULTIDISCIPLINARY
QUARTERLY RESEARCH JOURNAL

AJANTA

Volume - IX Issue - III JULY - SEPTEMBER - 2020

MARATHI PART - I

Peer Reviewed Referred and UGC Listed Journal

Journal No. 40776

ज्ञान-विज्ञान विमुक्तये

IMPACT FACTOR / INDEXING

2019 - 6.399

www.sjifactor.com

❖ EDITOR ❖

Asst. Prof. Vinay Shankarrao Hatole

M.Sc (Maths), M.B.A. (Mktg.), M.B.A. (H.R.),
M.Drama (Acting), M.Drama (Prod. & Dir.), M.Ed.

❖ PUBLISHED BY ❖

Ajanta Prakashan

Aurangabad. (M.S.)

B.Aadhar' International Peer-Reviewed Indexed Research Journal
Impact Factor - { (SJIF) -7.675,
Issue No,235
ISSN : 2278-9308
June 2020

साताऱ्याचे छत्रपती रामराजे यांचा राज्याभिषेक सोहळा

प्रा. डॉ. [illegible]

इतिहास विभाग प्रमुख, आर.सी.पटेल कला, वाणिज्य व विज्ञान महाविद्यालय,
शिरपूर जि.धुळे

सारांश :

दिर्घकाळ छत्रपतींचे वास्तव्य असण्याचे भाग्य लाभलेली स्वराज्याची राजधानी सातारा, साताऱ्यावर प्राचीन काळात सम्राट अशोकानंतर, सातवाहन, चालूक्य राष्ट्रकुट आणि देवगिरीच्या यादवांनी राज्य केले. देवगिरीच्या यादवांच्या पाडावानंतर हा प्रदेश बहामनी सुलतानाच्या प्रभूत्वाखाली आला. 17 व्या शतकात छत्रपती शिवाजी महाराजांनी आपल्या सत्तेचे केंद्रे या प्रदेशास बनविले. छत्रपती राजारामांनी सातारा या किल्ल्यास राजधानीचा मान दिला. छत्रपती शाहू महाराजांचा मोगलाच्या कैदतून सुटका झाल्यानंतर शाहू महाराज स्वराज्यात आले आणि शाहू महाराज, महाराणी ताराबाई संघर्षात शाहू महाराज विजयी झाले आणि साताऱ्यावर आपली सत्ता प्रस्थापित केली.

छत्रपती शिवाजी महाराजांनी 6 जून 1674 रोजी विधीपूर्वक राज्यारोहण केले आणि छत्रपतींचे कुळ सुरु केले. त्याच्या राजासहासनाचा वारसा त्यांच्या मृत्यूनंतर छत्रपती संभाजी महाराज आणि दुसरी राजाराम महाराज यांनी चालविला. छत्रपती महाराजांच्या मृत्यूनंतर महाराणी ताराबाईने छत्रपती राजाराम महाराजांच्या मुलाला म्हणजेच शिवाजीला पन्हाळा किल्यावर छत्रपती पदावर बसविले. 12 जानेवारी 1708 रोजी छत्रपती शाहू महाराजांनी स्वतःला सातारा येथे राज्याभिषेक करुन घेतला. छत्रपती शाहू महाराजानंतर रामराजाचा राज्याभिषेक [illegible] पेशवा यांनी चितपीस परंदरे करण आणि इतर व्यक्तिंना रामराजास आणण्यासाठी नागपुर येथे पाठविले आणि ही मंडळी रामराजास घेवून साताऱ्यास आली आणि 4 जानेवारी 1750 रोजी या दिवशी राज्यारोहण समारंभ झाला. मराठ्यांच्या राज्याचे पहिले छत्रपती म्हणून शिवाजी महाराजांचे नाव घेतले जाते.

सातारा आणि कोल्हापुर येथे छत्रपतींच्या वारसाची परंपरा सुरु आहे.

प्रस्तावना

सातारा व कोल्हापूरच्या छत्रपतींच्या, नागपूरकर भोसले व इतर मराठा राज्यकर्त्यांच्या राज्यात व दरबारात हिंदूचे सण-समारंभ व उत्सव मोठ्या उत्साहाने साजरे करण्यात येत असत. तशाच प्रकारचे सण उत्सव व समारंभ साताऱ्याच्या छत्रपतींच्या कारकिर्दीत त्यांच्या राज्यात व दरबारात साजरे करण्यात येत असत. त्यातील काही सण उत्सव धार्मिक स्वरुपाचे असत. त्यात प्रामुख्याने राज्याहोरण समारंभ, विजयादशमी, गणपतीउत्सव, दसरा, दिवाळी, श्रीरामनवमी, मंगळागौरी, रक्षाबंधन, विवाहसमारंभ, जन्मोत्सव, गोकूळअष्टमी, होळी, अंबाबाईचा गोंधळ, दसनवमीचा उत्सव आणि मकरसंक्रांत साजरे होत असत.

साताऱ्याच्या छत्रपतींच्या दरबारात अनेक सण व उत्सव साजरे केले जात होते. अशा सण उत्सवात राजकीय उत्सव म्हणून राज्यारोहण समारंभ हा महत्वाचा समारंभ होता.

छत्रपती शिवाजी महाराजांनी अन्यशा साधनाद्वारे व राष्ट्रमाता जिजाबाई यांच्या मार्गदर्शनाने व प्रेरणेने जहांगिरीचे रुपांतर स्वराज्यात केले आणि 6 जून 1674 रोजी काशीचे विद्वान पंडीत गागाभट्टांच्या आशीर्वादाने छत्रपती शिवाजी महाराजांनी रायगडावर विधीपूर्वक राज्यारोहण केले आणि [illegible] आणि या राज्याच्या

206

B.Aadhar International Peer-Reviewed Indexed Research Journal

Impact Factor - (SJIF) - 7.675,
Issue No.235

ISSN : 2278-9308
June 2020

Impact Factor – 7.675 ISSN – 2278-9308

B.Aadhar

Peer-Reviewed Indexed

Multidisciplinary International Research Journal

JUNE - 2020

ISSUE No – CCXXXV (235)

Aadhar International Publication

ISSN 2250 - 1185
UGC CARE - 94

भारतीय इतिहास आणि संस्कृति

इतिहास संशोधन मंडळ, मुंबई

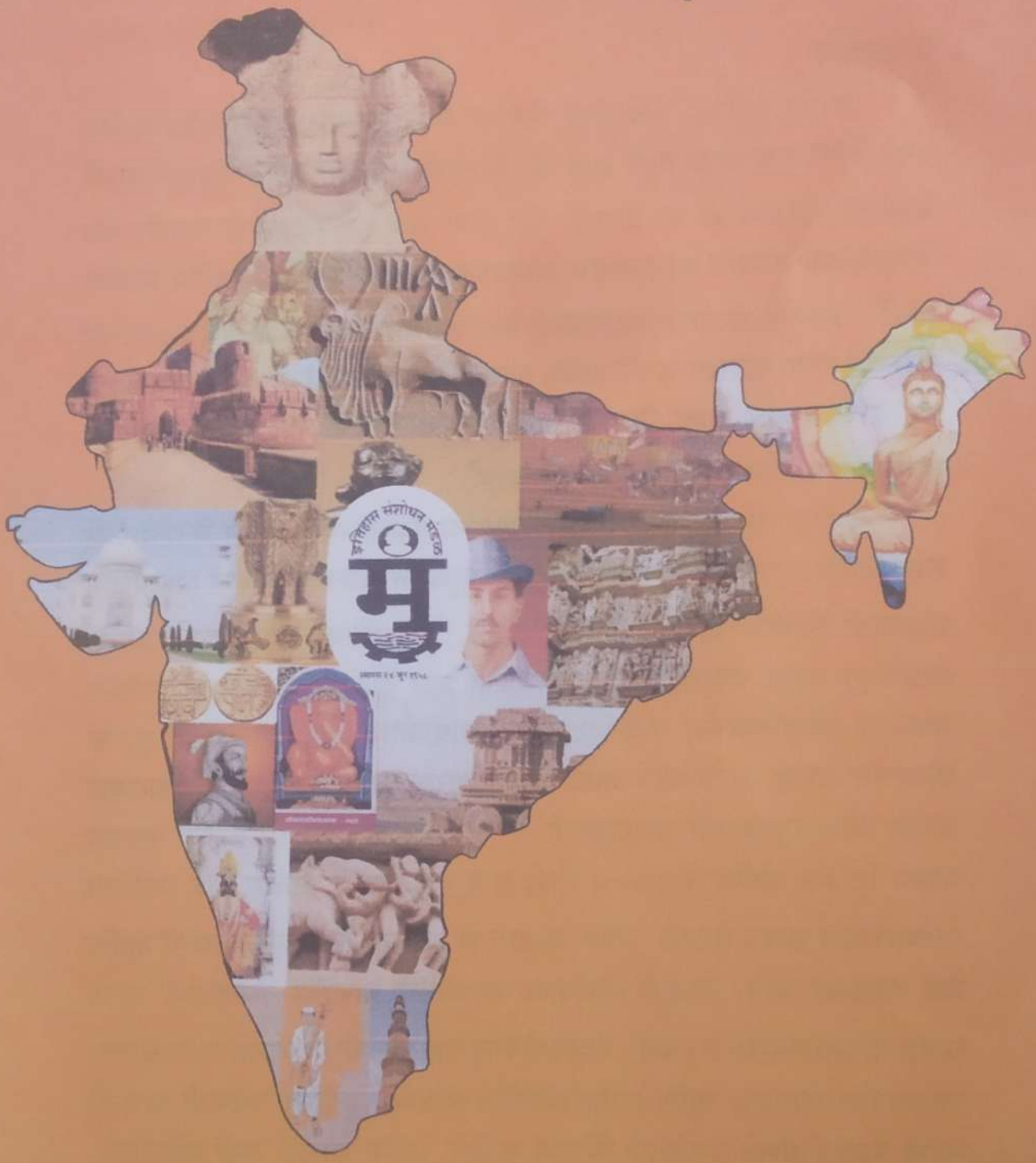

(वर्ष: ५७) एप्रिल २०२० ते मार्च २०२१ (पुस्तक २२५ ते २२८)

UTKAL HISTORICAL RESEARCH JOURNAL

VOLUME:XXXIV 2021

DEPARTMENT OF HISTORY
UTKAL UNIVERSITY, VANI VIHAR
BHUBANESWAR-751004, (ODISHA) INDIA

UTKAL
HISTORICAL RESEARCH JOURNAL

CERTIFICATE OF PUBLICATION

This is to certified that the article entitled

THE ADMINISTRATIVE SYSTEM IN THE PROVINCE OF BARODA DURING THE TIME OF MAHARAJA SAYAJIRAO GAIKWAD III: AN OVERVIEW

Authored By
Dr. R. D. Jadhav
HOD, History Dept. (Guide) R.C. Patel College Shirpur, Dist. Dhule.

Published in Vol. 34, No.01 : 2021
Utkal Historical Research Journal with ISSN : 0976-2132
UGC Care Approved, Peer Reviewed and Referred Journal

UGC
University Grants Commission
Approved Journal

Editor
Dr. Basanta Kumar Mallik
Professor & Head
Dept of History, Utkal University

Mukt Shabd Journal

ISSN NO : 2347-3150

Role of Banjara Community in the Trade and Transportation in Medieval India

Dr. Ramesh Dhanraj Jadhav
Head and Research Guide
Dept. Of History
R. C. Patel Arts, commerce & Science College
Shirpur, Dist- Dhule M.S
jadhavramesh1969@gmail.com

Abstract

Despite the abundant work on mediaeval Indian history, it is a fact that much is not written on trade and transportation system prevailing in in that particular period. The present paper is an honest attempt to trace the trade and transportation services rendered by a Nomadic tribe; Banjara. Banjara community has given everything to ease the complexities of transportation encountered by masses of all walks of life. The paper minutely records the references of some historians who paid much attention towards the system of trade and transportation particularly controlled by this dedicating community. In spite having many obstacles of social and economical backwardness, Banjaras continued their services under various regimes.

Keywords: Banjara community, trade, transportation

Introduction:

Each community or section of society has always been a part of constructive programme in each state. Banjara is such a section of the social heritage which is usually seen as nomadic people .This section of the Hindu community predominantly dwells in the northwestern belt of India in Rajasthan, Karnataka, Maharashtra, Aandra Pradesh and Telangana. Their ancestors were transporters of goods such as grains, wood, salt, pepper, cattle and other domestic products. This is the evident of fact that their role in trade and transportation has been crucial in the dynasty of all rules, ranging from medieval to modern. Banjaras were known as the drovers of cattle, heavy loads and other objects .In the medieval, Indian people used to do trade activities by utilizing transportation by means of bulls , camel, donkey , etc. Most of the commoners carry stack on their heads .In northern parts of the

Mukt Shabd Journal

UGC CARE GROUP - I JOURNAL

ISSN NO : 2347-3150 / web : www.shabdbooks.com / e-mail : submitmsj@gmail.com

CERTIFICATE OF PUBLICATION

This is to certify that the paper entitled

Role of Banjara Community in the Trade and Transportation in Medieval India

Authored by

Dr. Ramesh Dhanraj Jadhav

From

Dept. of History, R. C. Patel Arts, commerce & Science College, Shirpur

Has been published in

Volume IX, Issue VI, JUNE/2020

DOI : 10.37896/MSJ

Sumit Ganguly
Editor-In-Chief
MSJ
www.shabdbooks.com

Source details

nternational Journal of Scientific and Technology Research

Scopus coverage years: from 2018 to 2020
coverage discontinued in Scopus)
Publisher: International Journal of Scientific and Technology Research
E-ISSN: 2277-8616
Subject area: Social Sciences: Development
Business, Management and Accounting: Management of Technology and Innovation
Engineering: General Engineering
Source type: Journal

CiteScore 2019
0.2

SJR 2019
0.123

SNIP 2020
0.485

View all documents > | Set document alert | Save to source list | Source Homepage

CiteScore | CiteScore rank & trend | Scopus content coverage

Improved CiteScore methodology
CiteScore 2019 counts the citations received in 2016-2019 to articles, reviews, conference papers, book chapters and data papers published in 2016-2019, and divides this by the number of publications published in 2016-2019.

CiteScore 2019

$$0.2 = \frac{679 \text{ Citations 2016 - 2019}}{3{,}542 \text{ Documents 2016 - 2019}}$$

Calculated on 06 May, 2020

CiteScore rank 2019

Category	Rank	Percentile
Social Sciences – Development	#215/239	10th
Business, Management and Accounting – Management of Technology and Innovation	#209/231	9th

View CiteScore methodology > | CiteScore FAQ > | Add CiteScore to your site

IJSTR
ISSN 2277-8616
Indexing coverage
Mar 2018 to May 2020

International Journal of Scientific & Technology Research - ISSN 2277-8616

Ref: IJSTR-0320-32253

Certificate of Publication

This is to certify paper titled "***Role of Irrigation in Agricultural land Practices â□□ A micro level study of Shirpur Tehsils in Dhule District (MS).***" submitted by Author(s) ***Dr.Bharat Daga Patil*** has been published in open access International Journal of Scientific & Technology Research (IJSTR) Volume 9 - Issue 3, March 2020 Edition.

Editor in-chief
Email:- chiefeditor@ijstr.org
www.ijstr.org

To verify the authenticity of this certificate, please visit: http://www.ijstr.org/verify-certificate.php

"No signature is required as this is a computer generated letter"

Role Of Irrigation In Agricultural Land Practices – A Micro Level Study Of Shirpur Tehsils In Dhule District (MS).

Dr.Bharat Daga Patil,

ABSTRACT: IN THIS PAPER AN ATTEMPT HAS BEEN MADE BY RESEARCHER TO STUDY REVENUE BLOCK WISE ANALYSIS OF ROLE OF IRRIGATION IN AGRICULTURAL PRACTICES. THEREBY TO FIND OUT IMPACT ON AGRICULTURAL LAND PRACTICES IN THE CONTEXT OF IRRIGATION FACILITIES. THE DATA ON LAND USE AND SOURCES OF IRRIGATION HAS BEEN TAKEN FOR AGRICULTURAL YEAR AS PER 2011. THE STUDY REGION FALLS UNDER ASSURED RAINFALL ZONE AND HAS RECEIVED 70 PERCENT AREA RAIN AMOUNTING 500 MM TO 1200 MM. THE AVERAGE ANNUAL RAINFALL IN STUDY AREA IS 780 MM. THE NORTHERN PART OF THE STUDY REGION RECEIVES MORE RAINFALL 800-1200 MM, WHILE SOUTH PART OF THE REGION RECEIVES LESS RAINFALL 500-700MM. BUT THE ERRATIC NATURE OF RAINFALL AFFECTS THE AGRICULTURAL PRACTICES. IN FACTS DECREASE IN RAINY DAYS, VARIATION IN INTENSITY OF RAINFALL AND COEFFICIENT OF VARIATION OF RAINFALL RANGES BETWEEN 20 TO 30 PERCENT SUGGESTS NEED OF IRRIGATION IN BOTH KHARIF AND RABI SEASONS. IN 2010-11, TOTAL 13252.15 HECTARE LAND AREA IS IRRIGATED OUT OF NET AREA SOWN (NAS) OF SHIRPUR TEHSIL. HIGHEST IRRIGATED AREA OBSERVED IN AKTHE REVENUE BLOCK THAT IS 3613.40 HECTARES AND LOWEST IN SANGAVI WITH 1004.76 HECTARES. IN THE STUDY REGION 21.55 % AREA IRRIGATED TO NET SOWN AREA OF TEHSIL IN AGRICULTURAL 2011.AS PER 2011, TOTAL POPULATION OF SHIRPUR TEHSIL IS 422137.THE PURPOSE BEHIND THE CHOICE OF THIS REGION FOR CARRIED OUT RESEARCH WORK BECAUSE OF ITS RICH AGRICULTURAL TRACK ENDORSED WITH ASSURED RAINFALL ZONE. DIVERSIFIED CROPPING PATTERN IS CULTIVATED UNDER BOTH RAIN FED AND WITH IRRIGATION FACILITIES. THE MAIN CROPS ARE GROWN SUCH AS CEREALS, PULSES, OILSEEDS, COTTON AND SUGARCANE ETC. GEOGRAPHICALLY, PRESENT STUDY AREA HAS UNIQUE FEATURES IN THE CONTEXT OF AGRICULTURAL PRACTICES, IRRIGATION FACILITIES. THE MAIN OCCUPATION OF THE PEOPLE IS AGRICULTURE IN THIS TEHSILS WITH COTTON AND SUGARCANE AS THE MAJOR PRODUCT. IT HAS THREE AGRO BASED INDUSTRIES LIKE TEXTILE, SUGAR FACTORY AND CORN MILL.

INDEX TERM : Irrigation, Revenue block, Density of Pumps, Net area sown, size of Holding.

1. INTRODUCTION –

In the context of present study the term "Irrigation" express as main factor to lead in the process of land use changes. In improving crop productivity supply of water is require at regular interval and in required quantities to soil. This could be done by artificial application of water and its termed as "Irrigation". Irrigation is the artificial application of water for increase soil moisture. Irrigation is essentially the artificial application of water to overcome deficiencies in rainfall for growing crops (Cantor, 1967). The irrigation and its role in the development of agriculture have been studied by many geographers. Such as "Irrigation and its impact on agricultural land use in Upper Krishna basin of Maharashtra" by C. T. Pawar (1989),In the book titled "Irrigated Agriculture", a special reference to West Bengal, India, Studied by Dr. Nandini Chatterjee (1995),Jasbir Singh and S. S. Dhillon, in his book entitled "Agricultural Geography" studied impact of irrigation on land use change in relation to physical and nonphysical factors.(1991).Jhujar Sing (1984) has pleaded in his article entitled "Tube well irrigation and spatial organisation of agriculture" that due to inadequate, unreliable and seasonally concentred nature of monsoon rainfall tube well play a critical role in agricultural economy

2. STUDY AREA -

Shirpur is a city and tehsils place in Dhule district of Nasik Division of Maharashtra. It is located on Mumbai (MS) Agra (UP) National Highway (NH3).The Arunavati River flows through the city. It has located between the coordinate of 21 0 21 ' 1 " and 74 0 52 ' 43 " and situated on the Northern part of Tapi (Tapti) river and foothills of Satpura mountain. AS per 2011 total population of Shirpur tehsil is 312000.The main occupation of the people is agriculture in this tehsils with cotton and Sugarcane as the major product. It has three agro based industries like Textile, Sugar Factory and Corn Mill. The relief of this region has Satpura Mountain on the northern side and Tapi or Tapti River flows in the south, the central part of this region has rich alluvial plain. The mountain region is very ragged ranging in height from 300 to 900 metres above the sea level.

3. DRAINAGE -

Tapi is the main river flowing through the southern part and its tributaries in north side of its. The Northern tributaries due to because of the proximity of the high ranges of the Satpura are relatively small in length.

Map no 1(a) Contour and (b) Drainage Map of Study Area

Risings from innumerable springs they have been put to use for irrigation, their peculiarity is that they are near the hills and again for several kilometer's before they fall into the Tapi Their streams flows throughout the year but in the middle belt where the course piedmont debris-slopes attain their maximum depth, their waters sink below, leaving the bed perfectly dry in the summer season. These streams are Aner, Dharamkhuli, Dahivad, Arunavati, kordi, lendi, Kasan, Aner, Arunavati, are relatively more important for irrigation purposes.

4. OBJECTIVE

The objectives of the present study are to analyses are as follows [1] to prepare a map of study area for interpretation of data and slop and contour map. [2]to analyse the revenue blocks wise Gross Irrigated Area, wells and Tub wells in the agricultural year 2011.[3] to calculate density of pump set and analysis of land holders wise uses of source of Irrigation 2011.

5. DATA COLLECTION AND WORK

Secondary data used for carried out research work this paper. It has been collected from a Socio-economic abstracts 2011 and District census handbook 2011. Field work – Revenue block wise survey conducted for field work and interview of farmers. In the all revenue block of the study area farmers are interviewed with those has Marginal, Small, Medium and Large size of agricultural land. Laboratory work is carried out for calculation of data. For comparative analysis Pearson's correlation coefficient and cartographic technique has been used. The map of study area has been scanned and then digitized manually by using GIS software's and analysis has been done with the help of the tables, maps, diagrams.

6. METHODOLOGY –

For the achieving result of this research paper entitled "Role of Irrigation in Agricultural land Practices – A micro level study of Shirpur Tehsils" following methods has been are used

6.1 Analysis of Revenue blocks wise Gross Irrigated Area.

The land, which is totally cropped in Kharif and Rabbi Seasons under irrigation during current agricultural year called as Gross Irrigated Area.

Table No. 1 Distribution of Irrigated Area

Name of the Revenue Block	Revenue block Wise gross Un-irrigated Land area in Hectare	% of total Un-irrigated area to NAS of the revenue block	Revenue block Wise Gross Irrigated land area in Hectare	% of total irrigated area to NAS of the revenue block	The revenue block wise Net Area Sown in Hectare
Borafi	9104.42	87.80	1265.00	12.91	10369.42
Sangavi	11255.13	91.80	1004.76	8.19	12259.89
Arthe	8676.71	70.39	3613.40	29.44	12190.11
Shirpur	4735.00	58.46	2187.04	31.59	6922.04
Thalner	6126.96	75.88	1947.11	24.11	8074.07
Holmarshi	9481.30	72.28	3244.84	27.71	11726.14
Tehsil	48259.5 8	78.44	13262.1 5	21.55	61521.7 3

(COMPILED BY RESEARCHER)

It represents the actual physical area of agricultural land falls under by all sources of irrigation. In this study region source of irrigation is available such as Government canals, Wells, tube well ,tank and lakes. In the context of source of irrigation well and tube wells are the dominated source of irrigation and very less by tanks and lacks. Canals as a source of water is applicable for irrigation when availability of water in projects. Table no 1 indicates, In 2011 total 13262.15 hectare land area is irrigated out of net area sown (NAS) of Shirpur tehsil. Highest irrigated area observed in Arthe revenue block that is 3613.40 hectares and lowest in Sangavi with 1004.76 hectares. In the study region 21.55 % area irrigated to net sown area of tehsil in agricultural 2011.

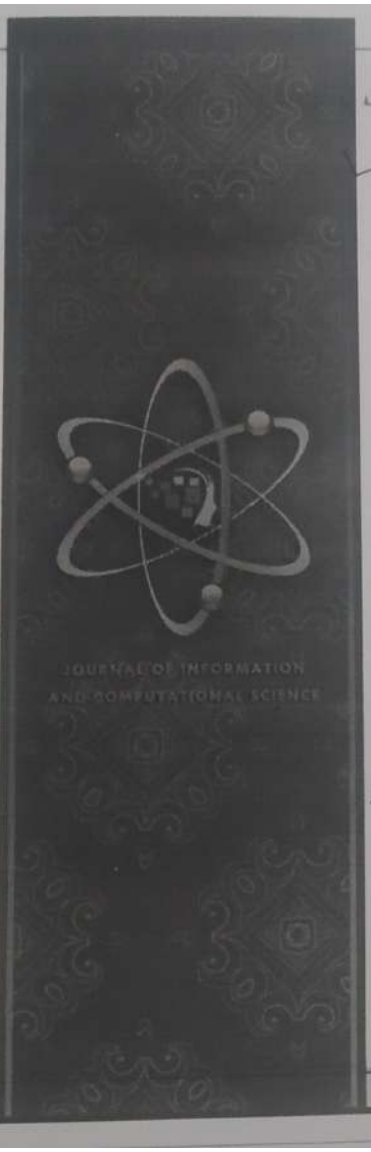

Journal of Information and Computational Science

UGC - Care Group - II Certified Journal

ISSN NO: 1548-7741 / web : www.joics.org / E-mail : submitjoics@gmail.com

Certificate of Publication

This is to certify that the paper entitled

Tehsil wise Distributional Pattern of population in Dhule district of Maharashtra State.

Authored by :

PROF. BHARAT DAGA PATIL

From

R. C. PATEL ARTS, COMMERCE AND SCIENCES COLLEGE, SHIRPUR, AFFILIATED TO KBCNM, UNIVERSITY, JALGAON. MAHARASHTRA STATE

Has been published in

JOURNAL OF INFORMATION AND COMPUTATIONAL SCIENCE,VOLUME 10 ISSUE 12,DECEMBER-2020

S. Joseph

Joseph Sung
Editor-In-Chief
JOICS

6.2

ISO International Organization for Standardization
7021-2008.

point of view of their utility in varies types of analytical studies, various types of densities are calculated. Trewartha G. T. (1969) in his case for population geography had suggested three types of density calculation arithmetic, physiological and agricultural densities. Rural density is also calculated by the geographers. While calculating density, total population is taken as numerator while total area is taken as denominator. This ratio gives density of population of a region. Density of population is expressed in terms of persons per square kilometre. Here calculate arithmetic, physiographic and agricultural density calculates on tahsil level using 2011 population data.

Arithmetic Density of Population: - Arithmetic density is a ratio between total population and total area of the region. It is useful in understanding the man-land relationship. Geographers and other social scientist have been making frequent use of such a calculation for planning and future management. In short population density gives the pressure of population over a land area, which can be measured in sq. km. or miles. Thus, it is a measurement of persons per sq. km. or per sq. miles of land area. In this arithmetic ratio calculation, numerator is population number and denominator is area. So, the general density is also known as 'Arithmetic Density'. It is calculated with the help of following equation- Arithmetic Density of population = Total Population / Total Area

Table no 2 Dhule District: Densities of Population in 2011

S. N.	Name of tehsil	Total Geographical Area	Total Population	Density of Population	Cultivated Area (In ha.)	Physiological Density	Population Engage in Agriculture	Agricultural Density
1	Shirpur	2364.53	422137	17	103562	40	1559	151
2	Shindkh	1300.53	323157	24	95708	33	1221	128
3	Sakri	2416.11	464913	19	126250	36	2106	167
4	Dhule	1981.94	840655	42	122306	68	1799	147
Dhule District		8063.11	2050862	25	447826	458	668675	149

Source: District census handbook of Dhule district and tabulated by researcher

Table 2 reveals arithmetic density of population in Dhule district. Overall in Dhule district arithmetic density of population is 254 persons per square km in 2011 Which is varies on tahsil level from 179 persons per square km in Shirpur to 424 persons per square km in Dhule tahsil. Highest arithmetic density of population observed in Dhule tahsil by 424 persons per square km because of being there Dhule town which is most populous city of Dhule district. Lowest arithmetic density of population noted in Shirpur tahsil with 179 persons per square km. Shirpur tahsil has lowest arithmetic density because half geographical area of tahsil acquires by mountainous and hilly area being there Satpura mountain ranges. Shindkheda tahsil has also moderate level (248 persons per square km of arithmetic density of population because of its plain nature of ground surface and high proportion of net sown areas to total geographical area of tahsils.

Physiological Density of Population

It is a ratio between total population and area under agriculture. It is expressed in terms of population per acre or hectare of area under agriculture. It is quite useful for the countries whose economy is based on agriculture. *The physiological density or real population density is the number of people per unit area of arable land. A higher physiological density suggests that the available agricultural land is being used by more and may reach its output limit sooner than a country that has a lower physiological density. Egypt is a notable example, with physiological density reaching that of Bangladesh, despite much desert (Wikipedia)*

Physiological Density = Total population / arable land. Physiological density of population always high than arithmetic density of population of any region because here considers only area under agriculture to calculate man land ratio. According to table 2.0, overall physiological density of Dhule district is 458 persons per hectare cultivated area in 2011. Highest physiological density of population recorded in Dhule tahsil by 687 persons per hectare cultivated area because of large size of population being there Dhule town and small size of cultivated area due to lack of water for irrigation and rocky surface area. While lowest physiological density of population noted in Shindkheda tahsil with 338 persons per hectare cultivated area because of its plain nature of surface which responsible for high proportion of net sown area. It has Sakri and Shirpur tahsils have physiological density by 368 and 408 persons per hectare cultivated area respectively.

Agricultural Density of Population

Agriculture population density indicates the density of population which is engaged in agriculture and area under agriculture. This is a quite useful tool in understanding the nature of man-land relationship. It is ratio between people engaged in agriculture and area under agriculture.

Agricultural Density = Number of People Engaged in Agriculture / Total Area under Agriculture in Hectares X 100. Therefore, the agricultural density is expressed in terms of agricultural population per unit of cultivated area. It has proved to be a useful index of man land relationship in primarily an agrarian context (Sing, 2006). Table 2.0 reveals that in Dhule district 668675 persons engaged in agriculture as cultivators and agricultural labours those are cultivating 447826 hectares area. In 2011, Dhule district has 149 agricultural densities. Highest agricultural density of population observed in Sakri tahsil by 167 persons engaged per 100 cultivated areas because in Sakri tahsil high share of population inhabited in rural areas and engaged in agricultural activities. Lowest agricultural density shows in Shindkheda tehsil by 128 because of high proportion of cultivated area in total geographical area of the tahsil. Shirpur and Dhule tahsils have moderate agricultural density by 151 and 147 persons (population engaged in agriculture) per 100 hectares cultivated area respectively in 2011. In Dhule and Shirpur tehsil have moderate agricultural density because its large portion of population inhabited in towns as urban population which engaged in non-agricultural activities.

Tehsil wise Distributional Pattern of population in Dhule district of Maharashtra State.

Prof. Bharat Daga Patil, *R. C. Patel Arts, Commerce and Sciences College, Shirpur.*

Affiliated to KBCNM, University, Jalgaon. Maharashtra State

E-mail – bharatdpatil1966@gmail.com

Mr. Lotan Zawaru Patil *(Research Student)* lotanpatil1664@gmail.com

Abstract

In this study the researcher has focuses on distributional aspects of population in the study region. Tehsil is an administrative unit in the district. Dhule district chosen as a study region for present work and has four tehsils and significant location. Satpura mountain ranges, Galna hill and river basins make the districts diversified topography and uneven population holding capacity. The region has northern and south western part is mountainous so holds low density of population while basin are of Tapi river and her tributaries has note moderate to high population density. According to 2011 Census the total population of Dhule District is 2050862. Out of total this population 1054031 is male and 996831 female populations. It constitutes 1.83% of State population spread over 3.82% of its area out of total geographical area of Maharashtra state. Dhule district has 72.16 percent proportion of population inhabited in rural areas which is higher than the state against 54.78%. Dhule district had 21.56 percent urban population to total population in 2011. In Dhule district arithmetic density of population is 254, physiological density is 458, and agricultural density is 149 persons per square kilometre as per 2011.In 2011, highest population concentration index observed in Dhule tahsil by 1.61 and lowest in Shirpur tahsil with 0.70 population concentration index. A study of population distribution is thus descriptive as well as analytical. The concept of population distribution and density is a very useful tool for the analysis of population distribution in space (Clarke, 1972). In present study population data have gathered from District Census Handbook, Dhule District for 1961 to 2011 on district level and 2001 to 2011 at tahsil level on male, female, schedule cast, schedule tribe, rural and urban population. Arithmetic, agricultural and physiological density has computed by using formula. Population concentration and population growth rate have calculated for identifying changes in population characteristics for study region. The present study deals with the distribution, of population in study region. The present study is based on secondary data. The present research work depends on the following sources of data. Primary Data and Secondary data collected from various governmental, semi-governmental, offices such as District Statistical Department, District Collector Office, Zilla Parishad Office. Dhule district is considered as the universe for the purpose of the present study.

Keywords: *population, density, concentration, correlation, distribution, Pattern.*

Introduction

The Distribution of population is important aspect of population characteristics. It is a geographical phenomenon and is uneven over the surface of the earth. It is mainly related to the location and area. The concept of distribution of population is concern with aerial variation and aggregative parts of the statistical units. In Population geography studied population change over time and space and it also studies the various determinants of population change and the impact of such changes on socio-economic development of region. It is not only necessary to describe how population distributed spatially in terms of density, composition and dynamics, but also to seek reasons for the patterns of this distribution and for spatial changes in these patterns, if any. A study of population distribution is thus descriptive as well as analytical. The concept of population distribution and density is a very useful tool for the analysis of population distribution in space (Clarke, 1972). The distribution of population means the dispersion of population in study region. The differences from place to place in racial and social character of population are studied in social science (James, 2011).The study of population gives an idea about the distribution and characteristics of population. The density is one of the parameters for measuring population ratio of the region. This can be measured by arithmetic, agricultural and physiological. The population distribution is studied in terms of population concentration. From this point of view, it is interesting to study the population and their changes in study region. The change in population is not only change in its numbers but also, its changes in structure, composition and distribution with respect to region and time. Population growth is the indicator of economic and social development. The study of measurement of such change, both temporal and spatial and comparative study gives an idea about changing characteristics of population of study region. According to Trewartha, Population Geography is the spatial study of human population concerned with its spatial distribution and arrangements. This view indicates that, the essence of population Geography lays in understanding the regional differences in the people covering the earth and the fact that population provides focal point in Geography. According to Ghosh B.N. (1985) Population Geography is the branch of the discipline which treats the spatial variations in demographic and non-demographic qualities of human population, and the economic and social consequences stemming from the interaction associated with a particular set of conditions existing in given areal unit.

Location of study Area

Dhule district is located at foot of Satpura ranges and Tapi basin in the north- western part of the Maharashtra State. It extends between 200 38' to 210 38' North latitude and 730 52' to 750 11' East longitude. Dhule district covers an area of 8063.11 sq. km., which is 2.62% of the total geographical area of the state. It spreads 108 km. from west to east and 112 km north

About the Author

Prof. Bharat Daga Patil

Prof. Bharat Daga Patil [M.A.M.Phil.Ph.D], Associate Professor of Geography at R. C. Patel Arts, Commerce and Sciences College, Shirpur, Karwand Road, Shirpur, Pin -425405 (Maharashtra State).he has thirty years teaching experience at undergraduate college. He actively engaged in doing research in the subject of geography. He has published twenty nine researches Paper in national and international journals and published three books. One student awarded Ph.D and currently one student doing research under the guidance of him.

Published by

Lulu.com
3101, Hillsborough St.
Raleigh, NC 27607,
United States.

9 781716 201660

Water Management and Inclusive Growth of Agriculture



Prof. Bharat Daga Patil

Kanpur Philosophers
ISSN 2348-8301
International Journal of humanities, Law and Social Sciences
Published biannually by New Archaeological & Genological Society
Kanpur India

Vol. VIII, Issue I (Summer) 2021

Gender Issues in Depression

Dr. Milind Bhagwanrao Bachute
R.C. Patel Arts. Commerce & Science College,
Shirpur Dist. Dhule
Maharashtra State.

Abstract
Depression is a common mental illness that affects over 264 million people around the world. It's marked by recurrent depression and a lack of interest or enjoyment in previously satisfying or pleasurable behaviours. It can also affect sleep and appetite, tiredness and poor concentration are common. Depression is a leading cause of disability around the world and contributes greatly to the global burden of disease the main objective of the study to investigate the depression, anxiety and stress of man and women. Deal with depression, anxiety, and stress. A total of 64 participants were chosen, including 32 men and 32 women. Using the DASS-42 Inventory, they were evaluated. There were no associations between male and female, according to the findings of the correlational study.
Keywords: Depression; Anxiety; and Stress; Gender Issue.

1. Introduction

Depression is a common mental illness that affects over 264 million people around the world. It is characterized by persistent sadness and also a lack of interest or pleasure in previously rewarding or enjoyable activities It can also affect sleep and appetite, tiredness and poor concentration are common. Depression is a leading cause of disabilities around the world and contributes greatly to the global burden of disease. The effects of depression can be long-lasting or recurrent and can dramatically affect a person's ability to function and live a rewarding life.

The causes of depression include complex interactions between social, psychological and biological factors. Life events such as childhood adversity, loss and unemployment contribute to and may catalyse the development of depression.

Psychological and pharmacological treatments exist for moderate and severe depression. However, in low- and middle-income countries, treatment and support services for depression are often absent or underdeveloped. An estimated 76–85% of people suffering from mental disorders in these countries lack access to the treatment they need.

1.1 Differences Between Male and Female Depression

Sr.No	Women with depression	Men with depression
1	Blame themselves	Feel others are to blame
2	Feel sad, apathetic and worthless	Feel angry, irritable and ego-inflated
3	Feel anxious and scared	Feel suspicious and guarded
4	Avoid conflicts at all costs	Create conflicts
5	Feel lethargic	May act overtly or covertly hostile
6	Have trouble with self-respect	Attack when feeling hurt
7	Sleep too much	Demand respect from others
8	Feel guilty for what they do	Feel the world set them up to fail

Kanpur Philosophers

CERTIFICATE OF PUBLICATION

This is to certify that the article entitled

Gender Issues in Depression

Authored By

Dr. Milind Bhagwanrao Bachute

R.C. Patel Arts, Commerce & Science College, Shirpur Dist. Dhule, Maharashtra State.

Published in Vol.-VIII, Issue-I : 2021
Kanpur Philosophers with ISSN 2348-8301
UGC-CARE List Group I

UGC
University Grants Commission

Editor-in-Chief

KANPUR PHILOSOPHERS

ISSN 2348-8301

International Journal of Humanities, Law and Social Sciences Published Biannually by New Archaeological & Genological Society Kanpur India

Vol. VIII, Issue-I, 2021

DRSR
Journal

ISSN 2347-7180

UGC CARE Group I Journal

CERTIFICATE
OF PUBLICATION

This is to Certify that the Paper Entitled

A STUDY ON NEW WORK OPENINGS IN THE RUSTIC REGION WITH SPECIAL REFERENCE TO NORTH MAHARASHTRA

Authored by

Dr. Anil G. Sonawane
Associate Professor, R. C. Patel ACS College Shirpur

Vol. 10 Issue. 12 No. 03 Month **December** Year. 2020

Has been published in

Dogo Rangsang Research Journal

Impact Factor : 7.12

DRSRJ

Editor

Impact Factor 7.12

UGC
University Grants Commission
Approved Journal

doi
crossref

A STUDY ON NEW WORK OPENINGS IN THE RUSTIC REGION WITH SPECIAL REFERENCE TO NORTH MAHARASHTRA

Dr. Anil G. Sonawane Associate Professor, R. C. Patel ACS College Shirpur[1]
Mr. Yogesh C. Shethiya Assistant Professor, RCPET's IMRD, Shirpur[2]

Abstract:
Increase of new work opportunity has been an indispensable motivation behind advancement arranging in India. There has been an extensive development in work throughout the long term. On the other hand, a relatively privileged growth of populace and labor force has show the way to a boost in the number of idleness from one period to another. The extraordinary promise of the current Government of India to sincerely deal with the need for employment creation is a favorable prospect to put into action approach for engender full employment in the rural areas. The most important aspire of rural persons is to get hold of good and well-paid employment chance. This research study observes the drawing closer for area explicit profitability development, work, credit markets, and framework to add to the advancement of steady, generously compensated work in provincial territories.
The significant motivation behind this exploration study is to get a capable insight of work openings, in which country people are involved. The significant regions that have been considered are, the climate of joblessness in the rustic zone of the North Maharashtra district, kinds of work openings in the provincial gathering of people, factors that convince individuals to get occupied with business openings, and variables impacting the obtaining of business openings.

Keywords: Employment Opportunities; Productivity growth Expansion; Development

Introduction

India has come sent as one of the brief developing nations in the globe with exhaustive reform in its rustic market as much as in the all in all market. All the rising nation, India extras basically country with about 70% of its kin and around 65 % of its laborers unmoving operational and living in rustic territories, While by the focal of the most recent decade over half the world's kin were vocation in metropolitan regions, there is proceeding with the quick relationship of individuals to metropolitan zones. India with a provincial populace of 842 million, which is already predominant than China's rustic populace of 725 million (Proctor and Lucchesi 2012), will stay home to the biggest country populace on the planet even in 2050 – regardless of whether its provincial populace diminishes in size to about 30%. This builds it even more critical to know about the technique of progress in country India with regards to the nearly quick extension.

This exploration study clarifies the dynamic of revamping with fussy reference to provincial work and environmental factors of life and job of rustic business. One of the significant breakdowns of monetary improvement in post-Independent India hangs about its inadequacy to impressively recoil the dependence of laborers on cultivating. Notwithstanding the way that add to Gross Domestic Product induces from cultivating has gone down from throughout half at the hour of Independence to almost 14% as of now, add to laborers occupied with cultivating, which was about 70% in 1951, still extras at over half. This has prompted make more extensive space flanked by income in cultivating and nonagricultural regions, which is shallow to be one of the main justification for the goal of insufficiency in the country. The space flanked by the numeral of new country representatives and the numeral of imaginative employment opportunity formed in cultivating is growing. Hence, the provincial utilize broadening towards the non-farming region has extended perilous centrality over the long haul. The organization of India is amazingly fearful with the notable insufficiency and being without occupation in the provincial territories and has full in excess of a couple of plan including the execution of Mahatma Gandhi National Rural Employment Guarantee Scheme (MGNREGS). The rustic area in India is going through a change and the commitment of provincial non-ranch area to the country pay and work is developing. A few examinations on country work broadening in India (Kumar, 2009; Mukhopadhyay and Rajaraman, 2007; Chadha and Sahu,

Half Yearly -
Issue XI ol II , Oct. 2020 | Peer Reviewed SJIF | ISSN : 2319 - 8648 Impact Factor : 7.139

Current Global Reviewer

UGC Approved International Research
Refereed Multidiciplanary Journal

Editor In Chief
Mr. Arun B. Godam

ISSUE X Volume I (Half Yearly) Nov. 2017 To Apr. . 2018

Published on Feb. 2018

Editorial Office Address :

Khadgaon Road, Kapil Nagar, Latur,
Dist. Latur 413512 (M.S.) India

Contact- 8149668999

Email-
hitechresearch11@gmail.com

Publisher
Shaury Publication
Kapil Nagar, Latur
Contact- 8149668999

Rs. 400/-

www.rjournals.co.in

Present Preface Message

Honourable Prof.,

Here's a great pleasure to hand over this + research Journal title **'Current Global Reviewer'** At Present different papers are published through various branches ofknowledge.But they are concerned to specific subject or thought. We are very glad in publishing this paper to get the more information about research to new learner about research in all the spheres. This is the age of supersonic. That is why we must concentrate at present at a large scale in higher education. It's very important in this modern phase for researchers and to encourage for the effort put by us. In the long run it will very useful for us as guide lines and directions.

'Current Global Reviewer' has been started to publish the research paper by great thinkers, intelligentia, scholars, lectures. Those who have contributed in the field of higher education and research for advanced knowledge. We are publishing research paper written in Marathi,Hindi& English, Languages. It has been included research papers in language and literature, Social Science, Social work , commerce, Management, Law, Computer Science etc.

Hope you will remain in

Co- Operation in future

Thank You.

Editor In Chief

Mr. Arun B. Godam

Editoral Board Member

CURRENT GLOBAL REVIEWER
Half Yearly - Issue XI ol II , Oct. 2020 | Peer Reviewed SJIF | ISSN : 2319 - 8648 Impact Factor : 7.139

Index

Sr. No.	Article Title	Author	Page No.
1	Innovative Teaching Methods And Their Significance	*Dr. BalidUjwala Shimon*	1
2	Corn Productivity in Solapur District : A Geographical Study	Dr.P.Y. Magare	5
3	Comparative Politics	MrsMaimanatJahanAra	10
4	Demonetization and Electronic Payment System	Prof .DurdanaSiddiqui	16
5	Digital payment system: Financial Literacy	MemonSohelMohd Yusuf	23
6	Impact of Digital Payment System and Social Life	SiddharthNisargandha	29
7	Women Empowerment	DrPadmapaniBhagwanSawai	37
8	Issues In Rural Community DevelopmentShambhuDutt	SharadSuryakantPawar	42
9	*In Vitro* Antagonistic Activity of *Trichoderma*species against *Macrophominaphaseolina*(Tassi) Goid	Dr. AithalSadanand V.	45
10	६ महाराणा प्रताप : एक मातृभक्त स्वाभिमानी योध्दा	देशमुख गंगाधर बालाजीराव	50
11	भाषांतर-अनुवाद प्रक्रियचे स्वरूप	प्रा.डॉ. संतोष चंपतीहंकारे	55
12	छत्रपती शाहू महाराजांचे शैक्षणिक योगदान	डॉ. श्रीहरी दासु चव्हाण	59
13	संस्कृत बसवपुराण हस्तलिखितामध्ये वर्णिलेली महात्मा बसवेश्वराची आर्थिकसुधारणा	प्रा. शंकर धारबा घाडगे	62
14	डॉ. बाबासाहेब आंबेडकर यांच्या विचारातील आदर्श समाज आणि वास्तवता	दिपाली चंद्रकांत पांडे	66
15	" बुद्धतत्त्वज्ञानाची मुख्य आधारतत्त्वे व नैतिक शिकवण "	डॉ. बालाजी मा. गव्हाळे	69
16	‘‘महाराष्ट्रातील संत गाडगेबाबा ग्रामस्वच्छता अभियान : एक प्रशासकीय अभ्यास’’	प्रा. डॉ. श्यामसुंदर वाघमारे	75

17	भारतीय दर्शनातील 'आत्म' विषयक संल्पना	प्रा. शितल रुद्रमनी येरुले	80
18	तत्त्वज्ञानाच्या अध्यापनातील अडचणी व उपाय	प्रा.माधवीबादाडे	84
19	हरभरा पीक उत्पादकतेचा भौगोलिक अभ्यास : विशेष संदर्भ लातूर जिल्हा	प्रा.डॉ.आर.एस. धनुश्वर	87
20	धूमिल की भाषा	डॉ. सुभाष इंगळे	90
21	शारीरिक शिक्षणाची ध्येये व उद्दिष्ट्ये	डॉ. सतीश नारायण लोमटे	92